Canadian Beaufort Sea - Marine Ecosystem Assessment (CBS-MEA) report on the physical system - 2019

Ryan Galley, Andrea Niemi, Jane Eert, Andrew Majewski, and William Williams

Fisheries and Oceans Canada
Freshwater Institute
501 University Crescent
Winnipeg, Manitoba
Canada, R3T 2N6

2023

Canadian Technical Report of
Hydrography and Ocean Sciences 364

Fisheries and Oceans Canada | Pêches et Océans Canada

Canada

Canadian Technical Report of Hydrography and Ocean Sciences

Technical reports contain scientific and technical information of a type that represents a contribution to existing knowledge but which is not normally found in the primary literature. The subject matter is generally related to programs and interests of the Oceans and Science sectors of Fisheries and Oceans Canada.

Technical reports may be cited as full publications. The correct citation appears above the abstract of each report. Each report is abstracted in the data base *Aquatic Sciences and Fisheries Abstracts.*

Technical reports are produced regionally but are numbered nationally. Requests for individual reports will be filled by the issuing establishment listed on the front cover and title page.

Regional and headquarters establishments of Ocean Science and Surveys ceased publication of their various report series as of December 1981. A complete listing of these publications and the last number issued under each title are published in the *Canadian Journal of Fisheries and Aquatic Sciences*, Volume 38: Index to Publications 1981. The current series began with Report Number 1 in January 1982.

Rapport technique canadien sur l'hydrographie et les sciences océaniques

Les rapports techniques contiennent des renseignements scientifiques et techniques qui constituent une contribution aux connaissances actuelles mais que l'on ne trouve pas normalement dans les revues scientifiques. Le sujet est généralement rattaché aux programmes et intérêts des secteurs des Océans et des Sciences de Pêches et Océans Canada.

Les rapports techniques peuvent être cités comme des publications à part entière. Le titre exact figure au-dessus du résumé de chaque rapport. Les rapports techniques sont résumés dans la base de données *Résumés des sciences aquatiques et halieutiques*.

Les rapports techniques sont produits à l'échelon régional, mais numérotés à l'échelon national. Les demandes de rapports seront satisfaites par l'établissement auteur dont le nom figure sur la couverture et la page de titre.

Les établissements de l’ancien secteur des Sciences et Levés océaniques dans les régions et à l'administration centrale ont cessé de publier leurs diverses séries de rapports en décembre 1981. Vous trouverez dans l'index des publications du volume 38 du *Journal canadien des sciences halieutiques et aquatiques*, la liste de ces publications ainsi que le dernier numéro paru dans chaque catégorie. La nouvelle série a commencé avec la publication du rapport numéro 1 en janvier 1982.

Canadian Technical Report of
Hydrography and Ocean Sciences 364

2023

CANADIAN BEAUFORT SEA – MARINE ECOSYSTEM ASSESSMENT (CBS-MEA) REPORT ON THE PHYSICAL SYSTEM – 2019

by
Ryan Galley, Andrea Niemi, Jane Eert, Andrew Majewski, and William Williams

Fisheries and Oceans Canada
Freshwater Institute
501 University Crescent
Winnipeg, Manitoba
Canada, R3T 2N6

Cat. No. Fs97-18/364E-PDF ISBN 978-0-660-68338-6 ISSN 1488-5417

Correct citation for this publication:

Galley, R., Niemi, A., Eert, J., Majewski, A., and Williams, W. 2023. Canadian Beaufort Sea - Marine Ecosystem Assessment (CBS-MEA) report on the physical system - 2019. Can. Tech. Rep. Hydrogr. Ocean Sci. 364: ix + 115 p.

CONTENTS

List of Figures

List of Tables

ABSTRACT

Galley, R., Niemi, A., Eert, J., Majewski, A., and Williams, W. 2023. Canadian Beaufort Sea - Marine Ecosystem Assessment (CBS-MEA) report on the physical system - 2019. Can. Tech. Rep. Hydrogr. Ocean Sci. 364: ix + 115 p.

Rapid changes in the physical system of Canada's western marine Arctic will affect ecosystem functions. The Canadian Beaufort Sea – Marine Environmental Assessment (CBS-MEA, 2017-present) provides comprehensive ecosystem knowledge of offshore waters, supporting co-management and community priorities. CBS-MEA complements community, coastal efforts that support detection and explanation of ecosystem-level variability and change. Key components of the physical system in 2019 are presented, providing the annual environmental context for CBS-MEA and other studies in the region. The ship-based Conductivity-Temperature-Depth (CTD) data collected in August and September 2019 reveal physical oceanographic characteristics in the region at that time and are summarized herein with profiles of temperature, salinity, potential density, and N^2, temperature-salinity plots, and temperature and salinity sections. The freshwater and ocean heat content of the surface layer have also been derived for the 59 CBS-MEA stations sampled in 2019. Anomalously warm air temperatures coupled with export-friendly winds over the region reduced regional sea ice concentration much earlier than normal, resulting in positively anomalous solar radiation incident on the open ocean in March-October, resulting in ocean heat content at the end of summer in the CTD data. Regional summer sea ice coverage was anomalously low, and freeze up was delayed in 2019.

RÉSUMÉ

Galley, R., Niemi, A., Eert, J., Majewski, A., and Williams, W. 2023. Canadian Beaufort Sea - Marine Ecosystem Assessment (CBS-MEA) report on the physical system - 2019. Can. Tech. Rep. Hydrogr. Ocean Sci. 364: ix + 115 p.

Les changements rapides dans le système physique de l'ouest de l'Arctique marin canadien affecteront les fonctions de l'écosystème. L'évaluation environnementale marine de la mer de Beaufort canadienne (CBS-MEA, 2017-présent) fournit des connaissances écosystémiques complètes sur les eaux du large, à l'appui de la cogestion et des priorités communautaires. La CBS-MEA complète les efforts communautaires et côtiers qui soutiennent la détection et l'explication de la variabilité et du changement au niveau de l'écosystème. Les composantes clés du système physique en 2019 sont présentées, fournissant le contexte environnemental annuel pour CBS-MEA et d'autres études dans la région. Les données de conductivité-température-profondeur (CTD) recueillies par les navires en août et septembre 2019 révèlent les caractéristiques océanographiques physiques dans la région à ce moment-là et sont résumées ici avec des profils de température, de salinité, de densité potentielle et de N^2, des tracés de température-salinité et des sections de température et de salinité. Le contenu en eau douce et en chaleur océanique de la couche de surface a également été dérivé pour les 59 stations CBS-MEA échantillonnées en 2019. Des températures de l'air anormalement chaudes couplées à des vents favorables à l'exportation sur la région ont réduit la concentration régionale de glace de mer beaucoup plus tôt que la normale, ce qui a entraîné un rayonnement solaire anormal positif incident sur l'océan ouvert en mars-octobre, entraînant un contenu thermique de l'océan à la fin de l'été dans les données CTD. La couverture régionale de glace de mer estivale a été anormalement faible et l'englacement a été retardé en 2019.

1 Introduction

The Canadian Beaufort Sea–Marine Ecosystem Assessment (CBS-MEA, 2017-present) seeks to increase understanding of processes affecting and controlling the regional ecosystem in space and time. Following on from the Beaufort Regional Environmental Assessment–Marine Fishes Project (BREA-MFP, 2012-2014), CBS-MEA focuses on marine waters of the Inuvialuit Settlement Region (ISR) and was developed in consultation with co-management partners, including the Inuvialuit Game Council, the Fisheries Joint Management Committee, and community Hunter and Trapper Committees. The Department of Fisheries and Oceans (DFO), along with university and community partners, gather vital information on offshore physical oceanography, primary productivity, marine chemistry, zooplankton, fishes, and the benthos. Integrative science of this nature is important to understand the effects of climate variability and change in the region. The ecosystem-based approach of CBS-MEA also supports priority concerns related to subsistence food security, shipping, ocean management and marine spatial planning, and new stressors like microplastics and invasive species. CBS-MEA seeks to support the development of science advice for co-management of the Beaufort Sea to conserve and protect aquatic species from human impacts, and to inform adaptation strategies for a shifting subsistence food base.

The region assessed broadly encompasses the Canadian Beaufort Sea, M'Clure Strait, the Mackenzie Shelf, and Amundsen Gulf, roughly bounded by longitudes -140°E to -110°E and latitudes 68°N to 75°N (Figure 1). Key features of the region include the Anguniaqvia niqiqyuma (DFO, 2015, Niemi et al., 2020, DFO, 2022) and Tarium Niryutait (DFO, 2010) Marine Protected Areas (MPAs), as well as a number of ecologically and biologically significant areas (EBSAs, e.g., DFO, 2014) (Figure 1), the Mackenzie River plume, and the Cape Bathurst Flaw Lead Polynya Complex (see for e.g. Stirling, 1980). CBS-MEA provides information relevant to the six ISR communities, including variables related to elements of the regional marine food web, from phytoplankton to belugas and bowhead whales. This report provides an overview oceanographic data collected during summer (August-September) 2019, and the physical forcing and processes within the atmosphere, sea ice, and ocean surface throughout 2019.

2 Data and Methods

This assessment of physical conditions and drivers in the ISR during 2019 includes air temperature, sea level pressure, winds, and solar radiation at the ocean surface from reanalysis products, remotely sensed sea ice concentration and motion data, and the ship-based oceanographic sampling of CBS-MEA. Climatological averages (1983-2010) have been calculated to determine how anomalous the conditions

were in 2019. Climatological averages ending in 2010 are established in sea ice literature, see for example Serreze and Stroeve (2015). CTD data are used to identify the surface salinity and temperature, the thickness of the ocean surface layer at sampling stations, and then the corresponding freshwater content and ocean heat content in the surface layer is calculated. Finally, cross-sectional oceanographic plots are presented in areas of the study region where CTD transects were conducted.

2.1 Environmental Forcing

European Centre for Medium-range Weather Forecasts (ECMWF) Reanalysis v5 (ERA5) 2 m air temperature, sea level pressure, 10 m u- and v- winds, and surface solar radiation downwards (SSRD) data at six-hourly intervals (Hersbach et al., 2018) from January 1, 1983 to December 31, 2021 were obtained from the Copernicus Climate Change Service Climate Data Store (https://cds.climate.copernicus.eu/cdsapp#!/dataset/reanalysis-era5-pressure-levels?tab=overview). Monthly averaged 2 m air temperature (Figure 2), sea level pressure (Figure 4), and 10 m wind speed and direction (Figure 6) were created for each of the 4089 ERA5 grid cells in the study region for each month of 39 years (1983-2021) including 2019 presented here. Monthly climatological standard normals (i.e. averages) for 2 m air temperature, sea level pressure, 10 m winds were produced from all the available data in each month in 1983-2010 (28 years; note we use 28 for this period beginning in 1983 in order to maintain consistency with the sea ice data which begins in 1983 – explanation to follow in section 2.2). Monthly anomalies of air temperature, SLP, and 10 m winds in 2019 (Figures 3, 5, 7) were calculated using the monthly climatological standard normal. For example:

$$T_{a\ anomaly} = T_a - T_{a\ clim} \quad (1)$$

Where $T_{a\ anomaly}$ is the air temperature anomaly in a month in 2019, T_a is the average air temperature in a month in 2019, and $T_{a\ clim}$ is the climatological average air temperature (1983-2010) for the month. Positive anomalies occur when the monthly average is greater than the climatological standard normal for that month, negative anomalies occur when the monthly average is less than the climatological standard normal for the month.

2.2 Sea Ice Concentration and Motion

Average sea ice concentration maps for each month between 1983 and 2021 were created by downloading and gridding regional Canadian Ice Service (CIS) digital archive data for the western Arctic (https://iceweb1.cis.ec.gc.ca/Archive/page1.xhtml?lang=en) at 1 km resolution on the CIS Lambert

conformal conic projection. Analysis of the CIS data began in 1983 because the data is broken down by consistent source data and preparation method eras, and the quality index prior to 1983 is reduced (please see Tivy et al., 2011 for detailed information on the CIS data quality indices). Using all the available CIS charts in each month in each year, the monthly mean total sea ice concentration (in tenths) and mean partial concentrations (in tenths) for (i) old ice (a superset of multiyear and second-year ice), (ii) first-year sea ice, and (iii) new-plus-young sea ice (< 30cm thick, Fequet, 2005) stages of development were computed at 1 km resolution (Figures 8, 10, 12, 14). Monthly climatological averages for total sea ice concentration as well as old sea ice, first-year sea ice, and new-plus-young sea ice were calculated by averaging all the data in each month between 1983 and 2010 (inclusive). Monthly concentration anomalies in 2019 for total, old, first-year, and new-plus-young ice concentrations (Figures 9, 11, 13, 15) were created by subtracting the months' climatological (1983-2010) average sea ice concentration from the corresponding monthly average concentration for each stage of development.

Monthly average sea ice velocity and direction in the Beaufort Sea from 1983 to 2021 (see Figure 16 for 2019) were calculated from the National Snow and Ice Data Centre (NSIDC) Polar Pathfinder Daily 25 km EASE-grid sea ice motion vector data (Version 4) (Tschudi et al., 2019) for the northern hemisphere, freely available at https://nsidc.org/data/NSIDC-0116. Climatological monthly averages for each month were created using the u- and v- components for each month between 1983 and 2010 (inclusive). Monthly anomalies for 2019 (Figure 17) were created by subtracting the monthly climatological standard normal u- and v- components of the sea ice motion from the monthly average sea ice motion u- and v- components in each year.

2.3 Sea ice-adjusted Surface Solar Radiation Downwards

ECMWF ERA5 surface solar radiation downwards (SSRD, in J m^{-2}) data were also downloaded from the Copernicus Climate Change Service Climate Data Store (see link above) at six-hourly intervals between 1983 and 2021 (inclusive). SSRD is the amount of shortwave radiation (including both diffuse and direct radiation) that reaches a horizontal plane at the surface of the earth; it is the model equivalent of the shortwave radiation a pyranometer would measure at the surface. In this case in particular, SSRD may be thought of as light energy from the sun that may be converted to heat energy if it is absorbed by the surface of the ocean, either melting surrounding sea ice, or contributing to increased water temperatures. The SSRD must be adjusted for sea ice cover in order to conservatively approximate the amount of solar radiation incident only on the ocean surface in the Arctic marine environment. In each month of each year between 1983-2021, the CIS monthly mean total sea ice concentration grid was downscaled to the ERA5

grid resolution, divided by 10 to obtain a fractional coverage, and then subtracted from unity to obtain the monthly fractional open water area in each grid cell. The fractional open water area in a month was multiplied by the mean SSRD for the month to obtain the sea-ice adjusted SSRD (J m^{-2}) incident on the ocean surface in each grid cell (Figure 18). Monthly climatological averages (Figure 18) over the period 1983-2010 were calculated using the sea ice-adjusted monthly mean SSRD, and monthly anomalies of sea ice-adjusted SSRD (Figure 19) were calculated for each month in each year between 1983 and 2021. Again, this approach is very conservative. It is biologically important to note that SSRD is variably transmitted through even snow covered sea ice (see for e.g. Nicolaus et al., 2013).

2.4 CBS-MEA sampling

Physical oceanographic sampling during CBS-MEA (2 August-3 September 2019) was undertaken from *FV Frosti* at stations in central Amundsen Gulf, across Amundsen Gulf from Cape Bathurst to Sachs Harbour, near Cape Parry, in Franklin Bay, in Darnley Bay, Dolphin and Union Strait, Minto Inlet, and across the shelf break north of Kugmallit Bay (Figure 22). Conductivity, temperature, and depth (CTD) measurements were made using a Seabird SBE 911plus deployed as part of the ships' CTD-Rosette system. Average salinity (PSS-78) and temperature (ITS-90, °C) over 1 decibar (approximately one meter) increments were output after the CTD data underwent quality control (bottle salinity samples were collected with the rosette and used as part of data quality assurance and control processes, salinity is considered to be accurate within ±0.003). An altimeter was employed for water depth measurements, and the noted depth at each station (Table 1) was the median of the deepest two meters recorded. In the absence of altimetric measurements at a station, the deepest depth measured by the CTD was used.

The value of temperature and salinity measured closest to the surface (the minimum depth of the surface value was 1.2 dbar, the mean depth of the surface value = 2.33 dbar, and the maximum depth of the surface value was 5 dbar (Table 1)) at each of the 59 stations in 2019 were mapped. Potential density referenced to the surface ((σ, θ), minus 1000 kg m^{-3}) and N^2, the square of the buoyancy frequency (s^{-2}), were calculated for each depth in the CTD data using the OCE package (Kelley, 2018) for R (R Core Team, 2022). Potential density referenced to the surface is the density of seawater with the compressive effect of pressure removed, allowing better comparison between water from different depths. 1000 kg m^{-3} is subtracted as a way to highlight the small variations in seawater density that drive ocean dynamics. The buoyancy frequency squared (N^2) profile is one way to find the interface between two ocean layers. It is a measure of the variation of density with depth, indicating the strength of the ocean's density stratification. It is calculated as:

$$N^2 = \frac{g}{\rho} \times \frac{d\rho}{dz}$$

(2)

where *g* is gravity, ρ is density and *z* is depth.

The depth of the N^2 maximum was identified (Table 1) in each profile (Appendix A), and that value was used to connote the bottom of the surface layer of the water column. The N^2-maximum-derived surface layer depth at each of the 59 stations was used to calculate the total freshwater content (FWC, in meters) and the total ocean heat content (OHC, in kilojoules) in the surface layer at each station. The FWC and OHC values were integrated in a 1 m^2 column of water over the depth of the surface layer, using the FWC and OHC calculated for each 1-decibar interval. The FWC was calculated at each decibar of the N^2-maximum-derived surface layer:

$$FWC = \frac{S_o - S}{S_o}$$

(3)

where S_o is the reference salinity of 34.8 and *S* is the salinity at each depth interval. The FWC values at each depth from the surface to the surface layer depth were summed. The OHC relative to 0°C was calculated at each decibar depth interval in the of the N^2-maximum-derived surface layer:

$$OHC = c_{sw} \times \rho \times \Theta$$

(4)

where c_{sw} is the specific heat capacity of seawater (set to 4 for the observed temperature and salinity ranges, see Sharqawy et al., 2010), ρ is seawater density calculated using absolute salinity and conservative temperature, Θ. The OHC values at each depth from the surface to the N^2-derived surface layer depth were summed.

3 Results and Discussion

Air temperature, sea level pressure (SLP), wind, sea ice concentration and motion, and surface solar radiation results and discussion are presented by season with winter (January February, March), spring (April, May, June), and summer (July, August, September), summarizing key processes and physical drivers prior to and during the CBS-MEA cruise (2 August-3 September). Finally, autumn (October, November, December) conditions are presented to provide the full annual perspective of temperature, SLP, sea ice

concentration and motion, and solar radiation in a marine area assessed largely corresponding to the marine area of the Inuvialuit Settlement Region.

3.1 Winter

In January 2019, the marine and terrestrial environments in the study region experienced very warm air temperatures (Figure 2) that were up to 8 °C greater than the climatological standard normal (Figure 3). In February 2019, the region was again warmer than average along the continental shelf areas west of Cape Bathurst and in M'Clure Strait, with positive air temperature anomalies across western Amundsen Gulf (3-5 °C) and Banks lsland. Colder than average air temperatures existed over the Beaufort Sea west of Banks Island and in eastern Amundsen Gulf and Dolphin and Union Strait in February 2019, a pattern that persisted and strengthened in March 2019 (Figures 2, 3).

Winter in the region is typically characterized by low SLP in the southwest over the Brooks Range in northeastern Alaska, high SLP in the northwest (i.e., the Beaufort High), and high SLP over the north coast of the mainland. In January 2019, the SLP was lowest in the southwest and lower than average over most of the ISR region, with very small positive SLP anomalies over Victoria Island and the south end of Dolphin and Union Strait (Figures 4, 5). Through February and March the Beaufort High strengthened in the northwest, while lower pressure occurred in the southwest and northeast corners of the region (Figure 4). High SLP areas in February and March were higher than average, while low pressure regions in the southwest and northeast were lower than average (Figure 5). The wind direction in winter 2019 was similar to the climatological standard normal. But, due in part to the intensity and proximity of the positive and negative SLP anomalies in the region, the winter wind speeds were much greater than the climatology (Figures 6, 7) especially in the western Beaufort Sea and in M'Clure Strait. Very small negative wind speed anomalies occurred in eastern Amundsen Gulf in winter 2019 (Figure 7).

Sea ice coverage in winter 2019 was nearly complete in all three months (January, February, March) (Figure 8) with landfast sea ice ($10/10^{ths}$, darkest red, Figure 8) occurring in Dolphin and Union Strait, Prince of Wales Strait, much of M'Clure Strait, and near-shore areas along the continental coast and its embayments. Mobile sea ice, indicated by sea ice concentrations less than $10/10^{ths}$, dominated the region including the Beaufort Sea and the entirety of Amundsen Gulf in winter 2019 (Figure 8). Within the winter total sea ice concentration, old sea ice was predominately sequestered in the northwest quadrant of the region and in M'Clure Strait. First-year sea ice dominated the total sea ice concentration from the northwest corner of Banks Island over much of the southern Beaufort Sea and shelf and in Amundsen Gulf

and its embayments (Figure 8). New-plus-young sea ice concentrations (<30 cm thick) were considerable in the flaw lead area along the Mackenzie Shelf, around the circumference of Amundsen Gulf, and along the west coast of Banks Island in winter 2019 (Figure 8). The extension of the high concentration old sea ice westward over the three winter months, substantial and increasing concentrations of first-year sea ice south of the old ice zone, and new-plus-young sea ice production in all or part of the Cape Bathurst flaw lead polynya complex in winter (Figure 8) indicate consistent, substantial westward sea ice motion in those months.

Winter 2019 sea ice concentration anomalies in the region were substantial (Figure 9). M'Clure Strait contained much more old sea ice than the climatological average, and the northwest quadrant of the study region contained a little more old sea ice than average (Figure 9). Much less old sea ice than the climatological average was observed in the southern periphery of the Beaufort Sea pack, which instead contained substantial positive first-year sea ice concentration anomalies (Figure 9). The westernmost reaches of the study region contained the greatest positive first-year sea ice anomalies in winter 2019. Positive new-plus-young sea ice concentration anomalies occurred in winter 2019 in the Cape Bathurst flaw lead polynya complex (Figure 9), the presence of which in monthly average plots under consistently cold air temperatures (Figure 2) is evidence of persistent divergence in the ice pack. The effect of the enhanced, consistent easterly winds (Figure 6) in winter 2019 are obvious in the sea ice concentration data (Figure 8, 9), especially with respect to the first-year and new-plus-young sea ice concentrations. Persistent and strong easterly winds (Figure 6) were likely responsible for moving sea ice away from the west coast of Banks Island and Amundsen Gulf in all three winter months. The heightened presence of new-plus-young sea ice in January despite slower easterly winds than in February and March is likely due to thinner first-year sea ice with lower internal stress in the mobile pack as a whole in January. Thinner, more deformable ice was prevalent throughout the region and across the Alaskan coast and into the Chukchi Sea in January, allowing for enhanced wind-driven ice motion, specifically western export from the study area. In February and March, the effect of wind on the sea ice pack west of the mouth of Amundsen Gulf is notable, particularly in the first-year sea ice concentration maps (Figures 8, 9). It is clear that first-year sea ice was exported westward from the ISR in February 2019 especially (Figures 6, 8). Finally, March westerly winds were consistent and fast, blowing into M'Clure Strait. Sea ice motion in the winter months (Figures 16, 17) lends further credence to the wind-driven processes discussed above; anticyclonic (clockwise) ice motion was prevalent in the region in January and March (Figure 16) at anomalously high velocities (Figure 17). In February, the regional sea ice motion pattern was dissimilar to

the climatological average. Sea ice moved west out of the study region across the southern Beaufort Sea (Figure 15) at relatively high velocity (Figure 17).

3.2 Spring

In April 2019, air temperatures were warm across the Beaufort Sea shelf, and cooler in eastern Amundsen Gulf and in the northern half of the Beaufort Sea (Figure 2). The coldest April air temperatures occurred terrestrially on Banks and Victoria Islands. The April 2 m air temperature anomalies (Figure 3) indicate that normally warm areas were warmer than the climatological standard normal (1983-2010) for April, while normally cold areas were colder than the climatological standard normal. In May and June the air temperature in the region warmed (Figure 2), with May being anomalously warm over the whole of the region (Figure 3). Almost the entire study region was above 0 °C on average in June 2019 (Figure 2) and the terrestrial areas became warmer than the marine areas in the region. Positive air temperature anomalies occurred in June 2019 over much of the mainland, across the southern Beaufort Sea and shelf extending northeast across western Amundsen Gulf and Banks Island (Figure 3).

The SLP in spring maintained its general winter pattern for April and May, while in June there occurred high pressure in the middle of the region at the mouth of Amundsen Gulf, as well as over central Victoria Island (Figure 4). In June, lower SLP occurred in the northwest and southwest corners of the region. Monthly SLP anomalies indicate that the pressure was higher than the climatological standard normal over the entire region in April and May, and was negatively anomalous over the entire region in June (Figure 5). Following on from the SLP, the monthly mean winds and their corresponding anomalies are shown in Figures 6 and 7. The mean wind direction in April and May was typical of the climatological standard normal; winds were generally anticyclonic and blowing from the north towards the mainland, and from the northeast away from the coast of Banks Island and across the region (Figure 6). In April the wind speed was anomalously high in the southwest quadrant of the marine study region (Figures 6, 7). It was high and southeasterly in M'Clure Strait similar to March. In June the wind speed was much slower than the climatological standard normal for the area, and the direction was anomalous. Instead of anticyclonic winds prevailing over the Beaufort Sea and easterlies blowing out of Amundsen Gulf, the wind direction was weak (Figure 6) due to the position and strength of the high pressure region at the mouth of Amundsen Gulf in June (Figure 4). June winds were southerly in the northern half of the Beaufort Sea and faster than the climatological average, and northerly nearest the mainland and in Amundsen Gulf and slower than the climatological average (Figures 6, 7).

The mean total sea ice concentration in the region in April (Figure 10) began to show signs of spring breakup. Substantial new-plus-young sea ice concentrations occurred in much of the Cape Bathurst flaw lead polynya (along the coast of the mainland from the Mackenzie River to Dolphin and Union Strait, around the coast of Amundsen Gulf, and along the west coast of Banks Island), in western Amundsen Gulf extending westward into the Beaufort Sea, and at the mouth of M'Clure Strait (Figure 10) due to cold air temperatures (Figure 2). Much of the new-plus-young sea ice concentrations are highly anomalous for April (Figure 11). It is likely that strong wind forcing in April (Figure 6) was responsible for the substantial divergence and subsequent new-plus-young sea ice formation observed in the sea ice pack of April 2019, though the effect of the wind forcing was muted by internal stress and near-complete "downstream" ice cover in the western Beaufort and Chukchi Seas. As a result of the total sea ice concentration reduction, this small area of the flaw lead showed sea-ice-adjusted surface solar radiation downwards (SSRD) at the ocean surface in April for the first time during 2019 (Figure 18).

In an anomalously warm May (Figures 2, 3), with wind direction and speed typical of the climatological standard normal (Figures 6, 7), sea ice breakup by dynamic removal from the study region was spatially substantial (Figure 10). The total sea ice concentration decreased in May 2019, principally in the Cape Bathurst flaw lead polynya along the west coast of Banks Island, in Amundsen Gulf, and along the Mackenzie shelf north of the continental coast (Figure 10). Divergence of the pack was also observed in the Beaufort Sea (Figure 10). These areas exhibited negative total sea ice concentration anomalies in May and June (Figure 11). Despite the anomalous warm air temperatures in the region in May (Figures 2, 3), the air was still cool enough to produce new ice in May 2019 (Figure 2) over almost all the areas where total sea ice concentrations decreased (Figure 10), resulting in positive new-plus-young sea ice concentration anomalies in those areas (Figure 11). However, substantial open ocean areas were available for potential transmission of sea-ice-adjusted surface solar radiation downward (SSRD) (Figure 18) which was positively anomalous (Figure 19) compared to the climatological standard normal (1983-2010) for May.

Breakup advanced in June 2019, which saw the mostly old sea ice pack retreat to the North and West in the study region, leaving the sea ice concentrations anomalously low (Figure 11) over the whole of Amundsen Gulf, the Mackenzie shelf, and the flaw lead area west of Banks Island with less than $2/10^{ths}$ sea ice. The regional air temperatures were too warm for new sea ice production (Figure 10), so low sea ice concentration areas showed very large positively anomalous SSRD at the ocean surface (Figures 18, 19) again in June. Finally, it is noteworthy that M'Clure Strait was packed with positively anomalous old

sea ice concentrations throughout spring 2019 (Figure 11). Spring sea ice motion tells the same story in 2019; anticyclonic sea ice motion at anomalously high speeds in April and May (Figures 16, 17) broke up the region in earnest beginning in the Cape Bathurst flaw lead polynya complex. In June, the regional sea ice motion regime changed (Figures 16, 17), bringing old sea ice from the northern reaches of the region to the southern and eastern edges of the ice pack, resulting in positive old sea ice anomalies in those areas in that month (Figure 11). Sea ice export from the region slowed in June stabilizing the sea ice cover for summer melt.

3.3 Summer

In July, August, and September (summer) 2019, the 2 m air temperatures (Figure 2) were positively anomalous in all three months over the entire region, save for negative air temperature anomalies in the northwest quadrant of the region July (Figure 3). In particular, warm anomalies were prevalent over the Mackenzie Shelf and along the southern coast of Amundsen Gulf in July and August (Figure 3) in the area devoid of sea ice in June (Figure 10). In September 2019, the entire region was warmer than the climatological standard normal for the month, with the northwest quadrant of the region exhibiting the greatest positive 2 m air temperature anomalies (Figure 3).

Mean sea level pressure over the region in summer 2019 (Figure 3) was near typical of the climatological standard normal pattern in July and August. In September the SLP pattern departed from the standard normal; instead of high pressure in the north and lower pressure in the south with isobars aligned roughly by latitude, the SLP pattern in September 2019 consisted of higher pressure in the south and lower pressure in the north with isobars roughly aligned by latitude (Figure 4). The regional wind speed and direction followed on from the SLP in summer 2019. July and August were very typical of the climatological mean wind speed and direction in the region (Figures 6, 7), while in September the wind speed and direction in the region were predominantly westerly-southwesterly, opposite in direction and much faster than the climatological average (Figure 6, 7).

Mean monthly sea ice concentrations in summer 2019 declined precipitously over July, August and September (Figure 12). The July Beaufort ice pack consisted of a narrow band of $6/10^{ths}$ old ice along its eastern and southern edges, with predominantly first-year sea ice to the northwest (Figure 12). In August the sea ice pack retreated dramatically south of M'Clure Strait, where only a narrow band of $8/10^{ths}$ sea resided, more than half of which was first-year sea ice. In September 2019 the sea ice pack had retreated further northward, consisting mainly of old sea ice, with some new-plus-young sea ice around its

periphery (Figure 12) due to colder air temperatures (Figure 2) in that part of the region. Summer sea ice concentration anomalies (Figure 13) are indicative of a changed ice pack; they reveal old sea ice loss through summer relative to the climatological standard normal, offset by more first-year sea ice than normal in the northwest portions of the region where old ice was once persistent (Figure 13). Finally, as a result of the low total sea ice coverage in September 2019, positive new-plus-young sea ice anomalies were observed surrounding the Beaufort pack (Figure 12) due to the open ocean surface newly available for thin sea ice production under cold atmospheric temperatures (Figure 2).

The summer sea ice motion data may be inaccurate in time and space on a pixel-by-pixel or day-to-day basis because the total sea ice concentration (on which the sea ice motion product is based) is so low, but in general the mean monthly summer ice motion (Figure 16) and their anomalies (Figure 17) ably elucidate regional scale processes. The sea ice flux was predominantly southward along the coast of Banks Island and towards Cape Bathurst from the north in July, August, and September 2019. The monthly sea ice anomalies (Figure 17) indicate that the motion in the region during summer 2019 was much faster than the climatological standard normals for those months.

As a result of the anomalously low sea ice concentrations in summer 2019, the sea ice-adjusted SSRD (the sun's energy that may be available to melt sea ice or heat the upper ocean) in July, August, and September is substantial (Figure 18). Sea ice-adjusted SSRD over the period could have potentially affected the open ocean even in the far northwest reaches of the study region, as well as in the more southern coastal shelf areas and in Amundsen Gulf. In particular, there were substantial positive sea ice-adjusted SSRD anomalies in Amundsen Gulf and at the mouth of M'Clure Strait in July, and in the northwest quadrant of the study region in August and September (Figure 19) where thick sea ice is normally present (Figure 13). In order to relate some indication of the potential for solar energy accumulation in the ocean surface layer prior to the physical oceanographic observations that took place starting in August 2019, the (i) mean sea ice-adjusted SSRD in each month in 2019 from January to August were summed, and (ii) the anomaly of the accumulated sea ice-adjusted SSRD compared to the 1983-2010 period were calculated for each grid cell in the study region (Figure 20). In the months prior to September 2019, the Cape Bathurst flaw lead polynya complex, as well as Amundsen Gulf and the mouth of M'Clure Strait had the opportunity to accumulate substantial and positively anomalous SSRD which may have melted sea ice or heated the upper ocean (Figure 20). In addition to these predominantly first-year sea ice areas, the normally ice-covered northwest quadrant of the Beaufort Sea in the study region also received substantial sea ice-adjusted SSRD in June, a little in July, and then a great deal in August (Figure 18, 19), which shows up as a

positive anomaly in the SSRD accumulated between January and August 2019 (Figure 20) and coincides with the total sea ice concentration (Figure 12). It is also notable that M'Clure Strait showed negative SSRD accumulation anomalies from January to August 2019 (Figure 20) due to relatively high and stable concentrations of sea ice in the area over spring and summer (Figures 10-13). The sea ice-adjusted SSRD accrued prior to September 2019 was mostly accumulated in May, June, July, and August (Figure 18) when the sea ice concentrations were low and the sun angle was closest to nadir.

3.3.1 Summer Ocean conditions

The CBS-MEA cruise was undertaken in the region between 2 August and 9 September 2019. The lowest ocean surface temperatures were on the Mackenzie Shelf (KUG stations, Figure 22) (1 - 2.5 °C) where the offshore surface waters were just beginning to warm, and east of Cape Bathurst where the surface waters were > 2 °C (Figure 23a). The warmest surface waters were found nearest Cape Bathurst (~5 °C), in Darnley Bay at the Bennett Point stations (~4.5 – 6 °C) and near the west and east coasts of the Dolphin and Union section (~5.5 – 6.5 °C) (Figure 23a). The surface salinity was lowest in Franklin Bay (~25 – 26) (Figure 23b), which is likely in part attributable to the Horton River mouth immediately west of those stations. Most of the stations in the study region had surface salinities between 26 and 29 (Figure 23b), with the highest surface salinity values observed on the east end of Dolphin and Union Strait, in central Amundsen Gulf, and near the southern tip of Banks Island (Figure 23b).

The surface layer depth (the depth of the N^2 maximum) of the water column in the study region generally extended to between 10-30 m, or between 45-55 m (Figure 24a). At Minto Inlet station 04 (MTI_04) definition of the surface layer based on the depth of the N^2 maximum yielded a 159 dbar surface layer because the ocean column at that station was highly stratified near the bottom (Table 1). Visual inspection of the profiles from station MTI_04 (Appendix 1) yielded a surface layer thickness of 29 dbar (Table 1). This is a similar depth to which the water column had been heated from the surface based on the temperature profile at that station, and similar to the N^2-derived surface layer depths at other stations in Minto Inlet (Table 1, Appendix 1).

Generally, the stations with deeper (~50 m) surface layers contained greater ocean heat content (Figure 24b) and freshwater content (Figure 24c). Stations in Franklin and Darnley Bays, and at the west end of Dolphin and Union Strait had the greatest ocean heat content in the surface layer (1000-1100 kJ), while the mean ocean heat content at all the stations was 389 kJ (standard deviation = 315 kJ). The KUG stations on the Mackenzie shelf and slope contained little ocean heat content compared to CPB stations in the

north end of Amundsen Gulf nearest Banks Island (Table 1). Central Franklin Bay contained the greatest freshwater content in the N^2-defined surface layer in the study region in 2019, almost 15 m at station FKN_HC2, while the west end of Dolphin and Union Strait also exhibited large freshwater content (7.5-8.3 m) (Figure 24c, Table 1). The mean freshwater content in the surface layer in 2019 was 4.5 m (standard deviation = 3.4 m). In general, the deeper the N^2-derived surface layer, the more freshwater content it held in 2019.

Salinity and temperature section plots are presented in Figures 24 to 33 for all the CTD sections shown on the map in Figure 22. For each section, the salinity and temperature over the full cast depth are shown, as well as plots that show only the top 50 m to highlight the surface layer. White dots on the section plots indicate the N^2-derived surface layer depth at each station in the sections.

The Dolphin and Union Strait (DUS) section from west to east is presented in Figure 25. The N^2-derived surface layer depth across the Strait was deepest at the west end (~50 m) and decreased to 20-30 m for much of the rest of the section. It is obvious that heat and freshwater accumulated near the coasts of this section in 2019, especially on the west side (Figures 24, 25). The surface layer across Dolphin and Union Strait was between 4 and 6 °C, with a salinity < 29. The mean freshwater content of the N^2-derived surface layer across Dolphin and Union Strait in 2019 was 4.2 m (standard deviation = 2.45 m), and the mean ocean heat content was 581 kJ (standard deviation = 306 kJ).

The West-to-east and south-to-north Minto Inlet sections (Figure 22) are shown in Figures 26 and 27. As previously mentioned, there is extremely strong stratification near the bottom of Minto Inlet (Figure 26a, c, depth = 159 m) which influenced surface layer detection based on N^2. The strong stratification could be an important ecological feature supporting Arctic Cod which appear to occur in high abundance at depth in Minto Inlet relative to other areas of the study region (Halliday et al., 2022). There was also substantial freshwater at the innermost Minto Inlet station (MTI_06) (figure 26b) which resulted in maximum N^2 very near the surface (2.3 m). The N^2-derived surface layer depth in Minto Inlet is roughly 25-43 m excluding two stations where anomalous surface layer thickness occurred. Surface layer salinity from west to east in Minto Inlet in 2019 showed a relatively diffuse gradient from 0-30 m depth (Figure 26a), while the surface layer temperature was warm and nearly isothermal between 4-5 °C above 30 m depth (Figure 26d). Only two stations were used to create the south-to-north section across Minto Inlet (Figure 22, Figure 27), but the general picture remains the same. The surface layer salinity existed on a relatively diffuse gradient down to about 30 m (Figure 27a, b), while the surface layer temperature was isothermal around 5 °C from 0-30 m depth (Figure 27c, d). The mean freshwater content at the stations with

meaningful surface layer thicknesses was 5 m (standard deviation = 1.44 m). The mean ocean heat content at the three stations with meaningfully accurate surface layer thicknesses was 609 kJ (standard deviation = 171 kJ).

Across Amundsen Gulf from Cape Bathurst to Cape Lambton at the southern tip of Banks Island, 12 stations from the Cape Bathurst (CPB) transect (Figure 22) were conducted in the first week of August 2019. The mean N^2-derived surface layer depth across the Cape Bathurst stations ranged from 5-24 dbar, with a mean of 13.1 dbar. The temperature and salinity sections (Figure 28) across Amundsen Gulf on the CPB transect show the presence of sea ice (see Figure 12) near the fourth and fifth stations from the south end (CPB_04, CPB_05). Sea ice is indicated by i) substantial freshening at the surface in the upper 10 m (Figure 28a, b) and ii) a depression of the surface layer water temperature to 2 °C (Figure 28c, d). As one moves northeast from CPB_04 and CPB_05, the salinity gradient in the upper 10-20 m of the water column is small, ranging from 28-28.5 at the surface to 31 below the surface layer thickness (Figure 28b), while the surface layer of the ocean was between 3.5-5 °C (Figure 27d). Relatively little OHC (mean = 192 kJ, standard deviation 130 kJ) and FWC (mean = 2 m, standard deviation = 0.91 m) occurred in the CPB stations in 2019.

The west to east Franklin Bay (FKN) section (Figure 22) is presented in Figure 29 using CTD data collected at six stations in August 2019. At the west end of the section (FKN_01), the N^2-derived surface layer is nearly incalculably thin (1.2 m) and the surface salinity ~20, but increases to >32 by 10 m depth. The surface temperature is > 4 °C decreasing to < 0 °C by 10 m depth, so we note the likelihood of Horton River influence at this station (see Appendix one FKN_01 for cast profile). Moving eastward across Franklin Bay, the surface layer thickened to ~45-55 dbar before decreasing to 9 dbar at FKN_06 at nearest Cape Parry. FKN_06 N^2, salinity, and temperature profiles indicate mixing in the whole water column (Appendix 1). In section, the surface layer contains more freshwater content in Franklin Bay from west to east as the salinity in the surface layer is as low as 25 (Figure 29a, b). The mean freshwater content from west to east across Franklin Bay was high; FKN_03, FKN_04, and FKN_05 contain 10.6 m, 13 m, and 12.3 m of freshwater respectively. The salinity sections (Figure 29a, b) present a thin, low salinity surface layer that thickens from west to east, which overlies a thicker layer of increasing salinity between 26 and 28.5 (Figure 29b). As the surface layer thickens from west to east across Franklin Bay, substantial heat is contained in the upper water column; much of the thickening surface layer is above 4 °C (Figure 29c, d). The mean ocean heat content in the N^2-derived surface layer in this west-to-east section in Franklin Bay follows a similar pattern to the FWC; FKN_03, FKN_04, and FKN_05 contain 810 kJ, 990 kJ, and 954 kJ respectively.

CTD data were also collected along a south-to-north transect in Franklin Bay (Figure 30) towards the Cape Bathurst section (Figure 22). From the south end of Franklin Bay northward, the N^2-derived surface layer thickness was ~60 dbar thick at the two most coastal stations and decreased northward very quickly to 18-20 dbar for the rest of the section. The salinity section (Figure 30a, b) presented a very uniformly saline surface layer (~27) to 55 m depth at FKN_07 in the south, followed by an even fresher surface salinity (~25.5) at FKN_HC2 above a gradient in salinity from 26-27 down to almost 60 m depth. FKN_03 was the same down to almost 40 m depth. North of these stations, the very surface of the water column remained relatively fresh, but the thickness of the layer with salinity <28 decreased (Figure 30b). The freshwater content of the N^2-derived surface layer along this section followed; nearest shore the freshwater content is 11.3 m, and 14.6 m, while farther north it decreased to ~4 m. This section is similarly well stratified by temperature. Nearest shore, the water column is above 4 °C and isothermal through the surface layer, while farther north, the surface layer cooled and thinned (Figure 30c, d). In the north half of the section, the surface layer of the water column is likely influenced by the presence of sea ice in the vicinity in August (Figure 12); the temperature sections indicate cool surface water below 1 °C overlying slightly warmer water that then cooled and shows evidence of mixing down to more than 150 m (Figure 30c). The ocean heat content near shore in this south-north section is 934 kJ and 1128 kJ at the two southernmost stations, decreasing northward to 62.8 kJ at CPB_06 (Table 1).

Four stations (CPY_01, CPY_02, HC1, CPY_03) constitute the Cape Parry (CPY) south-north section (Figure 31) from the northern tip of Cape Parry toward central Amundsen Gulf (Figure 22). This includes stations in what is now the Anguniaqvia niqiqyuam marine protected area (ANMPA). The depths of the N^2-derived surface layer at the four stations thinned progressing north away from Cape Parry (29, 32, 19, and 20 dbar). The salinity section indicated that the surface layer was isohaline (<28), before increasing rapidly with depth to 31 (Figure 31). The freshwater content was 5.52 m and 6.14 m in the two near-shore stations, and decreased to 4.09 m and 3.21 m farther off-shore. Nearest Cape Parry, the temperature of the water column was nearly isothermal above 4 °C, and warmed by almost 0.5 °C near the bottom at 30m depth. The CPY section continued to be warmest at 20-30 m depth with cooler water residing above that layer (Figure 31), likely indicative of sea ice in the area in August (Figure 12) due to south and westerly winds (Figure 6) resulting in ice motion into the mouth of Amundsen Gulf (Figure 16). The two stations nearest Cape Parry contained 473 kJ and 533 kJ of ocean heat content moving northward, after which the ocean heat content decreased to ~239 kJ and 219 kJ over the remainder of the section (Figure 31, Table 1).

The Amundsen Gulf (AMG) section runs from the Bennett Point (BPT) transect in Darnley Bay northward offshore toward the center of Amundsen Gulf (Figure 22). Moving northward over the four stations (BPT_03, AMG_01, AMG_02, AMG_03), the N^2-derived surface layer thickness thinned progressively from 50 to 41 dbar, then finally to 28 and 21 dbar in central Amundsen Gulf. The southern half of the salinity section (Figure 32a, b) presents a thin (10-15 m) low salinity (28-29) layer at the surface underlain by a layer of continually increasing salinity past the depth on the N^2-derived surface layer (Figure 32b). The northern half of the salinity section exhibits increasing surface salinity until it reaches nearly 29.7 at the north end of the section (AMG_03), and the salinity gradient to the surface layer depth became quite steep as that layer thinned (Figure 32b). The freshwater content in the N^2-derived surface layer in this section was greater than 8 dbar at the south end of the section, and decreased to 7.16 m at AMG_01, before decreasing with decreasing surface layer thickness and increasing surface salinity to 4.8 m and 2.7 m in the north half of the section (AMG_02, AMG_03). The temperature section from BPT_03 into the center of Amundsen Gulf (Figure 32c, d) shows that the water temperature is high in the N^2-derived surface layer; though that layer thins and cools slightly from ~5 °C in the south to greater than 4 °C in the middle of the section before returning to greater than 5 °C in the north. The gradient from higher surface temperatures to deeper water below 0 °C is very steep in this section (Figure 32d). The ocean heat content is 1021 kJ in the south at the middle of the Bennett Point line before decreasing northward with the thinning surface layer thickness to 696 kJ, and then to 403 kJ and 387 kJ at the northern two stations in the AMG section.

In Darnley Bay from west to east using the Bennett Point transect (BPT_01, BPT_03, BPT_HC1, BPT_05, Figure 22), the sections show evidence of mixing to the bottom in 2019 (Figure 33). As a consequence, the N^2-derived surface layer calculation is imperfect in this area. The N^2-derived surface layer was 12, 50, 7, 18.1 dbar from west to east along the BPT transect, the variability of which is due to mixing processes creating multiple peaks in the N^2 profile with variable magnitude over relatively shallow depths (see BPT cast profile plots in Appendix 1). The freshwater content values in the surface layer are also variable, ranging from 1.2 m to 8.1 m. The salinity section indicates a gradient of salinity from ~28.5 at the surface to >31 at the bottom, save for the easternmost cast because it is so shallow. The temperature sections across Darnley Bay also show vertical variability, though their range is warm, with much of the upper 30 m warmer than 4 °C, with surface temperatures greater than 5.5 °C (Figure 33d). Again due to the variability of the surface layer depth, the ocean heat content varies from 113 kJ to 1021 kJ.

Finally, the Kugmallit (KUG) transect on the Mackenzie Shelf was conducted over seven stations from on-shelf in 61 m of water to the northernmost station (KUG-08) in more than 1300 m of water (Figure 22). The N^2-derived surface layer along the Kugmallit section was uniform; the mean N^2-derived surface depth was 22.3 dbar with a standard deviation of only 1.82 dbar. Salinity along the Kugmallit section (Figure 34a, b) was ~27.5 in the uppermost 12-15 m layer for the length of the section, which deepened slightly moving northward. Below the low salinity layer at the surface the salinity gradient was very steep, reaching 31 by about 40 m depth across the section (Figure 34b) and reaching 34 by 150 m depth on the slope beginning at the second station from the south end (KUG-03) (Figure 34a). The mean freshwater content in the N^2-derived surface layer of the Kugmallit transect was 4.3 m (standard deviation = 0.6 m), and ranged from 3.5 m to 4.97 m. The surface temperature of the Kugmallit transect was relatively cool compared to the other sections surveyed in 2019, likely reflecting that the KUG stations had been ice covered in July and were sampled at the outset of the cruise in the second week of August. Early August sampling combined with July ice cover would have reduced the area's ability to warm from insolation reaching the ocean surface. The 12-15 m thick surface-most water was between 1.5 and 2.5 °C (Figure 34c, d), with the warmest water at the surface at the south end of the transect. Cold (<0 °C) water resided below the surface layer to a depth of 150-200 m below which the water warmed. The mean ocean heat content in the N^2-derived surface layer over the Kugmallit transect was 149 kJ (standard deviation = 30 kJ).

3.4 Autumn

Autumn 2019 (October, November, and December) cooled steadily month-by-month (Figure 2). Banks and Victoria Islands experienced the coolest air temperatures, along with the Brooks Range in northeastern Alaska (likely due to their elevation). Much of the marine sector of the study region was warmer than the terrestrial environment for the whole of autumn 2019 (Figure 2). The monthly 2 m air temperature anomalies (Figure 3) indicate that October, November and December 2019 were much warmer than the climatological standard normal (1983-2010) for each month; November was especially anomalously warm.

In October 2019, sea level pressure (SLP) was low over the eastern end of the Brooks Range in northeastern Alaska, and high over Banks and Victoria Islands and spanning Dolphin and Union Strait to the mainland (Figure 4) and marginally higher than the climatological average (Figure 5). In November the location of the SLP high moved to a more climatologically normal position in the northwest corner of the region, though a second pronounced high still existed over Victoria Island, and the low over the Brooks Range remained in its climatologically average position (Figure 4). In December the SLP pattern switched

again, with the highest pressure over the mainland coast at the south end of the study area (Figure 4). As a result of the monthly variability in the SLP pattern in autumn 2019, the mean wind speed and direction was generally anticyclonic (clockwise) in October and November (Figure 6) at speeds marginally below the climatological standard normal in the region (Figure 7). In contrast, the December wind direction was anomalously westerly in much of study area at speeds slower than the climatological average (Figures 6, 7).

Sea ice formation began in October 2019 within and at the periphery of the relatively high total sea ice concentration areas in the northwest quadrant of the study region. Total sea ice concentrations were composed completely of old ice which remained after summer (first-year sea ice that survives through September is re-categorized as old ice on October 1) (Figure 14). October sea ice anomaly maps by stage of development (Figure 15) indicate that both total and old sea ice concentrations in October were anomalously low, while new-plus-young sea ice experienced large positive anomalies in areas where old ice typically resided on average in October (Figure 15). New-plus-young sea ice formation occurred in locations where those stages of development have not historically formed in autumn. In November 2019, the region was still not completely ice covered; only medium concentrations of total sea ice, made mostly of new-plus-young sea ice, were present in eastern Amundsen Gulf (Figure 14). The November anomaly maps indicate eastern Amundsen Gulf is typically completely covered by sea ice in a climatologically average November, and that there was substantial missing old ice in 2019 compared to the climatological average, which had been replaced by first-year sea ice (Figures 14, 15). Further, widespread formation of new-plus-young sea ice along the Mackenzie Shelf and slope, along the west coast of Banks Island, and in the entirety of Amundsen Gulf (Figure 14) was highly anomalous (Figure 15) and indicative of delayed autumnal freeze up in the study region. The new-plus-young sea ice that normally forms in the southern areas of the region in October did not form until November in 2019 (Figure 14). Positively anomalous new-plus-young sea ice concentrations were still prevalent along the Mackenzie Shelf, along the west coast of Banks Island and in eastern Amundsen Gulf in December (Figures 14, 15) which further indicates substantially delayed freeze up. In light of the climatologically normal wind direction and speed (Figures 6, 7) and ice motion (Figures 16, 17) in November 2019, the delay in autumnal freeze up, and specifically the geographic locations of the new-plus-young sea ice in December, coincide with and are likely due to upper ocean heat accumulation (mean accumulated sea ice-adjusted SSRD) in 2019 (Figure 21a). Sea ice-adjusted SSRD was substantially positively anomalous along the Mackenzie Shelf, and in eastern Amundsen Gulf (Figure 21b). Sea ice-adjusted SSRD in these two areas was mainly accumulated in May, June and July 2019 (Figure 18), and was positively anomalous compared to the climatological standard

normal in all three months (Figure 19). This is an indication of how important open ocean surface around the summer solstice may have been to heat accumulation in the upper ocean, and subsequently to fall freeze up timing in 2019.

4 Conclusion

In winter 2019, warmer than average 2 m air temperatures occurred in all three months (January, February, March), specifically over the first-year sea ice areas. The SLP pattern was very typical with the Beaufort High positioned in the northwest corner of the study region. Stronger than average anticyclonic (clockwise) winds occurred throughout the region. M'Clure Strait was anomalously full of old sea ice, and greater than average first-year sea ice replaced the more typical old ice at the south periphery of the Beaufort pack. Sea ice in Amundsen Gulf was nearly completely mobile all winter due to winds that exported sea ice west and increased the speed at which the sea ice moved in these winter months. The influence of the winds on the sea ice also resulted in substantial and consistent new and young ice production in the flaw lead at the interface of the mobile sea ice and the landfast ice in the region.

In spring 2019, April air temperatures were cooler than the climatological average except for over the Mackenzie Shelf area where total sea ice concentrations were dynamically reduced by extremely high speed export-favorable easterly winds. Dynamic sea ice export continued in earnest in May due to export-favorable winds, further enabled by warmer than average air temperatures and space for the ice to move westward in the Beaufort Sea due to ice reductions west of Utqiagvik in the Chukchi Sea. 2019 experienced spatially significant early sea ice breakup, so early that new-plus-young ice was able to form in April and May, though June sea ice in the region was anomalously low.

In summer 2019, air temperatures of the southern marine region were anomalously warm, and the SLP pattern enabled low wind speeds that moved sea ice towards the mouth of Amundsen Gulf. Although these physical conditions in the region slowed regional sea ice loss in summer, substantial anomalies from spring loss were held over in the region through summer such that sea ice in the Beaufort Sea was extremely limited in summer 2019. As a result of early ice-off and sustained very low sea ice concentration over summer, the amount of shortwave energy (i.e., energy to melt sea ice or heat surface waters) that may have been absorbed by the upper ocean was positively anomalous in July, August and September.

In autumn 2019, October and November air temperatures over the marine environment were much warmer than normal, likely in part due to the amount of solar surface radiation downwards incident on the upper ocean over spring and summer. New and young sea ice formed in the northwest quadrant of

the region in October in areas typically covered by old sea ice, and sea ice formation in the southern half of the Beaufort Sea and Amundsen Gulf was delayed substantially by observed heat in the upper ocean prior to August, and by export-favorable easterly winds.

The warm, unstable sea ice conditions observed in 2019 would have had implications for the ecosystem including the timing of primary production, and water temperature anomalies may have had consequences for species thermal tolerances, habitat preferences. In the winter (January-March) period the community of Ulukhaktok reported the first ever overwintering of bowhead whales (Jared and Jordan Kitekudlak, personal communication, as cited in Insley et al., 2022). Hydrophone assessments detected bowhead overwintering across Amundsen Gulf including near Ulukhaktok on Victoria Island, near Pearce Point located to the east of Darnley Bay, as well as near and offshore at Cape Bathurst (Insley et al., 2022). The survival of the whales during this migratory anomaly may have been facilitated by the anomalously mobile ice pack. The state of the physical system in 2019 can also be considered with occurrences of marine mammal mortalities in the study region that year, and as part of the ongoing integrated ecosystem assessment supported by CBS-MEA.

5 Acknowledgements

We thank the Inuvialuit Game Council, the Fisheries Joint Management Committee, and the Western Arctic Marine Protected Area steering committee for supporting this work and providing valuable input into study objectives. Thanks to the Inuvik, Aklavik, Paulatuk, and Olokhaktomiut Hunters and Trappers Committees for logistical support and providing community science participants for the cruise. And finally, thanks to the crew and management team of the *F/V Frosti* for their tireless service and professionalism.

Funding for the 2019 field year was provided by various DFO sources including the National Conservation Plan, Aquatic Climate Change Adaptation Services Program, and the Arctic Science Fund. External funds were received from the Beaufort Regional Strategic Environmental Assessment (RSEA), administered through Crown Indigenous Relations and Northern Affairs Canada and the Joint Secretariat of the Inuvialuit Settlement Region.

6 References

DFO. 2010. Monitoring indicators for the Tarium Niryutait Marine Protected Area (TNMPA). DFO Can. Sci. Advis. Sec. Sci. Advis. Rep. 2010/059.

DFO. 2014. Re-evaluation of Ecologically and Biologically Significant Areas (EBSAs) in the Beaufort Sea. DFO Can. Sci. Advis. Sec. Sci. Advis. Rep. 2014/052.

DFO. 2015. Angunniaqvia Naiqiqyuam Area of interest: monitoring indicators, protocols and strategies. DFO Can. Sci. Advis. Sec. Sci. Advis. Rep. 2015/025.

DFO. 2022. Science Advice to Assist in the Development of an Ecological Monitoring Plan for the Anguniaqvia Niqiqyuam Marine Protected Area. DFO Can. Sci. Advis. Sec. Sci. Advis. Rep. 2022/015.

Fequet, D. (ed). 2005. Manual of standard procedures for observing and reporting ice conditions, Canadian Ice Service - Environment Canada, Catalogue No. En56-175/2005, ISBN 0-660-62858-9.

Halliday, W. D., Brittain, S. A., Niemi, A., Majewski, A. R., Mouy, X., Insley. S. J. 2022. The underwater soundscape of Minto Inlet, Northwest Territories, Canada. Arctic 75: 462-479. doi: 10.14430/arctic76400

Hersbach, H., Bell, B., Berrisford, P., Biavati, G., Horányi, A., Muñoz Sabater, J., Nicolas, J., Peubey, C., Radu, R., Rozum, I., Schepers, D., Simmons, A., Soci, C., Dee, D., Thépaut, J-N. 2018. ERA5 hourly data on single levels from 1959 to present. Copernicus Climate Change Service (C3S) Climate Data Store (CDS). (Accessed June 2022), 10.24381/cds.adbb2d47

Insley, S. J., Halliday, W. D., Mouy, X., Diogou, N. 2021. Bowhead whales overwinter in the Amundsen Gulf and Eastern Beaufort Sea. Royal Society Open Science, 8:202268. doi: 10.1098/rsos.202268

Kelley, D. E. 2018. Oceanographic analysis with R. Springer, New York, NY. ISBN: 978-1-4939-8844-0, doi: 10.1007/978-1-4939-8844-0, 290pp+xxi.

Nicolaus, M., Petrich, C., Hudson, S. R., Granskog, M. A. 2013. Variability of light transmission through Arctic land-fast sea ice during spring, The Cryosphere, 7, 977-986, doi: 10.5194/tc-7-977-2013.

Niemi, A., Majewski, A., Eert, J., Ehrman, A., Michel, C., Archambault, P., Atchison, S., Cypihot, V., Dempsey, M., de Montety, L., Dunn, M., Geoffroy, M., Hussherr, R., MacPhee, S., Mehdipour, N., Power, M., Swanson, H., Treau de Coeli, L., Walkusz, W., Williams, W., Woodard, K., Zimmerman, S., Reist, J. 2020. Data from the BREA-MFP and CBS-MEA research programs describing the Anguniaqvia niqiqyuam Marine Protected Area (ANMPA) ecosystem. Can. Data Rep. Fish. Aquat. Sci. 1316: ix + 90 p.

R Core Team, 2022. R: A language and environment for statistical computing. R Foundation for Statistical Computing, Vienna, Austria. https://ww.R-project.org/

Serreze, M. C. and Stroeve, J. 2015. Arctic sea ice trends, variability and implications for seasonal forecasting, Philosophical Transactions of the Royal Society A: Mathematical, Physical and Engineering Sciences, doi: 10.1098/rsta.2014.0159.

Sharqawy, M. H., Lienhard V, J., H., Zubair, S. M. 2010. Thermophysical properties of seawater: a review of existing correlations and data, Desalination and Water Treatment, 16: 354-380, doi: 10.5004/dwt.2010.1079.

Stirling, I. 1980. The biological importance of Polynyas in the Canadian Arctic. Arctic, 33: 303-315.

Tschudi, M., Meier, W. N., Stewart, J. S., Fowler, C., Maslanik, J. 2019. *Polar Pathfinder Daily 25 km EASE-Grid Sea Ice Motion Vectors, Version 4.* [1983-2021]. Boulder, Colorado USA. NASA National Snow and Ice Data Center Distributed Active Archive Center. doi: https://doi.org/10.5067/INAWUWO7QH7B. [June 2022].

Tivy, A., Howell, S. E. L., Alt, B., McCourt, S., Chagnon, R., Crocker, G., Carrieres, T., Yackel, J. J. 2011. Trends and variability in summer sea ice cover in the Canadian Arctic based on the Canadian Ice Service Digital Archive, 1960-2008, and 1968-2008. Journal of Geophysical Research, Oceans, 116(C3), doi: 10.1029/2009JC005855.

7 Figures

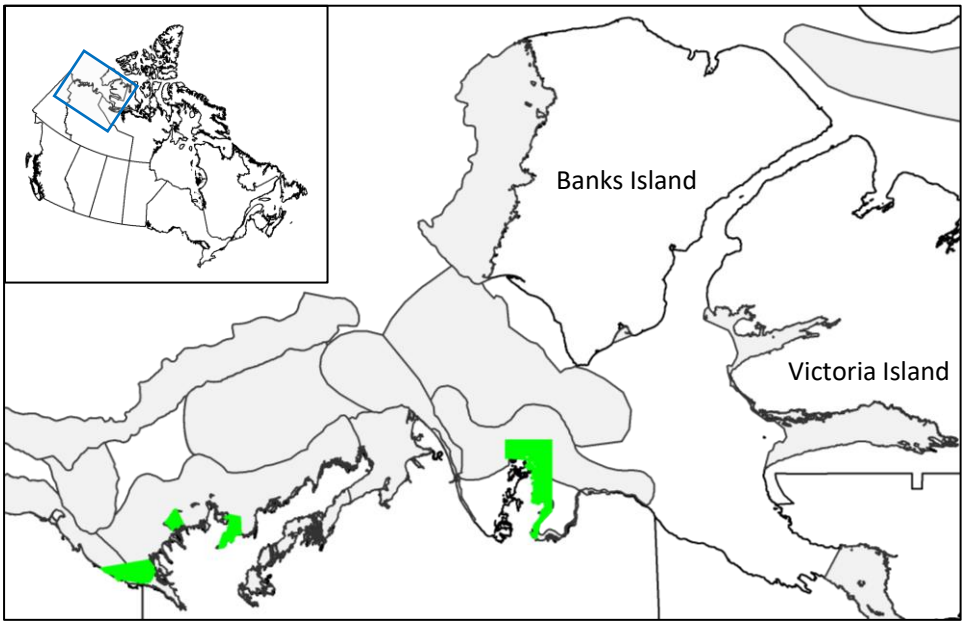

Figure 1. The CBS-MEA study region, encompassing the southern Beaufort Sea and Amundsen Gulf. Marine protected areas are mapped in green, Ecologically and biologically significant areas are mapped in light grey.

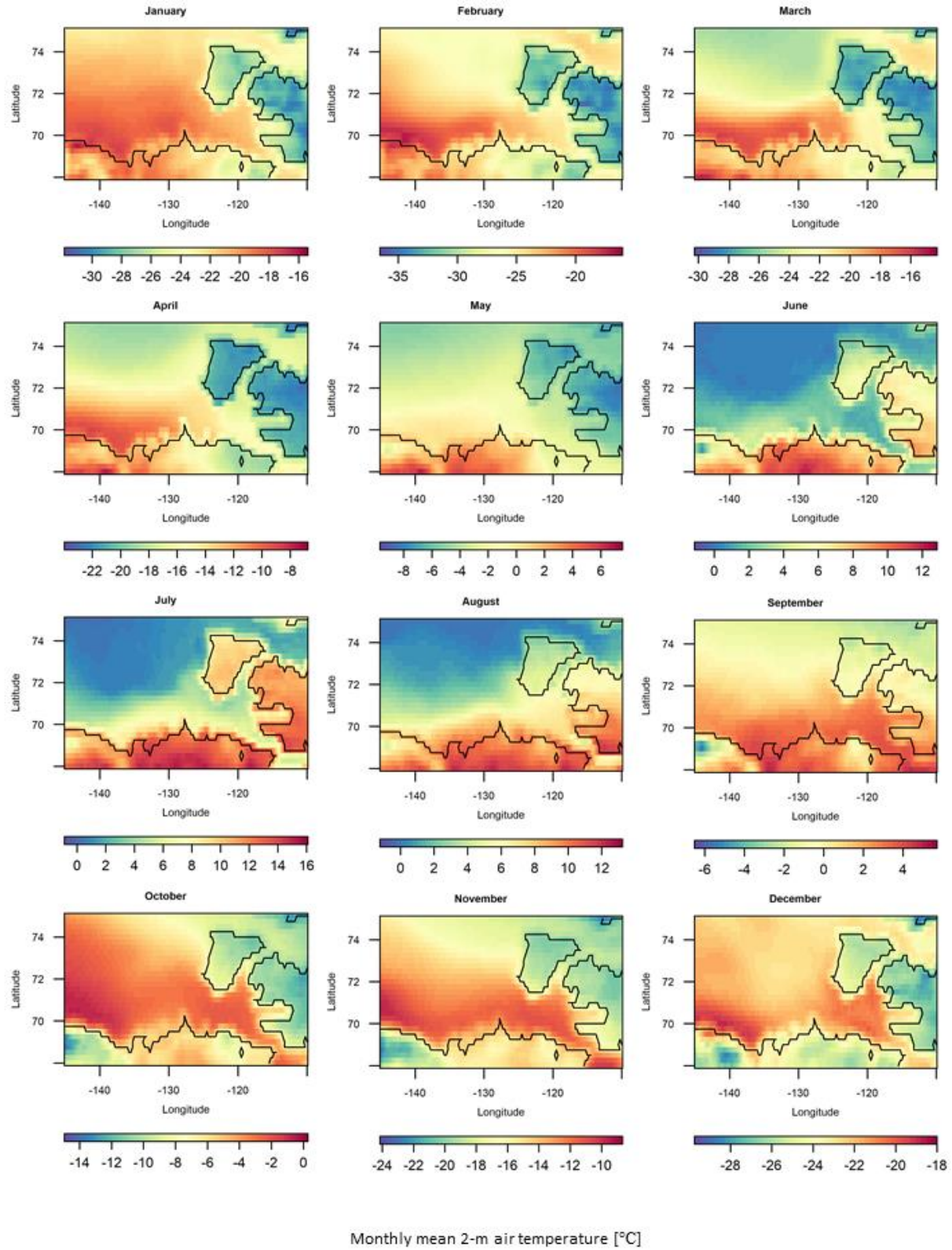

Figure 2. Monthly mean 2 m air temperature (°C) in 2019 over the Beaufort Sea and Amundsen Gulf.

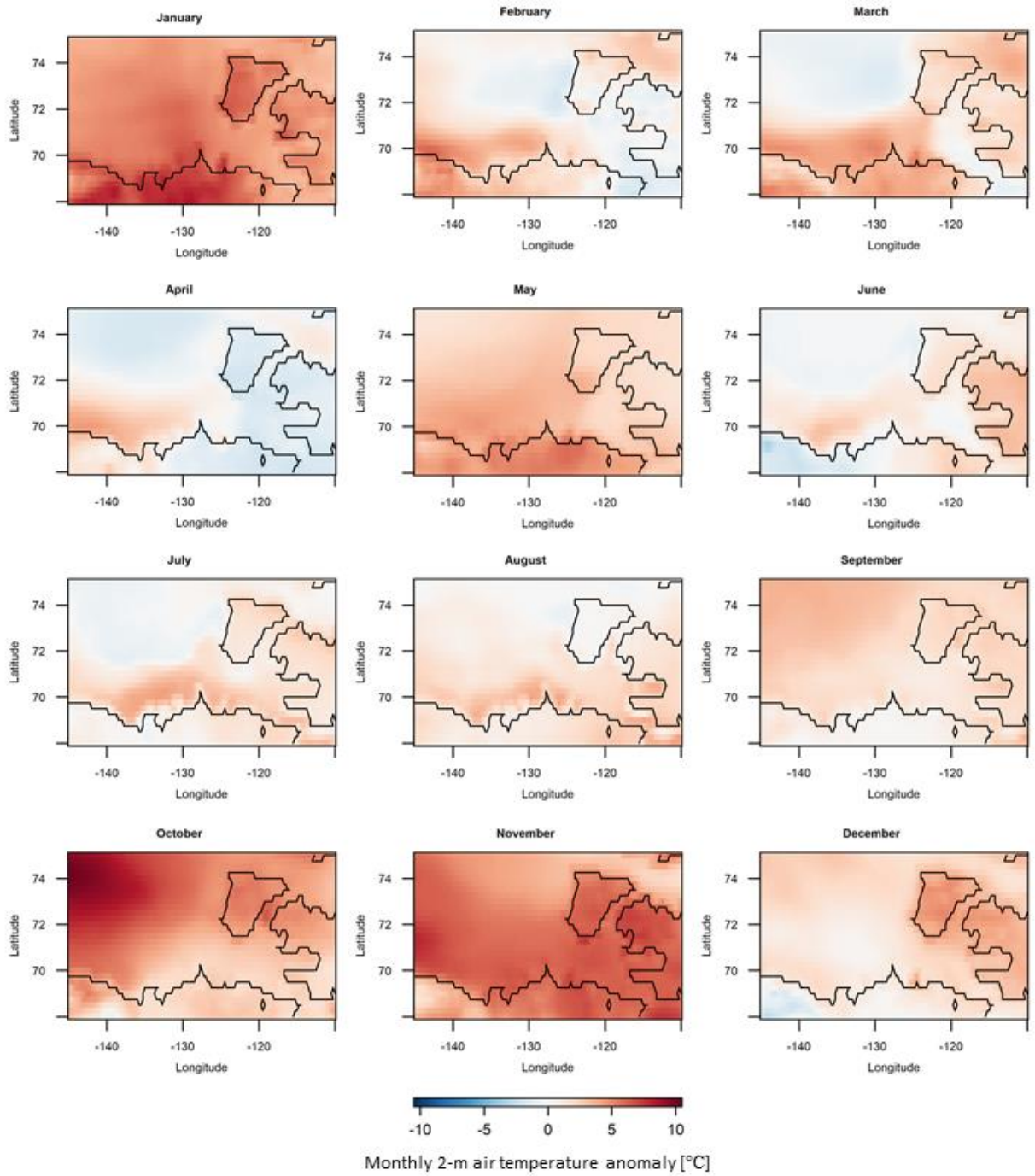

Figure 3. Monthly 2 m air temperature anomalies (°C) in 2019 from the climatological average period 1983-2010 in the Beaufort Sea and Amundsen Gulf.

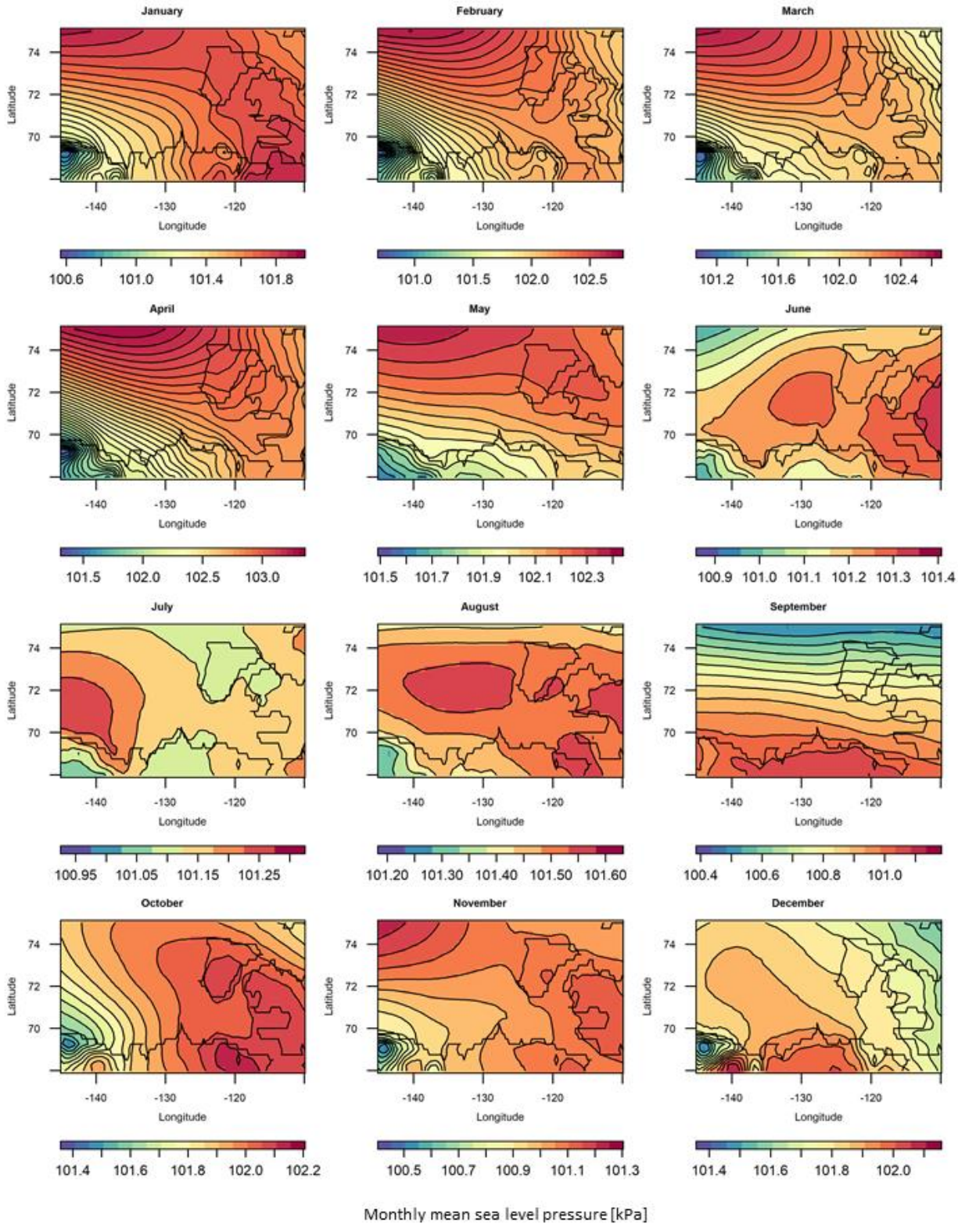

Figure 4. Monthly sea level pressure (kPa) over the Beaufort Sea and Amundsen Gulf in 2019.

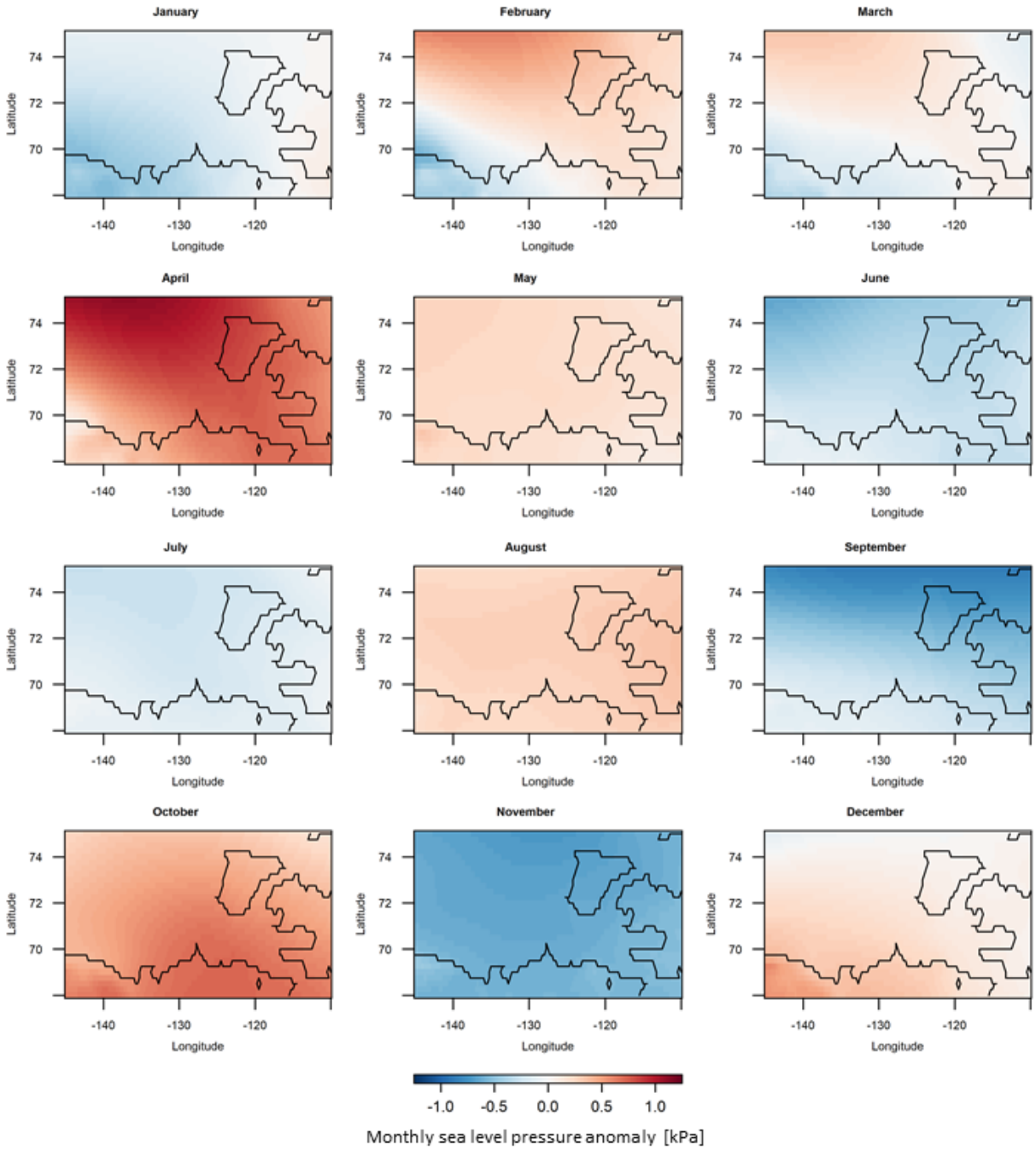

Figure 5. Monthly sea level pressure anomalies (kPa) in 2019 from the climatological average period 1983-2010 in the Beaufort Sea and Amundsen Gulf.

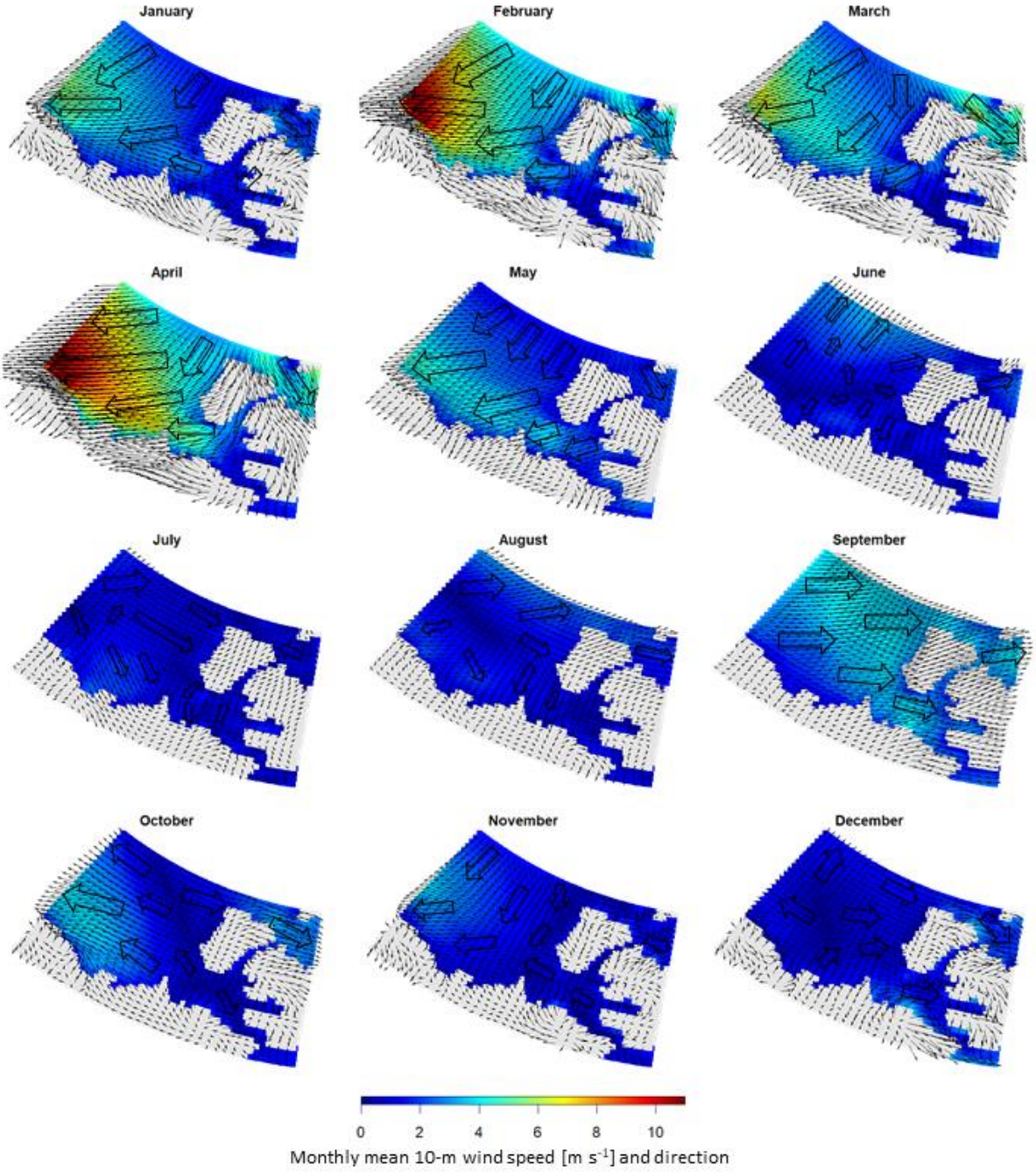

Figure 6. Monthly mean 10 m wind speed (m s^{-1}) and direction in 2019 in the Beaufort Sea and Amundsen Gulf.

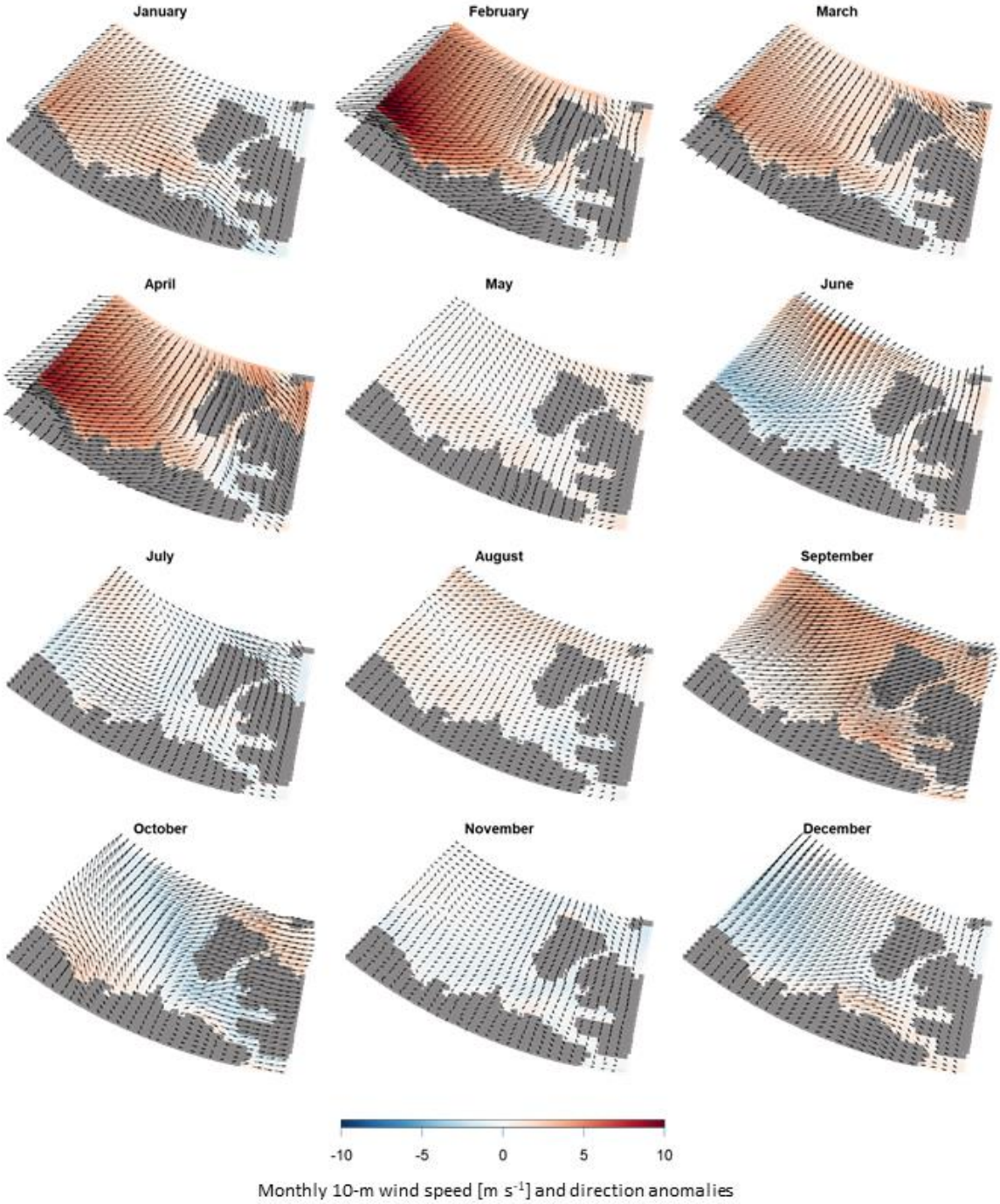

Figure 7. Monthly 10 m wind speed (m s^{-1}) and direction anomalies from the climatological average period 1983-2010 in the Beaufort Sea and Amundsen Gulf in 2019.

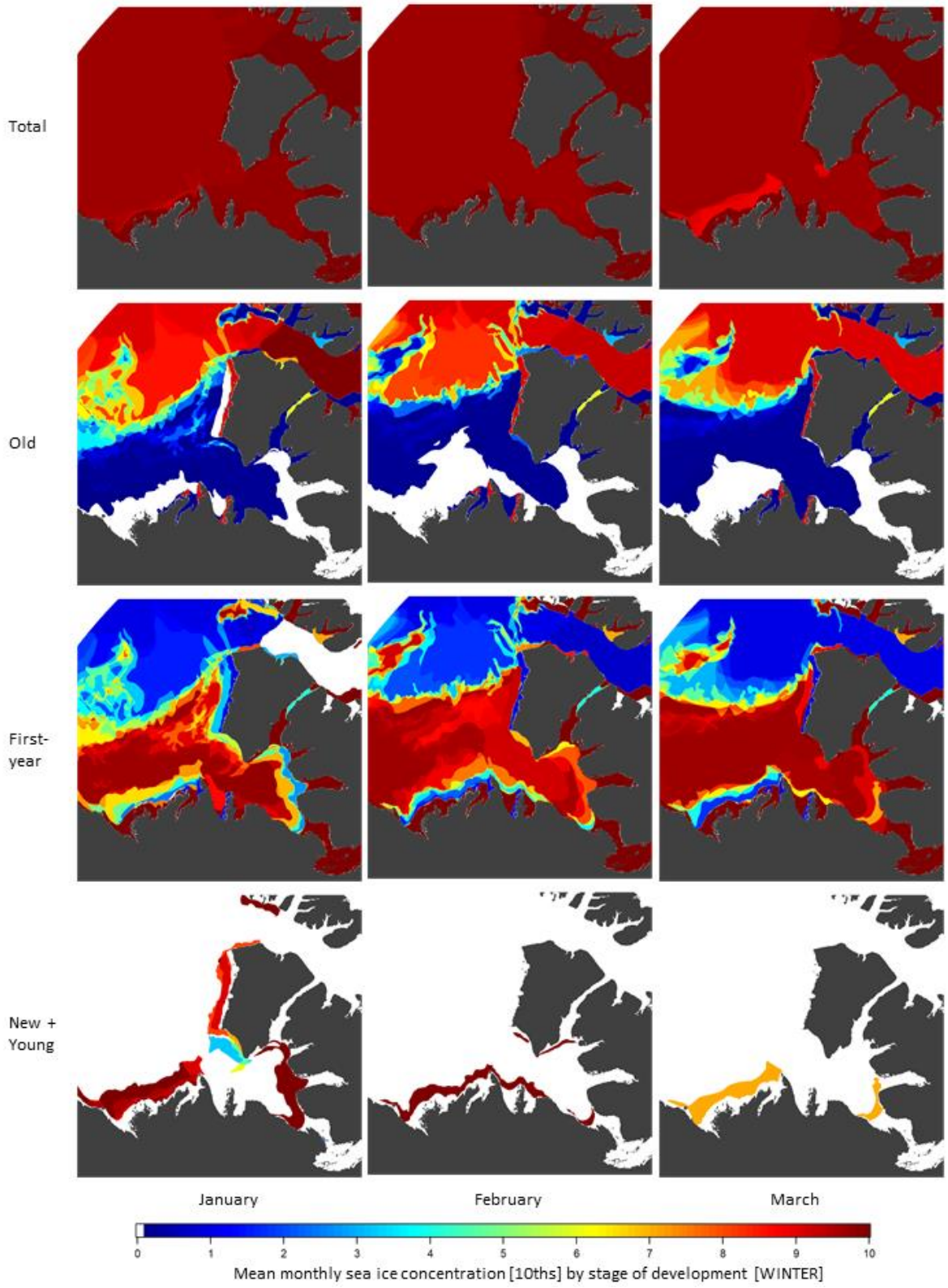

Figure 8. Mean monthly sea ice concentration (10^{ths}) for total sea ice and three stages of development (old, first-year, and young + new ice) for January, February, and March [winter] 2019.

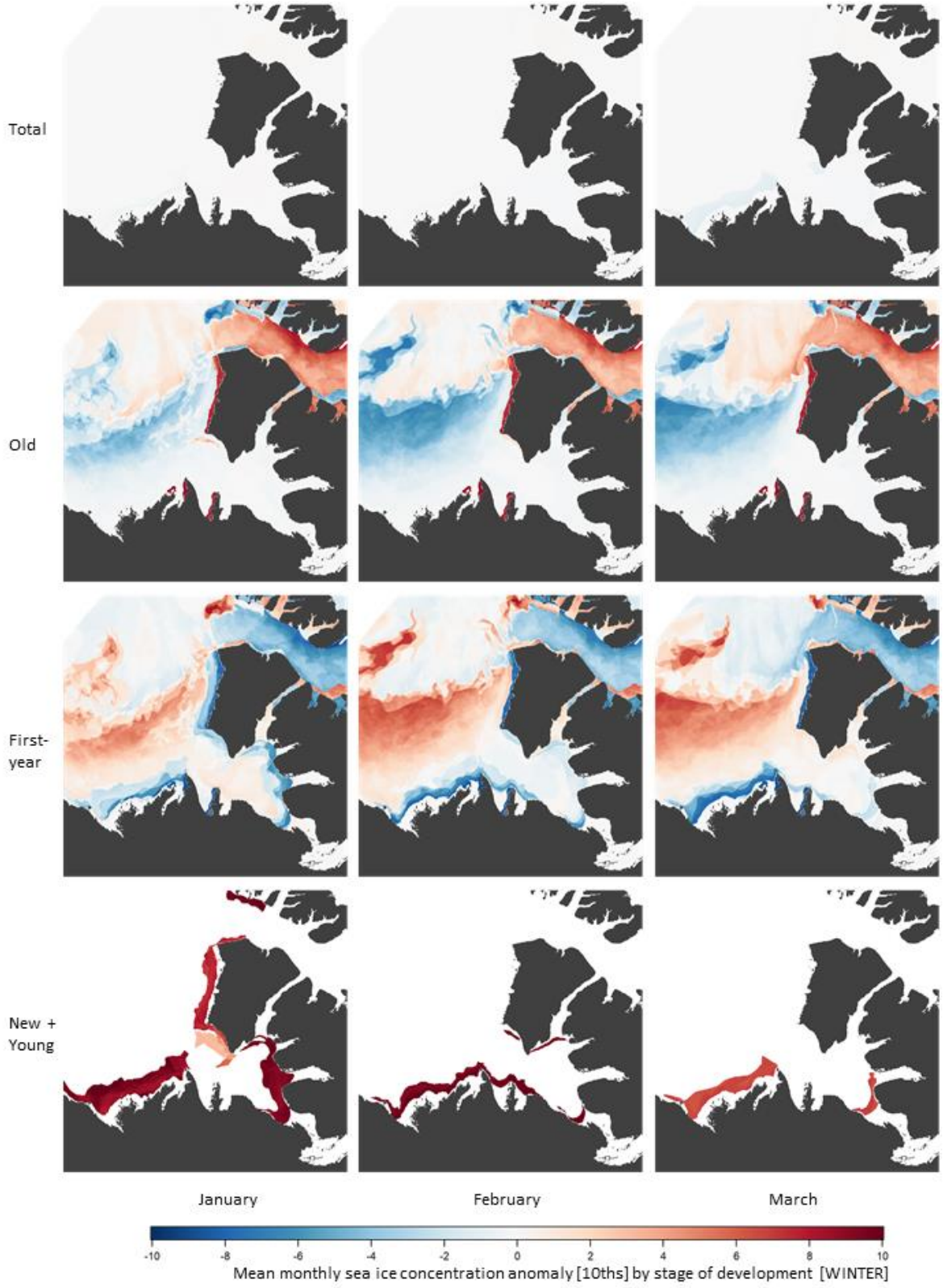

Figure 9. Mean monthly sea ice concentration anomalies (10^{ths}) for total sea ice and three stages of development (old, first-year, and young + new ice) for January, February, and March [winter] 2019.

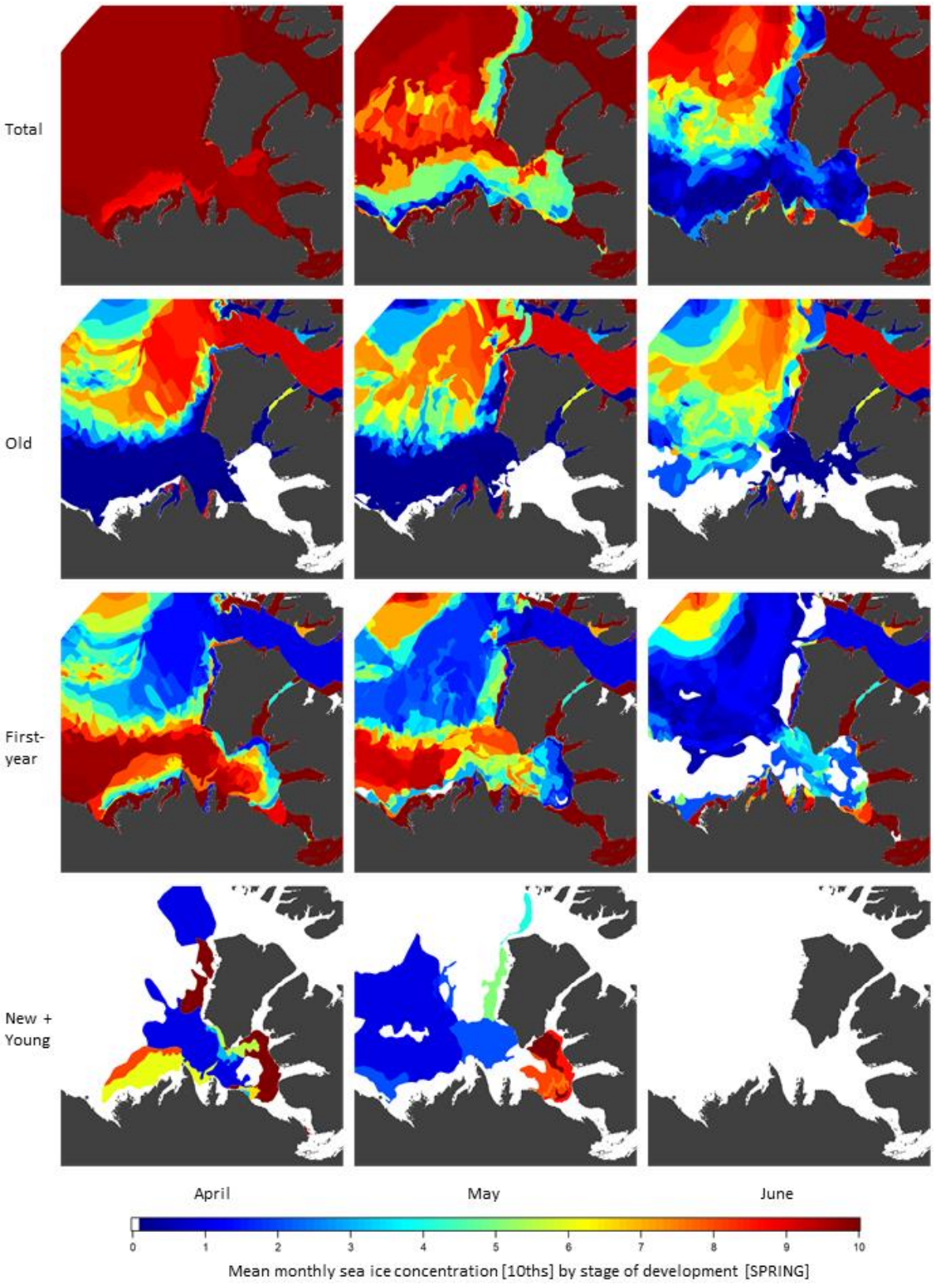

Figure 10. Mean monthly sea ice concentration (10^{ths}) for total sea ice and three stages of development (old, first-year, and young + new ice) for April, May, and June [spring] 2019.

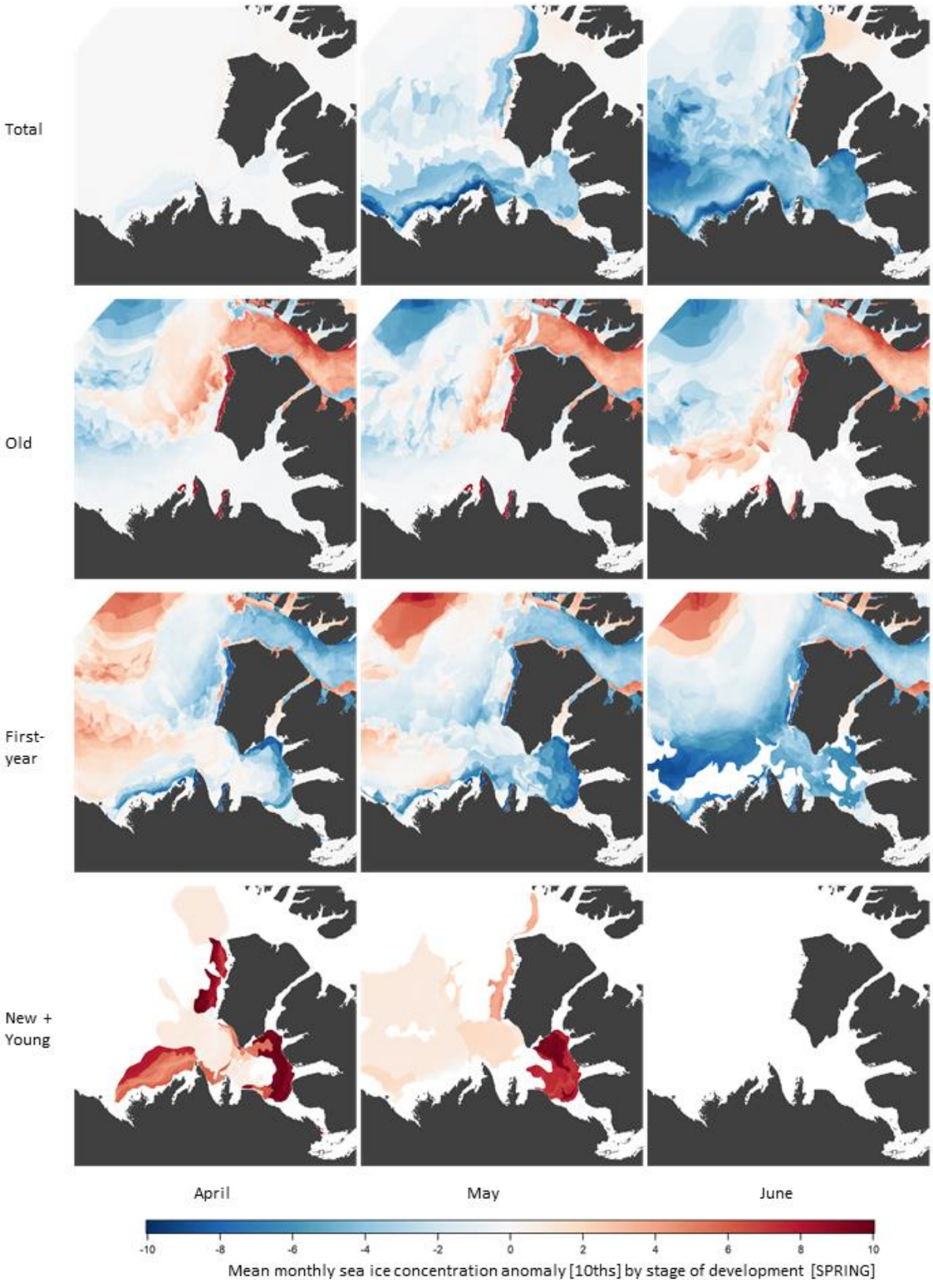

Figure 11. Mean monthly sea ice concentration anomalies (10^{ths}) for total sea ice and three stages of development (old, first-year, and young + new ice) for April, May, and June [spring] 2019.

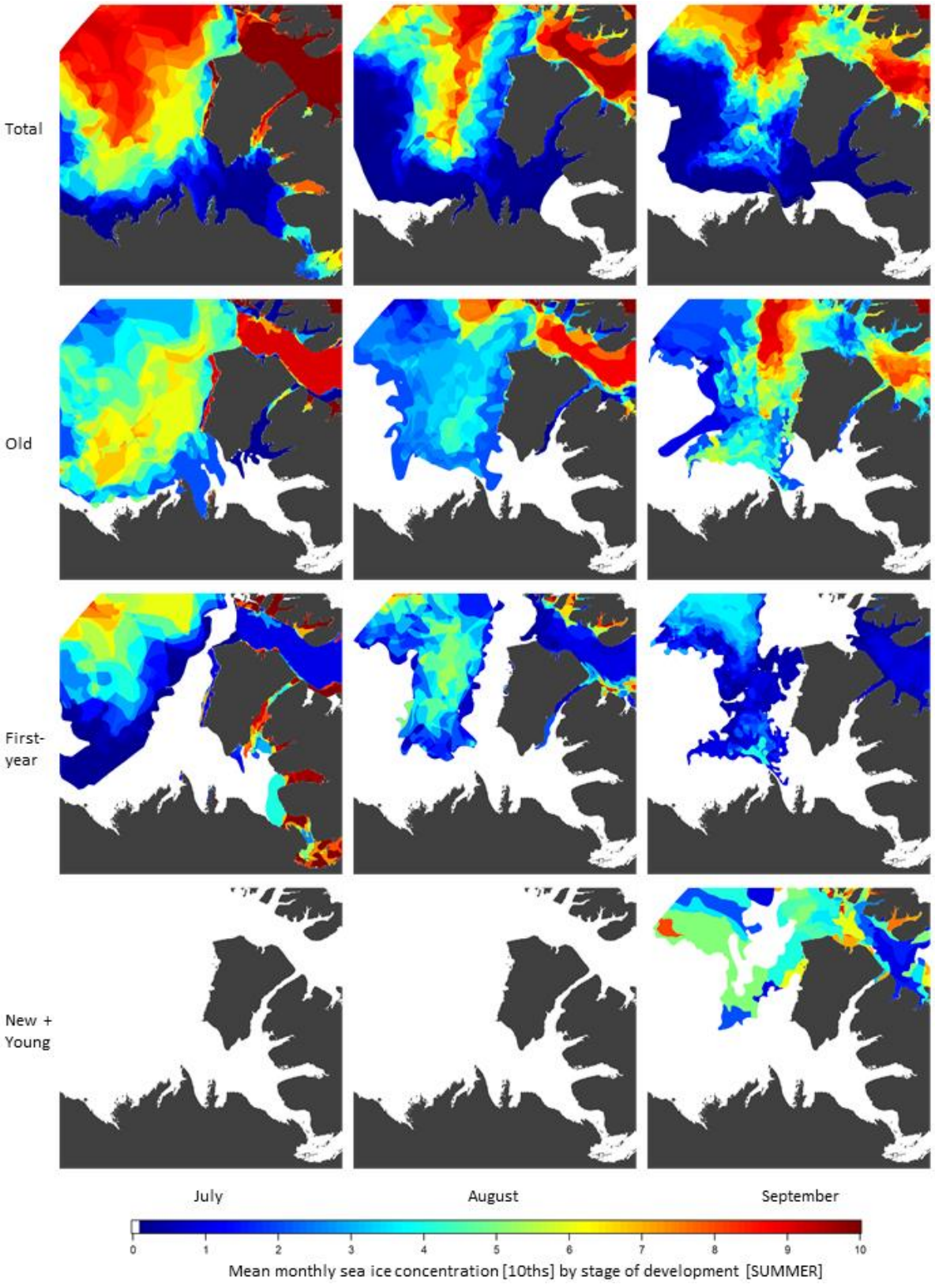

Figure 12. Mean monthly sea ice concentration (10^{ths}) for total sea ice and three stages of development (old, first-year, and young + new ice) for July, August, and September [summer] 2019.

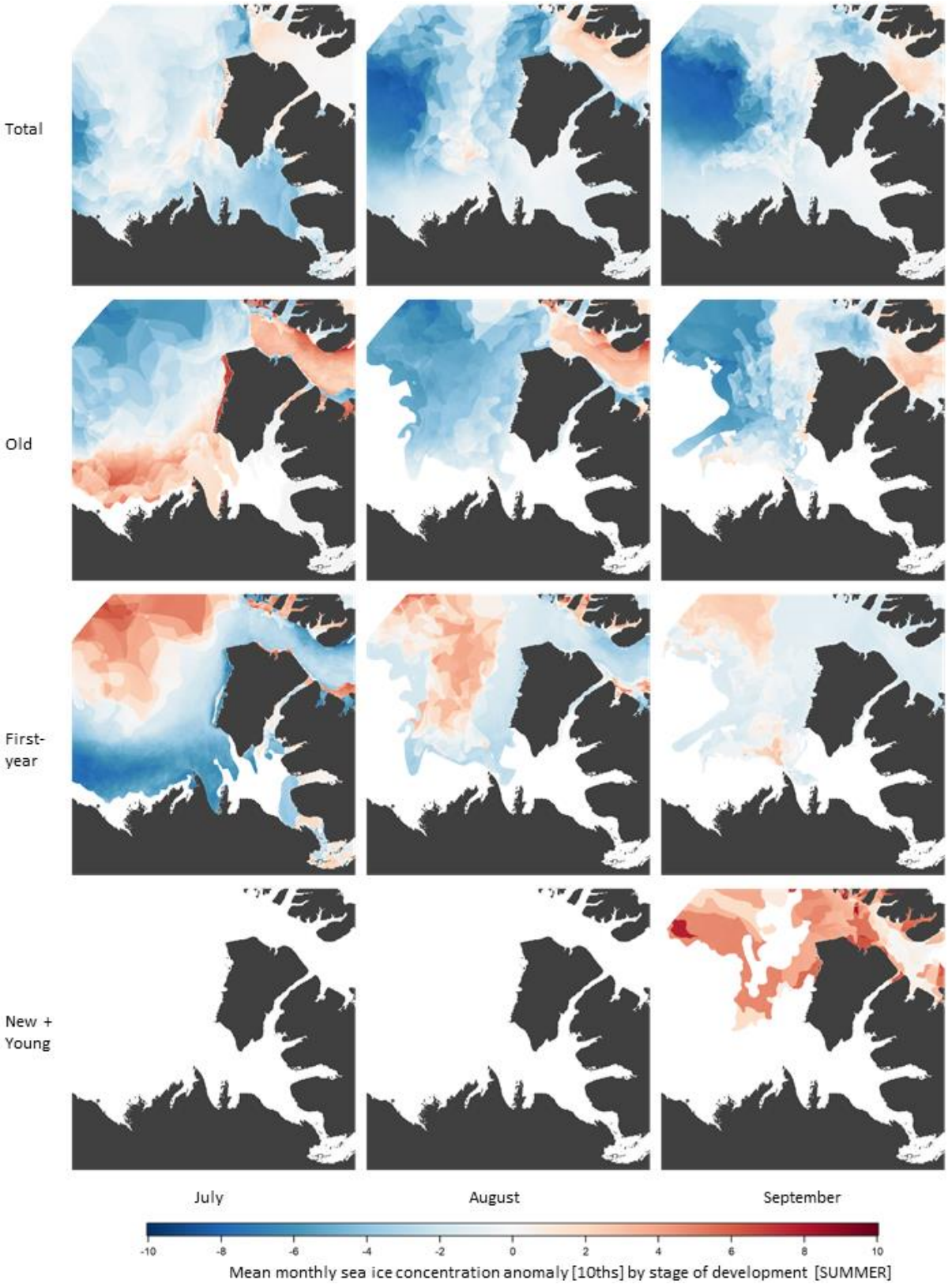

Figure 13. Mean monthly sea ice concentration anomalies (10^{ths}) for total sea ice and three stages of development (old, first-year, and young + new ice) for July, August, and September [summer] 2019.

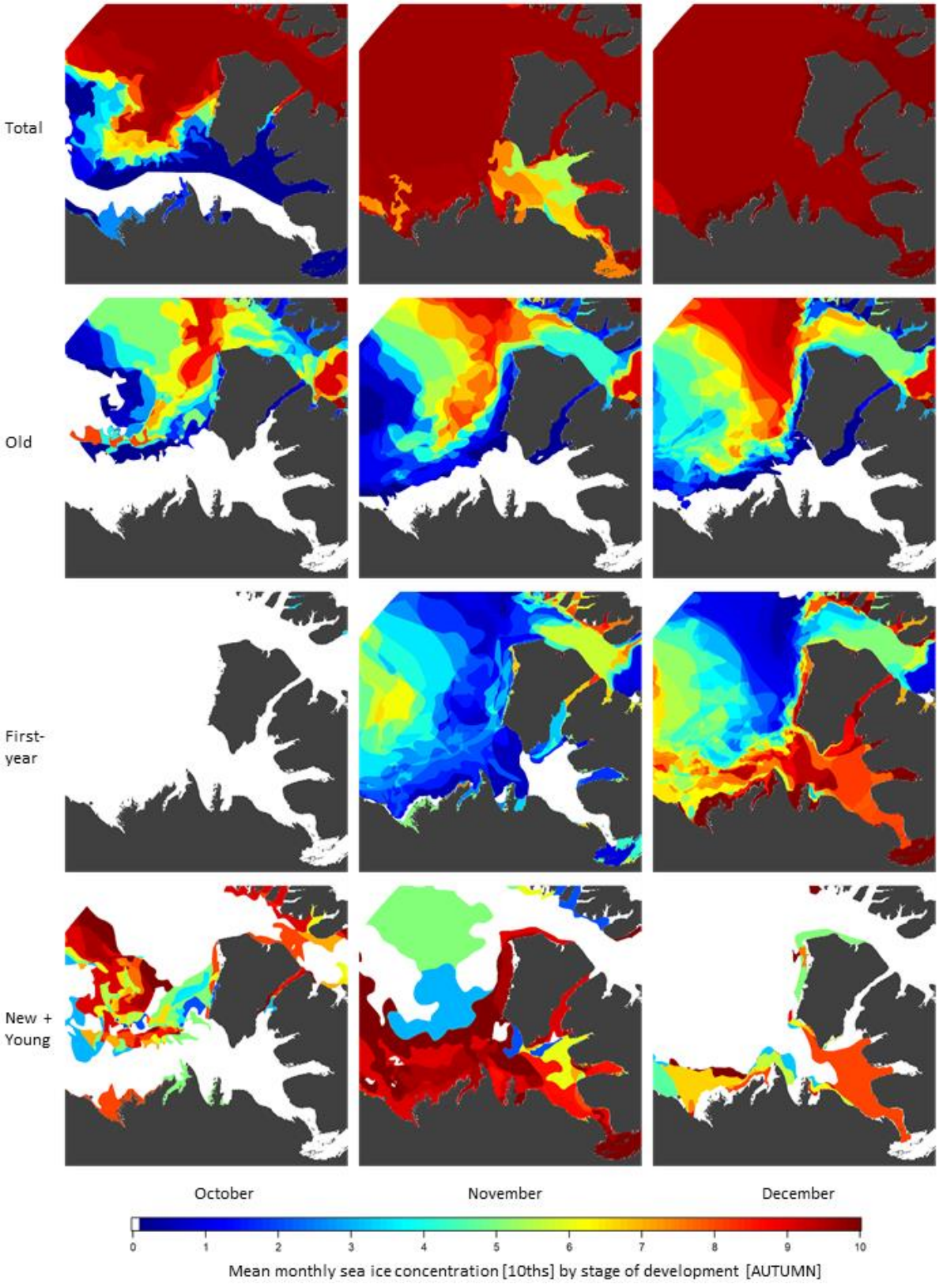

Figure 14. Mean monthly sea ice concentration (10^{ths}) for total sea ice and three stages of development (old, first-year, and young + new ice) for October, November, and December [autumn] 2019.

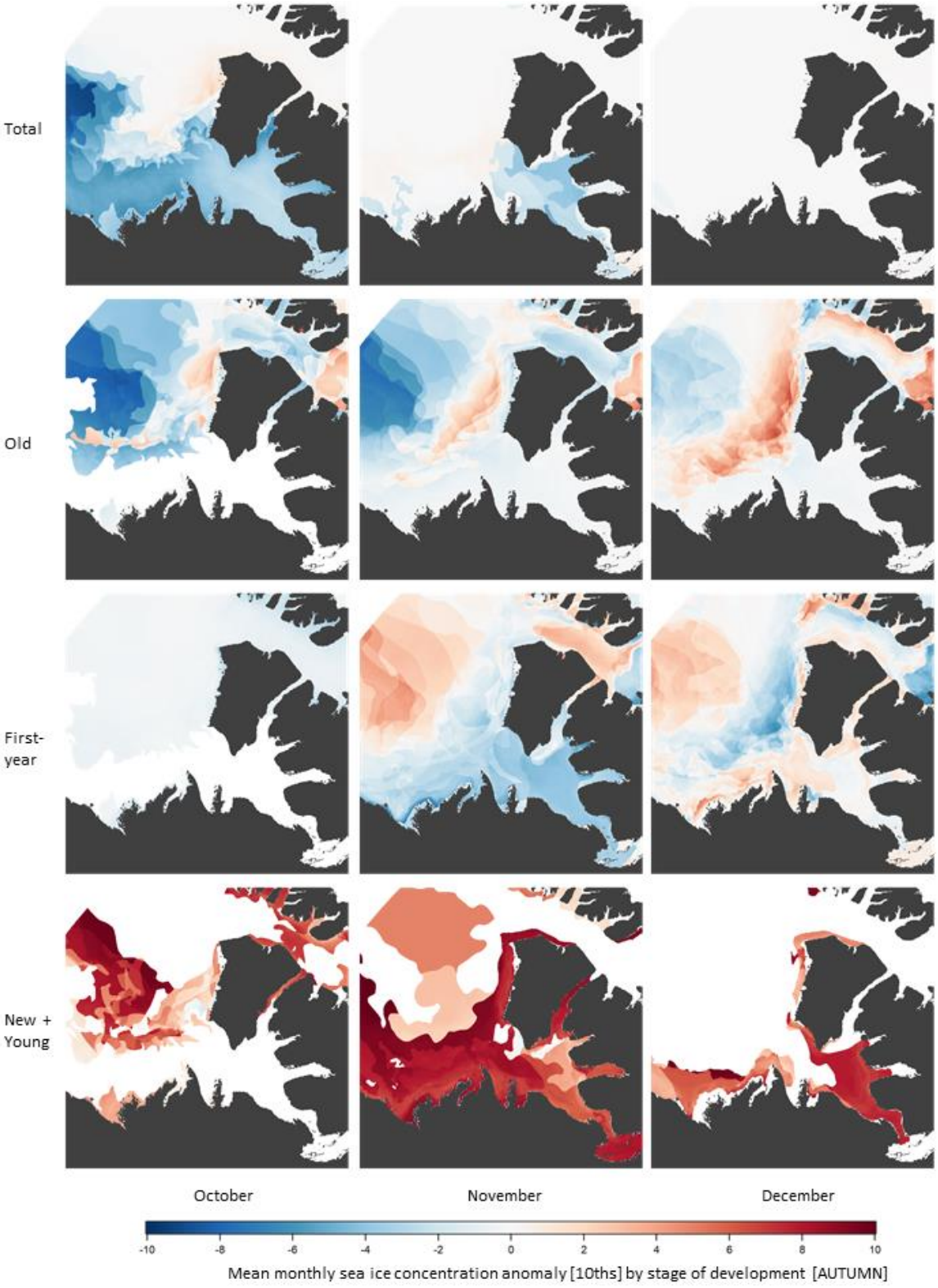

Figure 15. Mean monthly sea ice concentration anomalies (10^{ths}) for total sea ice and three stages of development (old, first-year, and young + new ice) for October, November, and December [autumn] 2019.

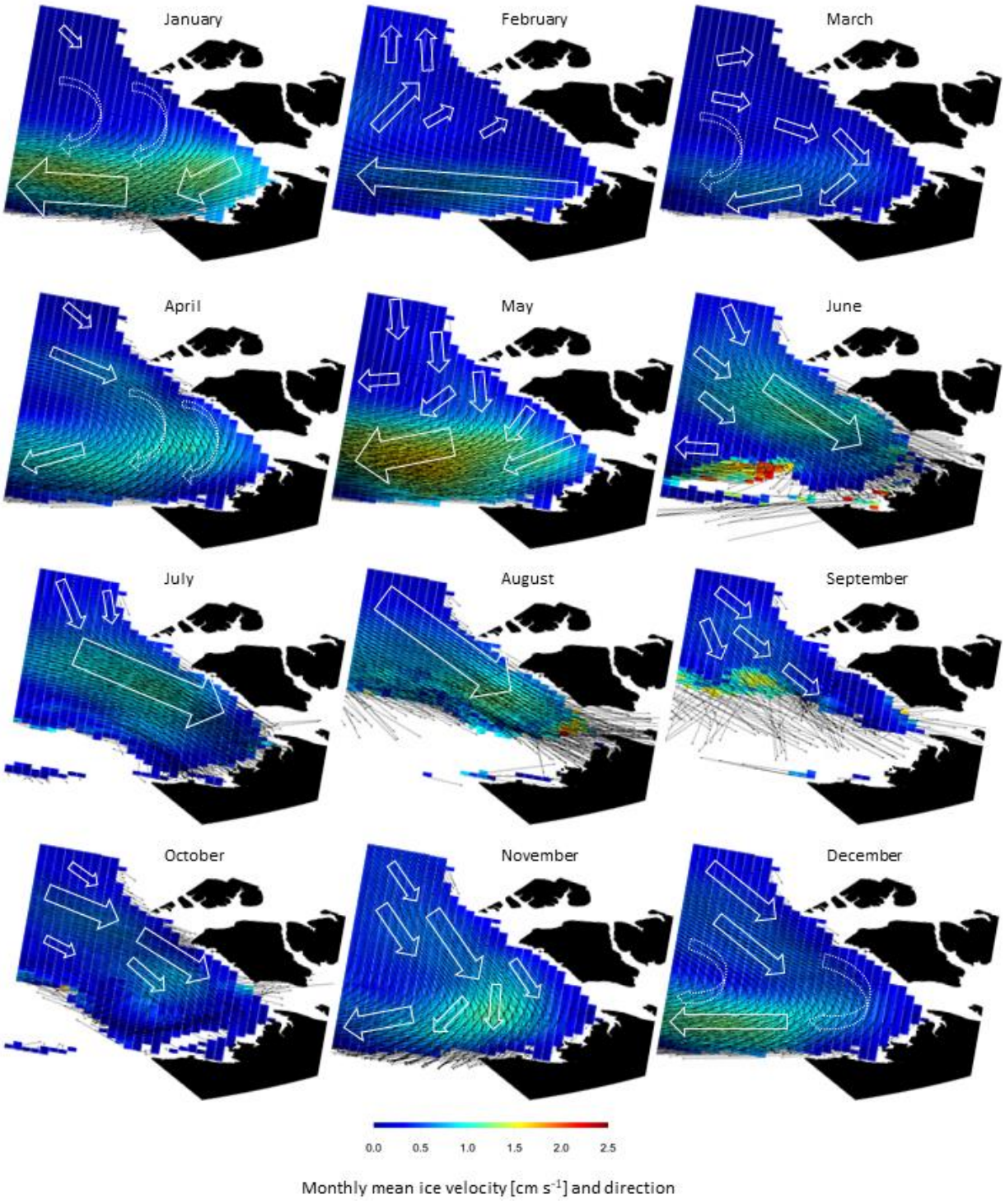

Figure 16. Monthly mean sea ice velocity (cm s^{-1}) and direction in 2019 in the Beaufort Sea and Amundsen Gulf.

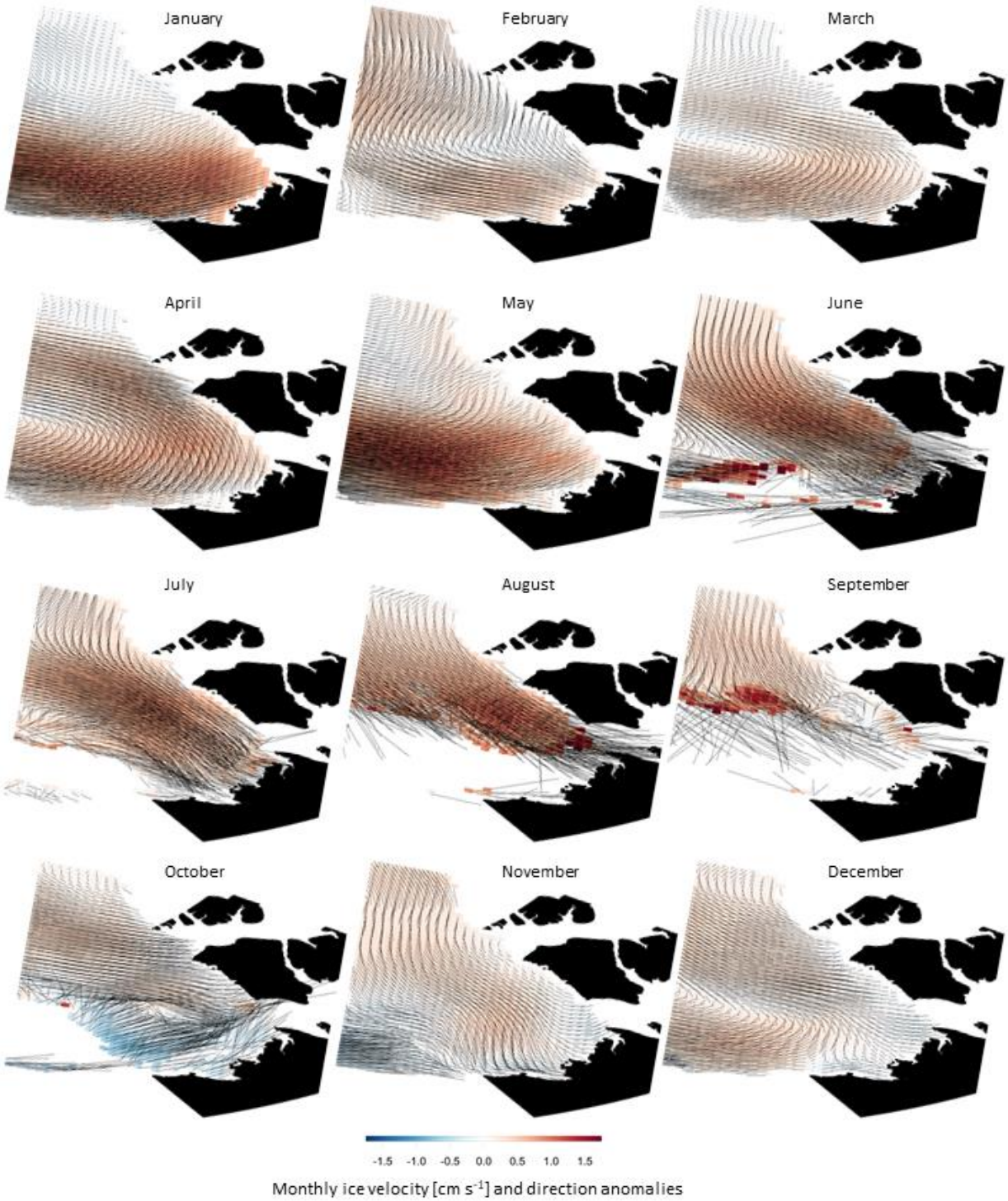

Figure 17. Monthly sea ice velocity (cm s^{-1}) and direction anomalies in 2019 from the climatological mean period 1983-2010 in the Beaufort Sea and Amundsen Gulf.

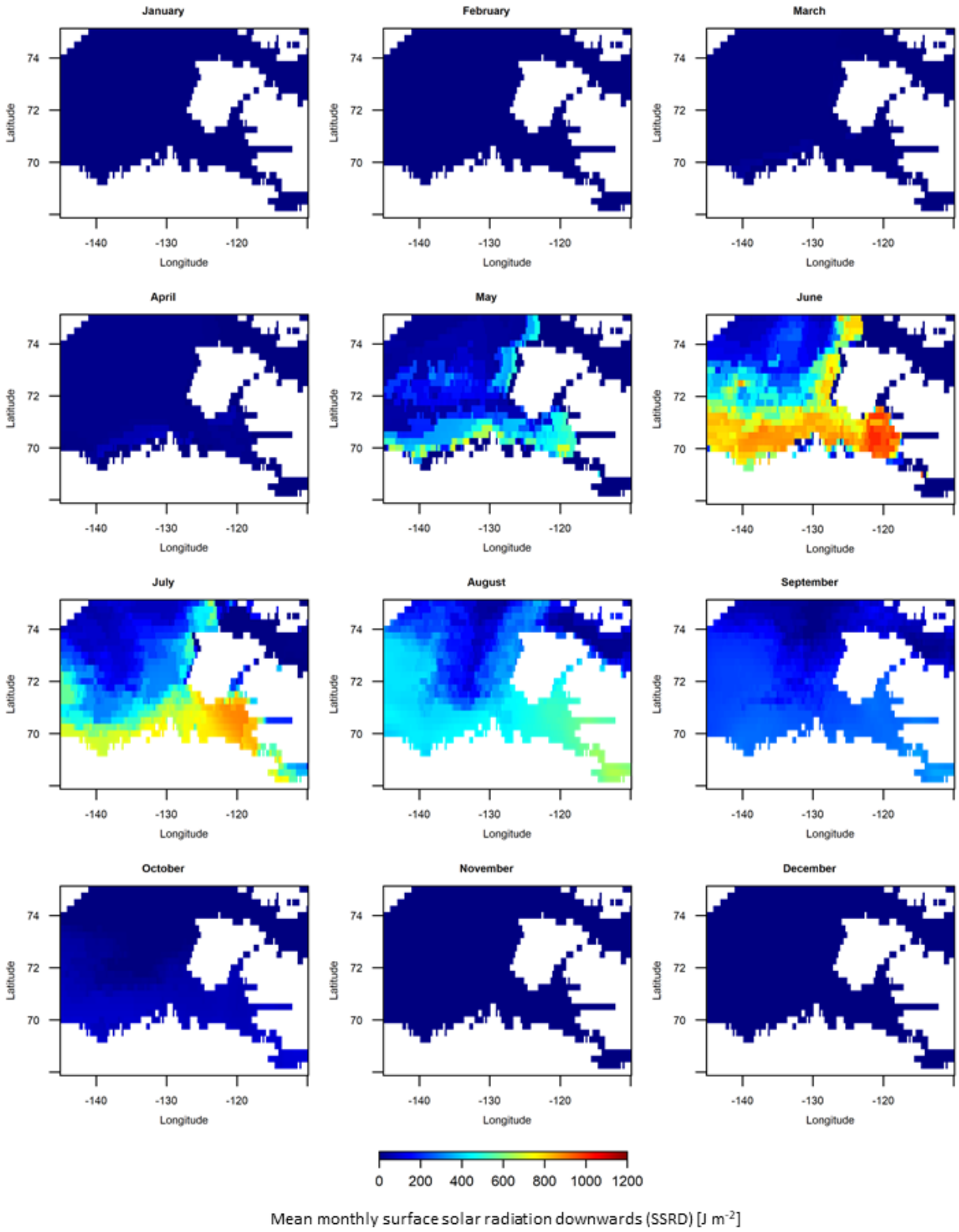

Figure 18. Mean monthly sea ice-adjusted surface solar radiation downwards (J m^{-2}) in 2019 in the Beaufort Sea and Amundsen Gulf.

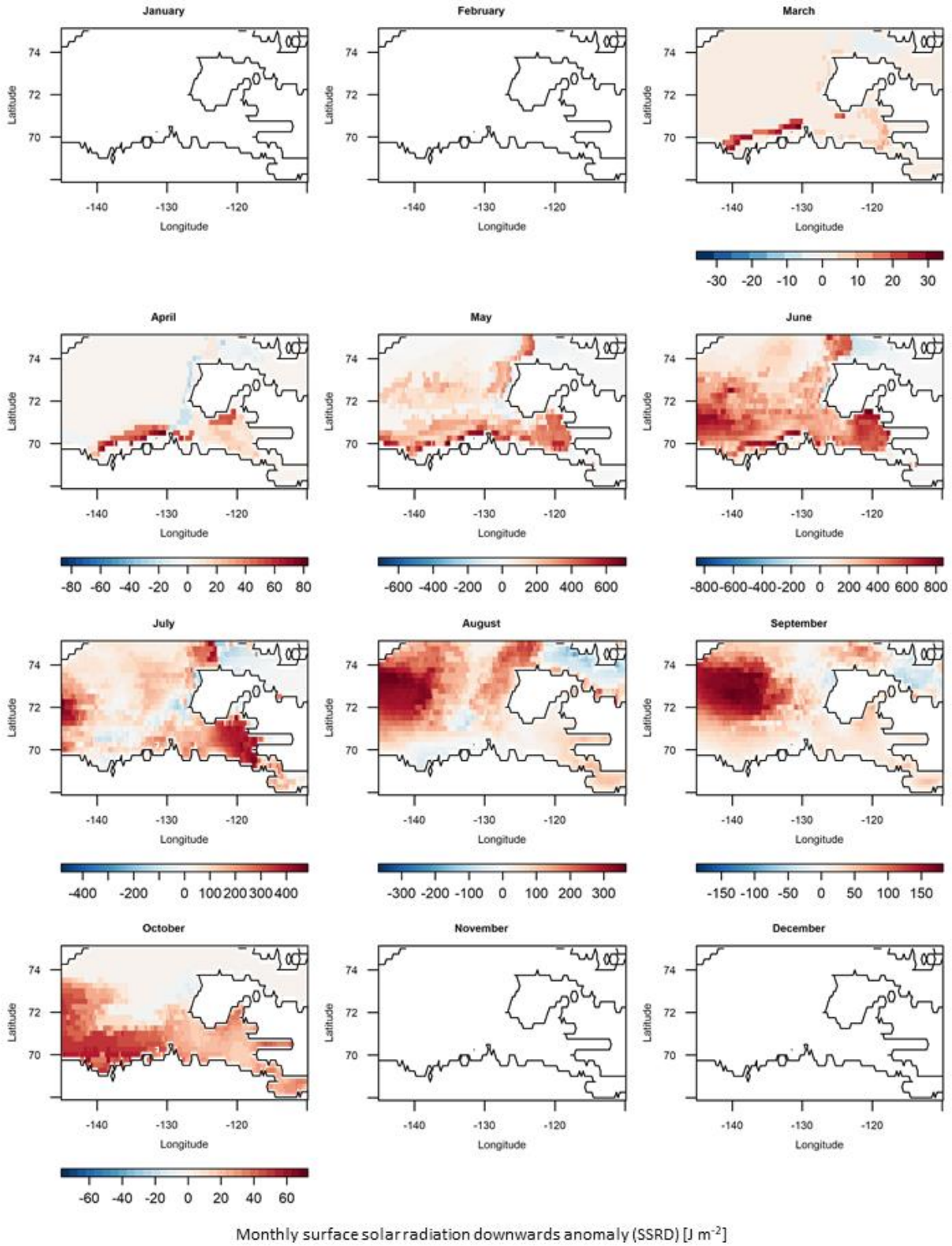

Figure 19. Monthly sea ice-adjusted surface solar radiation downwards anomalies (J m^{-2}) in 2019 compared to the climatological average period 1983-2010 in the Beaufort Sea and Amundsen Gulf.

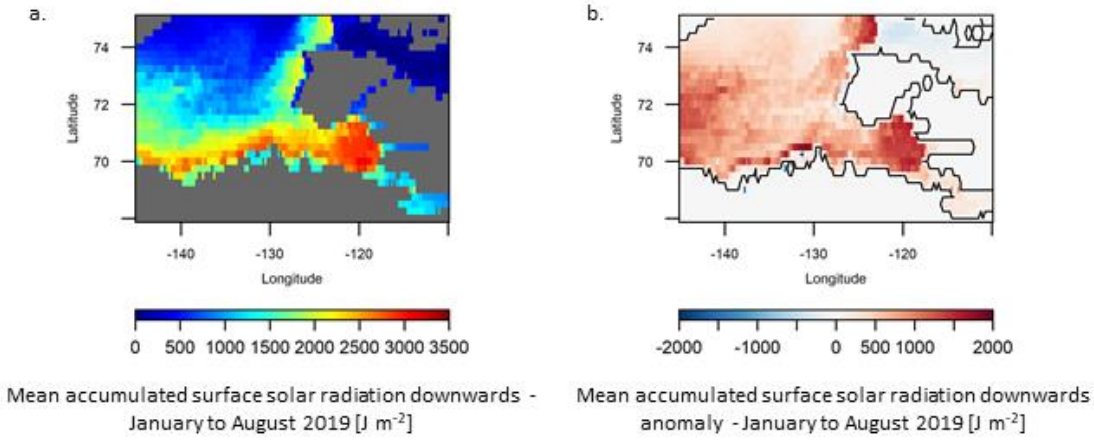

Figure 20. (a) Accumulated mean sea ice-adjusted surface solar radiation downwards (J m^{-2}) between January and August in 2019 (inclusive), and (b) accumulated sea ice-adjusted surface solar radiation downwards anomaly (J m^{-2}) between January and August 2019 (inclusive) compared to the climatological average over the period 1983-2010.

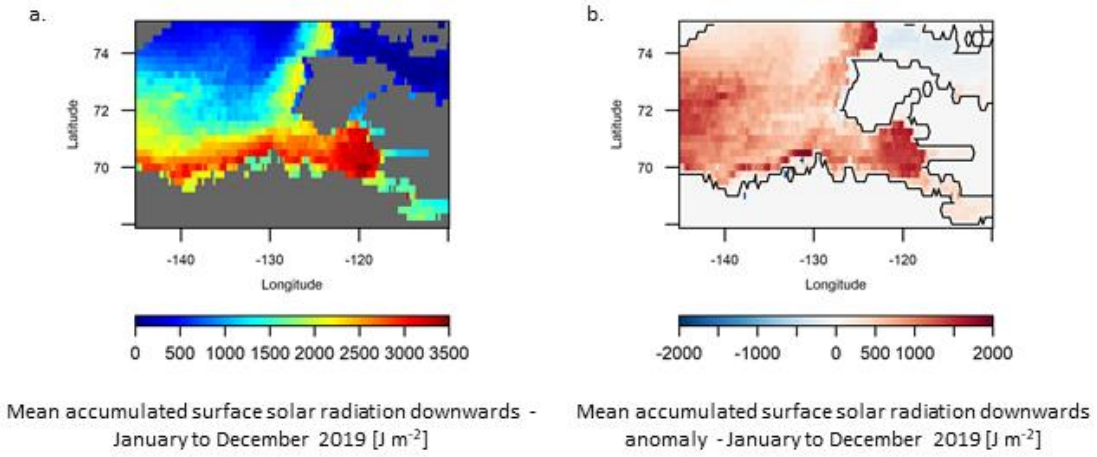

Figure 21. (a) Accumulated mean sea ice-adjusted surface solar radiation downwards (J m^{-2}) between January and December in 2019 (inclusive), and (b) accumulated sea ice-adjusted surface solar radiation downwards anomaly (J m^{-2}) between January and December 2019 (inclusive) compared to the climatological average over the period 1983-2010.

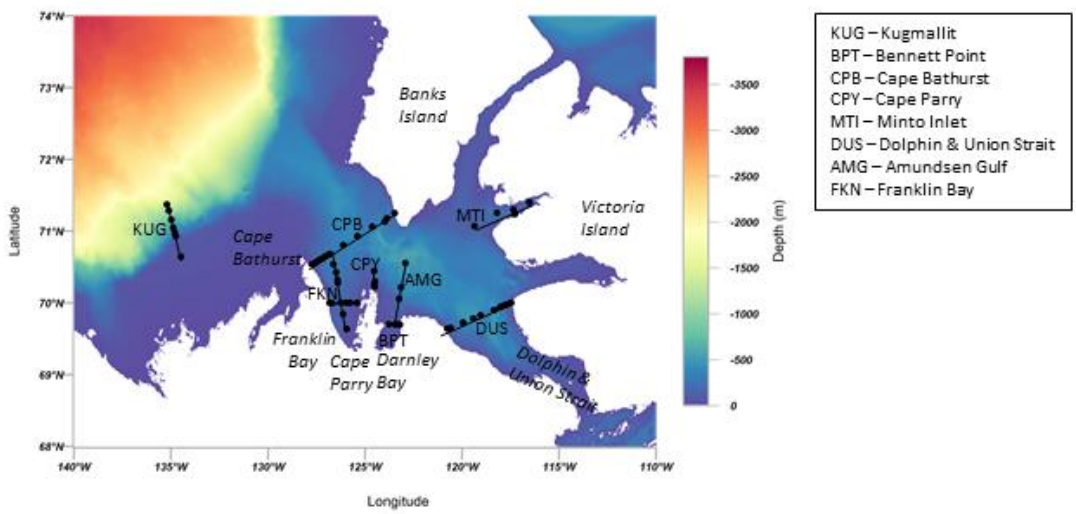

Figure 22. CBS-MEA CTD station and section locations in the 2019 study region, overlain on ETOPO1 bathymetry data.

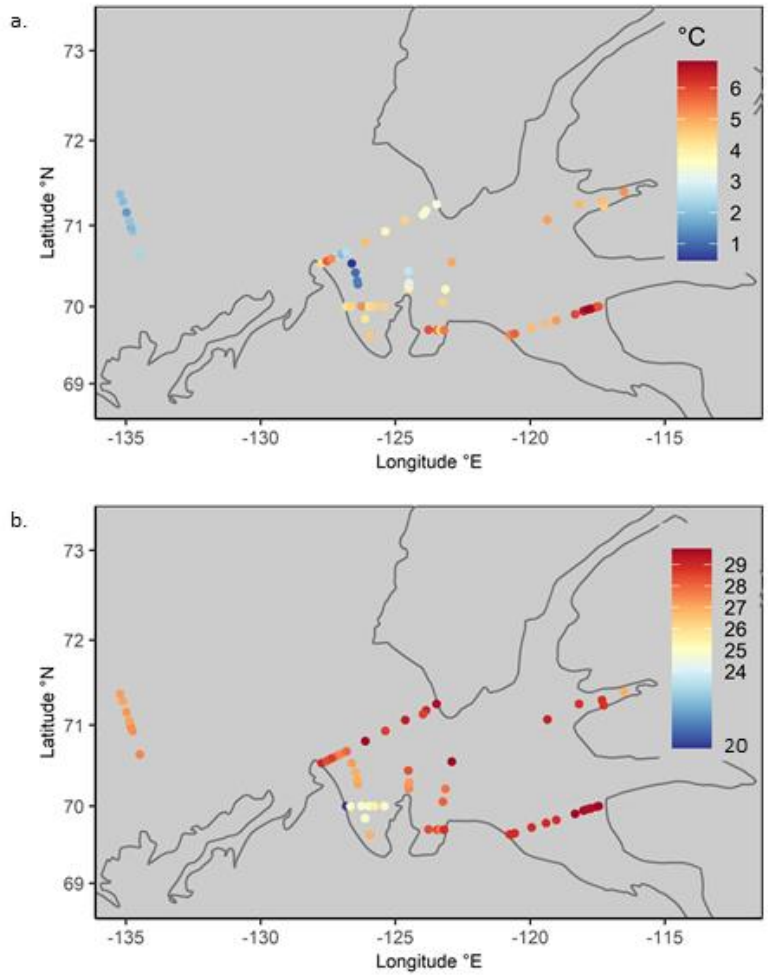

Figure 23. (a) Surface temperature (°C), and (b) surface salinity at each CBS-MEA station in 2019.

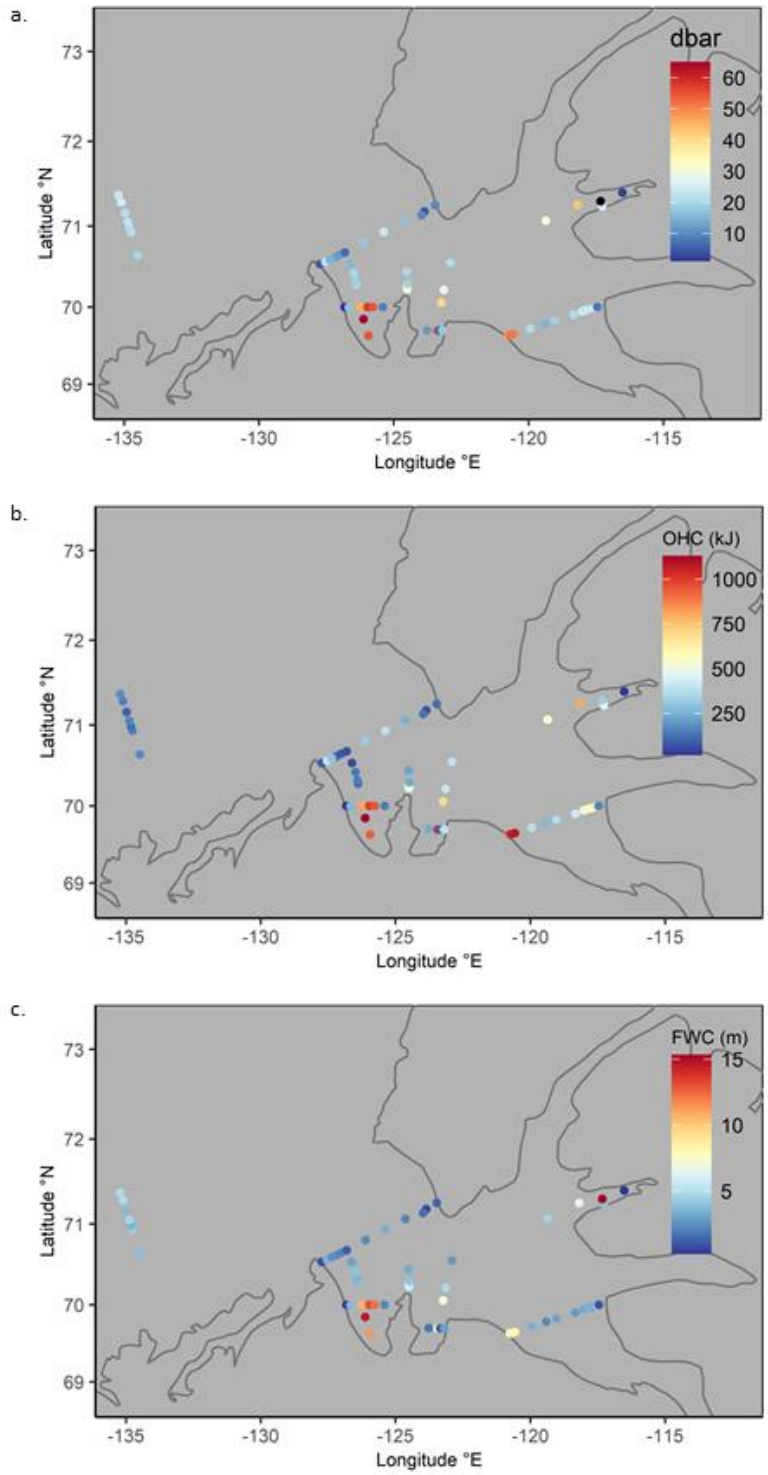

Figure 24. (a) Depth of the maximum N^2 in meters, (b) Integrated ocean heat content (OHC) relative to 0°C above the depth of the N^2 max (kJ), and (c) Freshwater content (FWC) relative to S = 34.8 integrated above the depth of the N^2 maximum; at each CBS-MEA station in 2019.

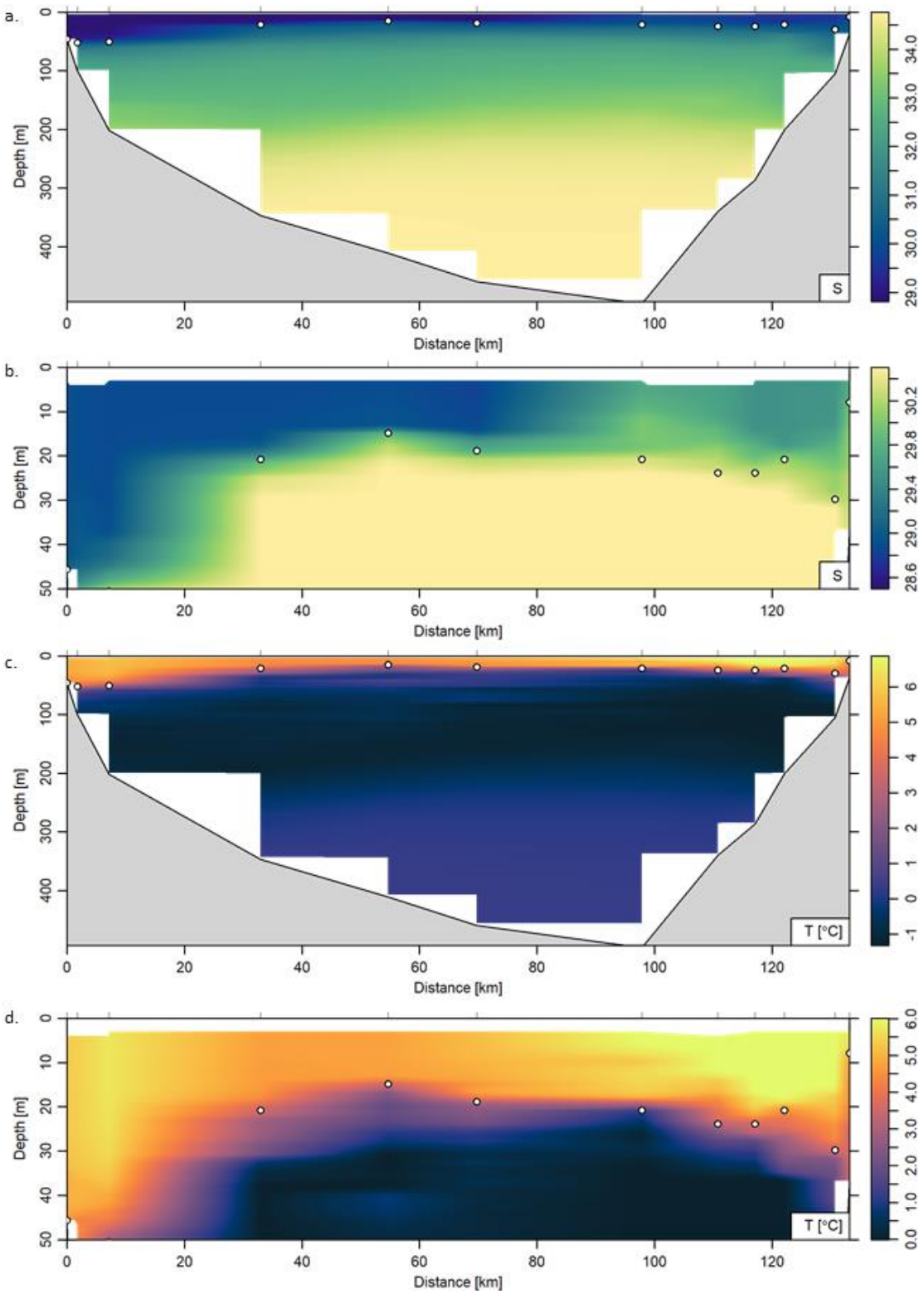

Figure 25. Sections from west to east across Dolphin and Union Strait in 2019: salinity (a, b) and temperature (c, d). Full depth is shown in (a, c) and enlarged to show only the top 50 m in (b, d). N^2-derived surface layer depths at each station are denoted by white dots.

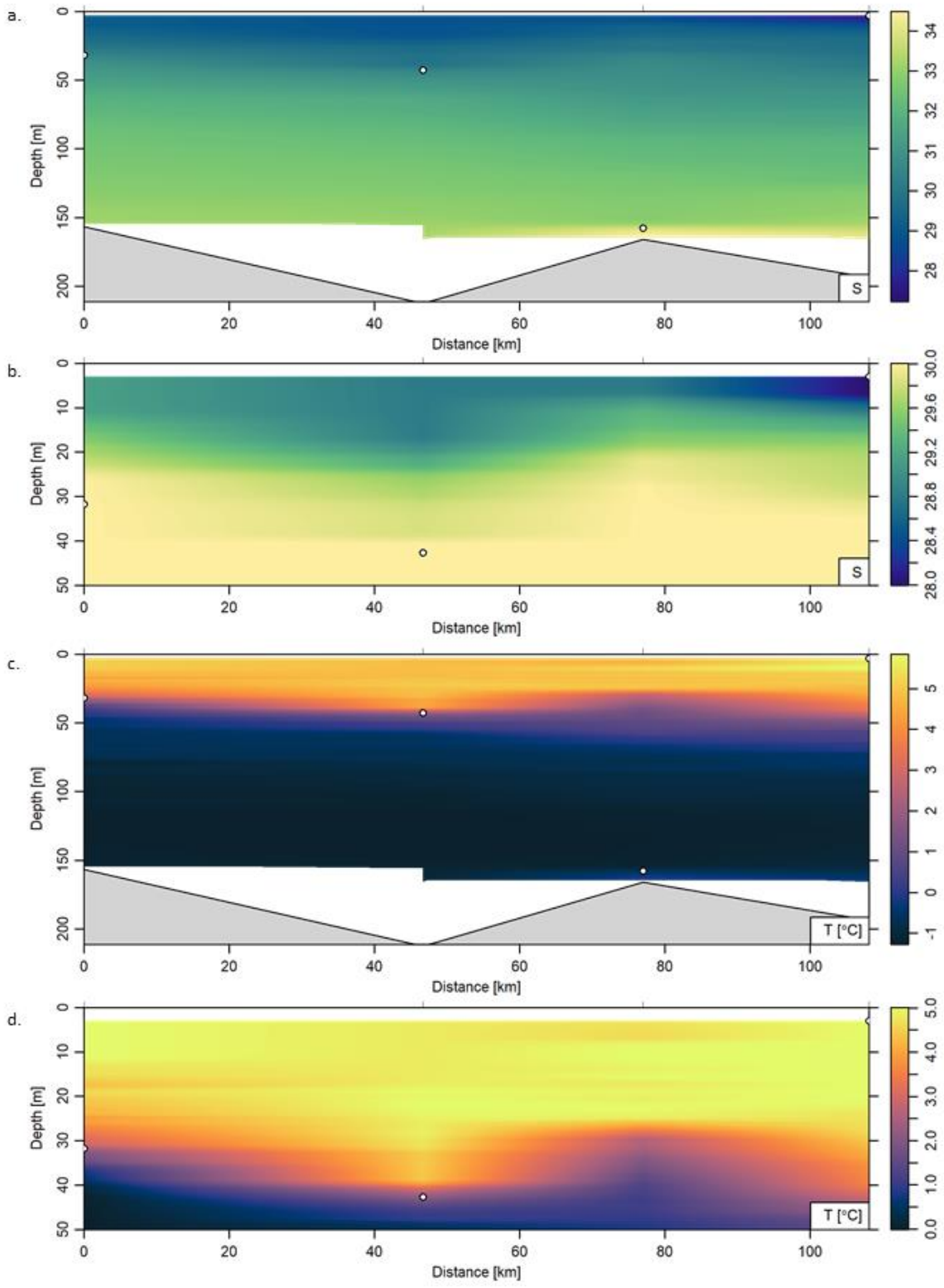

Figure 26. Sections from west to east along Minto Inlet in 2019: salinity (a, b) and temperature (c, d). Full depth (a, c) and enlarged to show only the top 50 m (b, d). N^2-derived surface layer depths at each station are denoted by white dots.

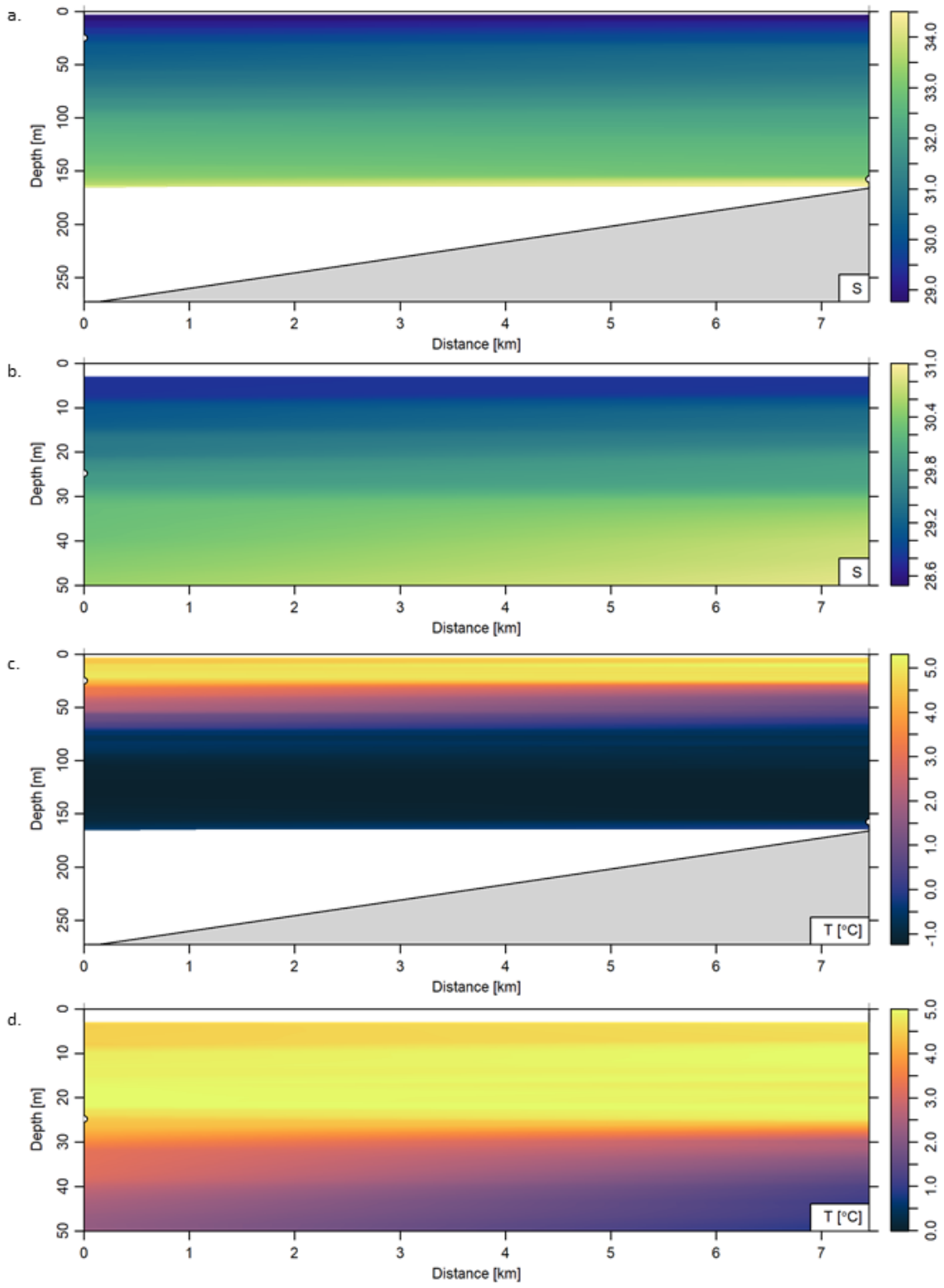

Figure 27. Sections from south to north across Minto Inlet in 2019: salinity (a, b) and temperature (c, d). Full depth (a, c) and enlarged to show only the top 50 m (b, d). N^2-derived surface layer depths at each station are denoted by white dots.

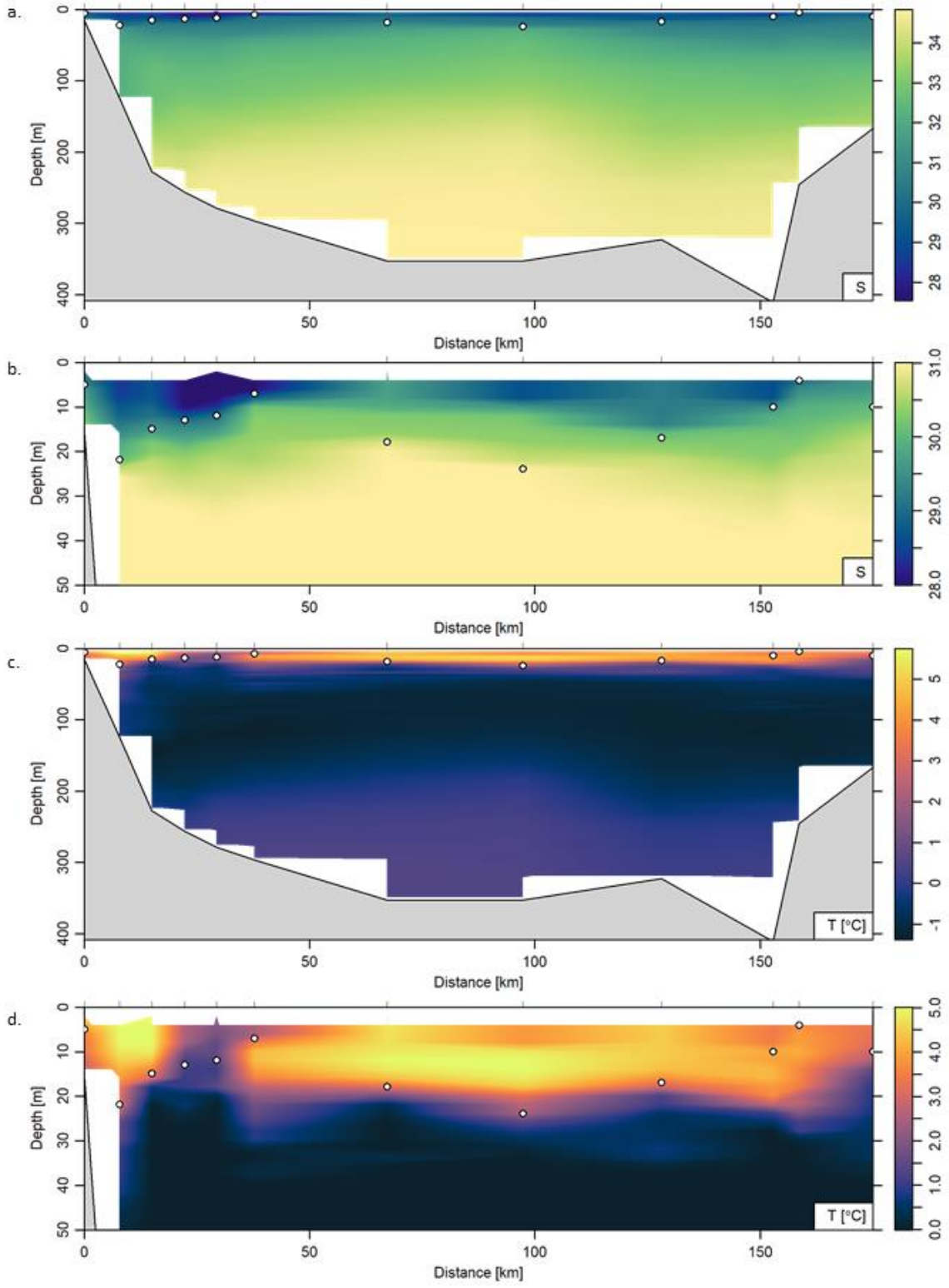

Figure 28. Sections from southwest to northeast along the Cape Bathurst transect in 2019: salinity (a, b) and temperature (c, d). Full depth (a, c) and enlarged to show only the top 5 0m (b, d). N^2-derived surface layer depths at each station are denoted by white dots.

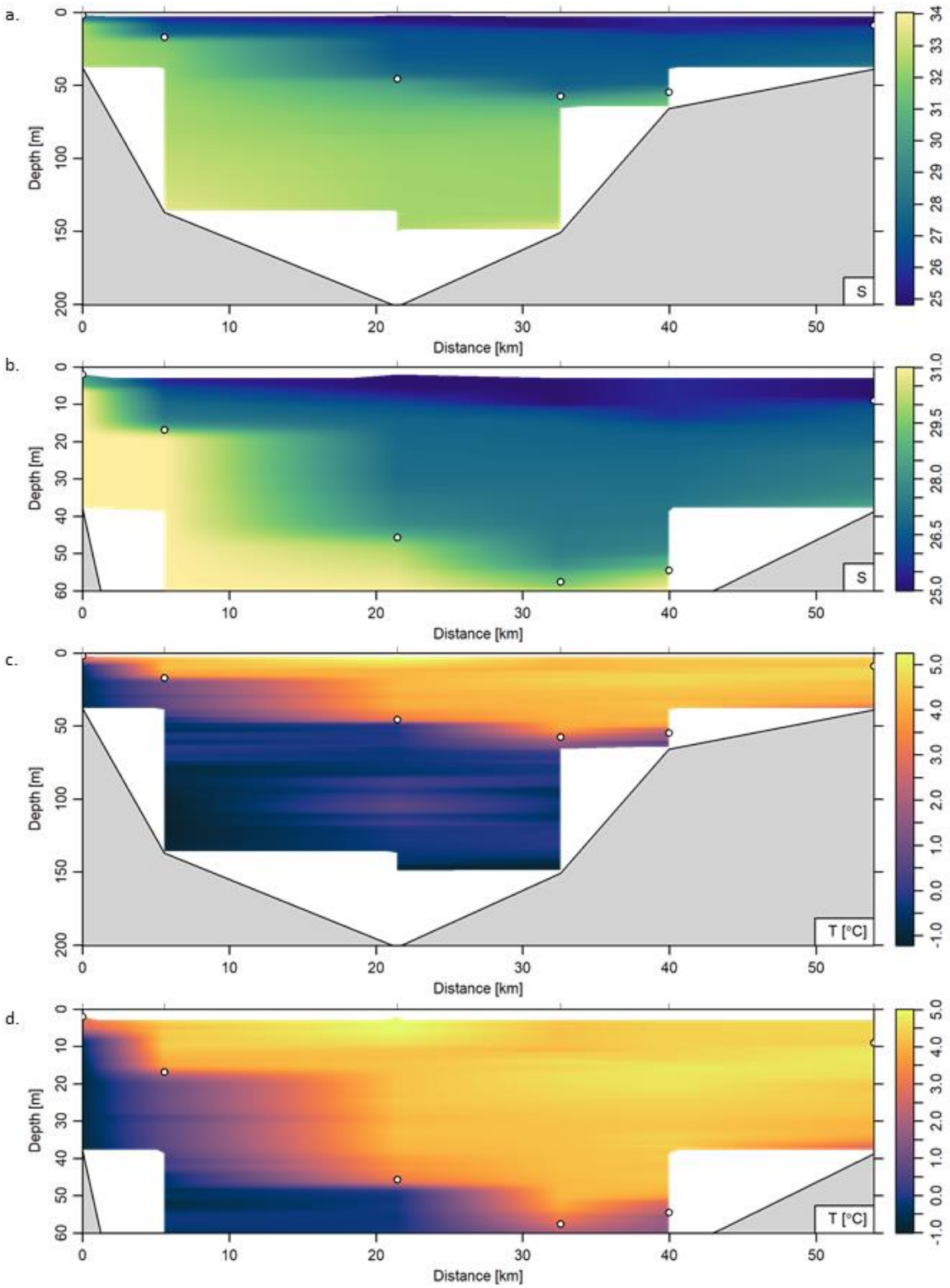

Figure 29. Sections from west to east across Franklin Bay in 2019: salinity (a, b) and temperature (c, d). Full depth (a, c) and enlarged to show only the top 50 m (b, d). N^2-derived surface layer depths at each station are denoted by white dots.

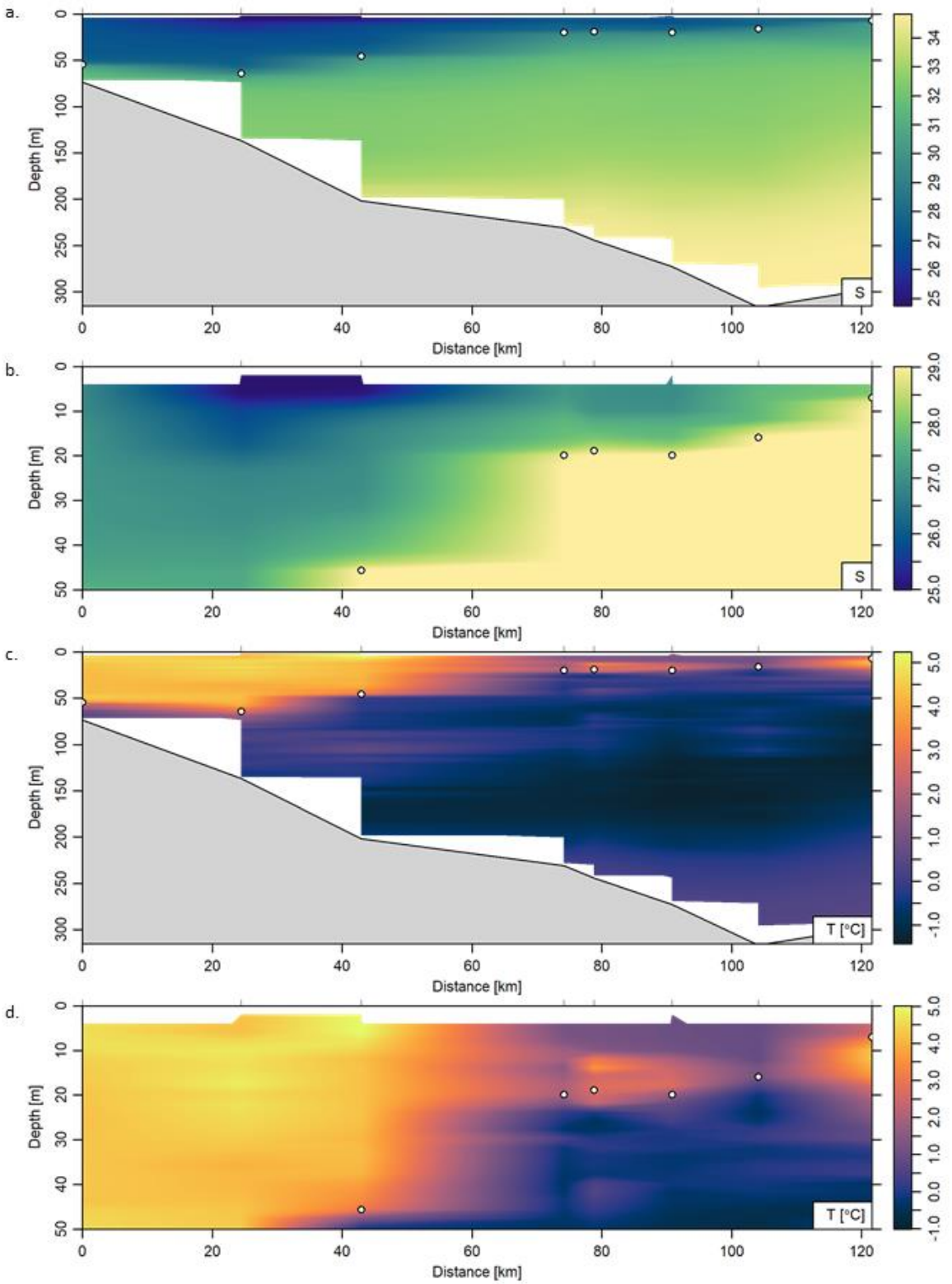

Figure 30. Sections from south to north in Franklin Bay in 2019: salinity (a, b) and temperature (c, d). Full depth (a, c) and enlarged to show only the top 50 m (b, d). N^2-derived surface layer depths at each station are denoted by white dots.

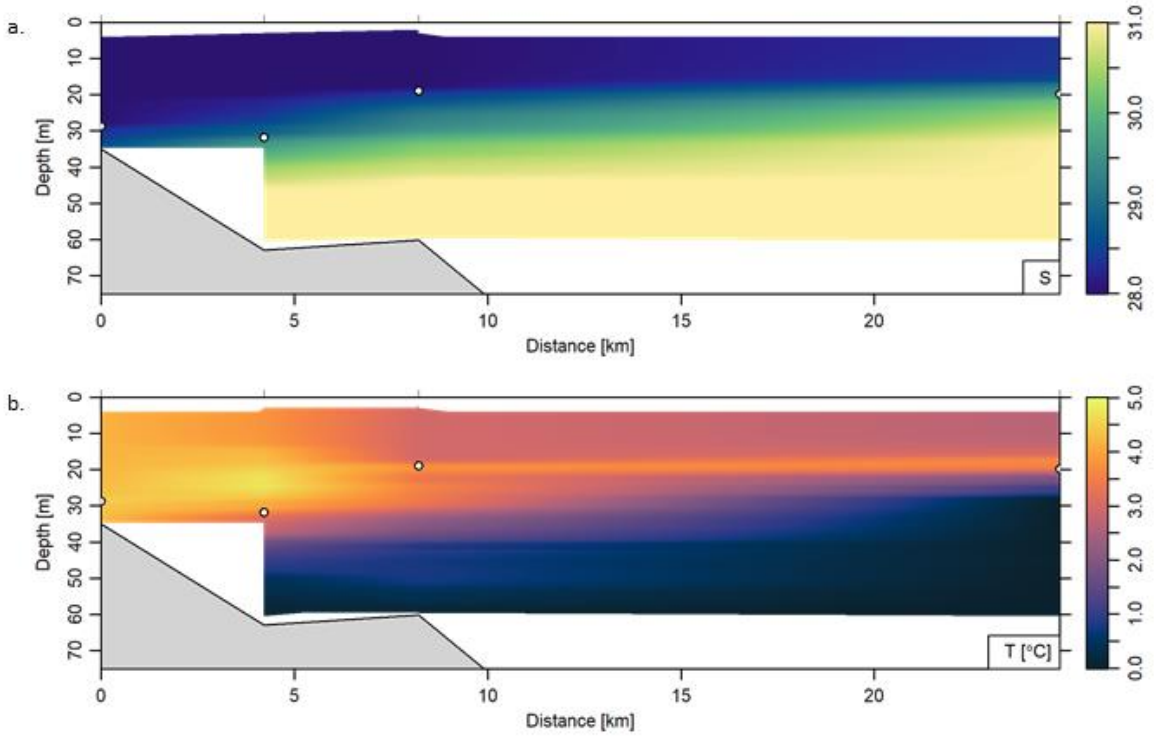

Figure 31. Sections from south to north over the Cape Parry stations in 2019: salinity (a, b) and temperature (c, d). Full depth (a, c) and enlarged to show only the top 50 m (b, d). N^2-derived surface layer depths at each station are denoted by white dots.

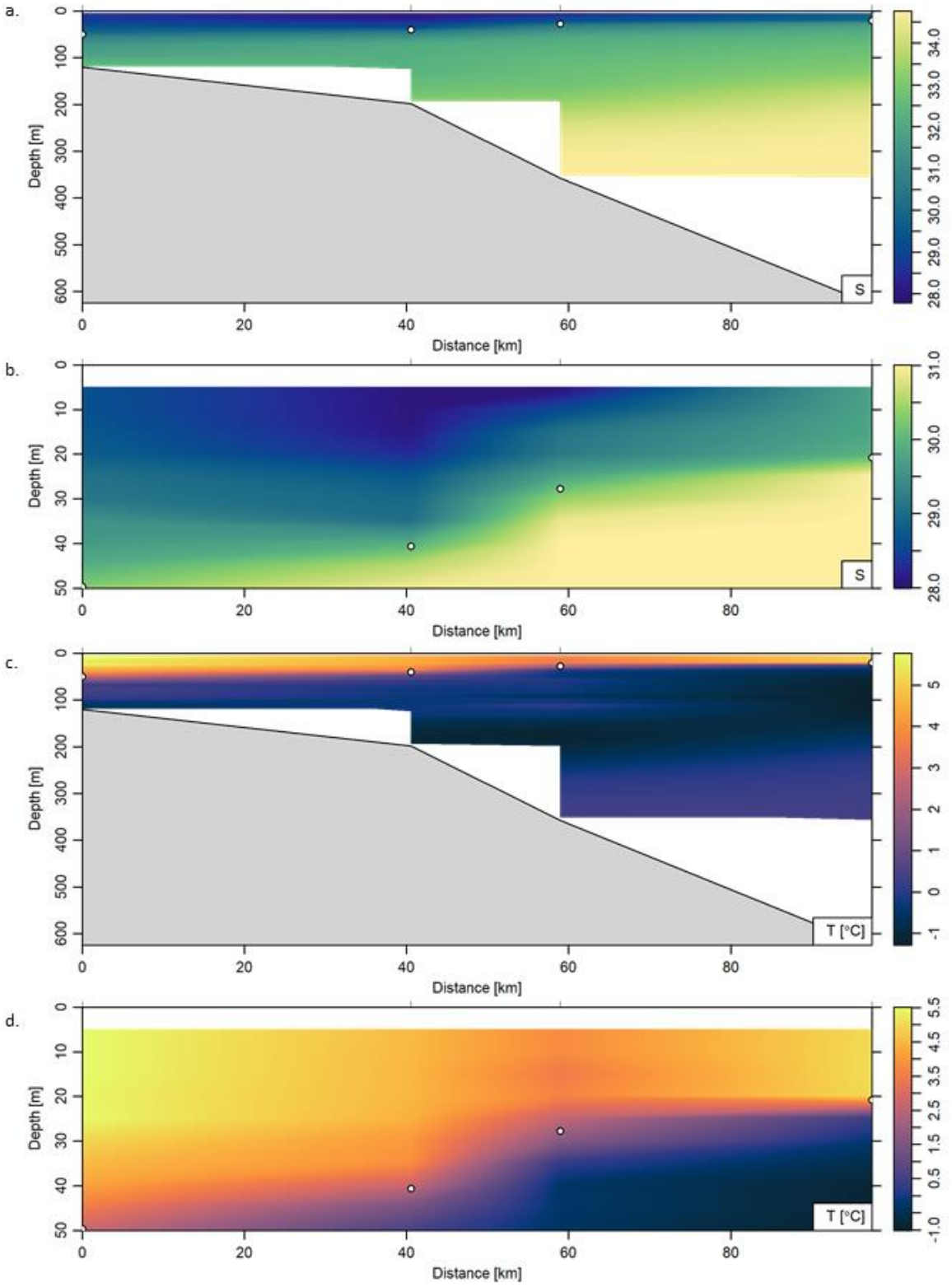

Figure 32. Sections from south to north from Bennett Point (BPT) through the Amundsen Gulf (AMG) stations in 2019: salinity (a, b) and temperature (c, d). Full depth (a, c) and enlarged to show only the top 50 m (b, d). N^2-derived surface layer depths at each station are denoted by white dots.

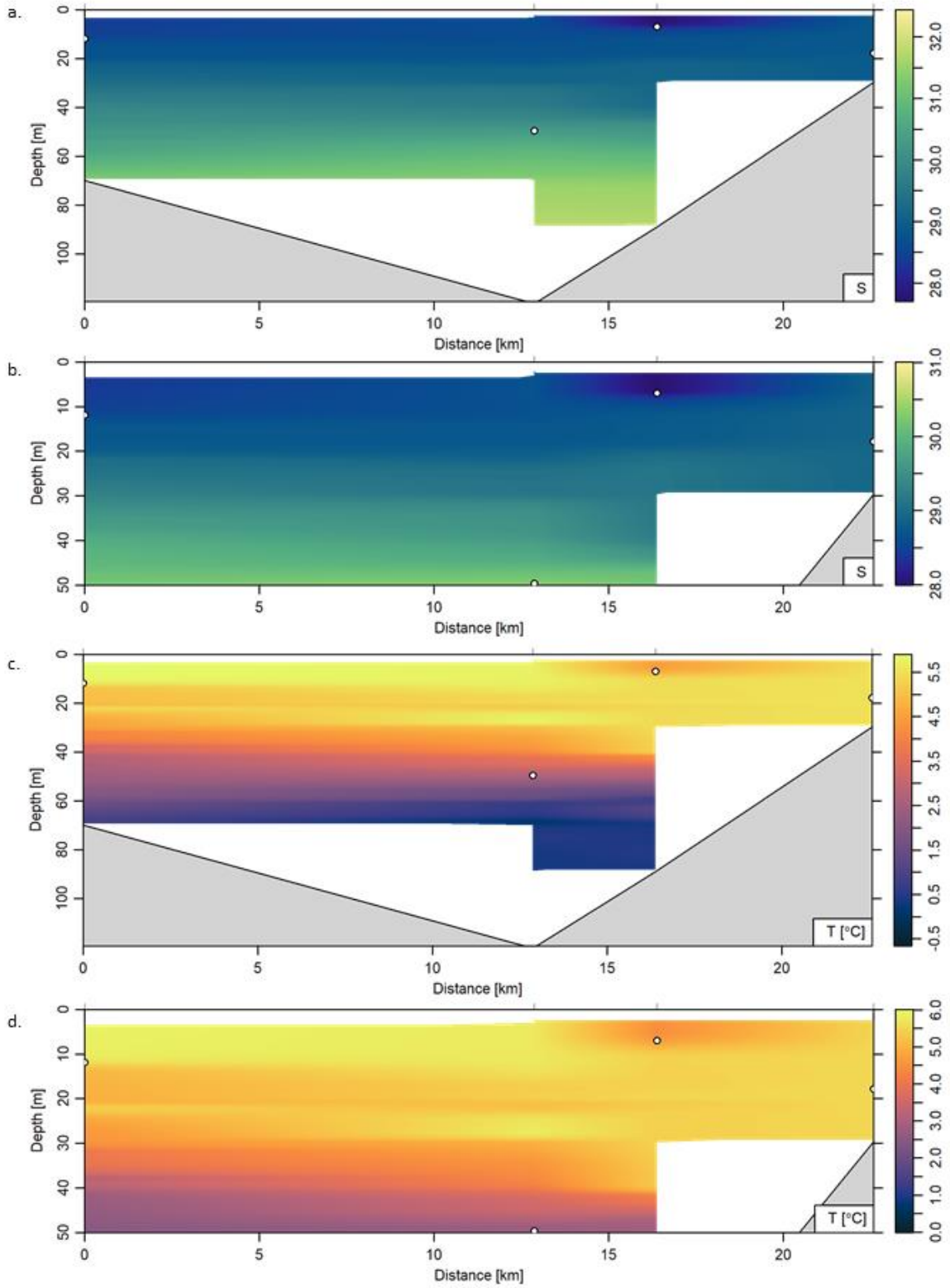

Figure 33. Sections from west to east across Darnley Bay using the BPT stations in 2019: salinity (a, b) and temperature (c, d). Full depth (a, c) and enlarged to show only the top 50 m (b, d). N^2-derived surface layer depths at each station are denoted by white dots.

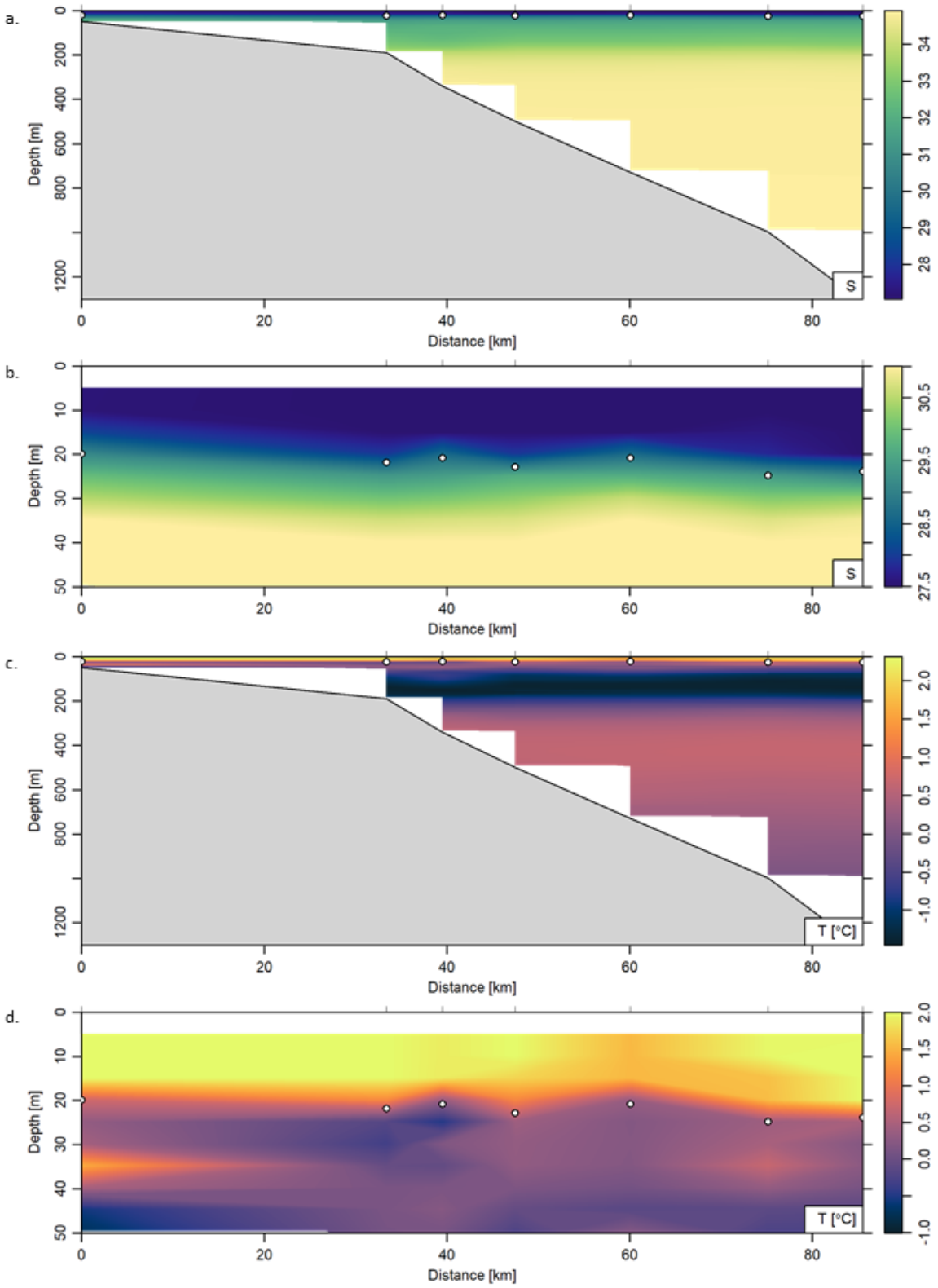

Figure 34. Sections from south to north along the Kugmallit (KUG) stations in 2019: salinity (a, b) and temperature (c, d). Full depth (a, c) and enlarged to show only the top 50 m (b, d). N^2-derived surface layer depths at each station are denoted by white dots.

8 Tables

Table 1. Surface and surface layer oceanographic parameters at each CBS-MEA station, August-September 2019. Freshwater content (FWC) and ocean heat content (OHC) is integrated over the surface layer (dbar) depth.

Station	Lat (°N)	Lon (°N)	Surface Temp (°C)	Surface Salinity	Surface depth (dbar)	Surface Layer (dbar)	OHC (kJ)	FWC (m)	Station Depth
DUS_01	69.64	-120.76	5.33	28.93	2.1	46.1	965.76	7.58	56
DUS_02	69.64	-120.71	5.41	28.90	3.1	51.9	1058.93	8.31	106
DUS_03	69.65	-120.58	5.73	28.88	2.2	51	1081.05	8.29	211
DUS_04	69.73	-119.94	4.73	28.87	2.1	21	376.40	3.34	354
DUS_05	69.78	-119.41	4.76	28.91	2.1	15	268.40	2.33	416
DUS_07	69.90	-118.34	5.99	29.72	2.2	21	425.17	2.81	506
DUS_08	69.94	-118.02	6.59	29.62	3.1	24	486.96	3.11	348
DUS_09	69.97	-117.74	6.78	29.52	2.1	21	533.22	3.00	209
DUS_10	69.99	-117.52	6.50	29.54	2.3	30	665.77	4.18	112
DUS_11	70.00	-117.46	5.84	29.72	2.3	8	162.00	1.01	43
DUS_HC1	69.96	-117.86	6.85	29.51	2.1	24	585.79	3.39	290
DUS_HC2	69.82	-119.03	5.14	28.82	2.3	19	360.58	2.99	463
MTI_05	71.24	-117.27	4.53	28.78	2.3	25	472.03	3.85	281
MTI_06	71.40	-116.53	5.24	26.96	2.3	2.3	21.74	0.23	203
MTI_04	71.30	-117.34	4.74	28.80	2.4	159 (29)	324.67 (547.18)	15.33 (4.30)	170
MTI_02	71.25	-118.19	4.82	28.80	2.4	43	801.48	6.61	222
MTI_01	71.07	-119.36	5.10	29.13	2.1	31.3	554.49	4.52	165
BPT_01	69.70	-123.77	5.89	28.38	3.1	12	241.27	1.83	76
BPT_03	69.70	-123.44	5.76	28.64	1.5	50	1021.25	8.10	125
BPT_HC1	69.70	-123.35	4.49	27.72	2.4	7	112.56	1.21	93
BPT_05	69.70	-123.19	5.47	28.84	2.3	18.1	386.85	2.90	38
CPB_01	70.54	-127.73	4.29	28.96	1.5	5	85.70	0.82	20
CPB_02	70.56	-127.54	5.74	28.37	2.1	22	394.85	3.48	133
CPB_04	70.62	-127.19	2.63	27.80	2.1	13	106.53	2.33	260
CPB_05	70.65	-127.02	2.02	27.56	2	12	79.43	2.17	286
CPB_03	70.59	-127.37	5.30	28.65	1.4	15	297.98	2.54	238
CPB_06	70.68	-126.82	2.51	27.99	2.3	6.9	62.78	1.17	305
CPB_07	70.81	-126.11	4.75	29.71	2	18	324.50	2.33	358
CPB_08	70.93	-125.38	3.82	28.61	2.3	24	386.19	3.32	358
CPB_09	71.06	-124.63	4.47	29.21	4	17	248.88	2.18	329
CPB_10	71.18	-123.87	3.68	28.98	2.2	4.9	60.94	0.67	255
CPB_11	71.25	-123.47	3.39	29.52	2.3	10	120.68	1.32	171
CPB_HC1	71.13	-123.98	3.45	28.60	2.1	9.9	133.15	1.57	417
CPY_01	70.22	-124.50	4.17	27.59	3.4	29	473.19	5.52	45
CPY_03	70.44	-124.52	2.67	28.34	3.1	20	218.66	3.21	192
CPY_02	70.26	-124.51	3.78	27.40	2.1	32	533.46	6.14	79
CPY_HC1	70.30	-124.49	2.98	27.22	1.4	19	239.33	4.09	72
FKN_01	70.00	-126.82	4.20	20.42	1.2	1.2	17.61	0.41	46
FKN_02	70.00	-126.67	4.40	25.10	2.4	17	271.64	3.68	152
FKN_03	70.00	-126.26	5.24	24.84	1.5	46	809.88	10.58	211
FKN_04	70.00	-125.97	4.24	24.86	2.4	58	990.07	13.03	159
FKN_05	70.00	-125.77	4.44	25.53	2.1	55	953.69	12.29	76
FKN_06	70.00	-125.41	4.51	24.87	2.1	9	149.24	2.26	49
FKN_07	69.63	-125.94	4.62	26.85	2.2	55	934.16	11.32	81
FKN_HC2	69.84	-126.12	4.20	24.77	2	65	1128.39	14.62	144
FKN_HC1	70.28	-126.39	1.21	27.12	2.2	20	128.94	3.93	238
AMG_04	70.32	-126.42	1.20	26.98	3.1	19	149.72	3.58	252
AMG_05	70.43	-126.49	1.02	26.90	2	20	136.18	4.02	282
AMG_06	70.54	-126.62	0.46	27.19	2.1	16	58.23	2.98	327
AMG_01	70.06	-123.24	4.51	28.07	2.4	41	695.96	7.16	206
AMG_02	70.22	-123.14	3.75	27.80	1.5	28	402.96	4.80	367
AMG_03	70.55	-122.91	5.01	29.73	3.2	21	387.37	2.72	642
KUG_01C	70.64	-134.48	2.31	27.56	2.2	20	169.66	3.79	61
KUG_03	70.93	-134.75	2.09	27.39	2.1	22	164.00	4.38	197
KUG_04	70.98	-134.81	1.90	27.39	5	21	118.13	3.52	348
KUG_05	71.05	-134.88	2.09	27.10	2	23	162.45	4.67	504
KUG_06	71.16	-134.97	1.55	27.26	4.4	21	96.66	3.74	737
KUG_07	71.29	-135.11	1.98	27.07	2.1	25	158.11	4.97	1008
KUG_08	71.37	-135.21	1.98	27.20	2.2	24.1	177.11	4.90	1306

Appendix A – Profiles of salinity, temperature, potential density anomaly, and N^2, and T-S plots for each of the 59 stations sampled during CBS-MEA 2019. Station name is indicated with the map, showing the station location as described in Figure 22 and Table 1.

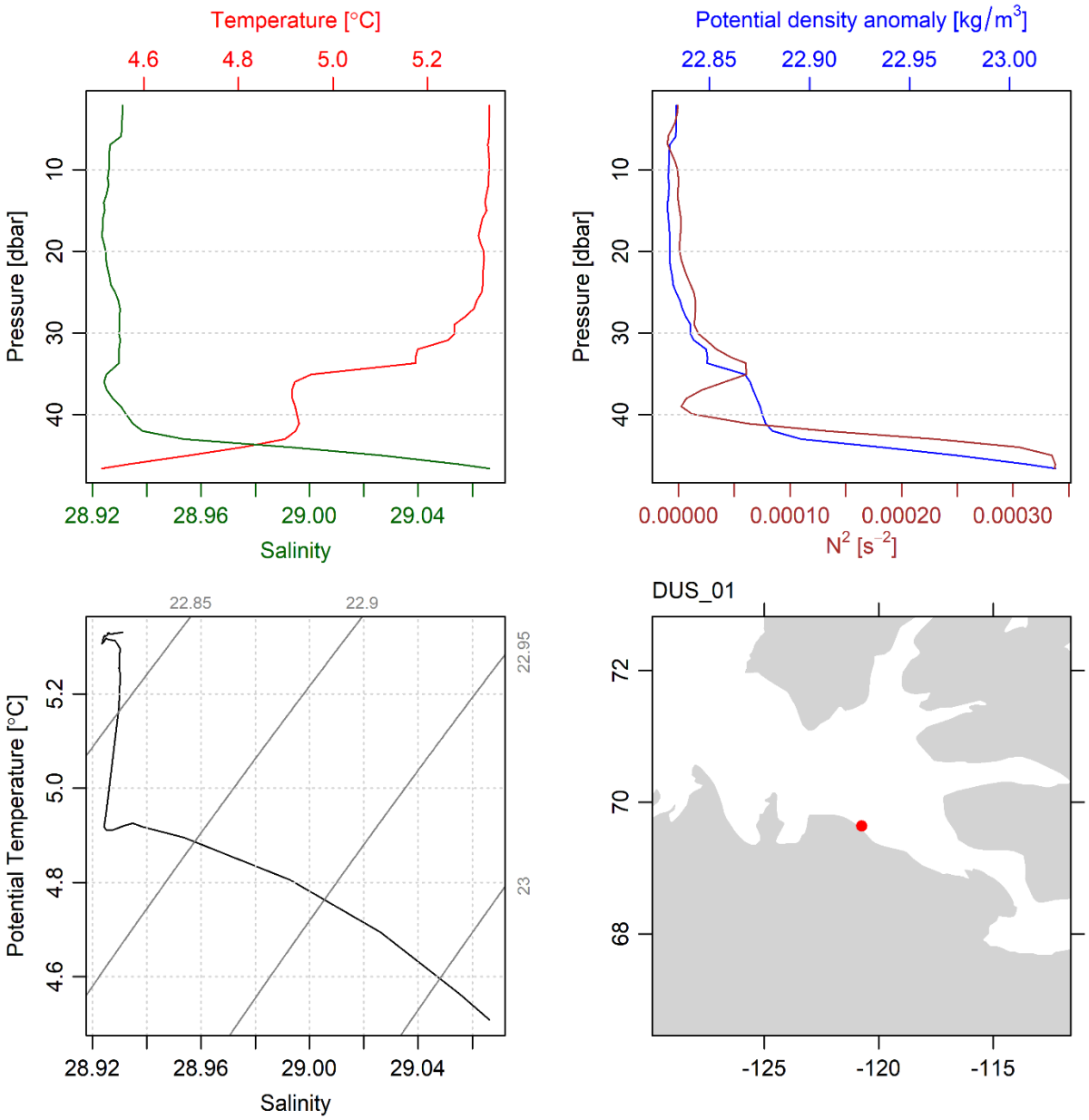

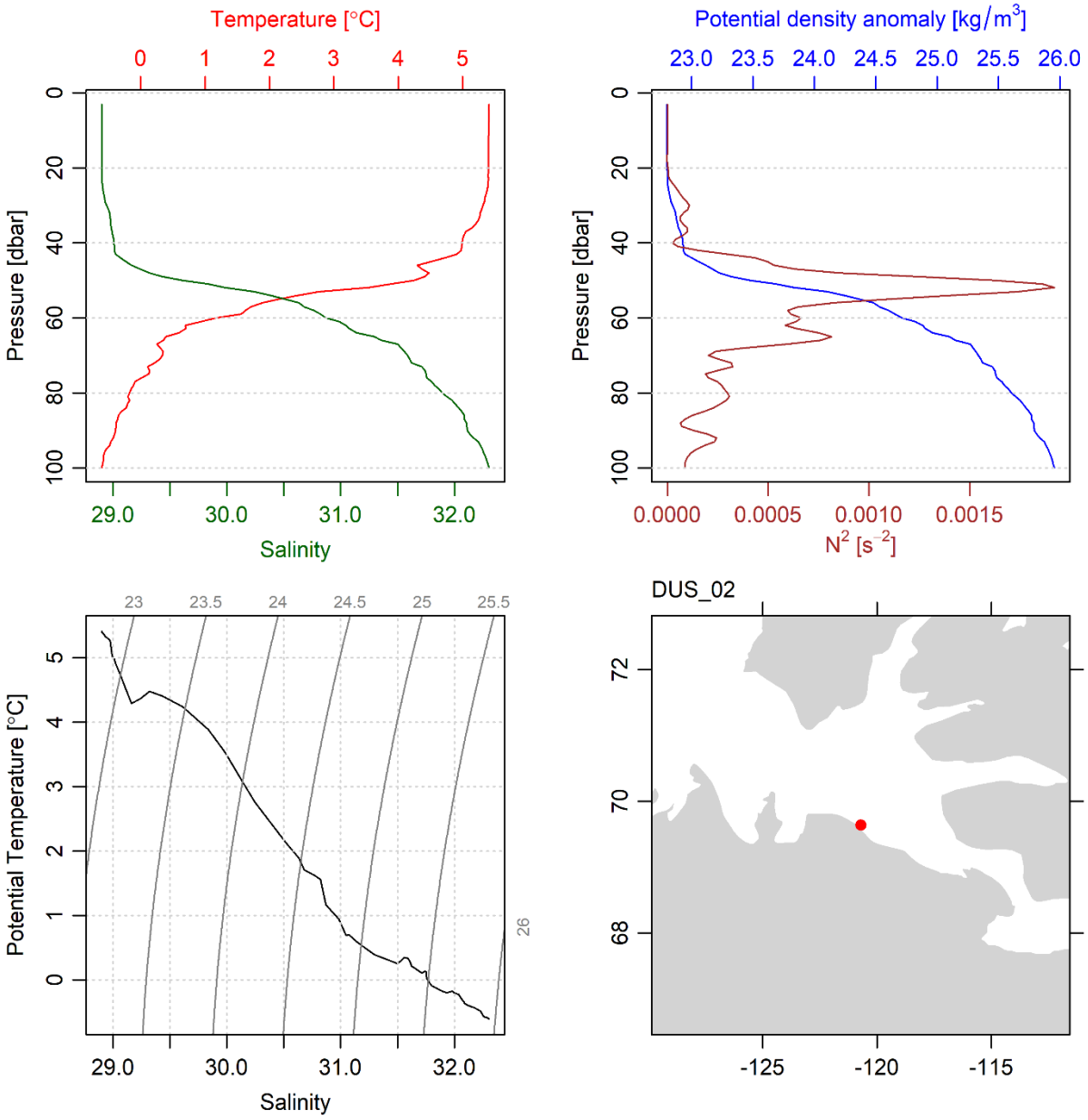
Temperature [°C]
0 1 2 3 4 5
Pressure [dbar]
0 20 40 60 80 100
29.0 30.0 31.0 32.0
Salinity
Potential density anomaly [kg/m3]
23.0 23.5 24.0 24.5 25.0 25.5 26.0
0.0000 0.0005 0.0010 0.0015
N2 [s−2]
Potential Temperature [°C]
23 23.5 24 24.5 25 25.5
26
DUS_02
72 70 68
-125 -120 -115

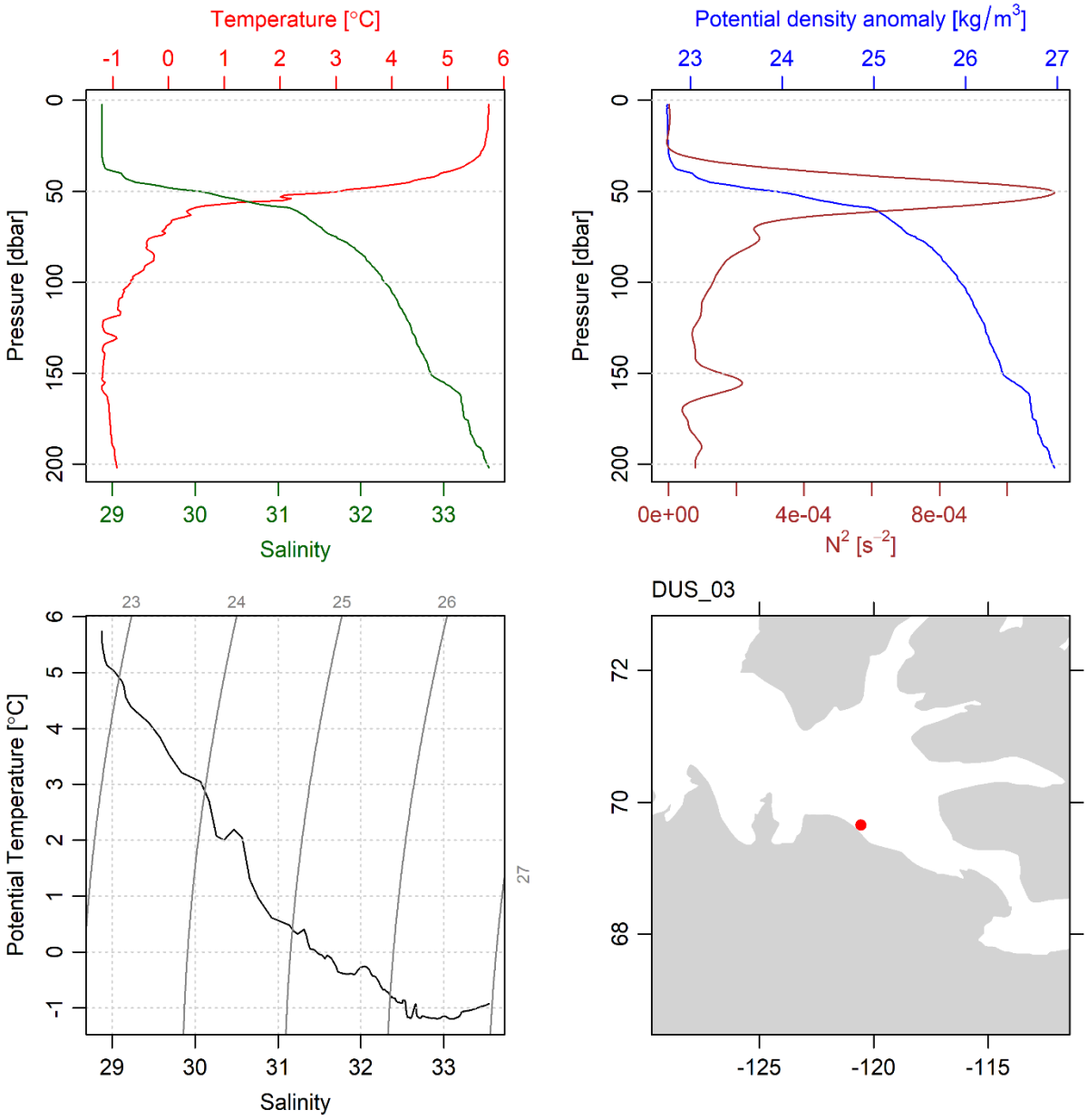
Temperature [°C]
-1 0 1 2 3 4 5 6
Pressure [dbar]
0 50 100 150 200
29 30 31 32 33
Salinity
Potential density anomaly [kg/m3]
23 24 25 26 27
0e+00 4e-04 8e-04
N2 [s−2]
Potential Temperature [°C]
23 24 25 26
27
DUS_03
72 70 68
-125 -120 -115

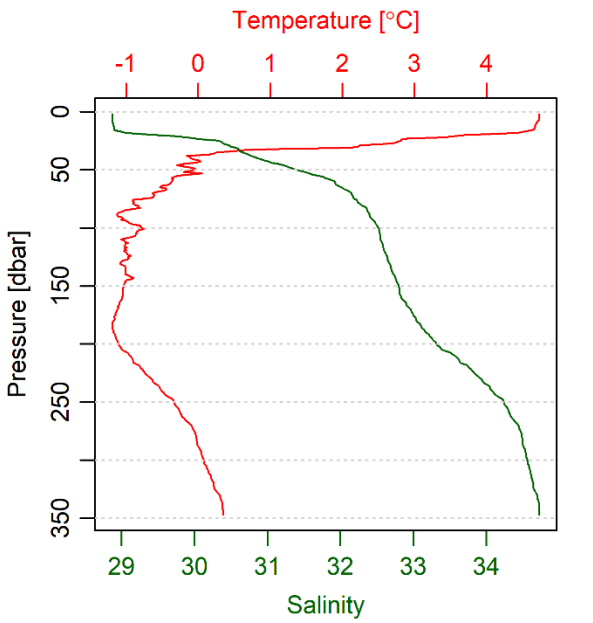
Temperature [°C]
-1
0
1
2
3
4
Pressure [dbar]
0
50
150
250
350
29
30
31
32
33
34
Salinity

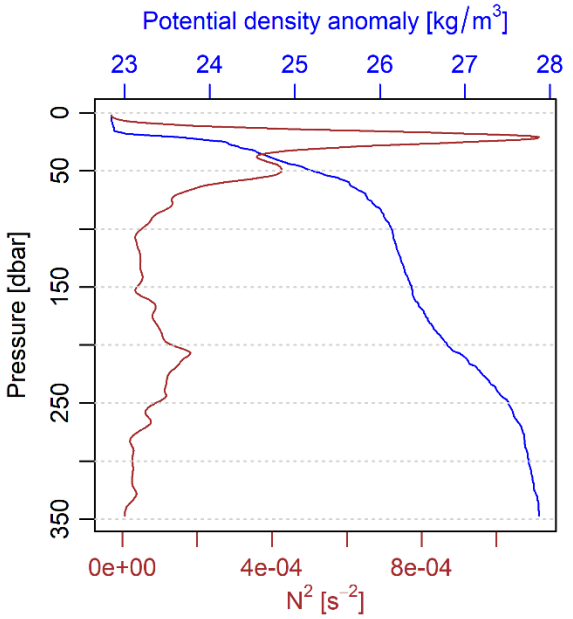
Potential density anomaly [kg/m3]
23
24
25
26
27
28
Pressure [dbar]
0
50
150
250
350
0e+00
4e-04
8e-04
N2 [s−2]

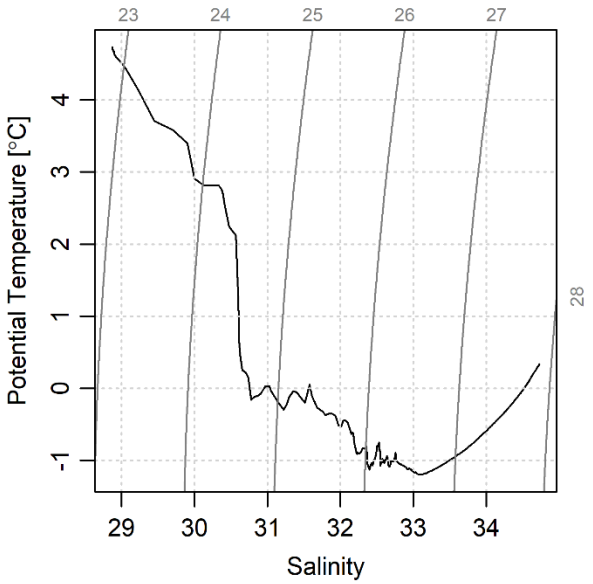
23
24
25
26
27
Potential Temperature [°C]
4
3
2
1
0
-1
28
29
30
31
32
33
34
Salinity

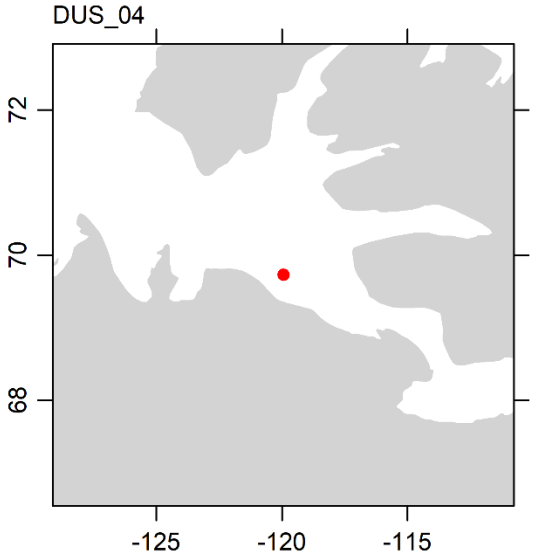
DUS_04
72
70
68
-125
-120
-115

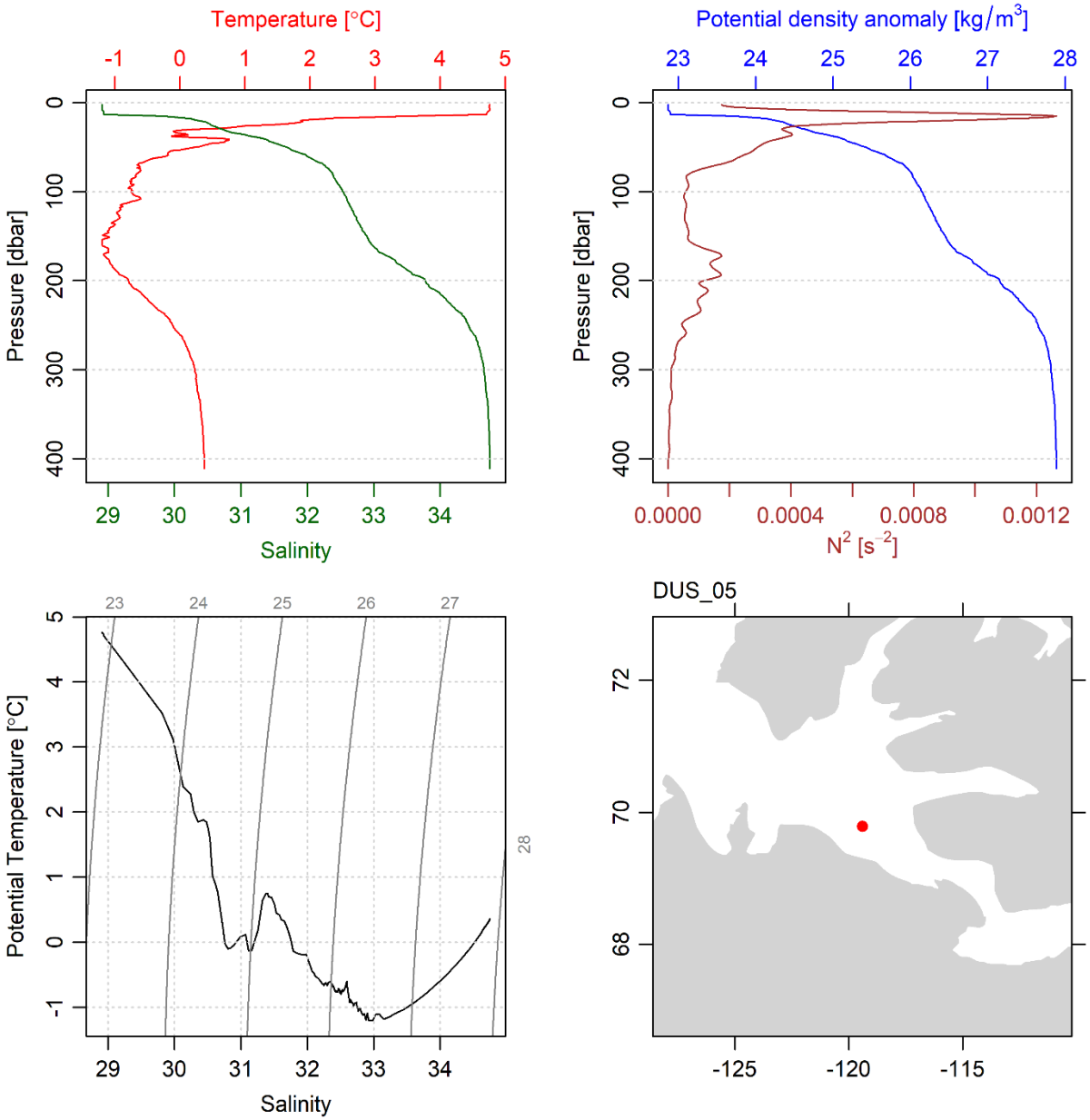
Temperature [°C]
-1 0 1 2 3 4 5
Pressure [dbar]
0 100 200 300 400
29 30 31 32 33 34
Salinity
Potential density anomaly [kg/m3]
23 24 25 26 27 28
Pressure [dbar]
0 100 200 300 400
0.0000 0.0004 0.0008 0.0012
N2 [s−2]
Potential Temperature [°C]
-1 0 1 2 3 4 5
23 24 25 26 27 28
29 30 31 32 33 34
Salinity
DUS_05
72 70 68
-125 -120 -115

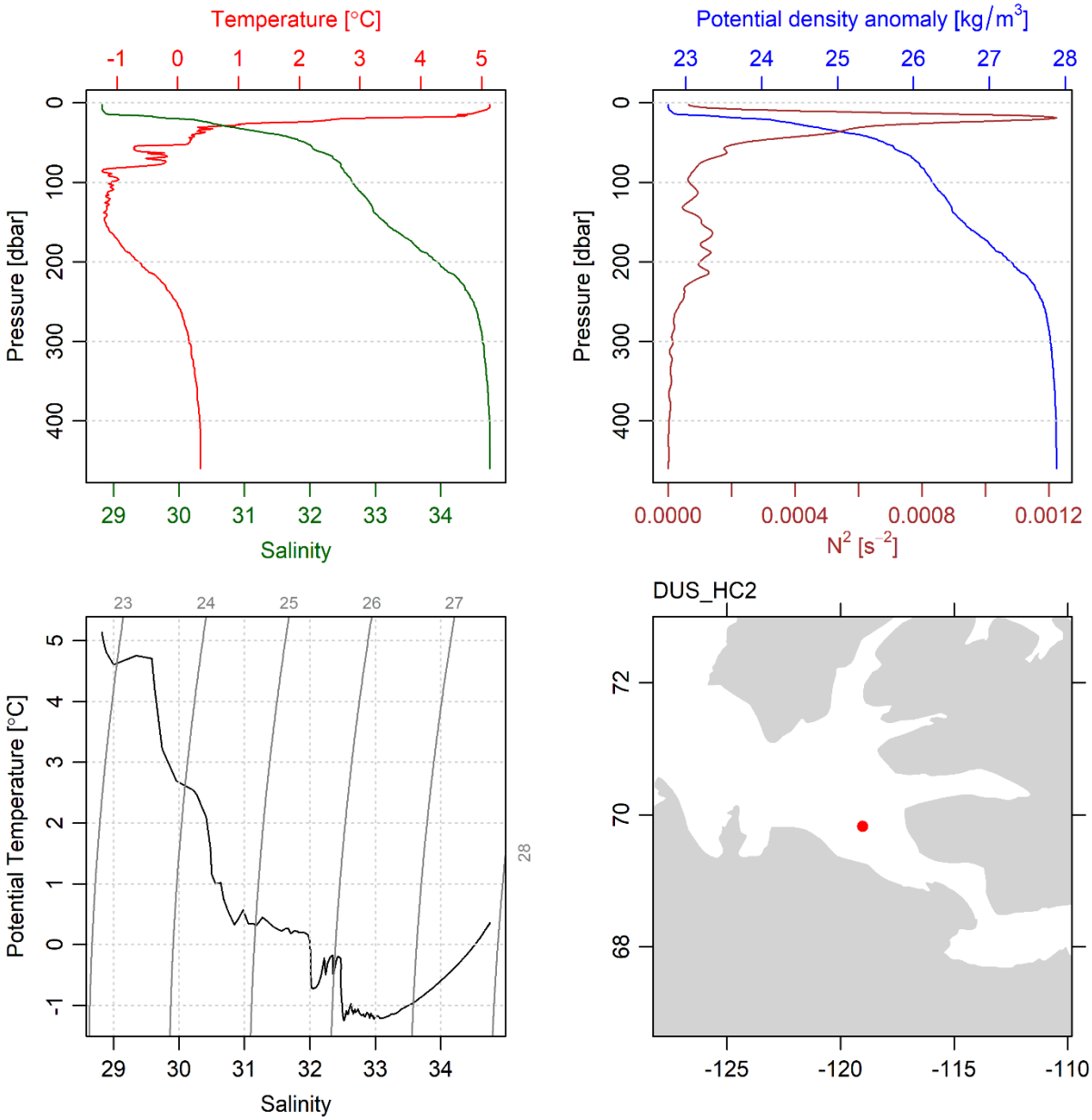
Temperature [°C]
-1 0 1 2 3 4 5
Pressure [dbar]
0 100 200 300 400
29 30 31 32 33 34
Salinity
Potential density anomaly [kg/m3]
23 24 25 26 27 28
0.0000 0.0004 0.0008 0.0012
N2 [s−2]
Potential Temperature [°C]
23 24 25 26 27
28
DUS_HC2
72 70 68
-125 -120 -115 -110

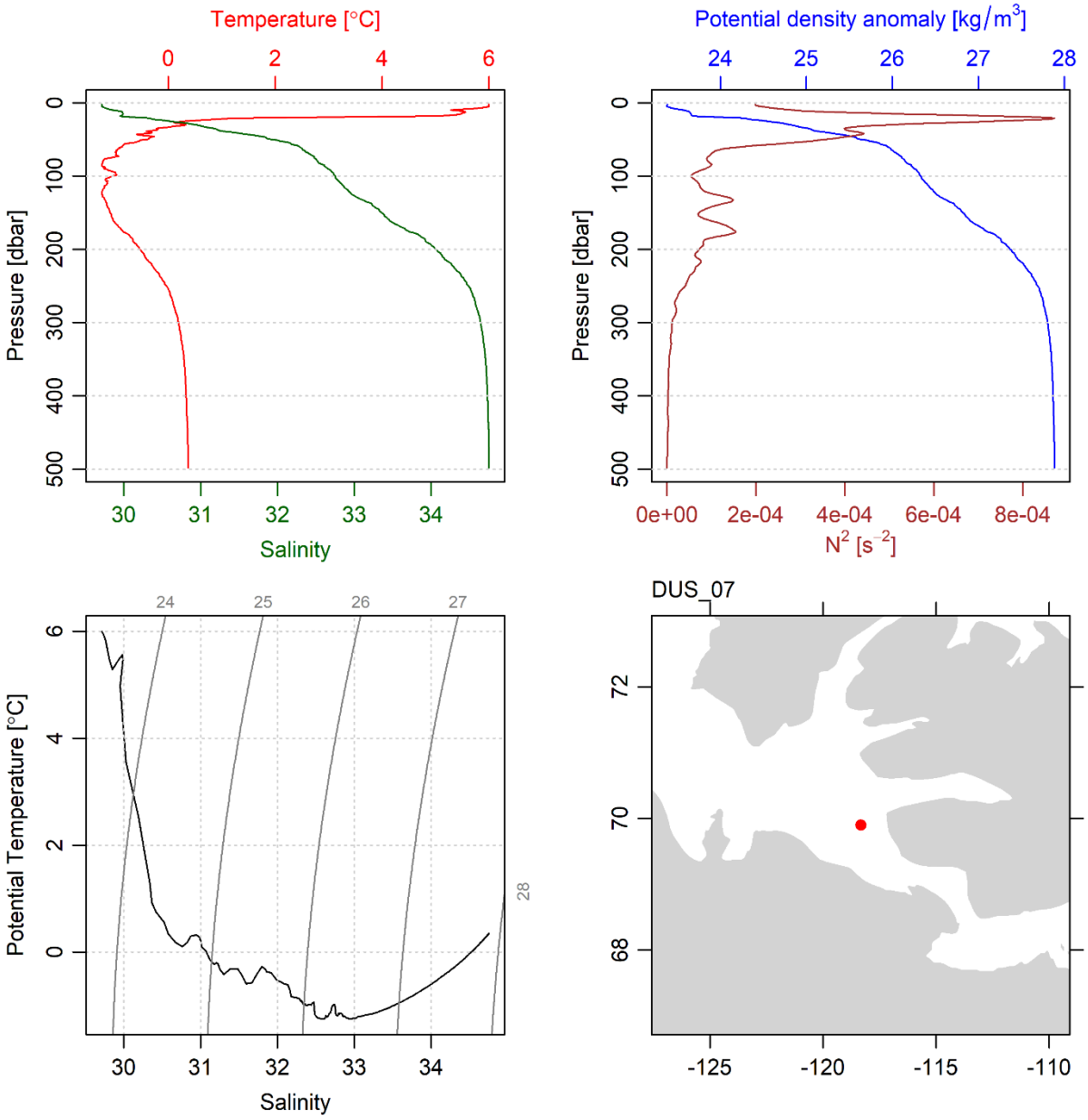
Temperature [°C]
0
2
4
6
Pressure [dbar]
0
100
200
300
400
500
30
31
32
33
34
Salinity
Potential density anomaly [kg/m3]
24
25
26
27
28
0e+00
2e-04
4e-04
6e-04
8e-04
N2 [s−2]
Potential Temperature [°C]
24
25
26
27
28
DUS_07
72
70
68
-125
-120
-115
-110

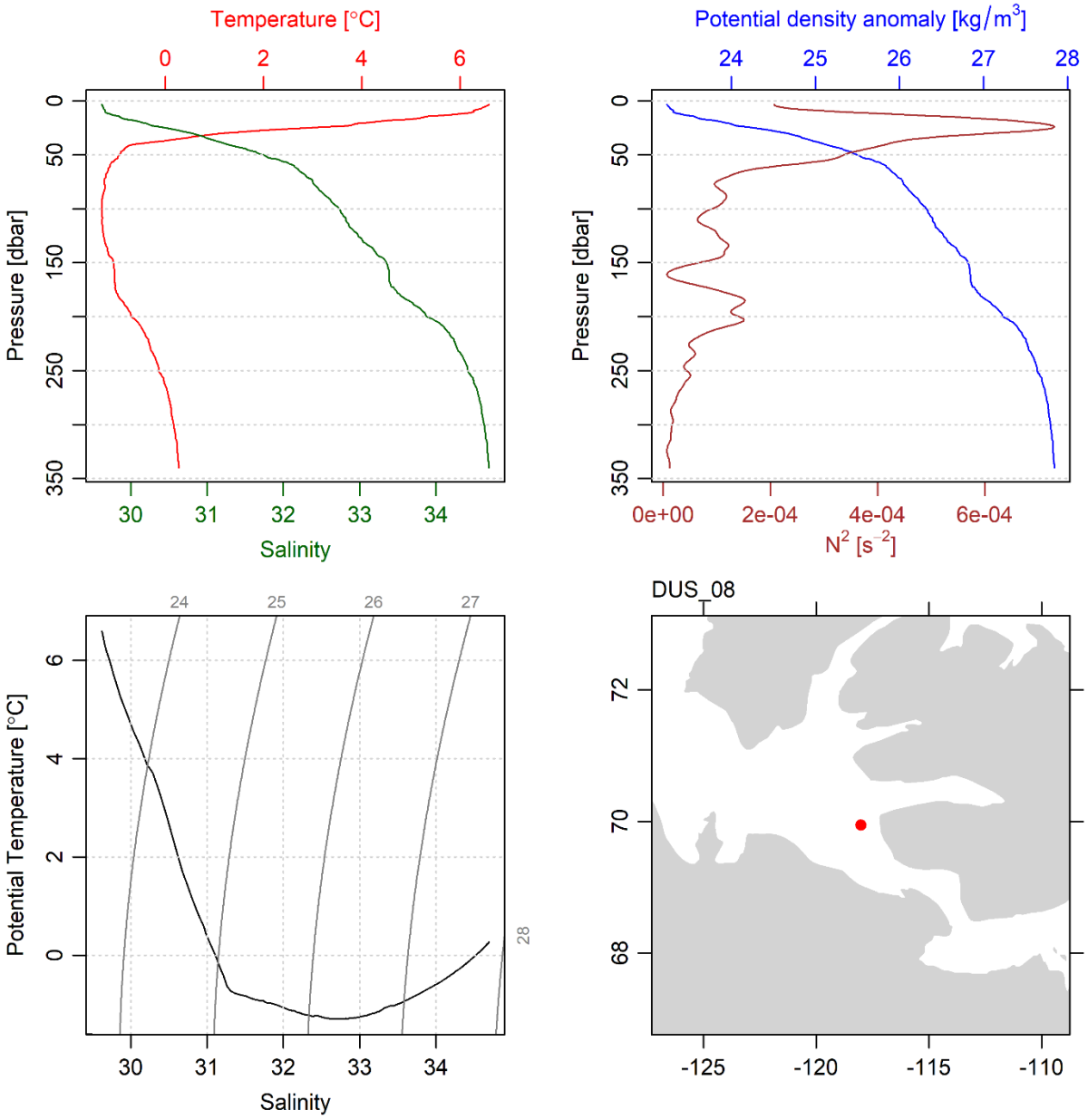
Temperature [°C]
0
2
4
6
Pressure [dbar]
0
50
150
250
350
30
31
32
33
34
Salinity
Potential density anomaly [kg/m3]
24
25
26
27
28
0e+00
2e-04
4e-04
6e-04
N2 [s−2]
Potential Temperature [°C]
24
25
26
27
28
DUS_08
72
70
68
-125
-120
-115
-110

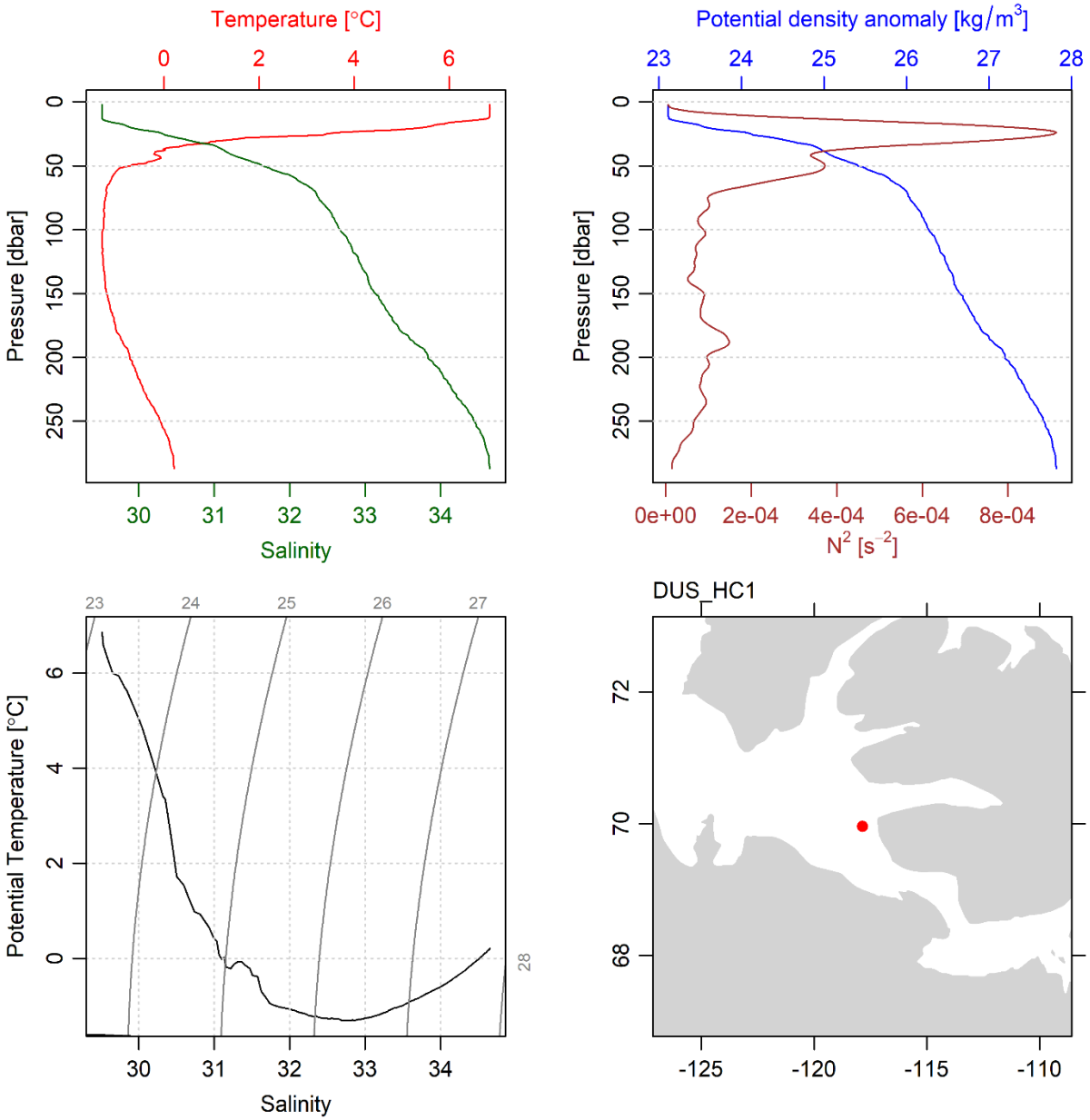
Temperature [°C]
0
2
4
6
Pressure [dbar]
0
50
100
150
200
250
30
31
32
33
34
Salinity
Potential density anomaly [kg/m3]
23
24
25
26
27
28
0e+00
2e-04
4e-04
6e-04
8e-04
N2 [s−2]
Potential Temperature [°C]
23
24
25
26
27
28
DUS_HC1
72
70
68
-125
-120
-115
-110

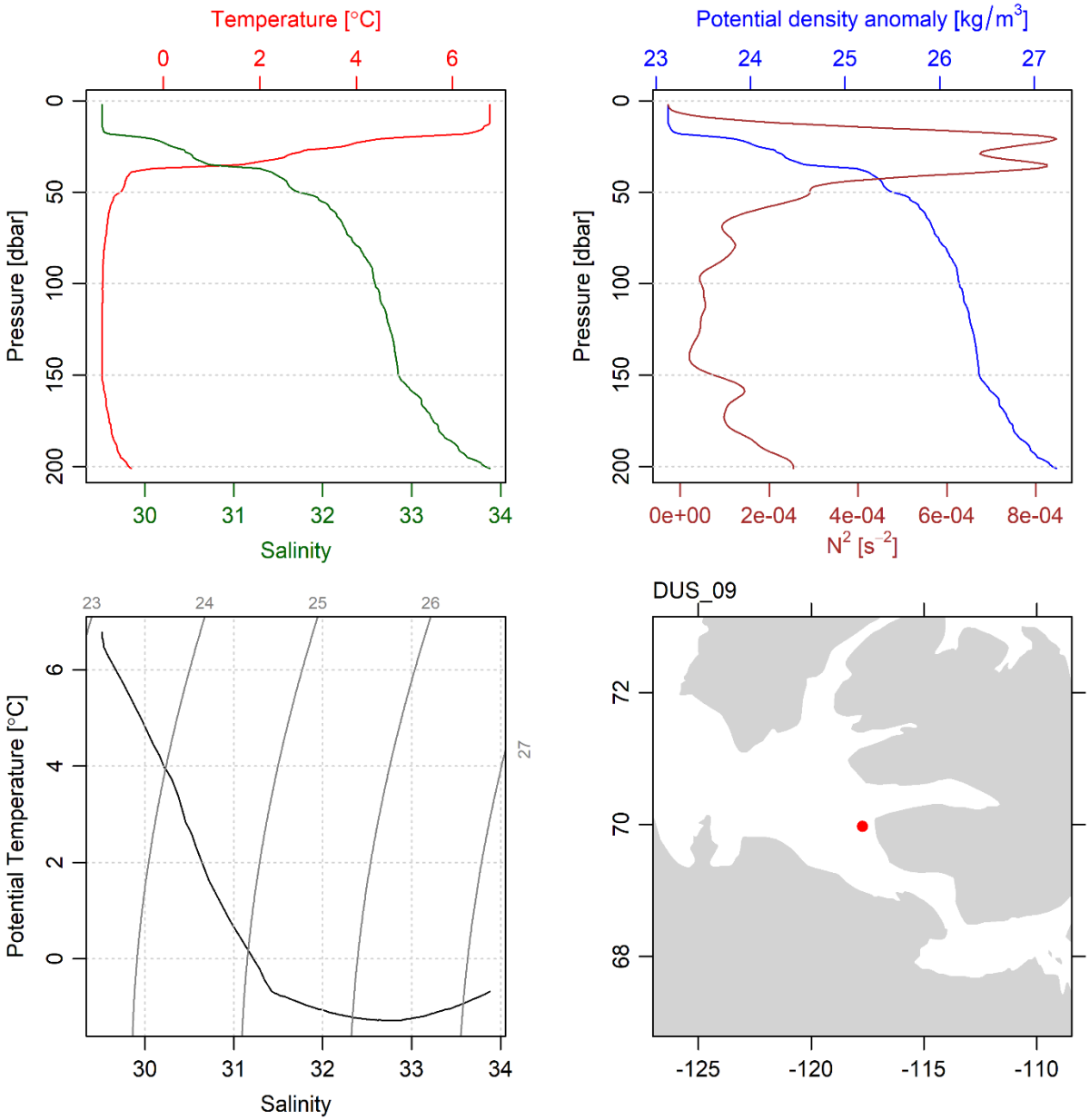
Temperature [°C]
0
2
4
6
Pressure [dbar]
0
50
100
150
200
30
31
32
33
34
Salinity
Potential density anomaly [kg/m3]
23
24
25
26
27
0e+00
2e-04
4e-04
6e-04
8e-04
N2 [s−2]
Potential Temperature [°C]
23
24
25
26
27
DUS_09
72
70
68
-125
-120
-115
-110

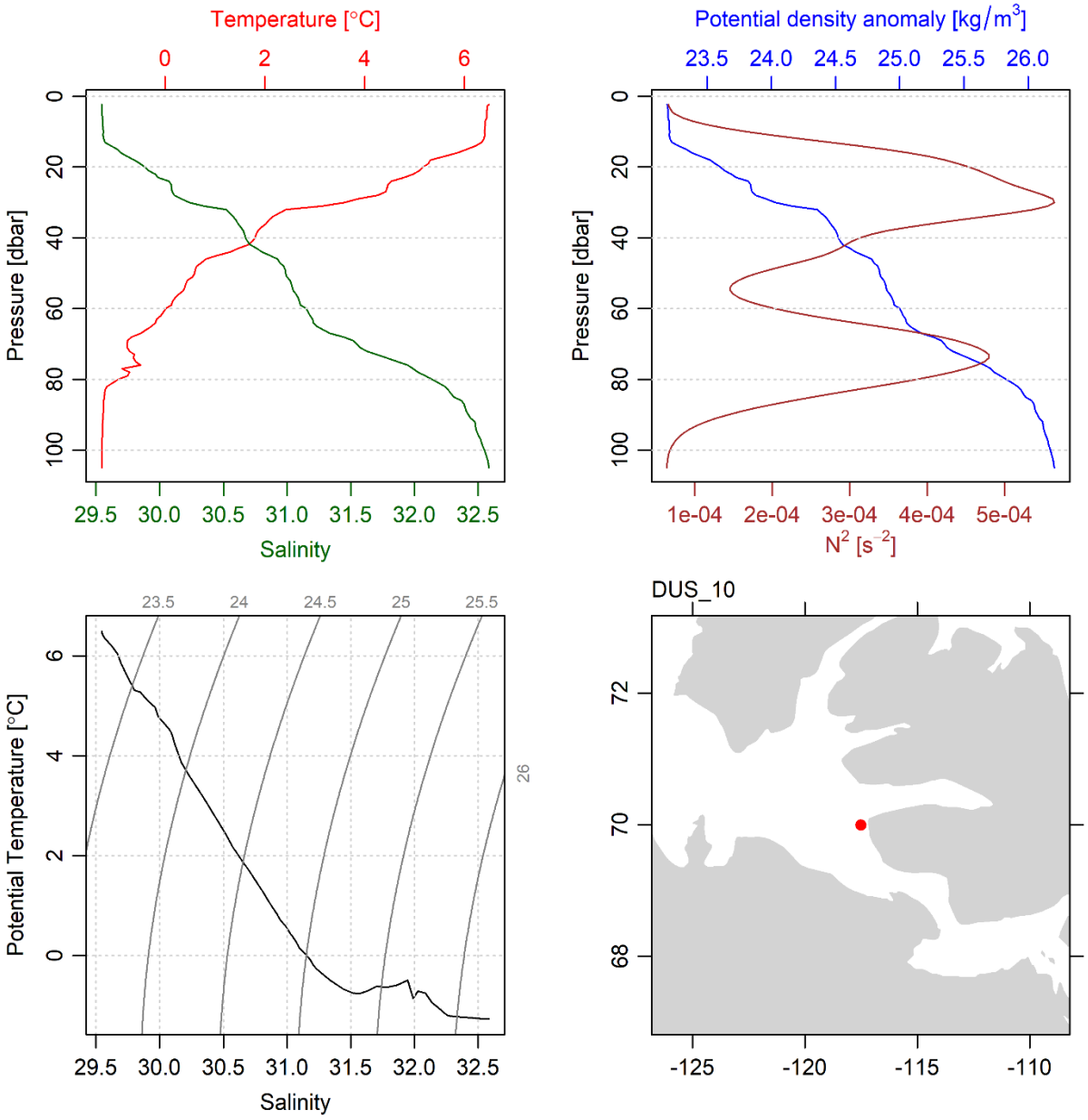
Temperature [°C]
0
2
4
6
Pressure [dbar]
0
20
40
60
80
100
29.5
30.0
30.5
31.0
31.5
32.0
32.5
Salinity
Potential density anomaly [kg/m3]
23.5
24.0
24.5
25.0
25.5
26.0
1e-04
2e-04
3e-04
4e-04
5e-04
N2 [s−2]
Potential Temperature [°C]
23.5
24
24.5
25
25.5
26
DUS_10
72
70
68
-125
-120
-115
-110

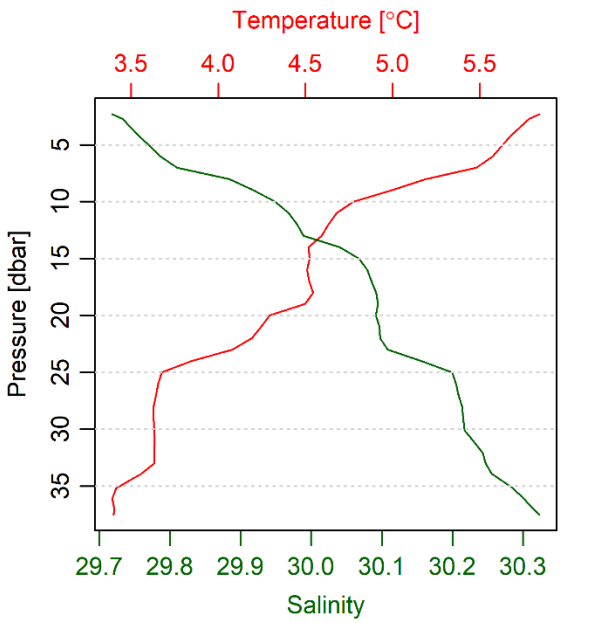
Temperature [°C]
3.5
4.0
4.5
5.0
5.5
Pressure [dbar]
5
10
15
20
25
30
35
29.7
29.8
29.9
30.0
30.1
30.2
30.3
Salinity

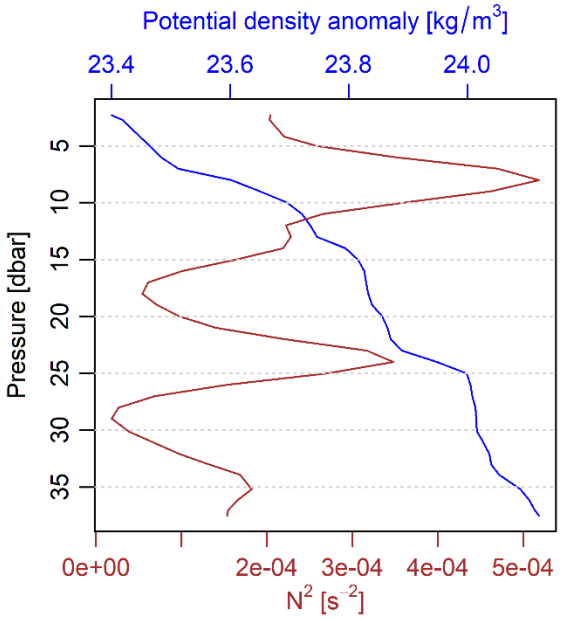
Potential density anomaly [kg/m3]
23.4
23.6
23.8
24.0
Pressure [dbar]
5
10
15
20
25
30
35
0e+00
2e-04
3e-04
4e-04
5e-04
N2 [s−2]

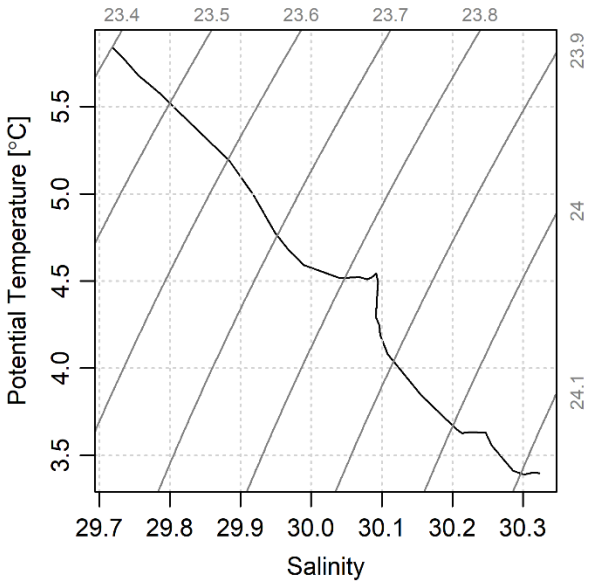
23.4
23.5
23.6
23.7
23.8
23.9
24
24.1
Potential Temperature [°C]
3.5
4.0
4.5
5.0
5.5
29.7
29.8
29.9
30.0
30.1
30.2
30.3
Salinity

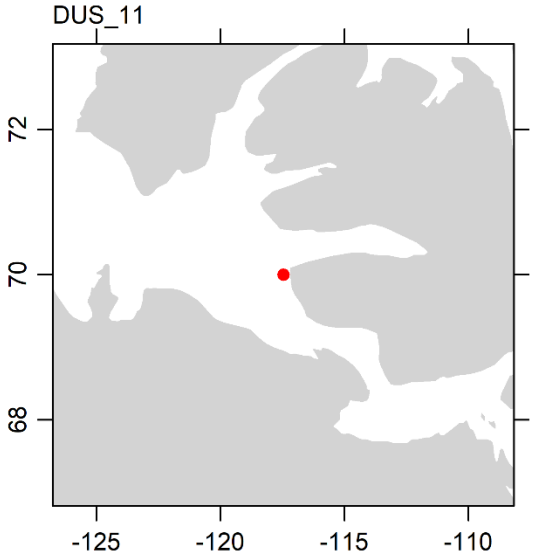
DUS_11
72
70
68
-125
-120
-115
-110

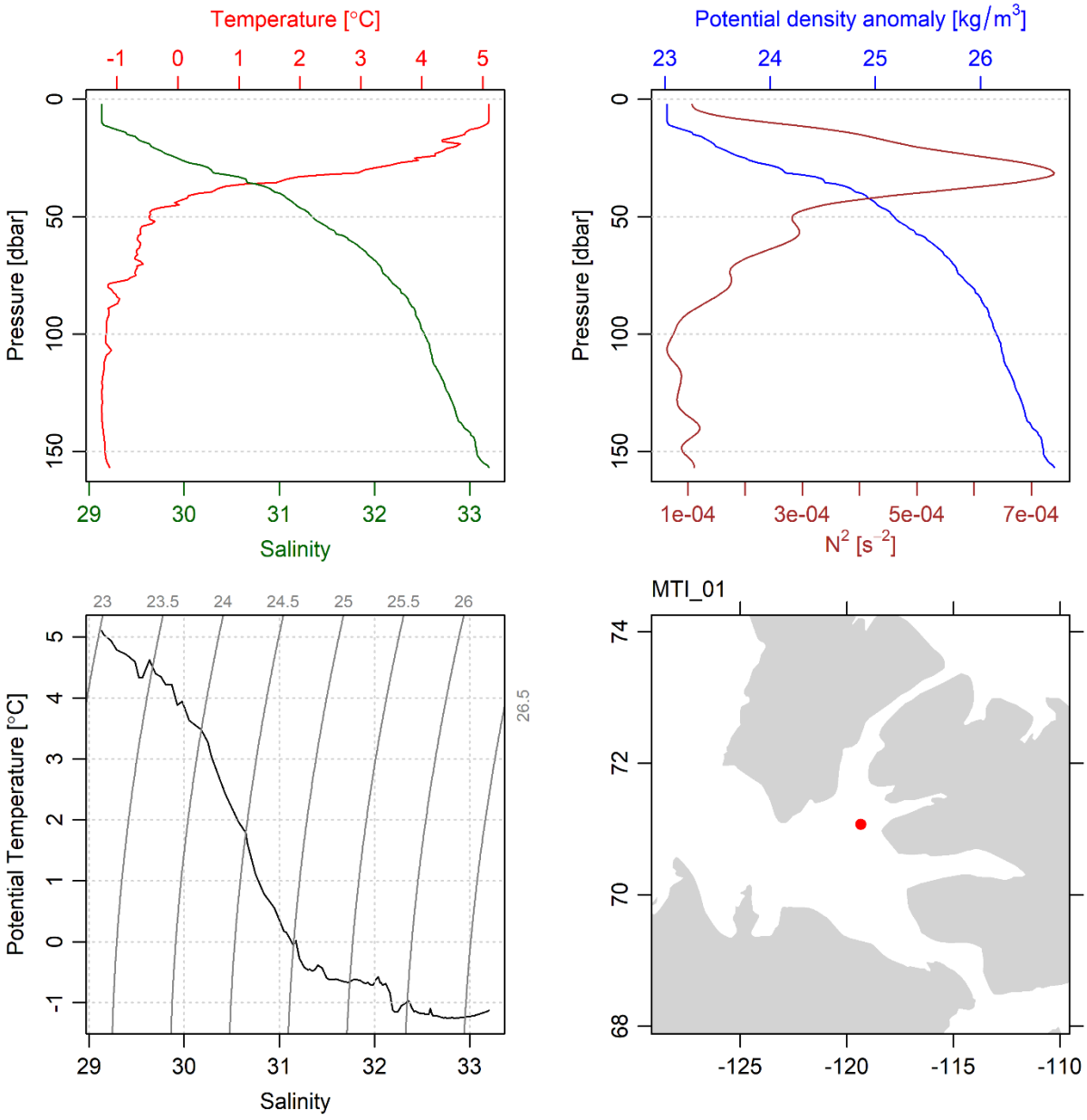
Temperature [°C]
-1 0 1 2 3 4 5
Pressure [dbar]
0 50 100 150
29 30 31 32 33
Salinity
Potential density anomaly [kg/m3]
23 24 25 26
1e-04 3e-04 5e-04 7e-04
N2 [s−2]
23 23.5 24 24.5 25 25.5 26
26.5
Potential Temperature [°C]
-1 0 1 2 3 4 5
MTI_01
74 72 70 68
-125 -120 -115 -110

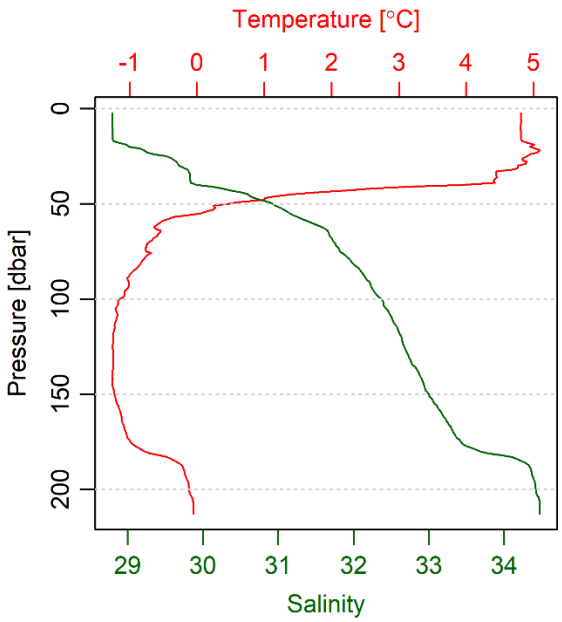
Temperature [°C]
-1
0
1
2
3
4
5
Pressure [dbar]
0
50
100
150
200
29
30
31
32
33
34
Salinity

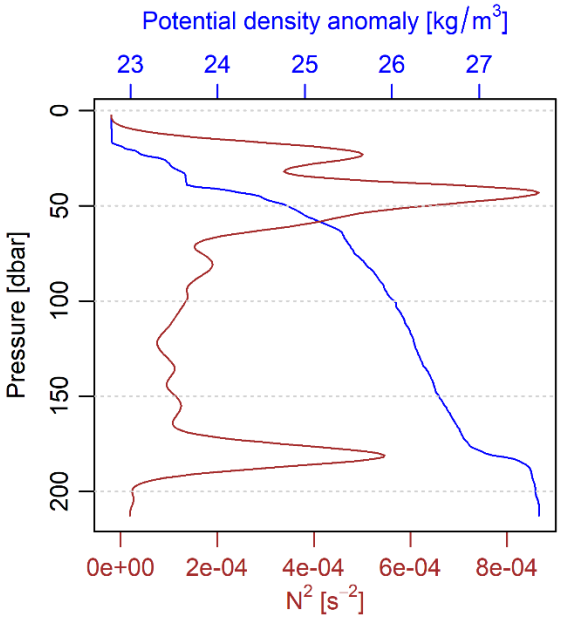
Potential density anomaly [kg/m3]
23
24
25
26
27
Pressure [dbar]
0
50
100
150
200
0e+00
2e-04
4e-04
6e-04
8e-04
N2 [s−2]

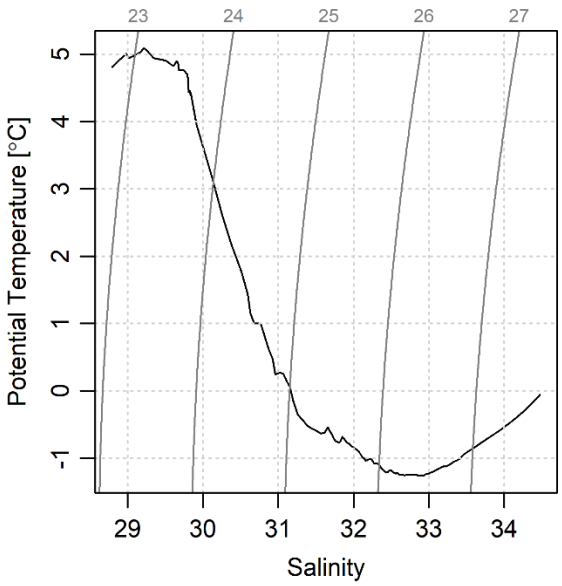
23
24
25
26
27
Potential Temperature [°C]
-1
0
1
2
3
4
5
29
30
31
32
33
34
Salinity

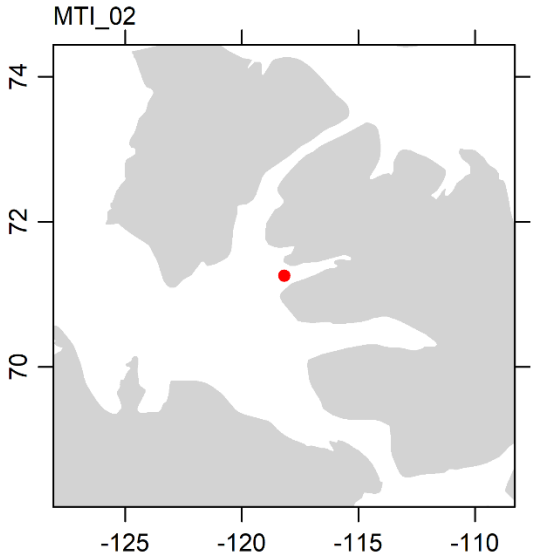
MTI_02
74
72
70
-125
-120
-115
-110

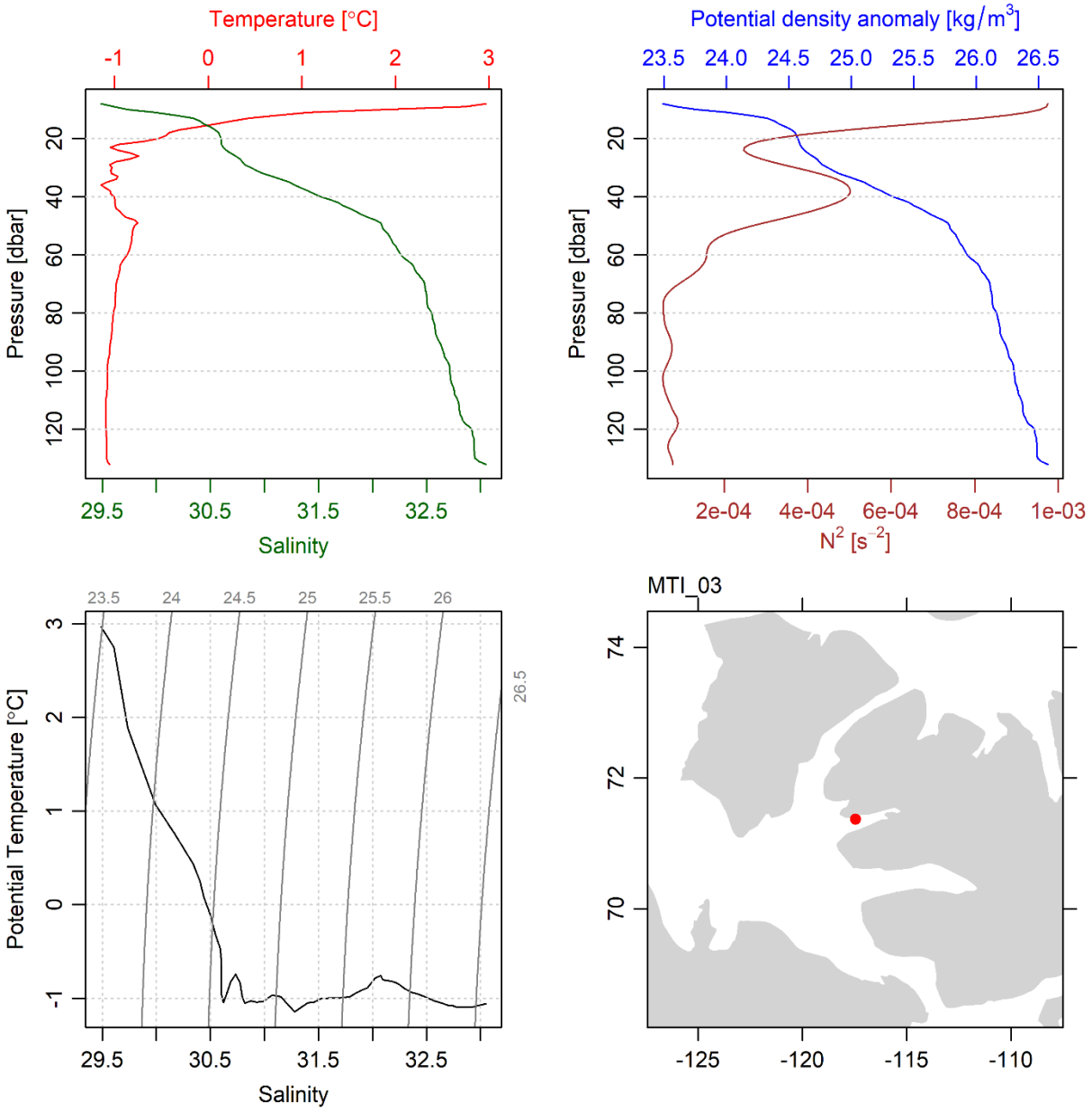
Temperature [°C]
-1
0
1
2
3
Pressure [dbar]
20
40
60
80
100
120
29.5
30.5
31.5
32.5
Salinity
Potential density anomaly [kg/m3]
23.5
24.0
24.5
25.0
25.5
26.0
26.5
2e-04
4e-04
6e-04
8e-04
1e-03
N2 [s−2]
Potential Temperature [°C]
23.5
24
24.5
25
25.5
26
26.5
3
2
1
0
-1
MTI_03
74
72
70
-125
-120
-115
-110

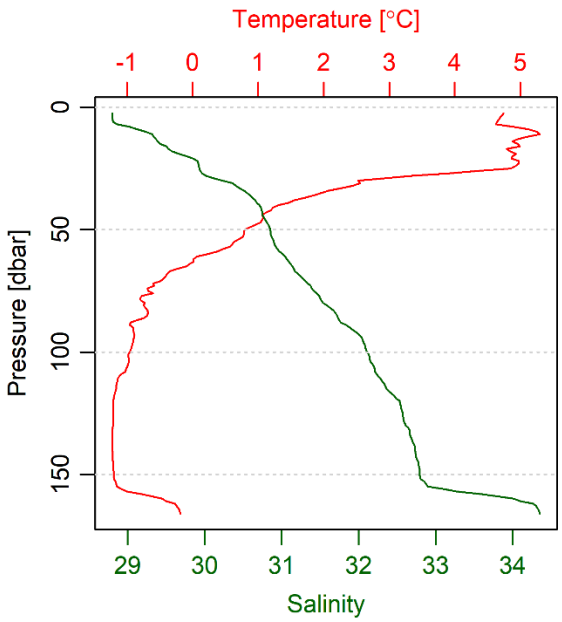
Temperature [°C]
-1
0
1
2
3
4
5
Pressure [dbar]
0
50
100
150
29
30
31
32
33
34
Salinity

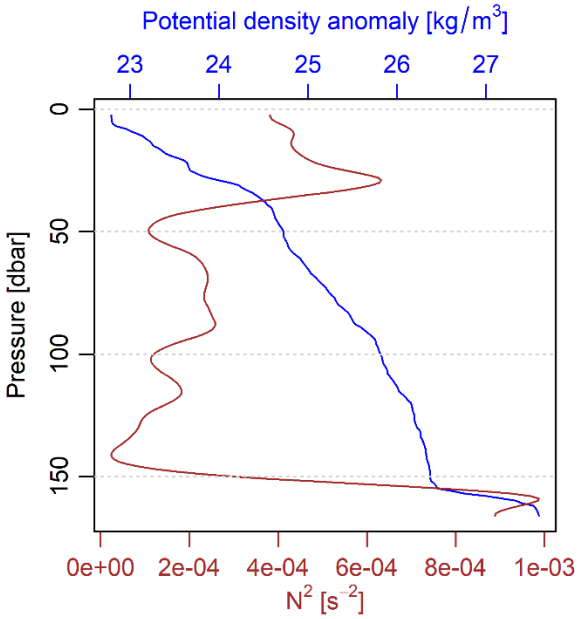
Potential density anomaly [kg/m3]
23
24
25
26
27
Pressure [dbar]
0
50
100
150
0e+00
2e-04
4e-04
6e-04
8e-04
1e-03
N2 [s−2]

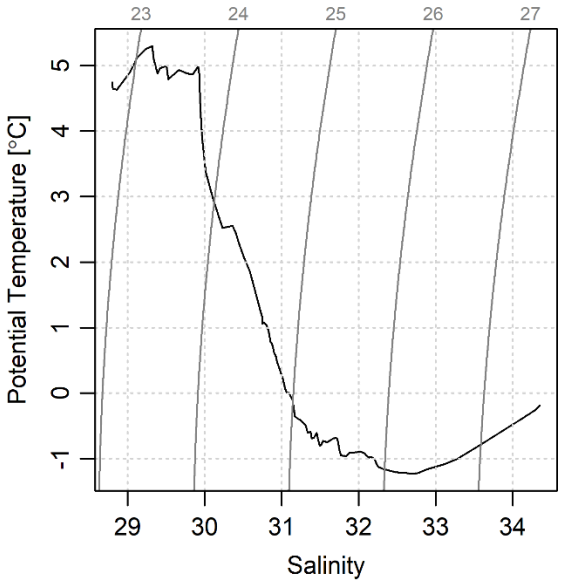
23
24
25
26
27
Potential Temperature [°C]
-1
0
1
2
3
4
5
29
30
31
32
33
34
Salinity

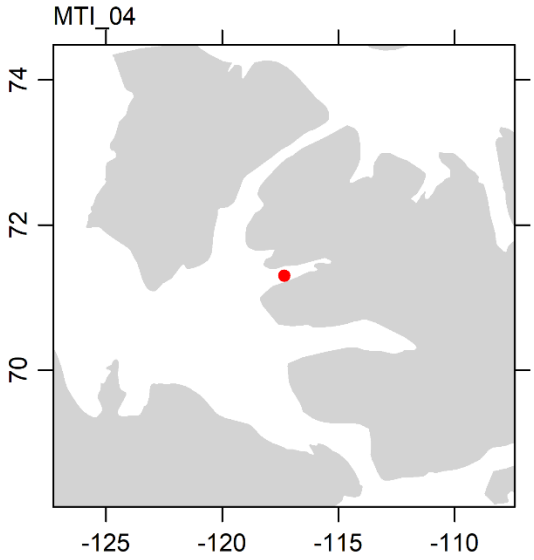
MTI_04
74
72
70
-125
-120
-115
-110

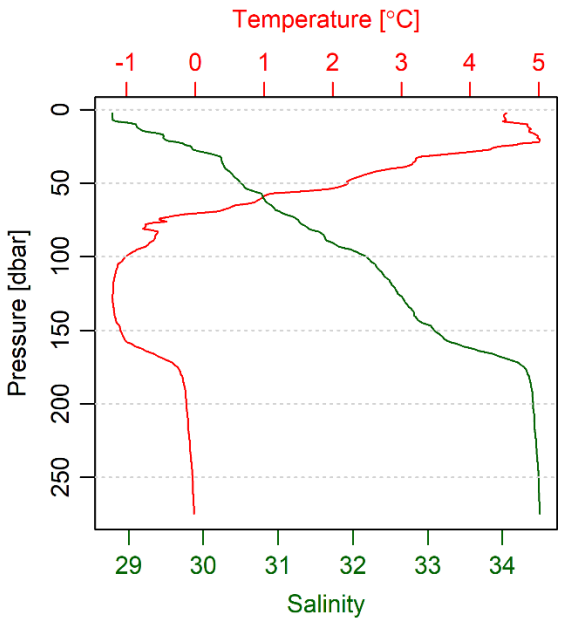
Temperature [°C]
-1
0
1
2
3
4
5
Pressure [dbar]
0
50
100
150
200
250
29
30
31
32
33
34
Salinity

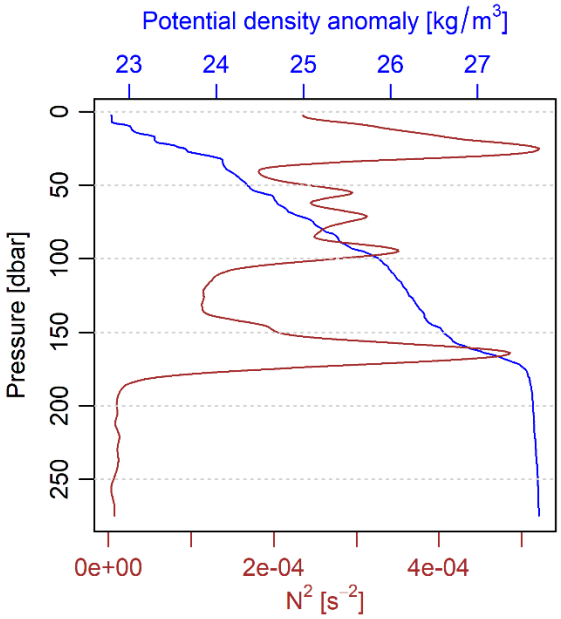
Potential density anomaly [kg/m3]
23
24
25
26
27
Pressure [dbar]
0
50
100
150
200
250
0e+00
2e-04
4e-04
N2 [s−2]

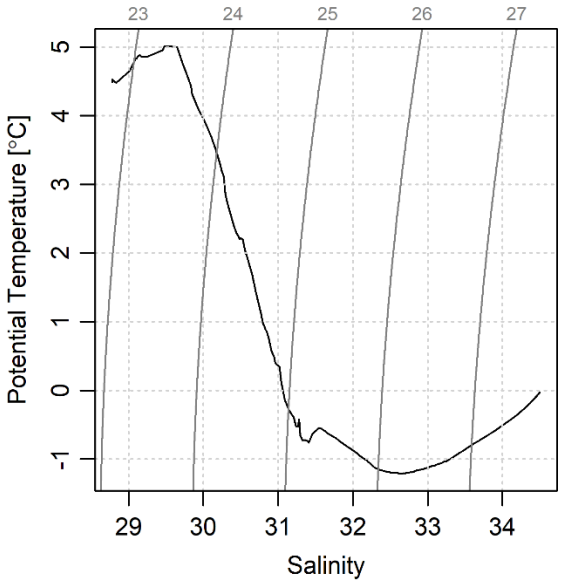
23
24
25
26
27
Potential Temperature [°C]
-1
0
1
2
3
4
5
29
30
31
32
33
34
Salinity

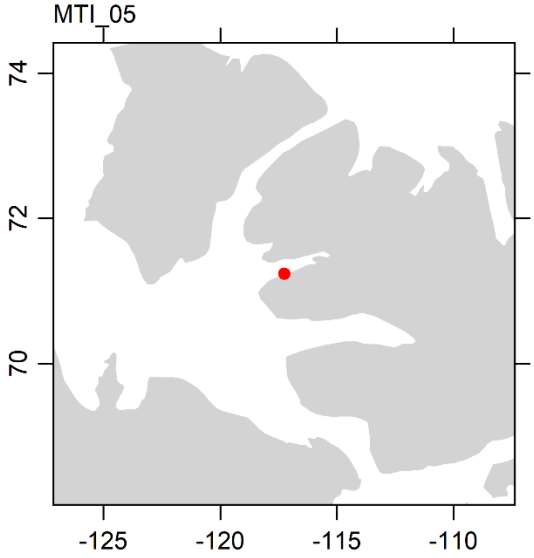
MTI_05
74
72
70
-125
-120
-115
-110

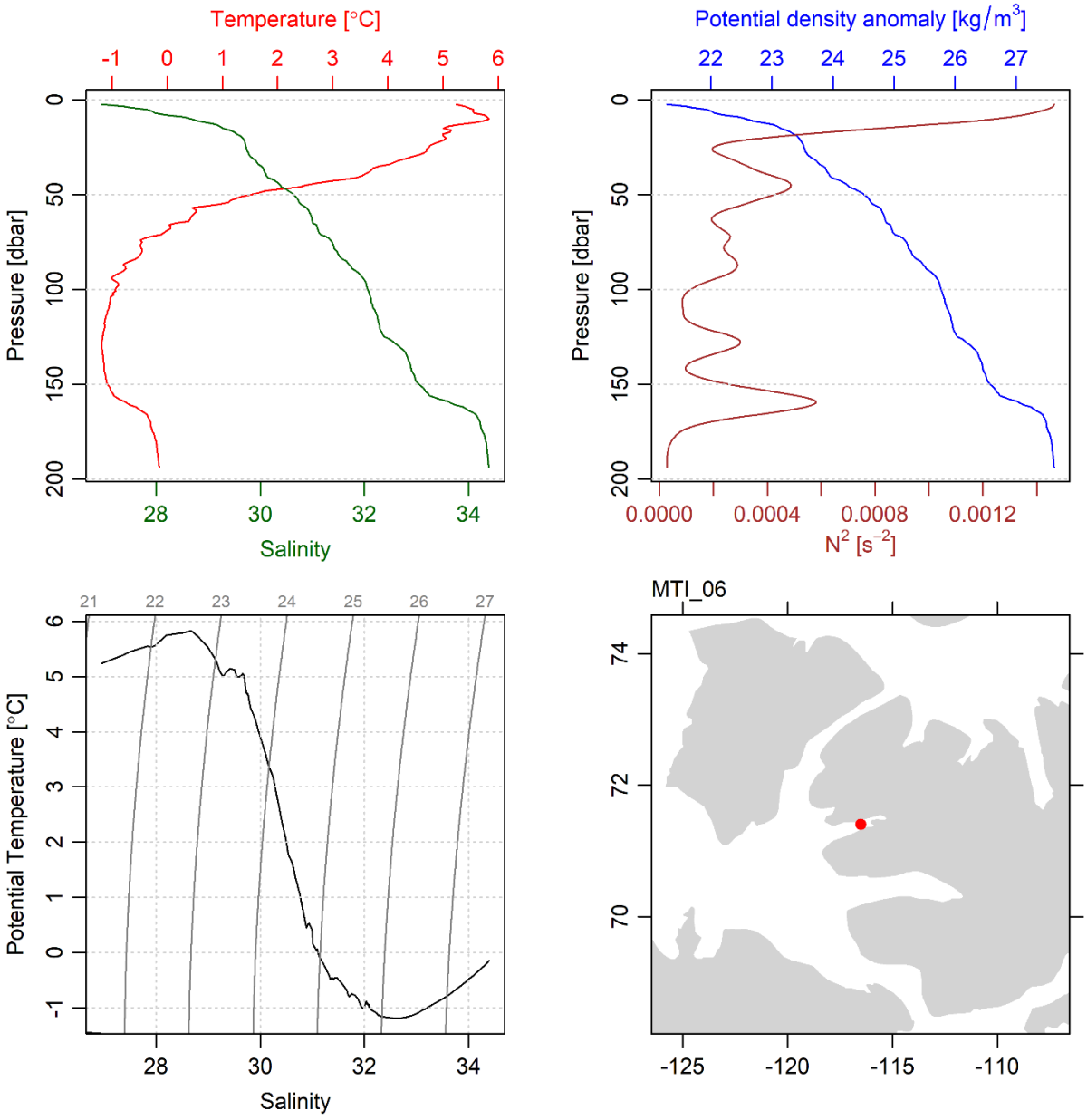
Temperature [°C]
-1 0 1 2 3 4 5 6
Pressure [dbar]
0 50 100 150 200
28 30 32 34
Salinity
Potential density anomaly [kg/m3]
22 23 24 25 26 27
0.0000 0.0004 0.0008 0.0012
N2 [s−2]
21 22 23 24 25 26 27
Potential Temperature [°C]
-1 0 1 2 3 4 5 6
28 30 32 34
Salinity
MTI_06
74 72 70
-125 -120 -115 -110

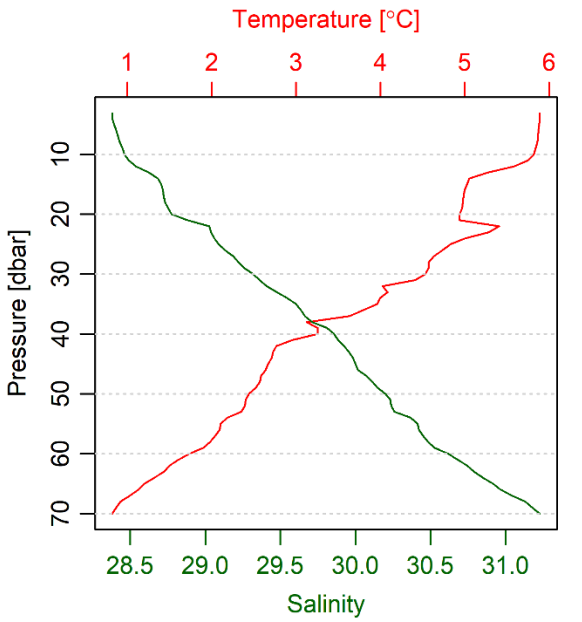
Temperature [°C]
1
2
3
4
5
6
Pressure [dbar]
10
20
30
40
50
60
70
28.5
29.0
29.5
30.0
30.5
31.0
Salinity

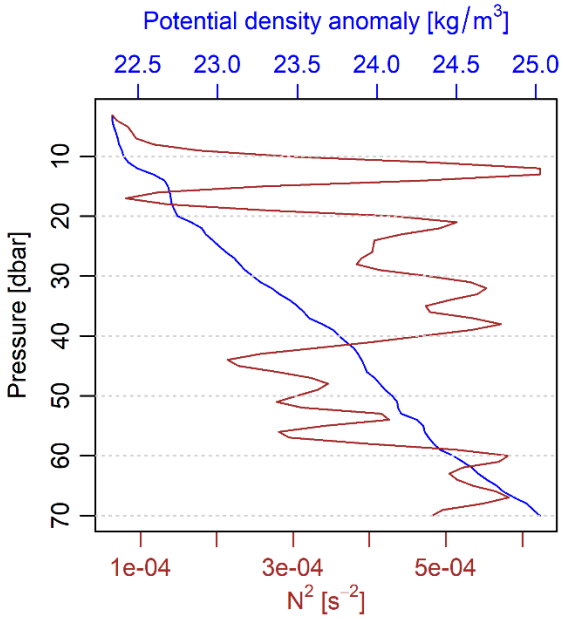
Potential density anomaly [kg/m3]
22.5
23.0
23.5
24.0
24.5
25.0
Pressure [dbar]
10
20
30
40
50
60
70
1e-04
3e-04
5e-04
N2 [s−2]

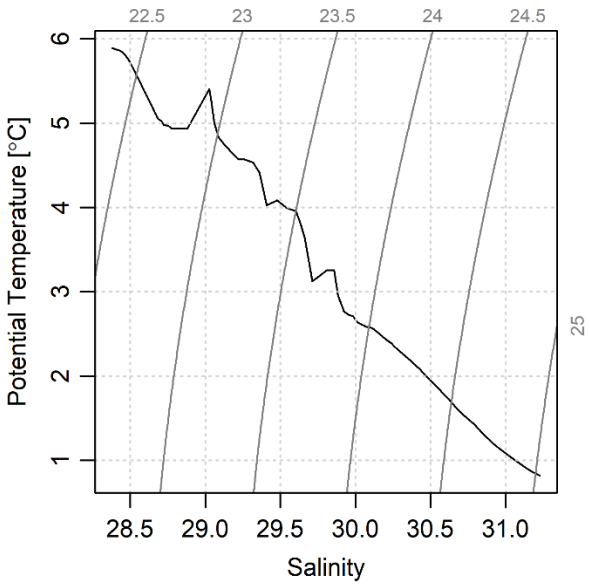
22.5
23
23.5
24
24.5
Potential Temperature [°C]
1
2
3
4
5
6
25
28.5
29.0
29.5
30.0
30.5
31.0
Salinity

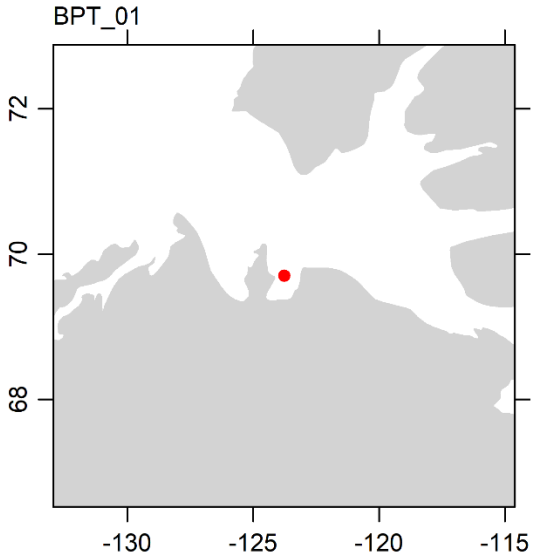
BPT_01
72
70
68
-130
-125
-120
-115

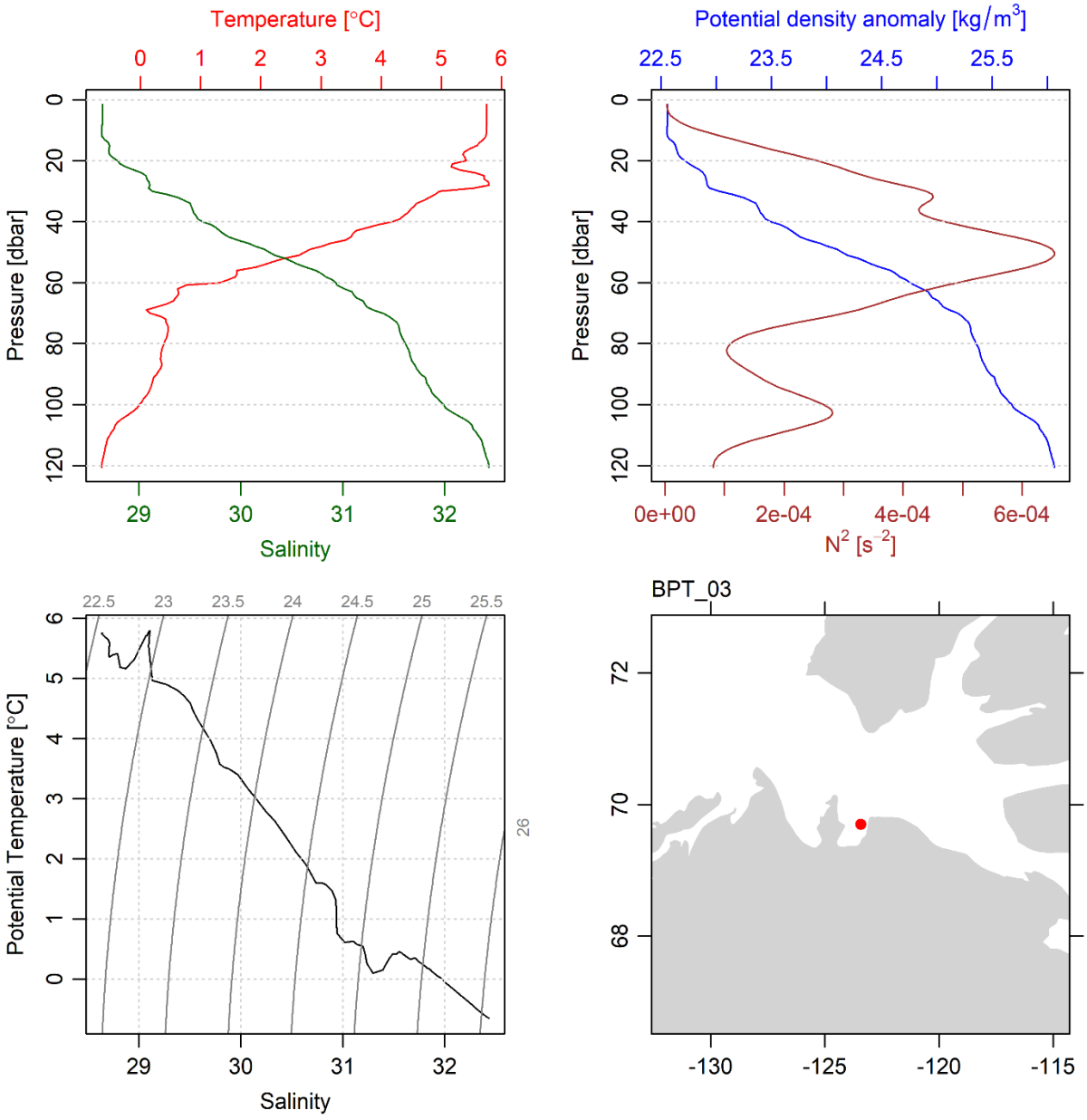
Temperature [°C]
0 1 2 3 4 5 6
Pressure [dbar]
0 20 40 60 80 100 120
29 30 31 32
Salinity
Potential density anomaly [kg/m3]
22.5 23.5 24.5 25.5
0e+00 2e-04 4e-04 6e-04
N2 [s-2]
Potential Temperature [°C]
22.5 23 23.5 24 24.5 25 25.5
26
BPT_03
72 70 68
-130 -125 -120 -115

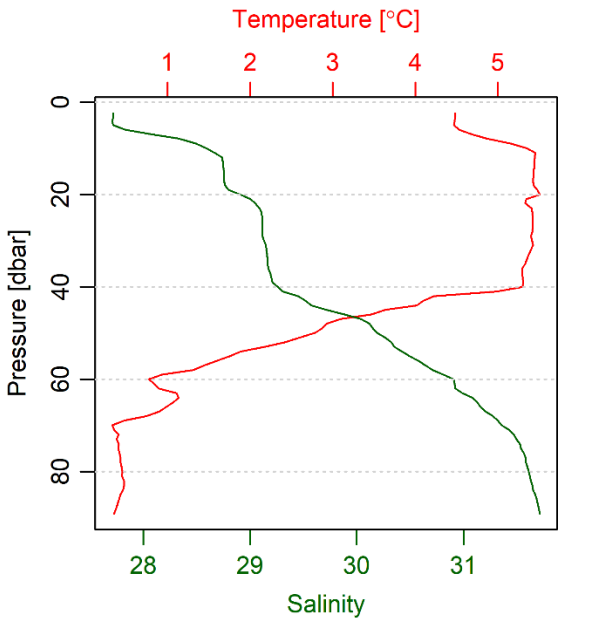
Temperature [°C]
1
2
3
4
5
Pressure [dbar]
0
20
40
60
80
28
29
30
31
Salinity

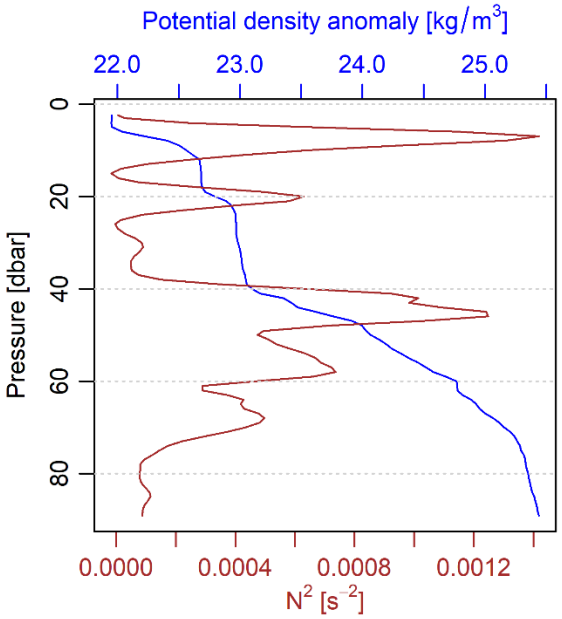
Potential density anomaly [kg/m3]
22.0
23.0
24.0
25.0
Pressure [dbar]
0
20
40
60
80
0.0000
0.0004
0.0008
0.0012
N2 [s−2]

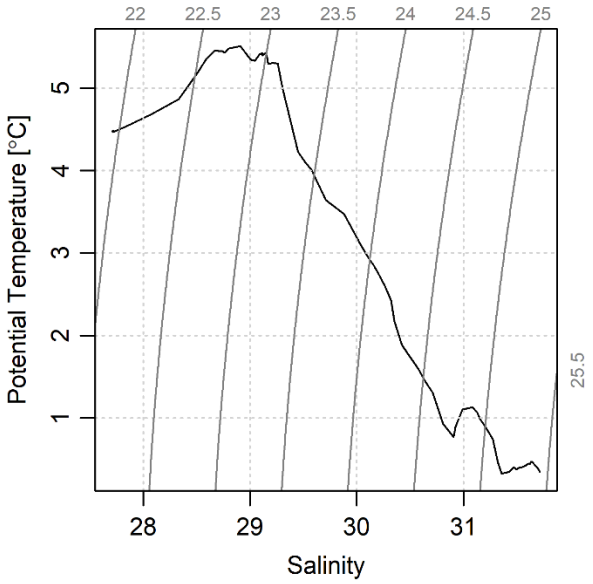
22
22.5
23
23.5
24
24.5
25
Potential Temperature [°C]
1
2
3
4
5
25.5
28
29
30
31
Salinity

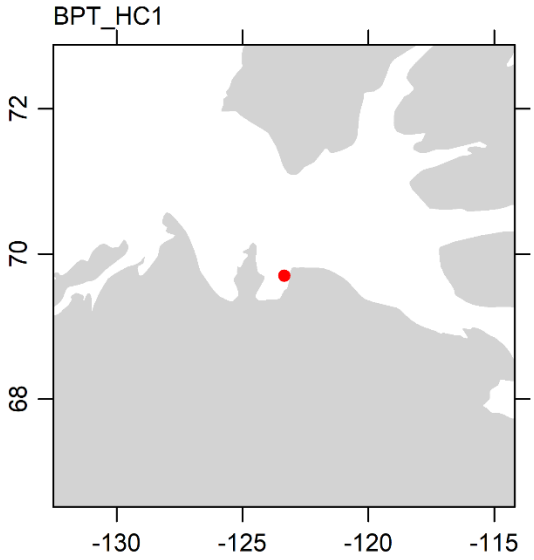
BPT_HC1
72
70
68
-130
-125
-120
-115

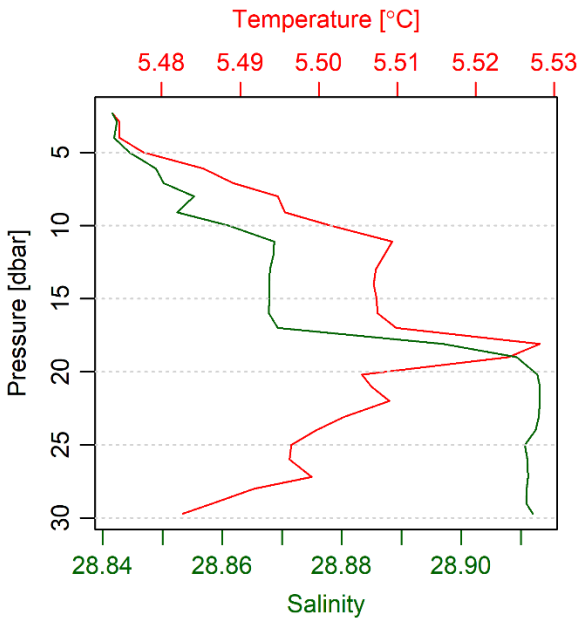
Temperature [°C]
5.48
5.49
5.50
5.51
5.52
5.53
Pressure [dbar]
5
10
15
20
25
30
28.84
28.86
28.88
28.90
Salinity

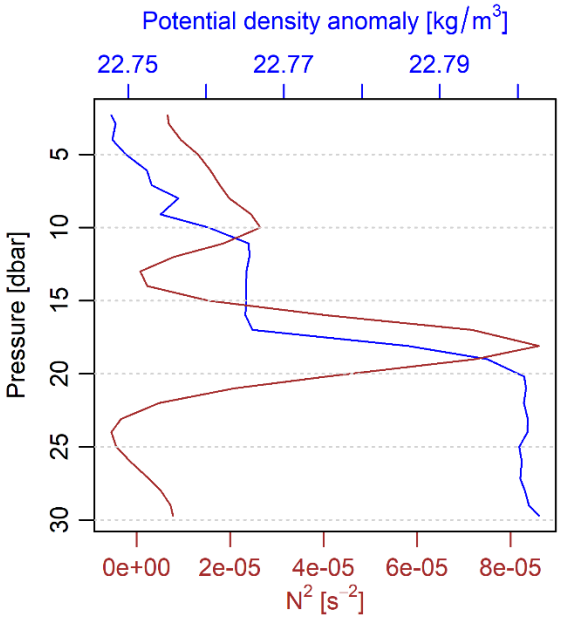
Potential density anomaly [kg/m3]
22.75
22.77
22.79
Pressure [dbar]
5
10
15
20
25
30
0e+00
2e-05
4e-05
6e-05
8e-05
N2 [s−2]

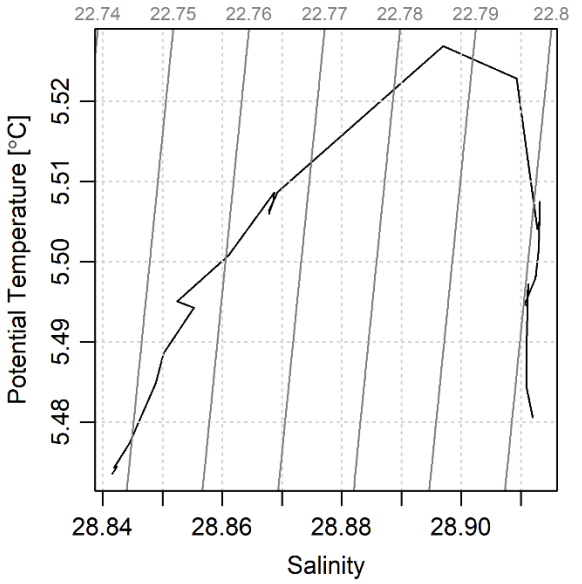
22.74
22.75
22.76
22.77
22.78
22.79
22.8
Potential Temperature [°C]
5.48
5.49
5.50
5.51
5.52
28.84
28.86
28.88
28.90
Salinity

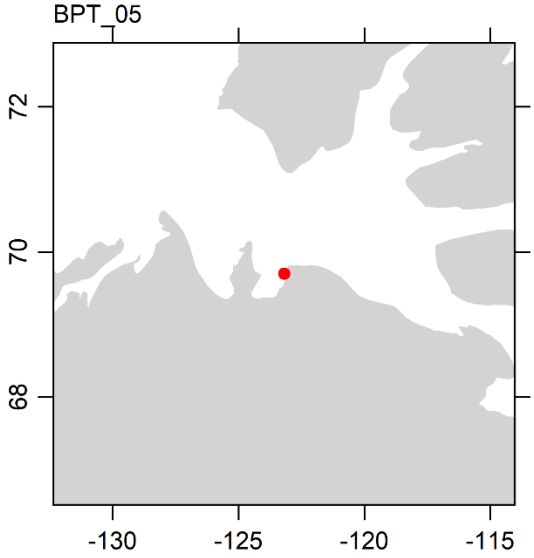
BPT_05
72
70
68
-130
-125
-120
-115

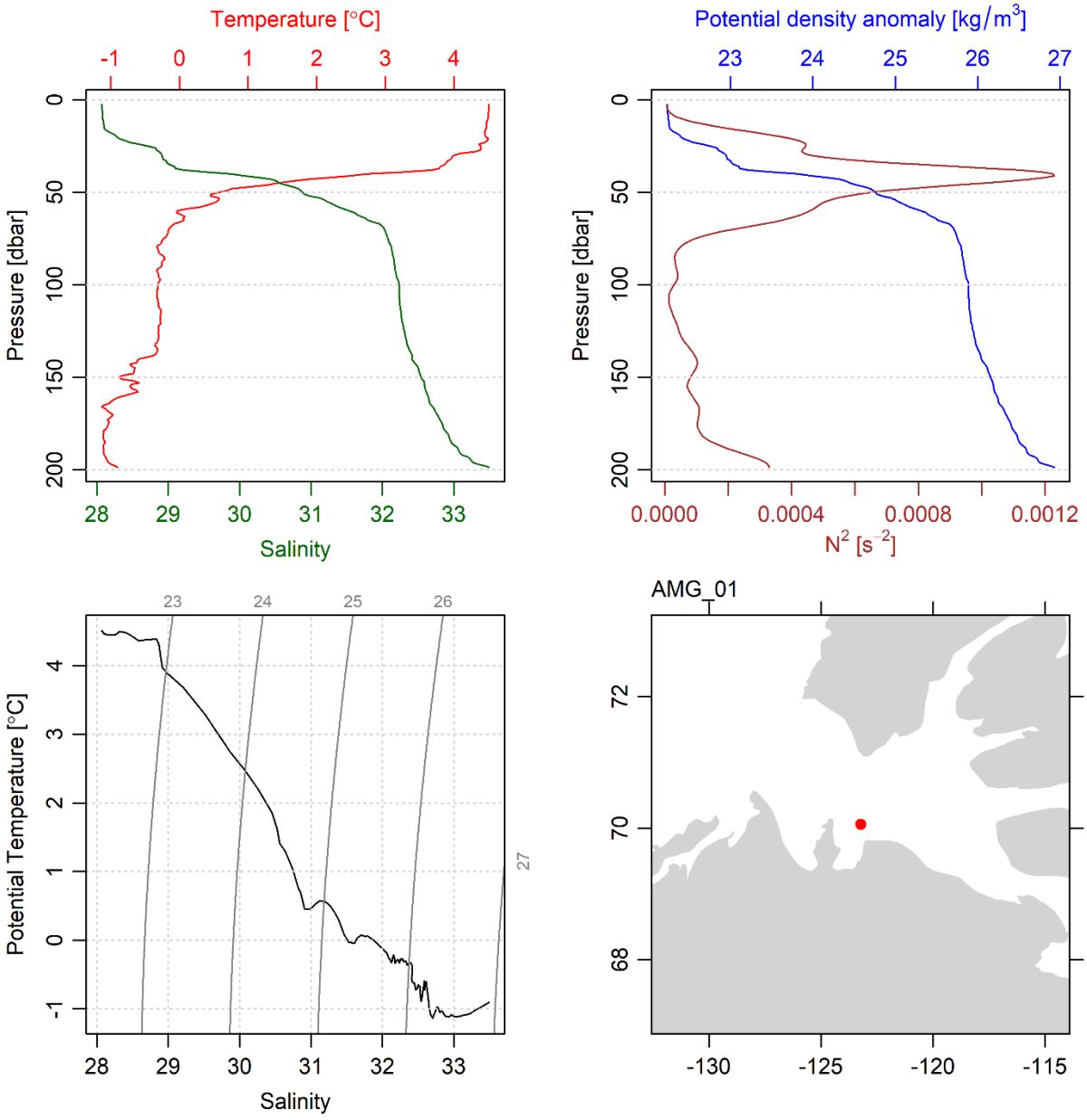
Temperature [°C]
-1
0
1
2
3
4
Pressure [dbar]
0
50
100
150
200
28
29
30
31
32
33
Salinity
Potential density anomaly [kg/m3]
23
24
25
26
27
0.0000
0.0004
0.0008
0.0012
N2 [s−2]
Potential Temperature [°C]
23
24
25
26
27
AMG_01
72
70
68
-130
-125
-120
-115

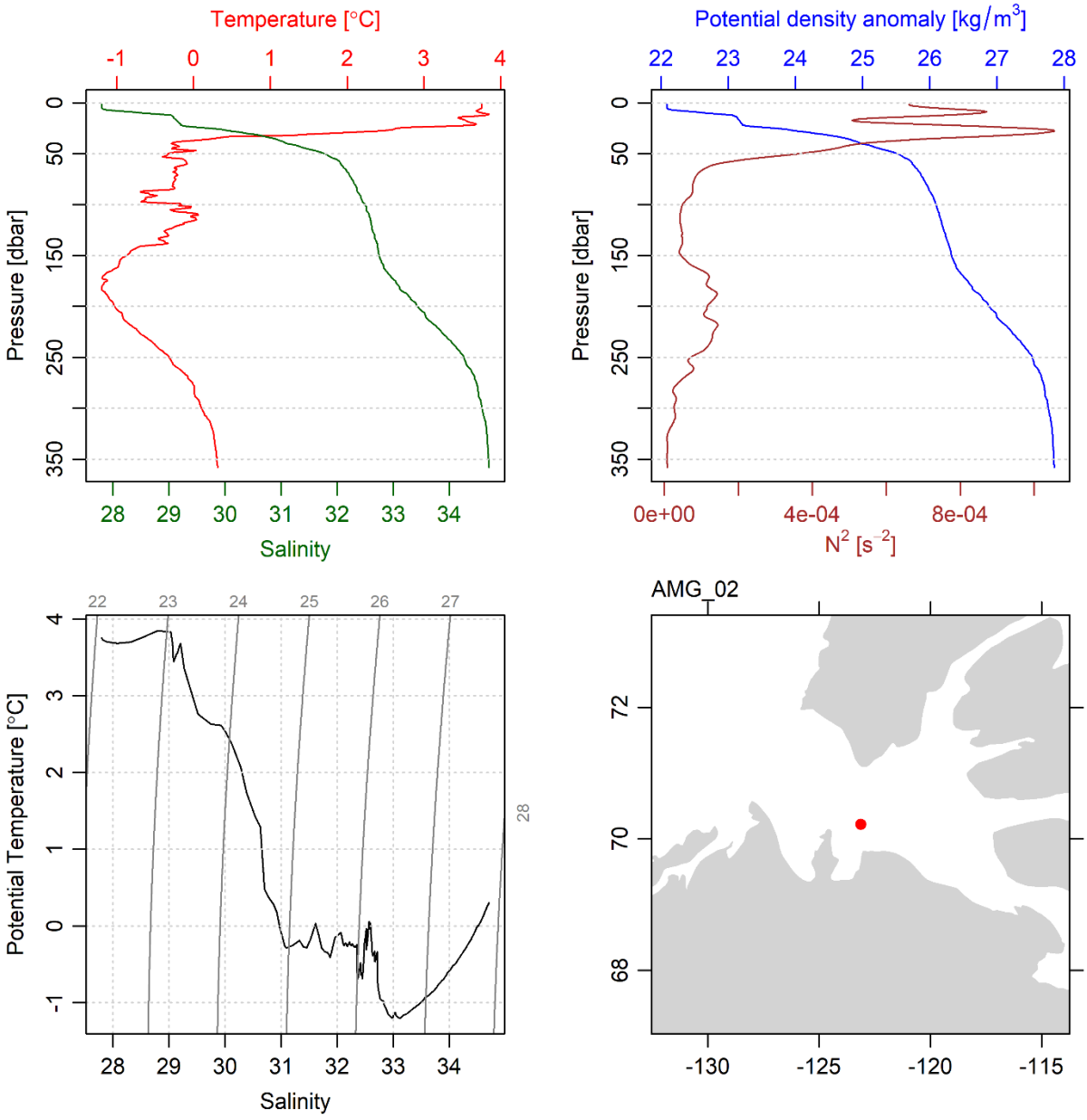
Temperature [°C]
-1 0 1 2 3 4
Pressure [dbar]
0 50 150 250 350
28 29 30 31 32 33 34
Salinity
Potential density anomaly [kg/m3]
22 23 24 25 26 27 28
0e+00 4e-04 8e-04
N2 [s-2]
Potential Temperature [°C]
22 23 24 25 26 27
-1 0 1 2 3 4
28 29 30 31 32 33 34
Salinity
28
AMG_02
72 70 68
-130 -125 -120 -115

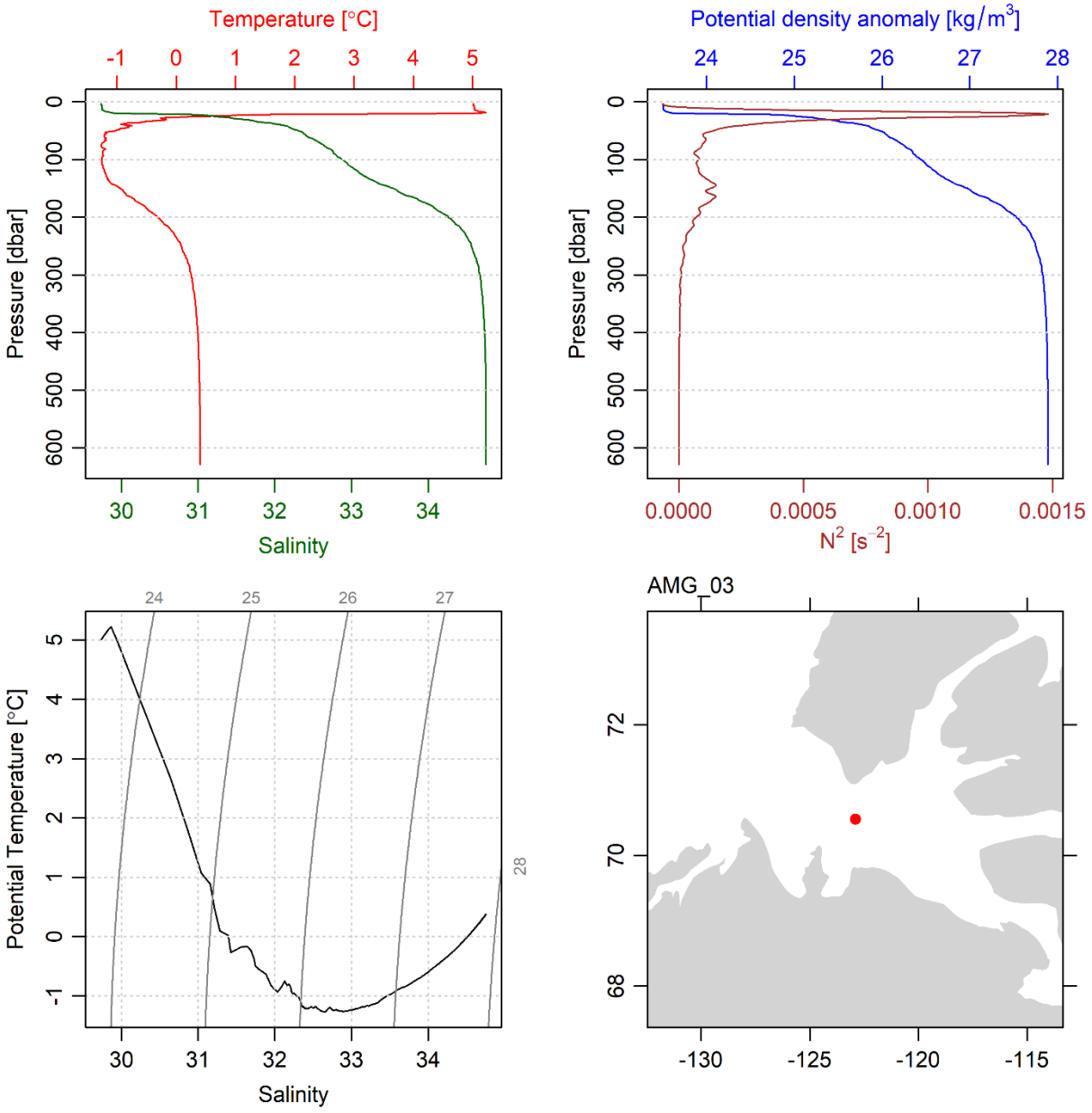
Temperature [°C]
-1 0 1 2 3 4 5
Pressure [dbar]
0 100 200 300 400 500 600
30 31 32 33 34
Salinity
Potential density anomaly [kg/m3]
24 25 26 27 28
0.0000 0.0005 0.0010 0.0015
N2 [s−2]
Potential Temperature [°C]
24 25 26 27 28
AMG_03
72 70 68
-130 -125 -120 -115

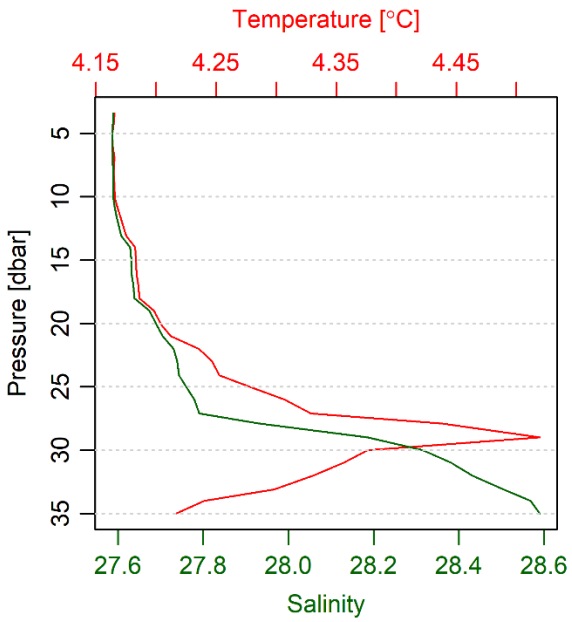
Temperature [°C]
4.15
4.25
4.35
4.45
Pressure [dbar]
5
10
15
20
25
30
35
27.6
27.8
28.0
28.2
28.4
28.6
Salinity

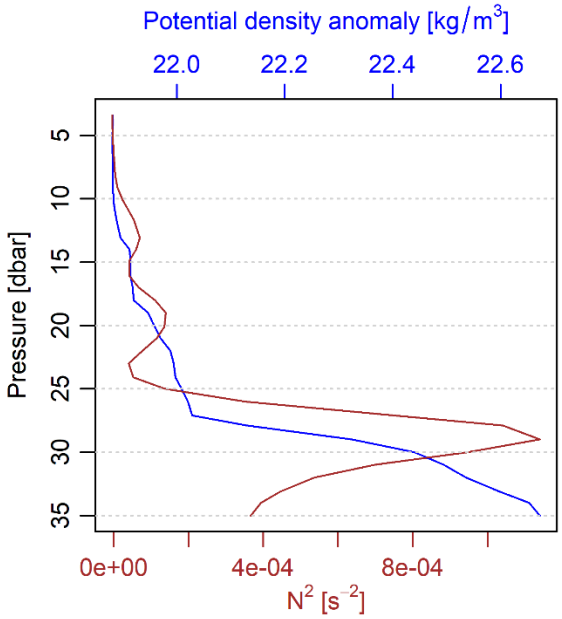
Potential density anomaly [kg/m3]
22.0
22.2
22.4
22.6
Pressure [dbar]
5
10
15
20
25
30
35
0e+00
4e-04
8e-04
N2 [s−2]

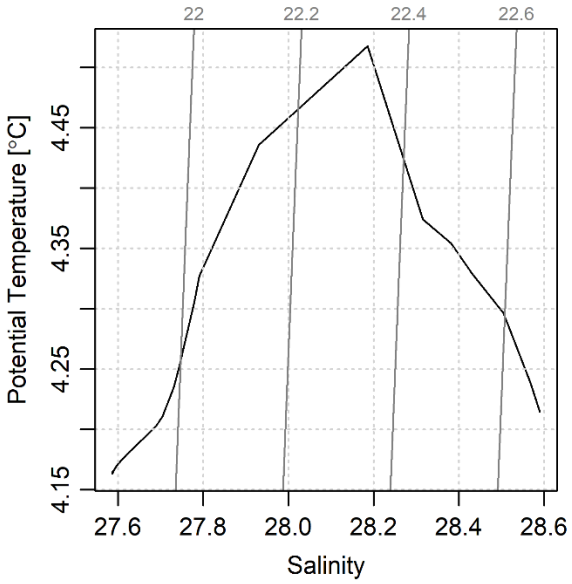
22
22.2
22.4
22.6
Potential Temperature [°C]
4.15
4.25
4.35
4.45
27.6
27.8
28.0
28.2
28.4
28.6
Salinity

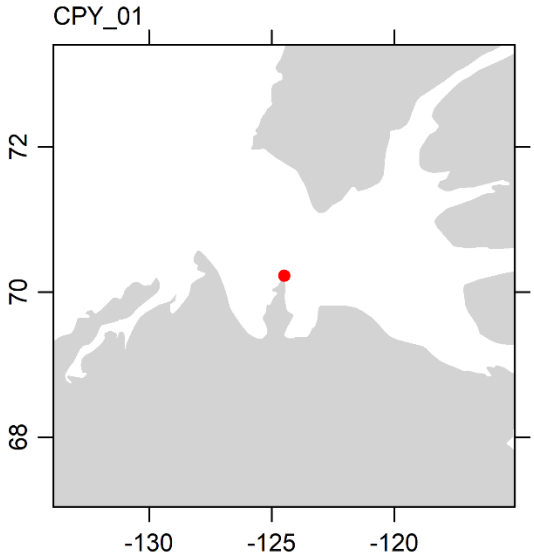
CPY_01
72
70
68
-130
-125
-120

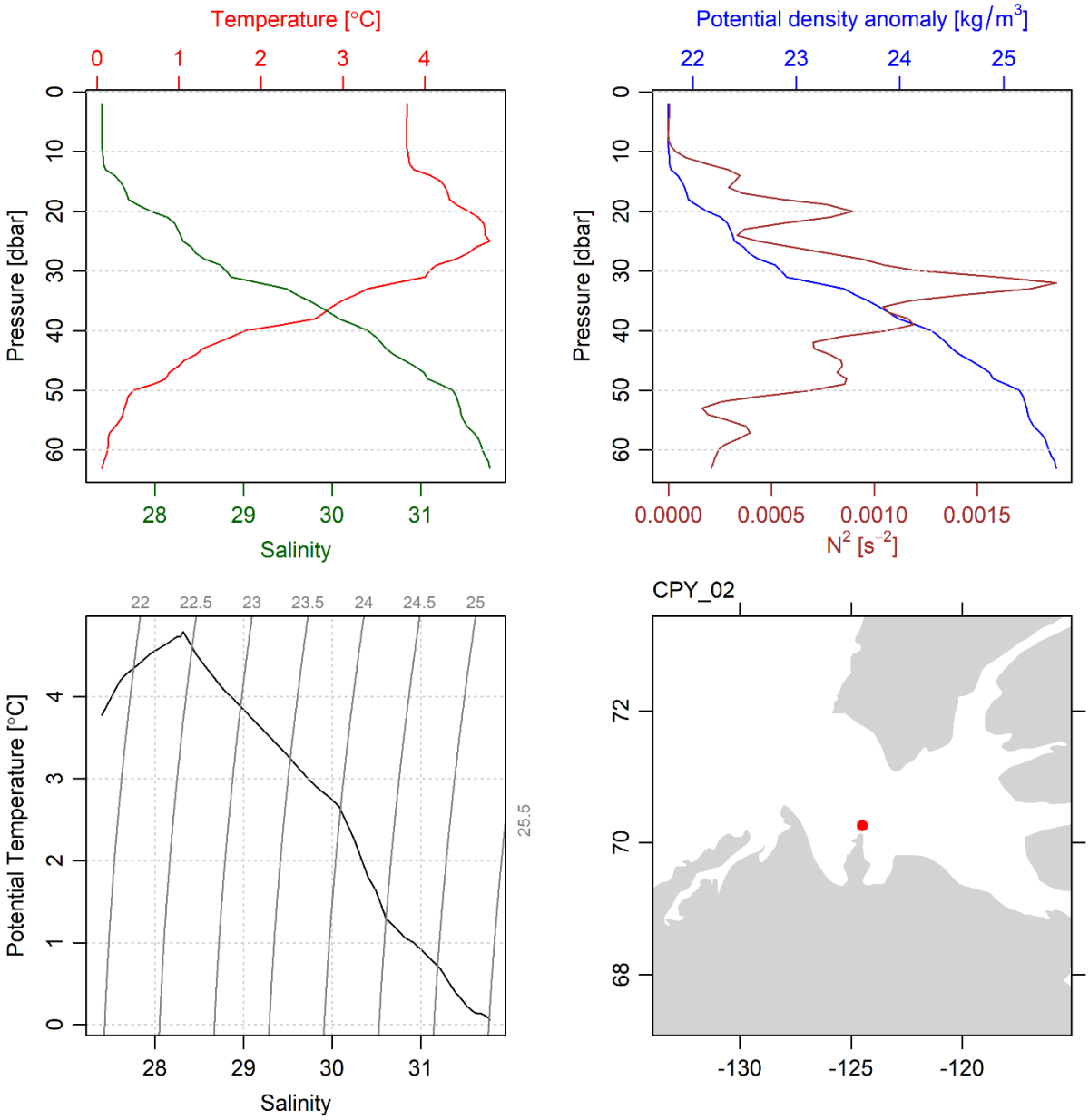
Temperature [°C]
0
1
2
3
4
Pressure [dbar]
0
10
20
30
40
50
60
28
29
30
31
Salinity
Potential density anomaly [kg/m3]
22
23
24
25
0.0000
0.0005
0.0010
0.0015
N2 [s−2]
Potential Temperature [°C]
22
22.5
23
23.5
24
24.5
25
25.5
CPY_02
72
70
68
-130
-125
-120

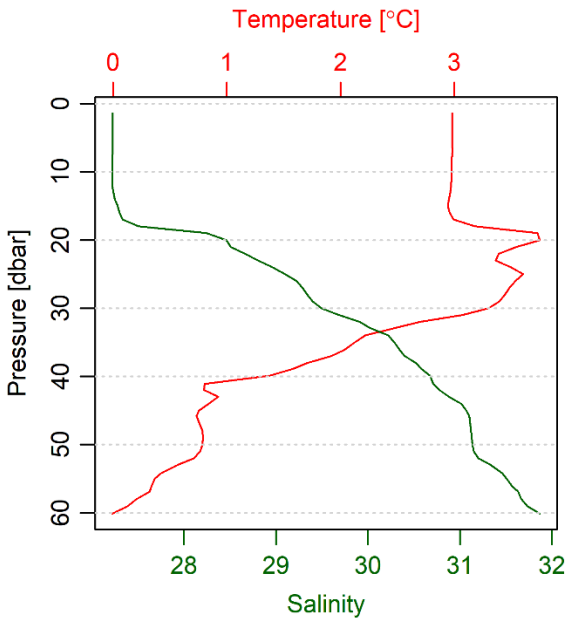
Temperature [°C]
0
1
2
3
Pressure [dbar]
0
10
20
30
40
50
60
28
29
30
31
32
Salinity

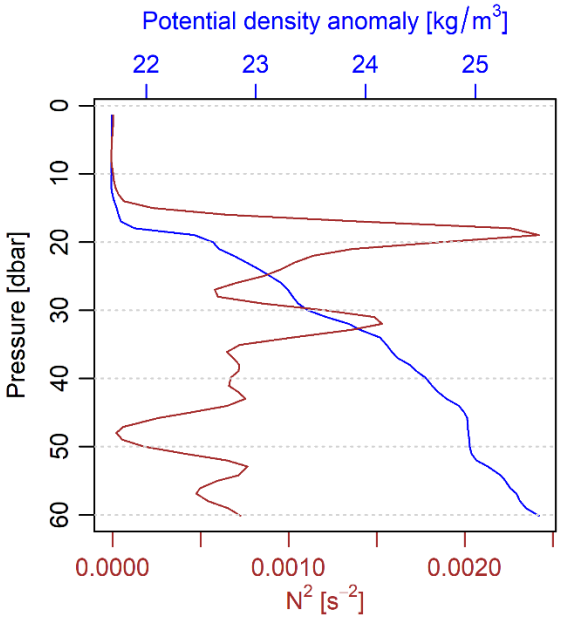
Potential density anomaly [kg/m3]
22
23
24
25
Pressure [dbar]
0
10
20
30
40
50
60
0.0000
0.0010
0.0020
N2 [s−2]

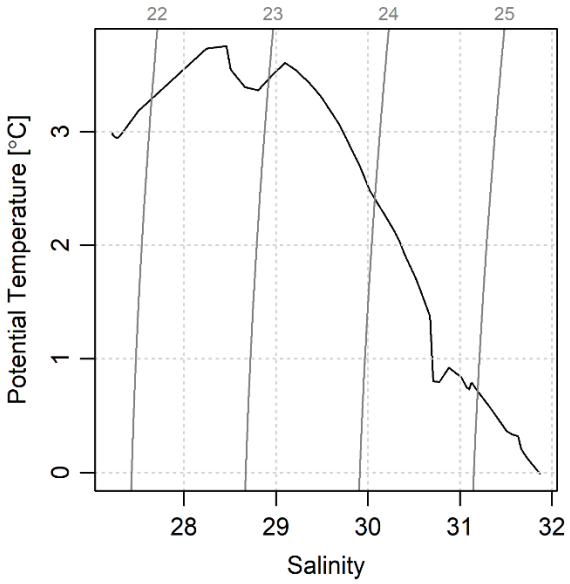
22
23
24
25
Potential Temperature [°C]
0
1
2
3
28
29
30
31
32
Salinity

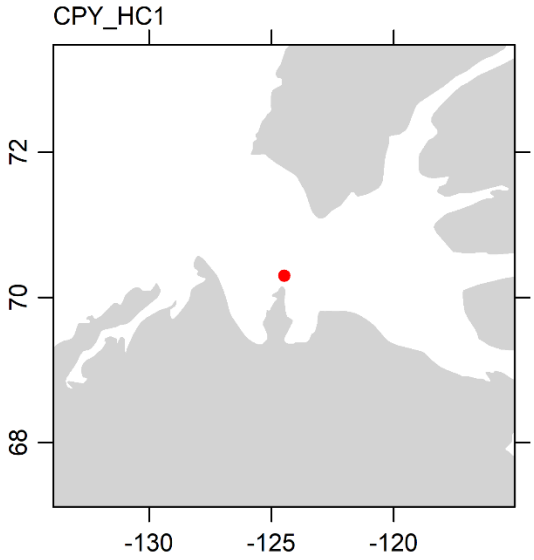
CPY_HC1
72
70
68
-130
-125
-120

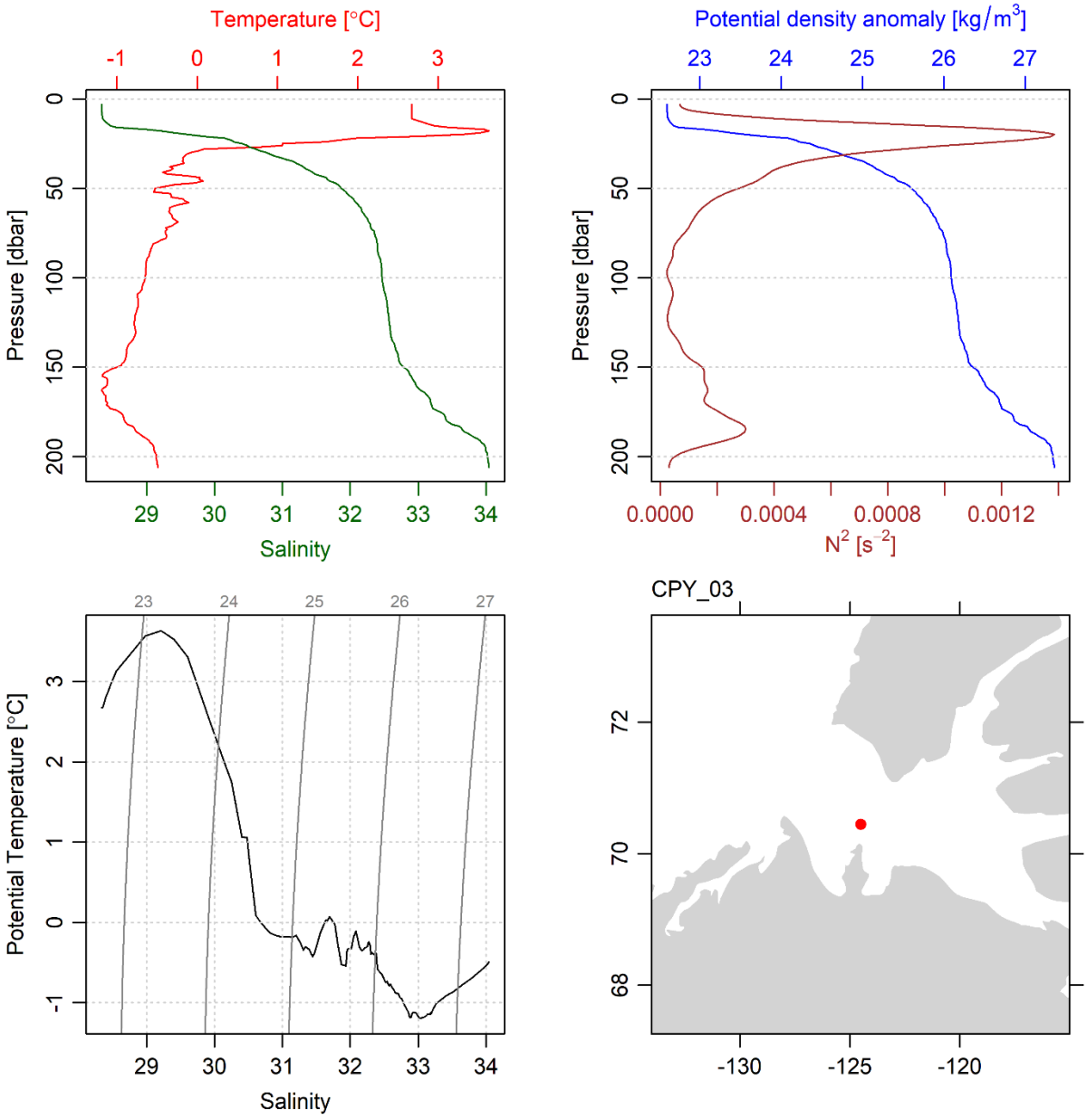
Temperature [°C]
-1
0
1
2
3
Pressure [dbar]
0
50
100
150
200
29
30
31
32
33
34
Salinity
Potential density anomaly [kg/m3]
23
24
25
26
27
0.0000
0.0004
0.0008
0.0012
N2 [s−2]
Potential Temperature [°C]
CPY_03
72
70
68
-130
-125
-120

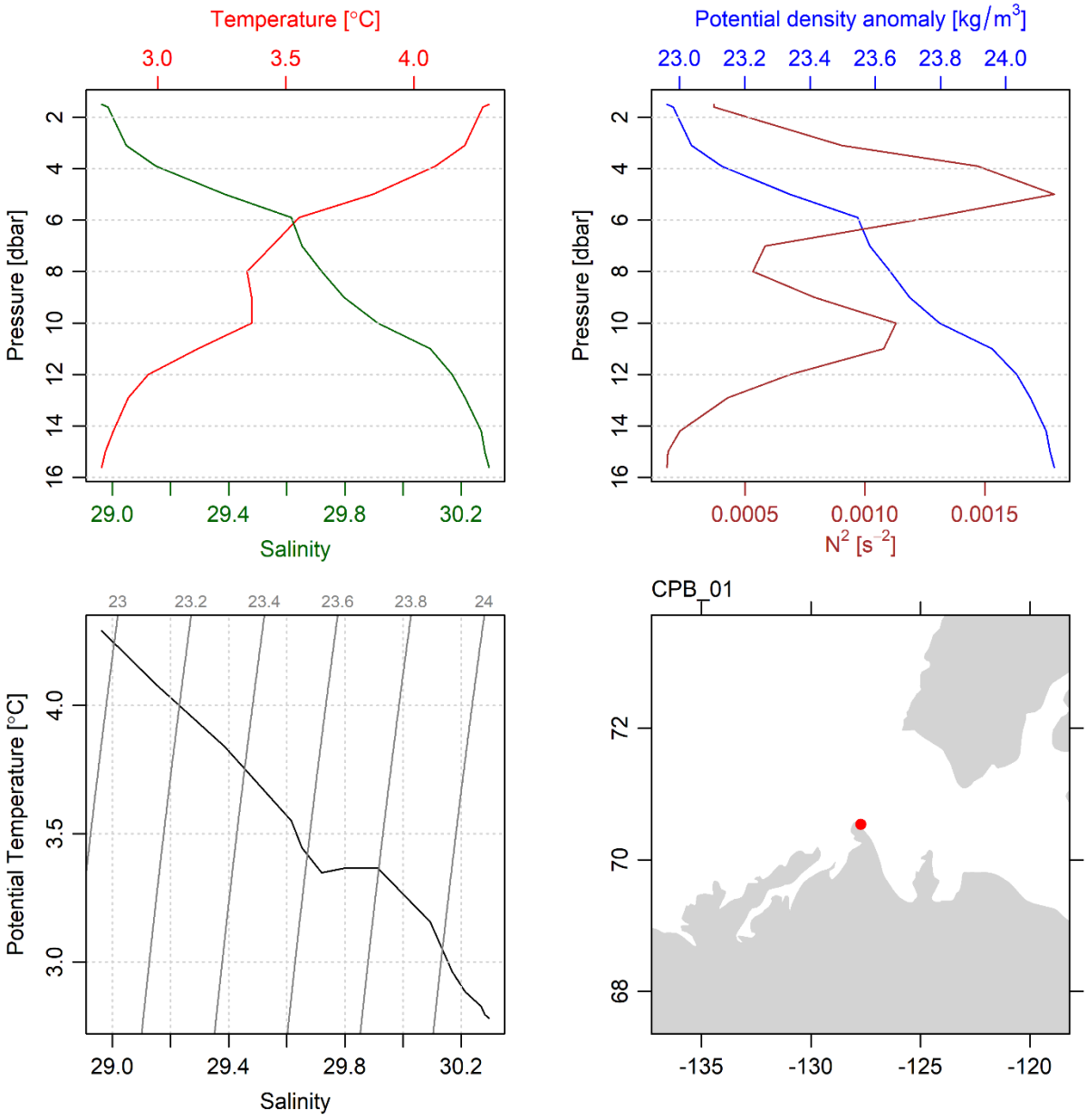
Temperature [°C]
3.0
3.5
4.0
Pressure [dbar]
2
4
6
8
10
12
14
16
29.0
29.4
29.8
30.2
Salinity
Potential density anomaly [kg/m3]
23.0
23.2
23.4
23.6
23.8
24.0
0.0005
0.0010
0.0015
N2 [s−2]
23
23.2
23.4
23.6
23.8
24
Potential Temperature [°C]
CPB_01
72
70
68
-135
-130
-125
-120

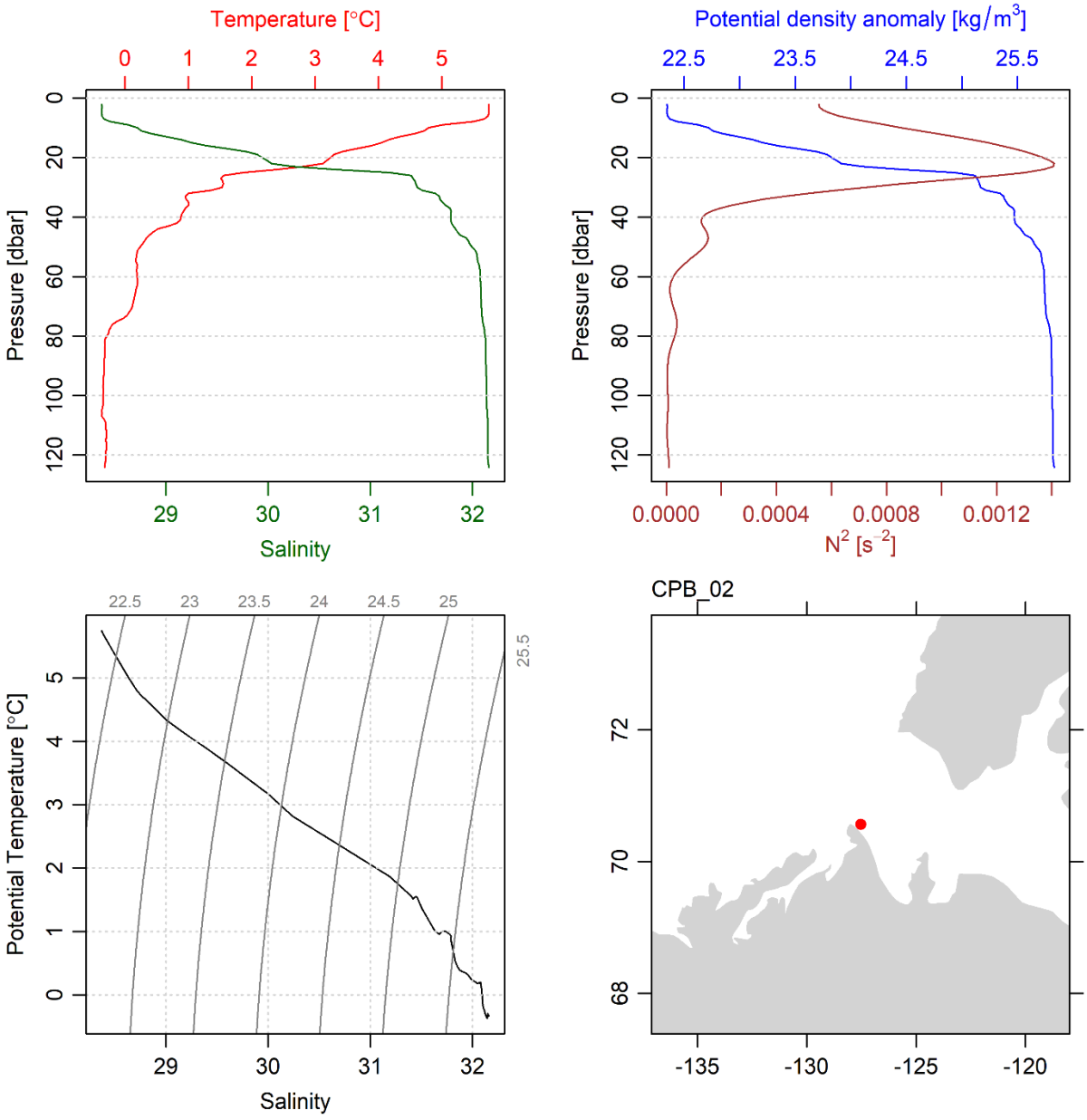
Temperature [°C]
0 1 2 3 4 5
Pressure [dbar]
0 20 40 60 80 100 120
29 30 31 32
Salinity
Potential density anomaly [kg/m3]
22.5 23.5 24.5 25.5
0.0000 0.0004 0.0008 0.0012
N2 [s−2]
22.5 23 23.5 24 24.5 25
25.5
Potential Temperature [°C]
0 1 2 3 4 5
29 30 31 32
Salinity
CPB_02
72 70 68
-135 -130 -125 -120

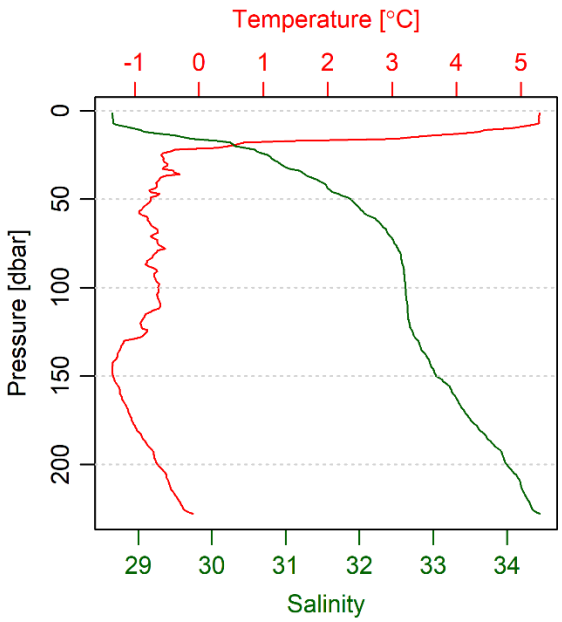
Temperature [°C]
-1
0
1
2
3
4
5
Pressure [dbar]
0
50
100
150
200
29
30
31
32
33
34
Salinity

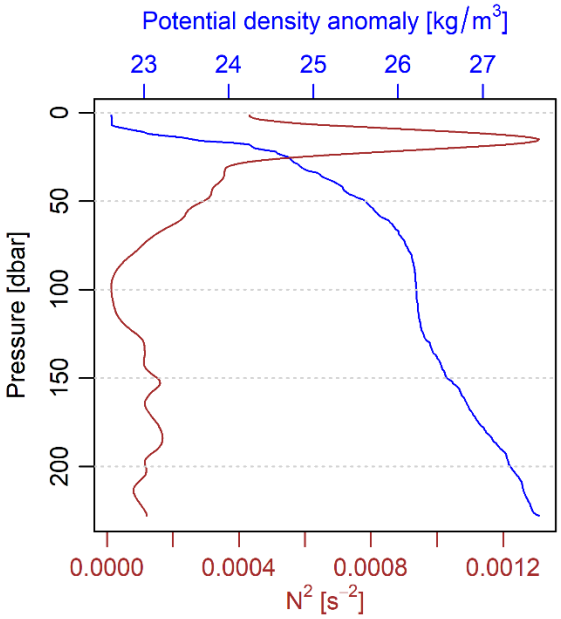
Potential density anomaly [kg/m3]
23
24
25
26
27
Pressure [dbar]
0
50
100
150
200
0.0000
0.0004
0.0008
0.0012
N2 [s−2]

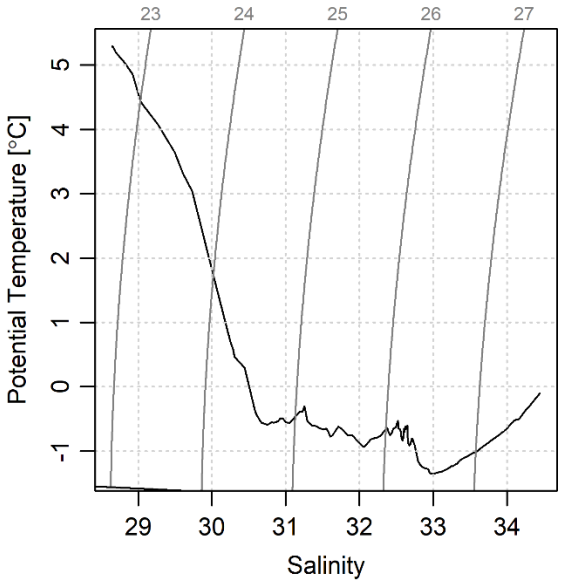
23
24
25
26
27
Potential Temperature [°C]
-1
0
1
2
3
4
5
29
30
31
32
33
34
Salinity

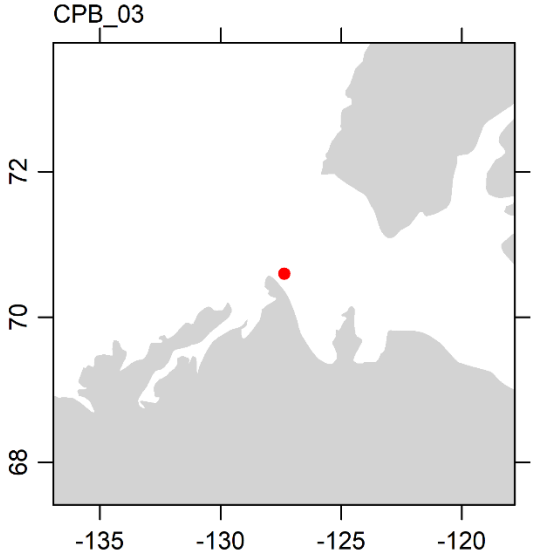
CPB_03
72
70
68
-135
-130
-125
-120

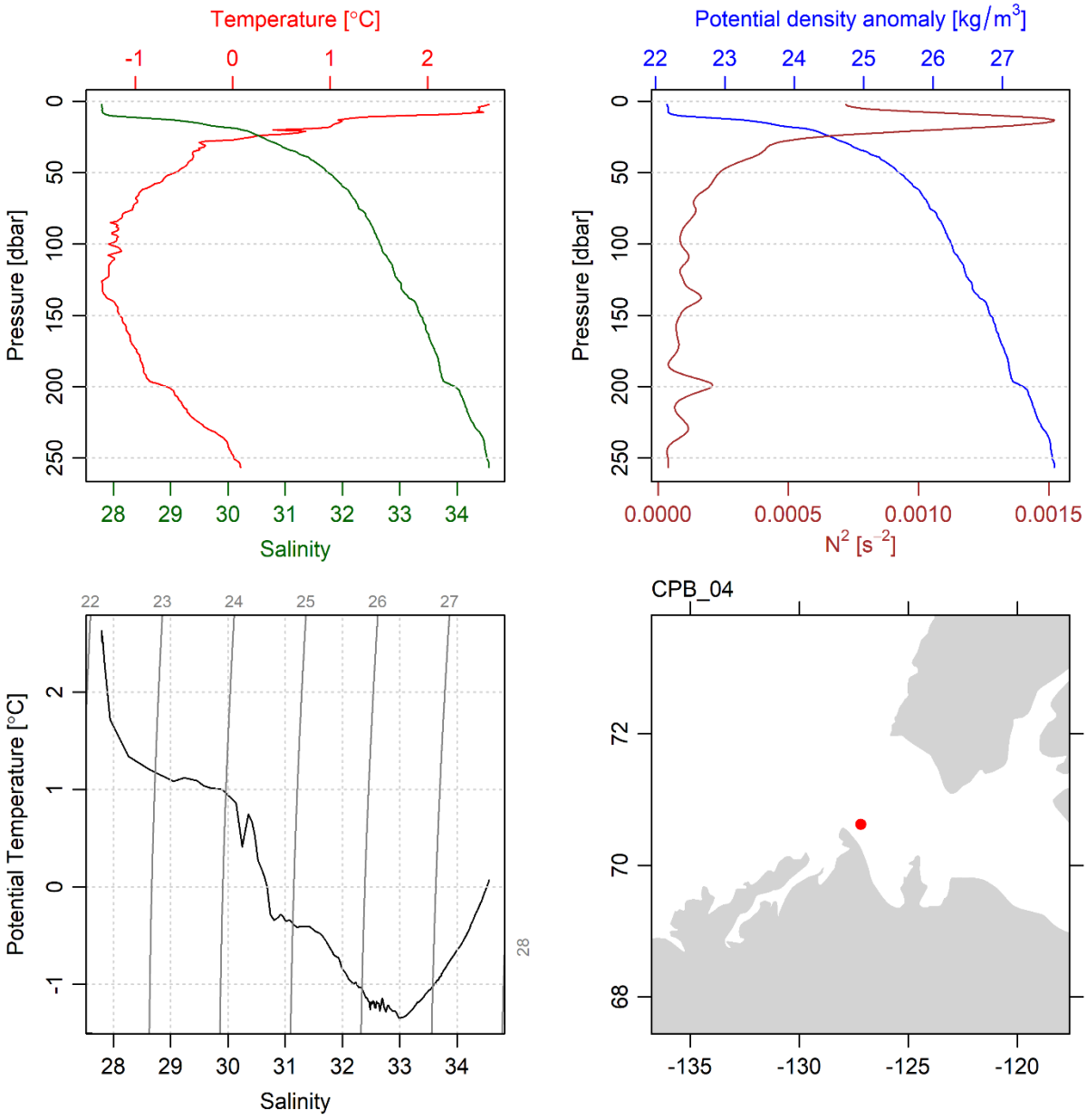
Temperature [°C]
-1
0
1
2
Pressure [dbar]
0
50
100
150
200
250
28
29
30
31
32
33
34
Salinity
Potential density anomaly [kg/m3]
22
23
24
25
26
27
0.0000
0.0005
0.0010
0.0015
N2 [s−2]
Potential Temperature [°C]
CPB_04
72
70
68
-135
-130
-125
-120

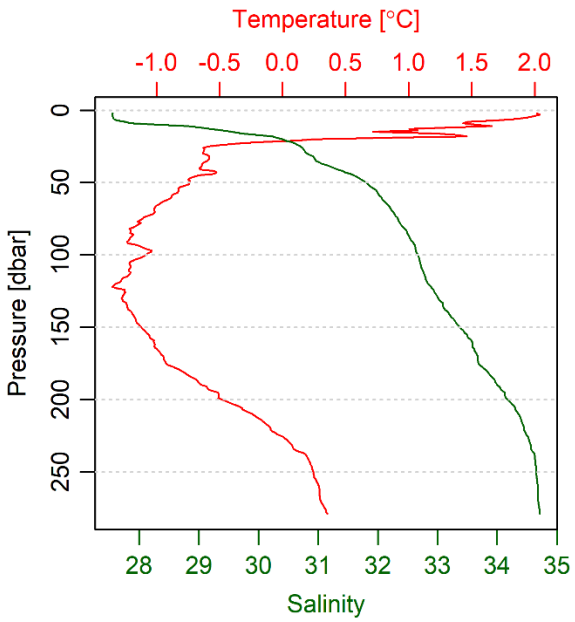
Temperature [°C]
-1.0 -0.5 0.0 0.5 1.0 1.5 2.0
Pressure [dbar]
0 50 100 150 200 250
28 29 30 31 32 33 34 35
Salinity

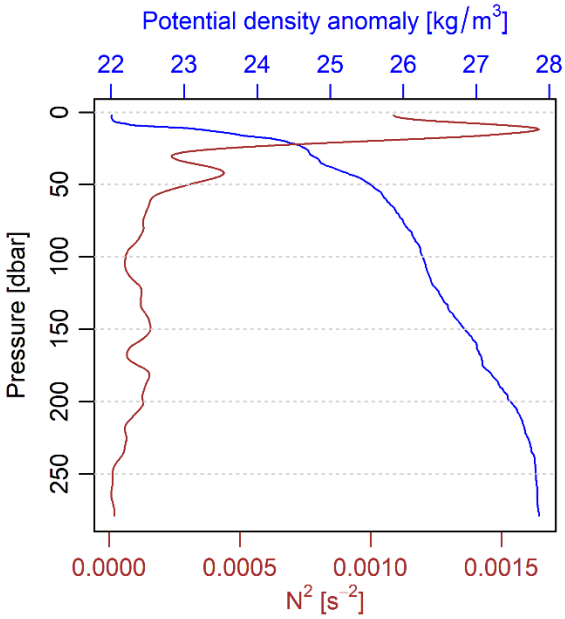
Potential density anomaly [kg/m3]
22 23 24 25 26 27 28
Pressure [dbar]
0 50 100 150 200 250
0.0000 0.0005 0.0010 0.0015
N2 [s−2]

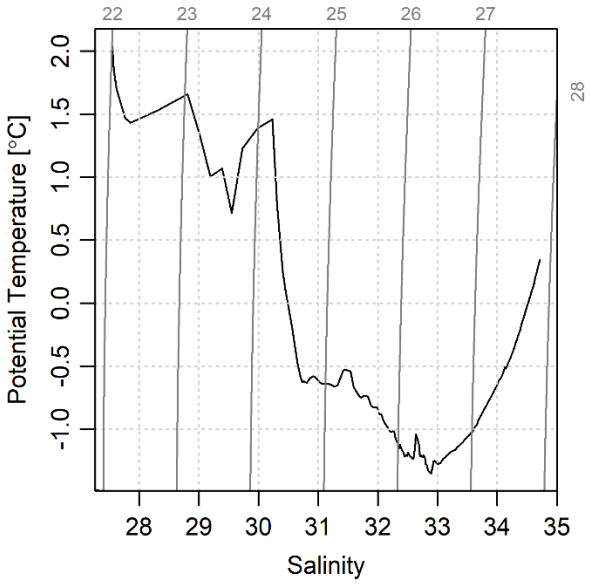
22 23 24 25 26 27
28
Potential Temperature [°C]
-1.0 -0.5 0.0 0.5 1.0 1.5 2.0
28 29 30 31 32 33 34 35
Salinity

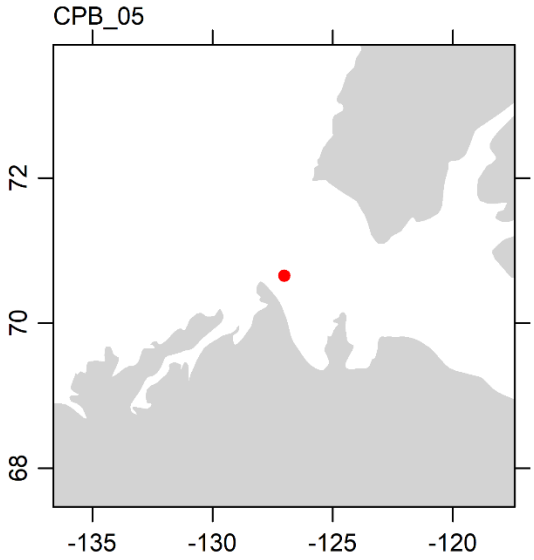
CPB_05
72
70
68
-135 -130 -125 -120

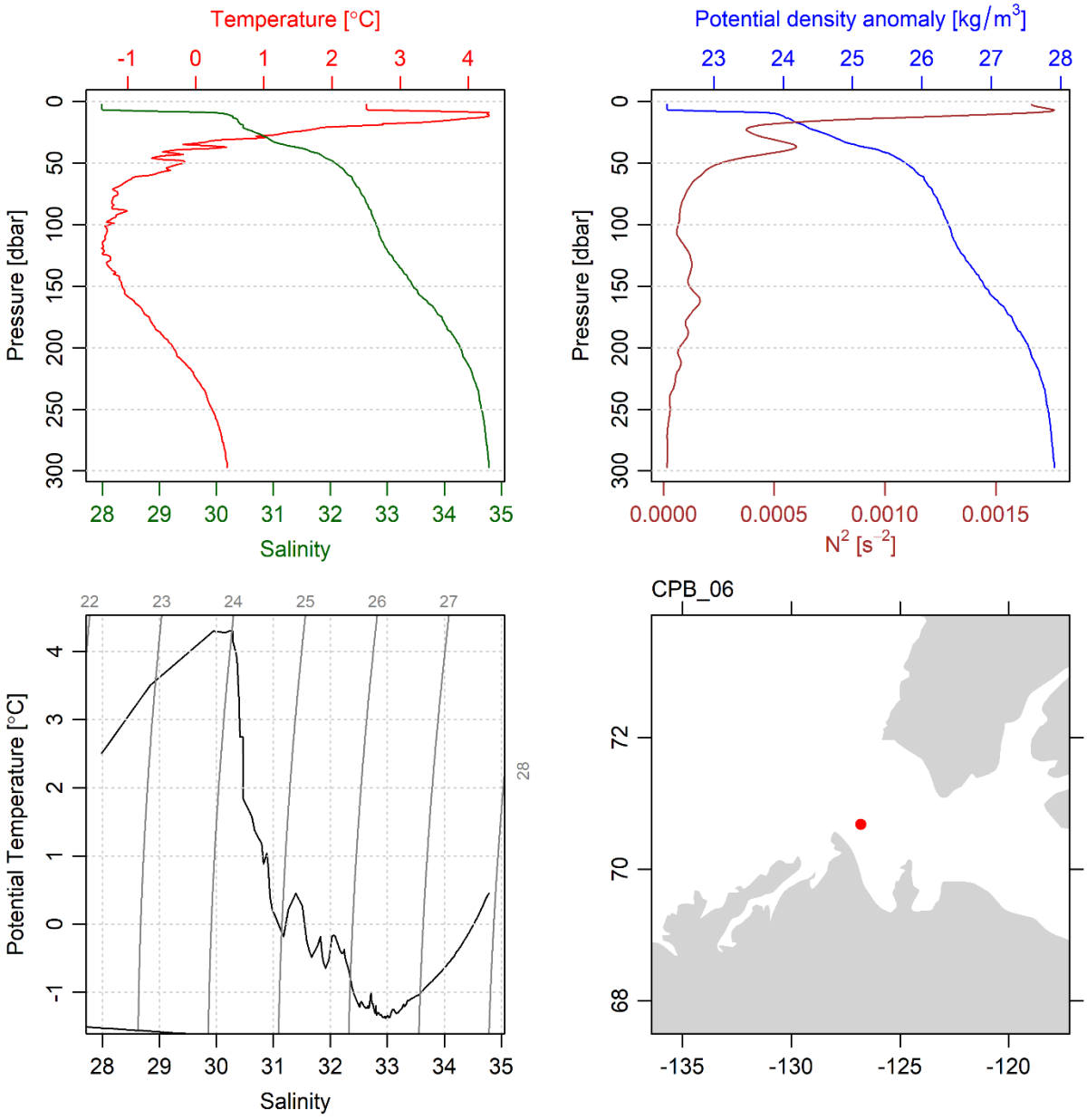
Temperature [°C]
-1 0 1 2 3 4
Pressure [dbar]
0 50 100 150 200 250 300
28 29 30 31 32 33 34 35
Salinity
Potential density anomaly [kg/m3]
23 24 25 26 27 28
0.0000 0.0005 0.0010 0.0015
N2 [s−2]
Potential Temperature [°C]
22 23 24 25 26 27
28
CPB_06
72 70 68
-135 -130 -125 -120

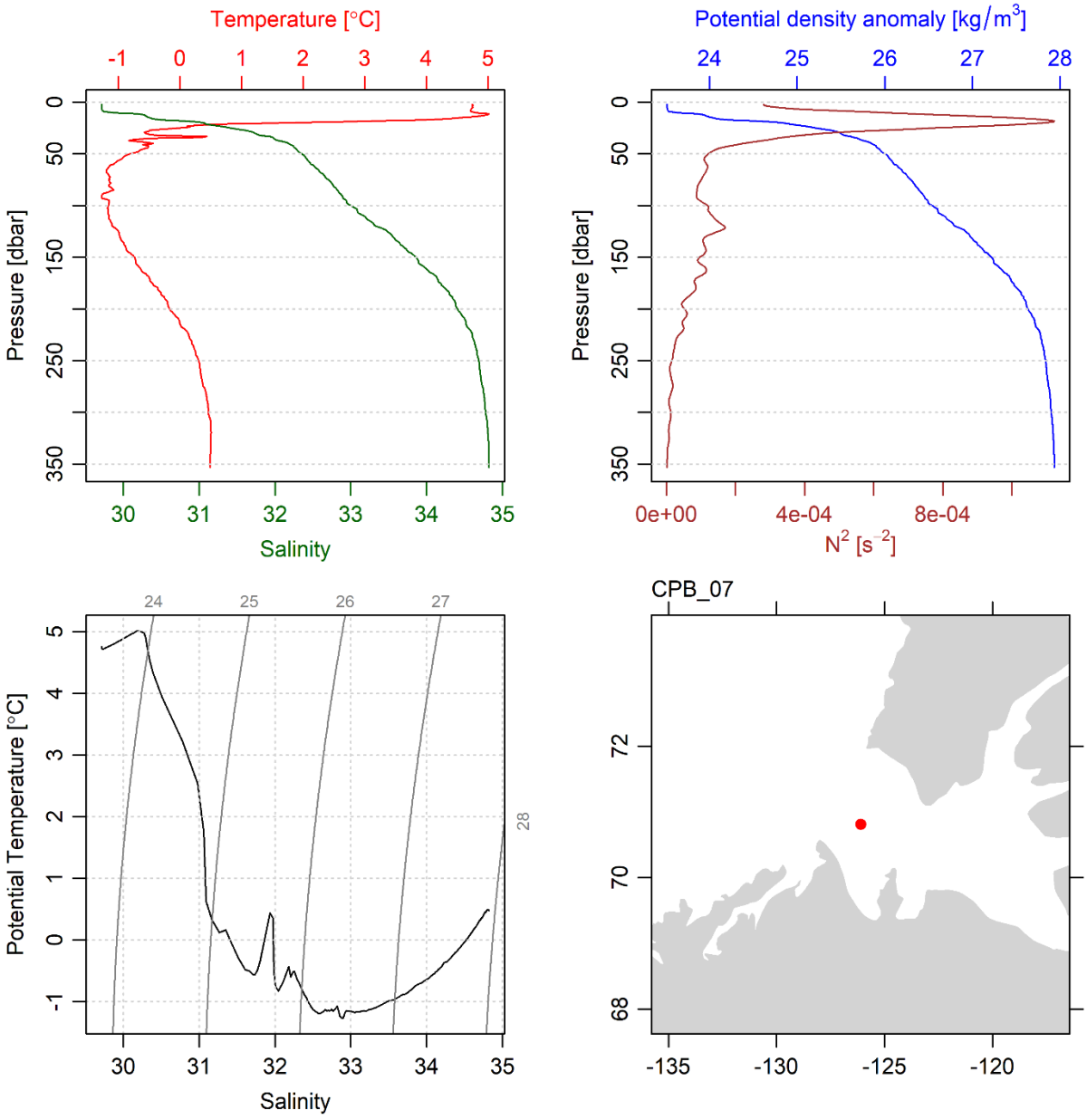
Temperature [°C]
-1 0 1 2 3 4 5
Pressure [dbar]
0 50 150 250 350
30 31 32 33 34 35
Salinity
Potential density anomaly [kg/m3]
24 25 26 27 28
0e+00 4e-04 8e-04
N2 [s−2]
Potential Temperature [°C]
24 25 26 27
28
CPB_07
72 70 68
-135 -130 -125 -120

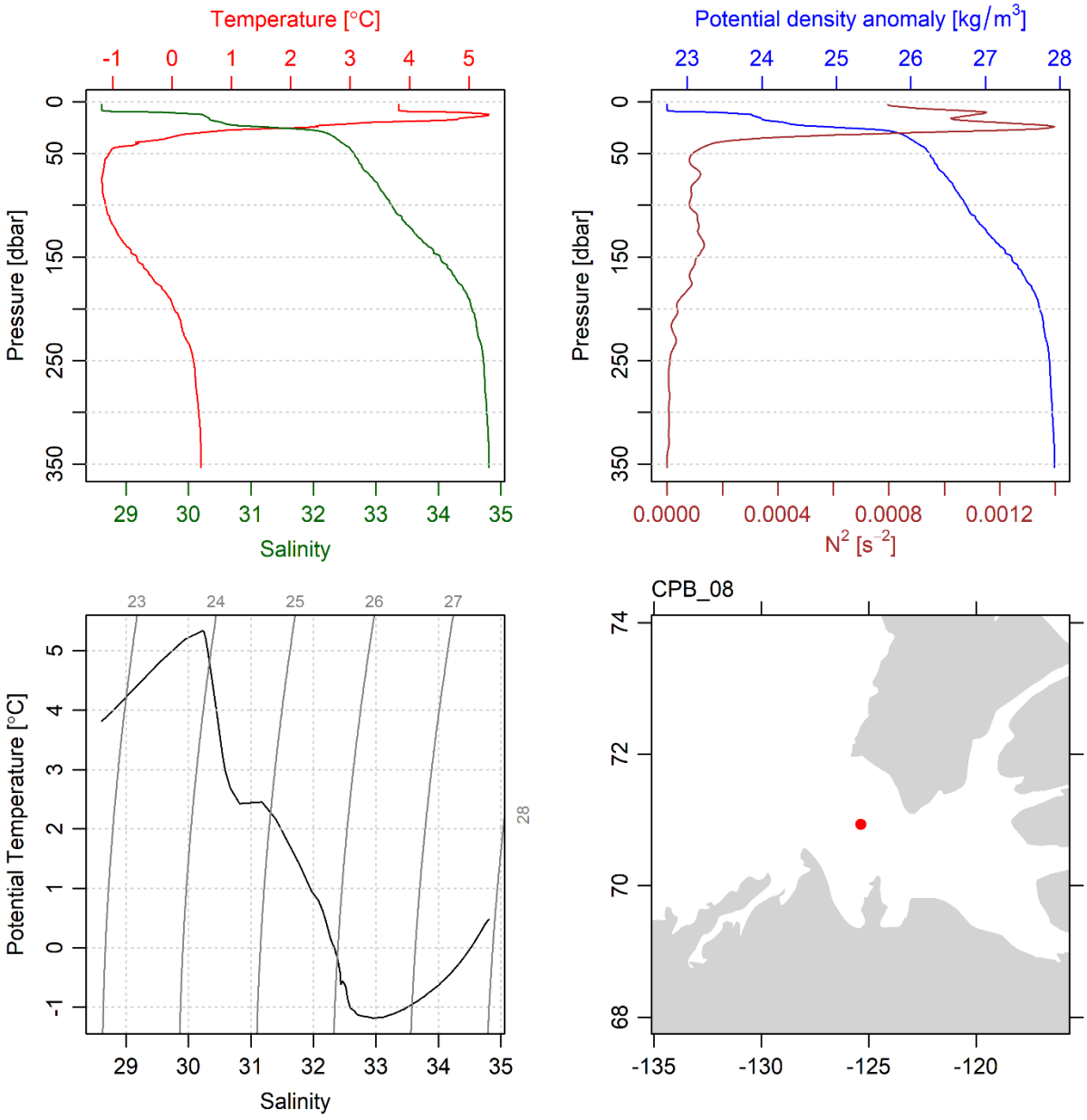
Temperature [°C]
-1 0 1 2 3 4 5
Pressure [dbar]
0 50 150 250 350
29 30 31 32 33 34 35
Salinity
Potential density anomaly [kg/m3]
23 24 25 26 27 28
0.0000 0.0004 0.0008 0.0012
N2 [s−2]
Potential Temperature [°C]
23 24 25 26 27
28
CPB_08
74 72 70 68
-135 -130 -125 -120

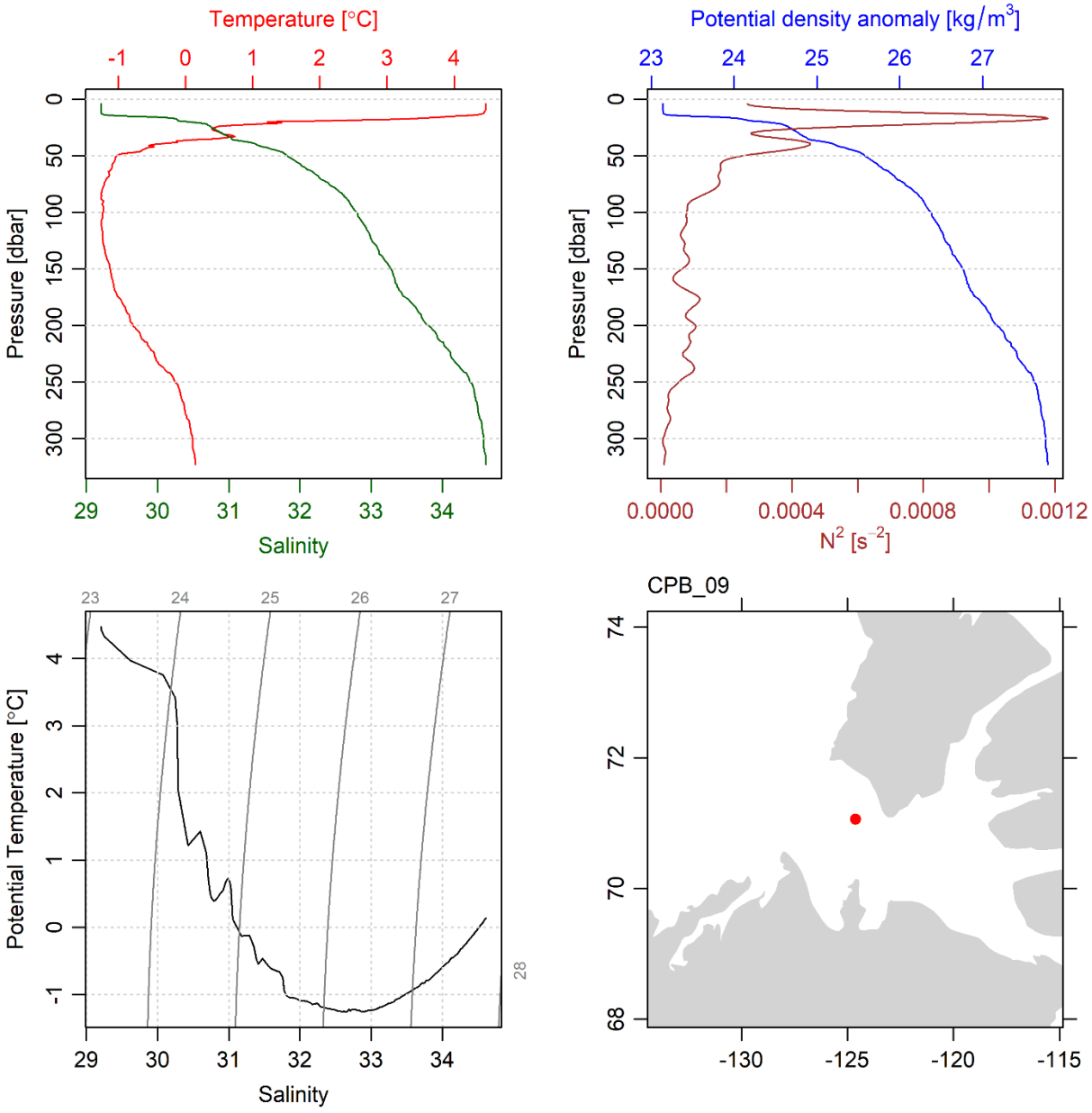
Temperature [°C]
-1
0
1
2
3
4
Pressure [dbar]
0
50
100
150
200
250
300
29
30
31
32
33
34
Salinity
Potential density anomaly [kg/m3]
23
24
25
26
27
0.0000
0.0004
0.0008
0.0012
N2 [s−2]
Potential Temperature [°C]
28
CPB_09
74
72
70
68
-130
-125
-120
-115

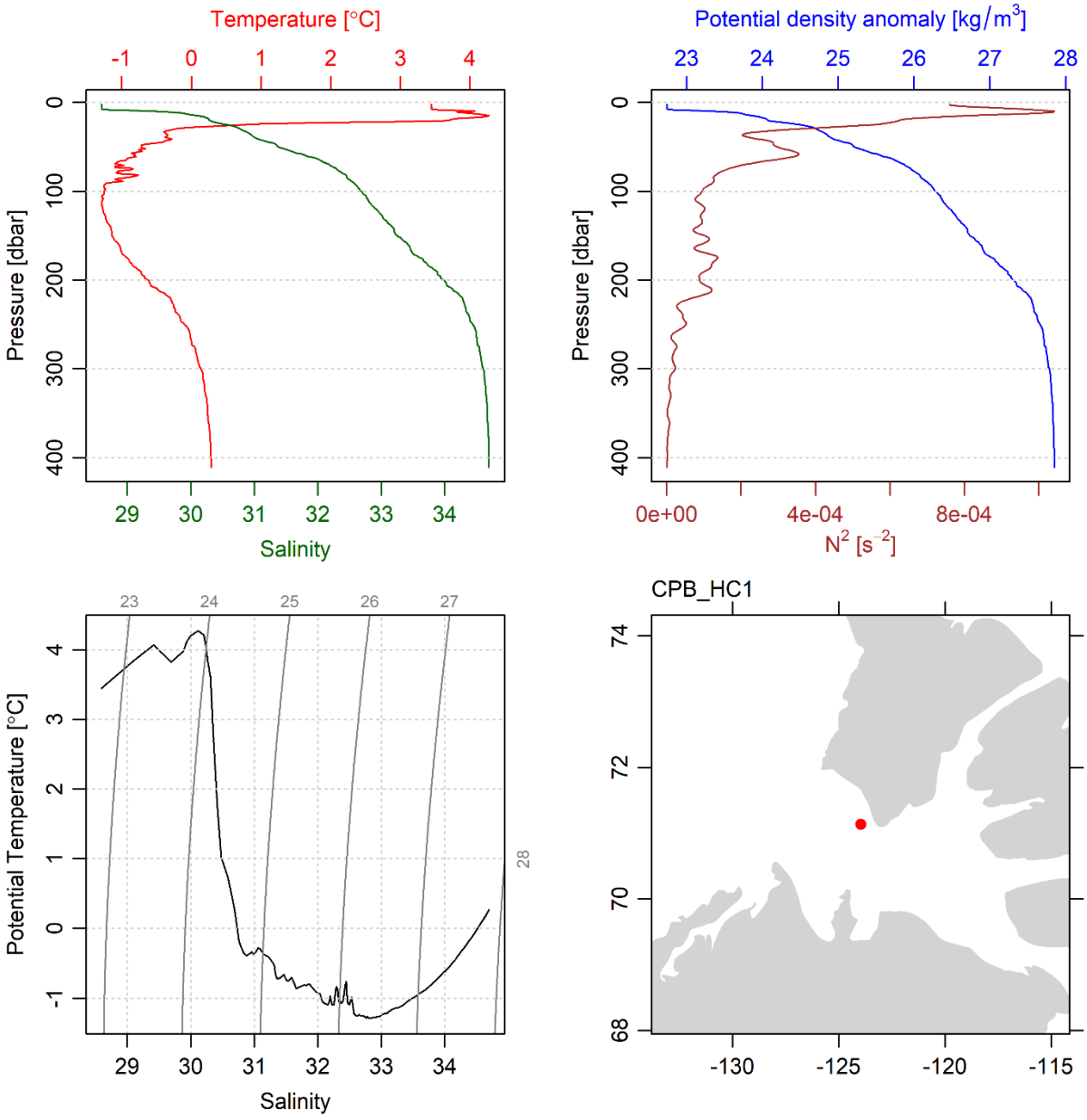
Temperature [°C]
-1
0
1
2
3
4
Pressure [dbar]
0
100
200
300
400
29
30
31
32
33
34
Salinity
Potential density anomaly [kg/m3]
23
24
25
26
27
28
0e+00
4e-04
8e-04
N2 [s−2]
Potential Temperature [°C]
CPB_HC1
74
72
70
68
-130
-125
-120
-115

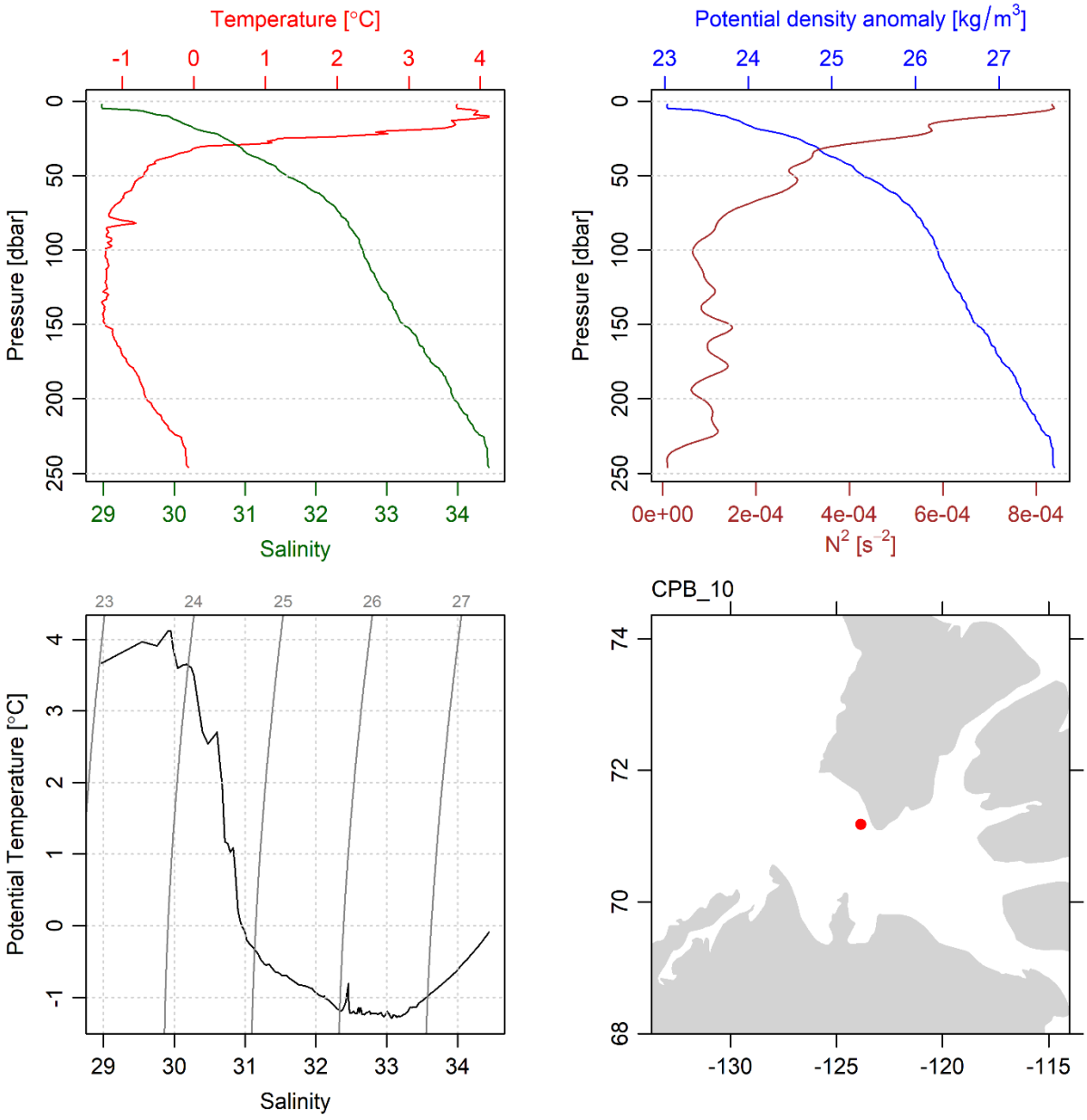
Temperature [°C]
-1
0
1
2
3
4
Pressure [dbar]
0
50
100
150
200
250
29
30
31
32
33
34
Salinity
Potential density anomaly [kg/m3]
23
24
25
26
27
0e+00
2e-04
4e-04
6e-04
8e-04
N2 [s−2]
Potential Temperature [°C]
CPB_10
74
72
70
68
-130
-125
-120
-115

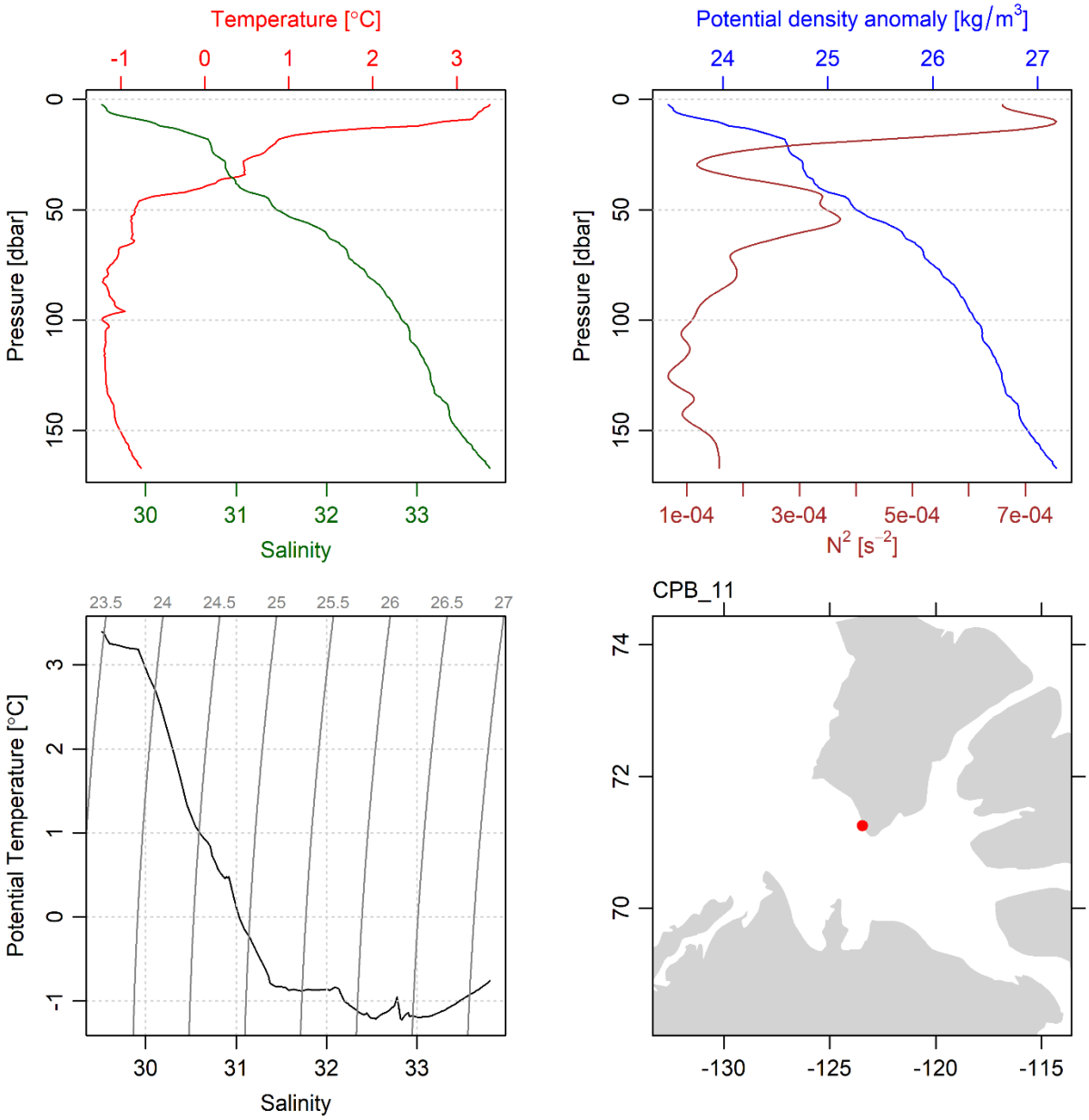
Temperature [°C]
-1
0
1
2
3
Pressure [dbar]
0
50
100
150
30
31
32
33
Salinity
Potential density anomaly [kg/m3]
24
25
26
27
1e-04
3e-04
5e-04
7e-04
N2 [s−2]
23.5
24
24.5
25
25.5
26
26.5
27
Potential Temperature [°C]
CPB_11
74
72
70
-130
-125
-120
-115

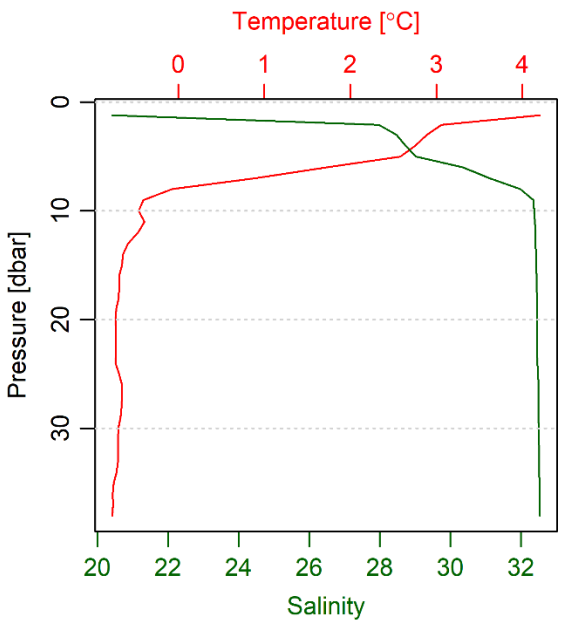
Temperature [°C]
0
1
2
3
4
Pressure [dbar]
0
10
20
30
20
22
24
26
28
30
32
Salinity

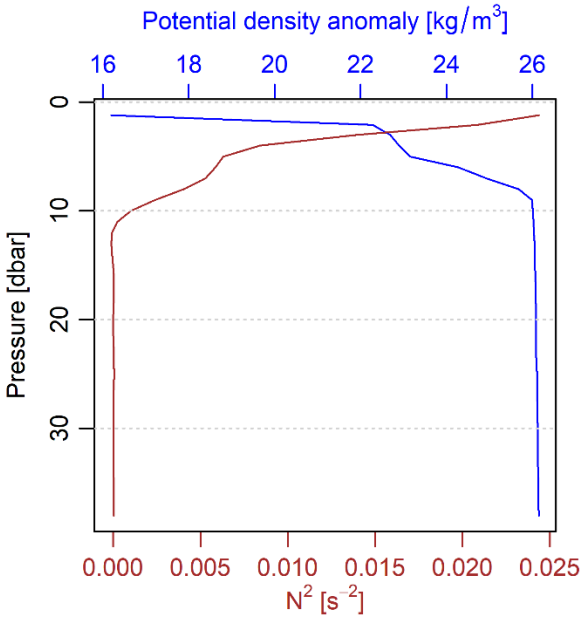
Potential density anomaly [kg/m3]
16
18
20
22
24
26
Pressure [dbar]
0
10
20
30
0.000
0.005
0.010
0.015
0.020
0.025
N2 [s−2]

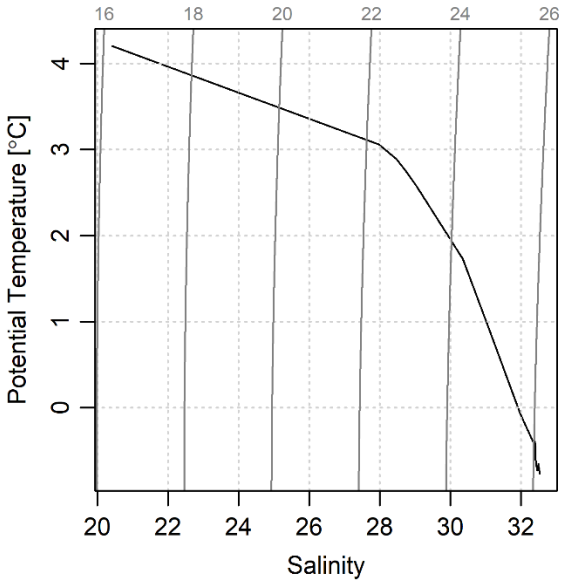
16
18
20
22
24
26
Potential Temperature [°C]
0
1
2
3
4
20
22
24
26
28
30
32
Salinity

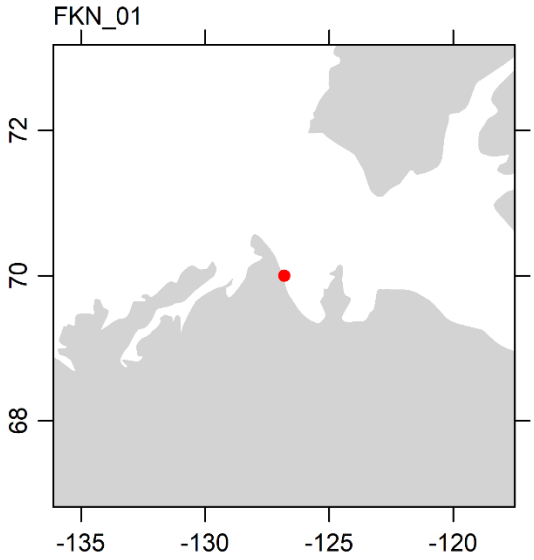
FKN_01
72
70
68
-135
-130
-125
-120

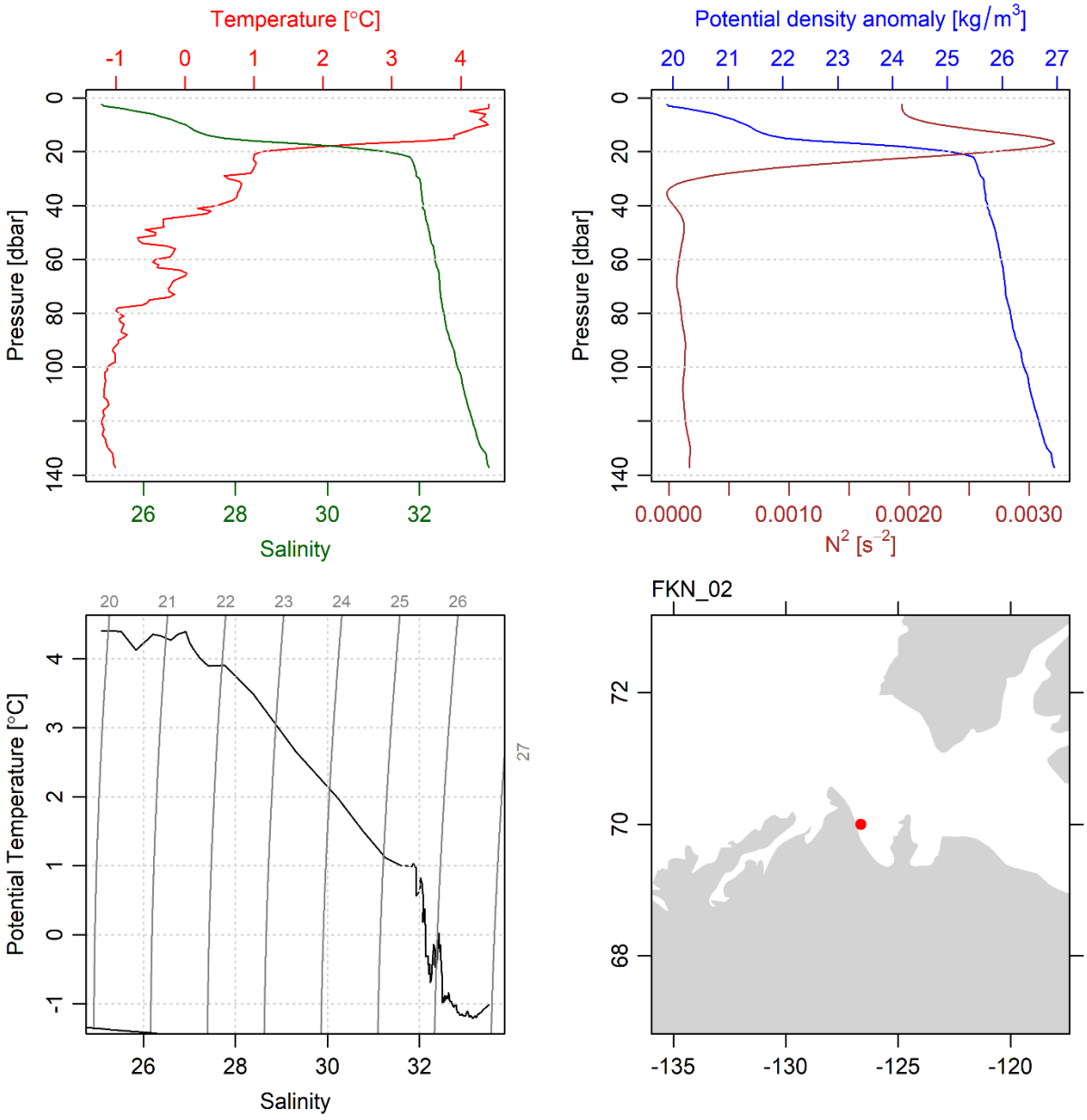
Temperature [°C]
-1
0
1
2
3
4
Pressure [dbar]
0
20
40
60
80
100
140
26
28
30
32
Salinity
Potential density anomaly [kg/m3]
20
21
22
23
24
25
26
27
0.0000
0.0010
0.0020
0.0030
N2 [s−2]
Potential Temperature [°C]
-1
0
1
2
3
4
20
21
22
23
24
25
26
27
FKN_02
72
70
68
-135
-130
-125
-120

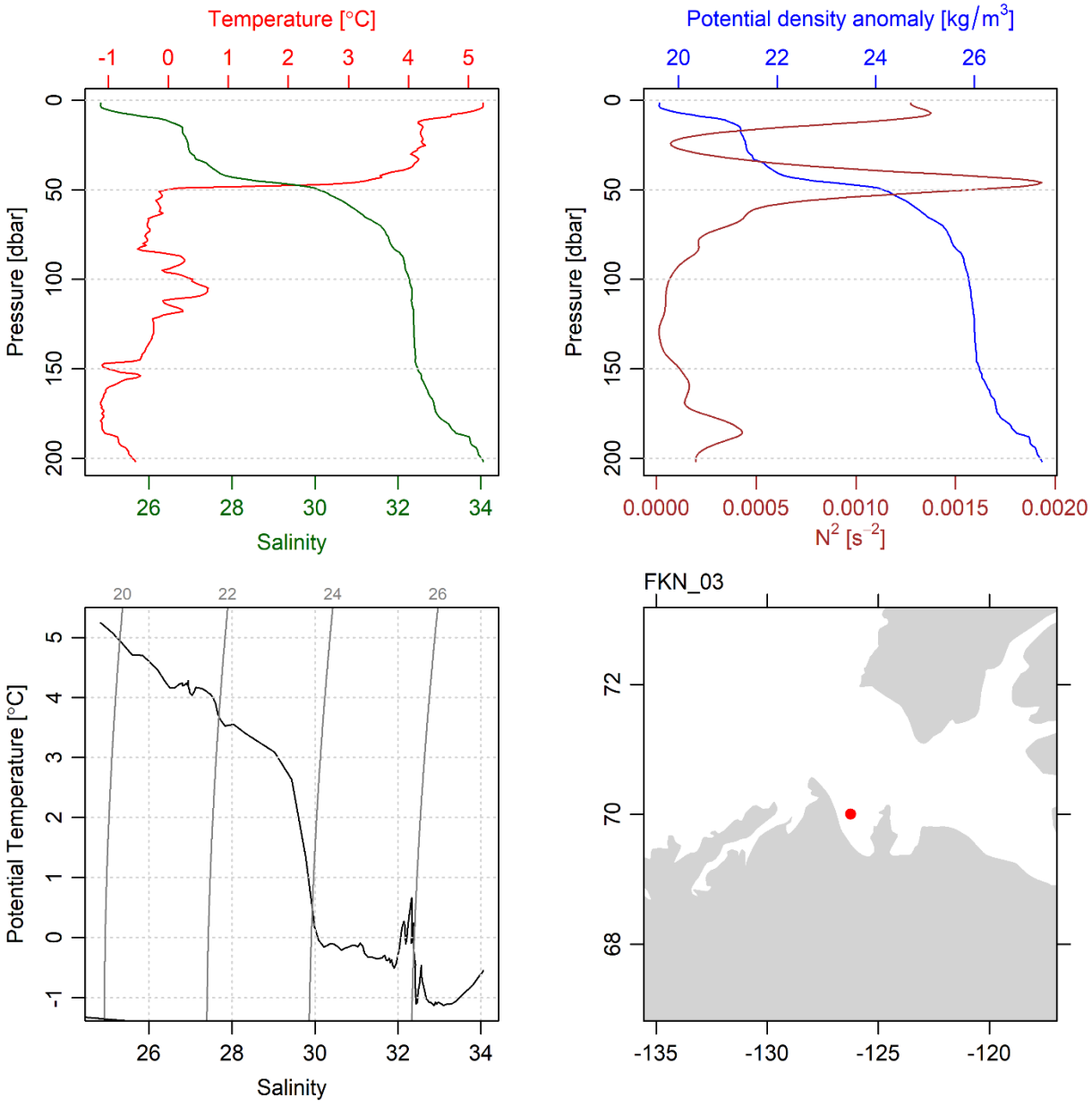
Temperature [°C]
-1 0 1 2 3 4 5
Pressure [dbar]
0 50 100 150 200
26 28 30 32 34
Salinity
Potential density anomaly [kg/m3]
20 22 24 26
0.0000 0.0005 0.0010 0.0015 0.0020
N2 [s−2]
Potential Temperature [°C]
-1 0 1 2 3 4 5
FKN_03
72 70 68
-135 -130 -125 -120

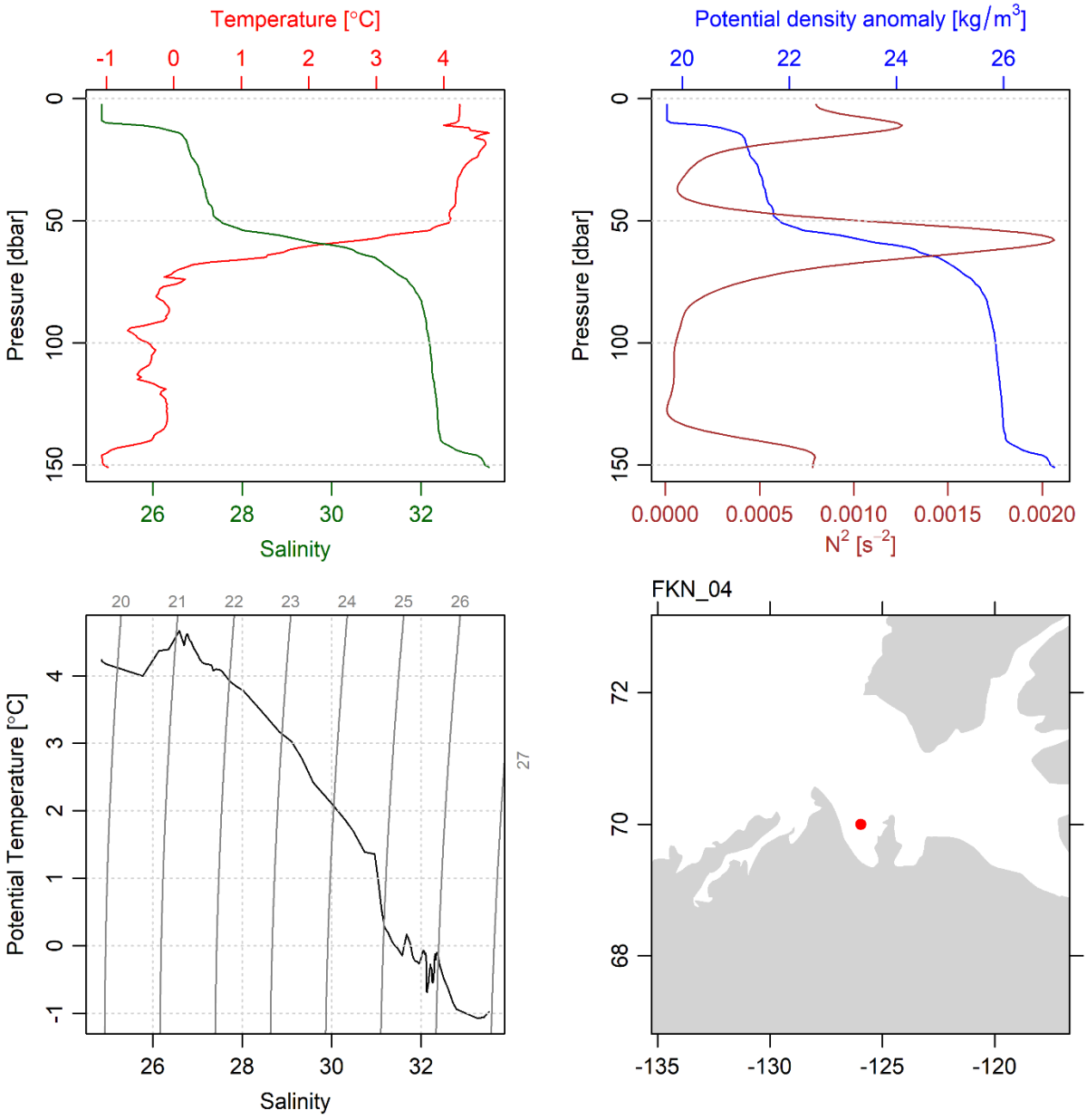
Temperature [°C]
-1
0
1
2
3
4
Pressure [dbar]
0
50
100
150
26
28
30
32
Salinity
Potential density anomaly [kg/m3]
20
22
24
26
0.0000
0.0005
0.0010
0.0015
0.0020
N2 [s−2]
Potential Temperature [°C]
20
21
22
23
24
25
26
27
FKN_04
72
70
68
-135
-130
-125
-120

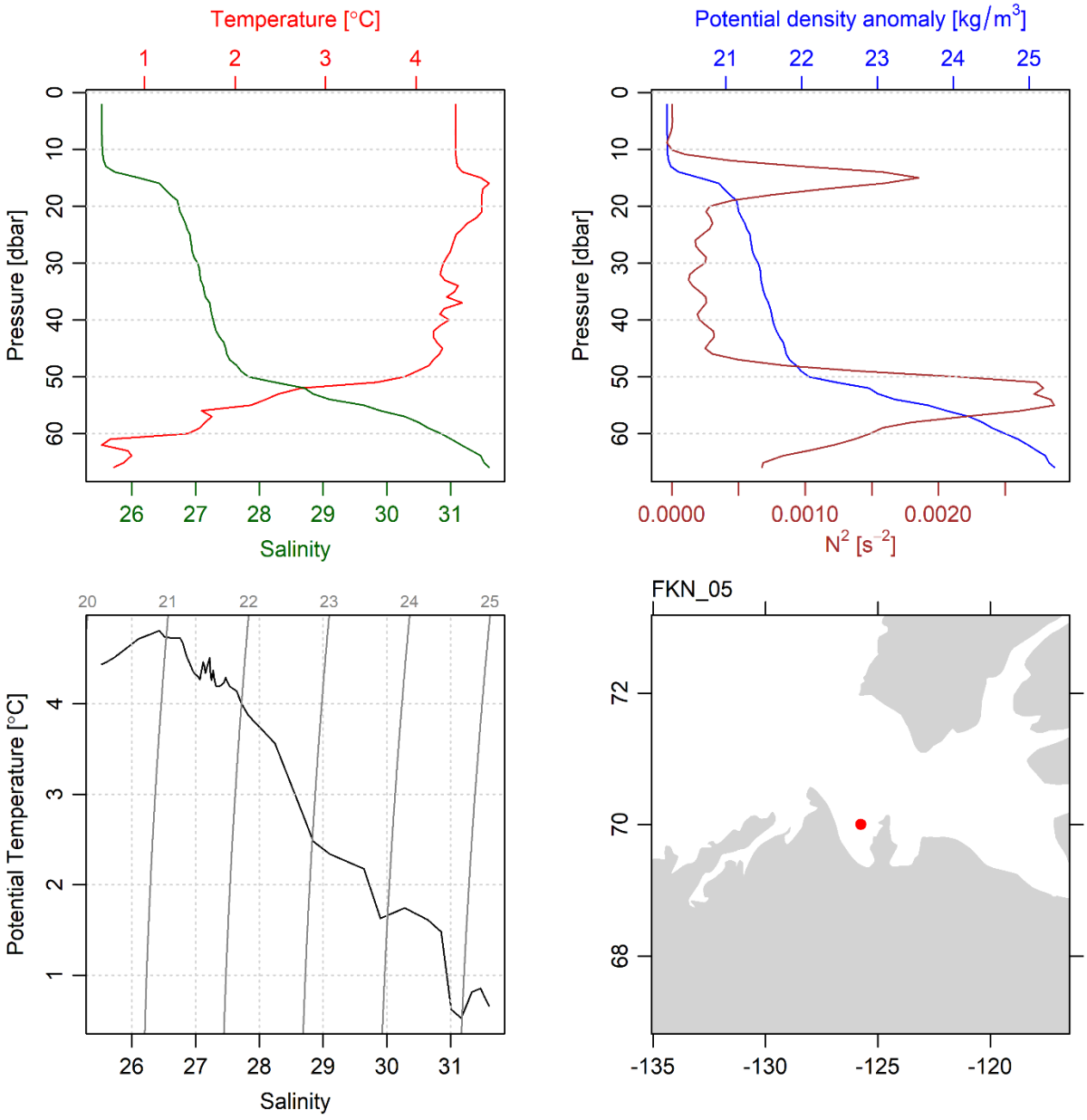
Temperature [°C]
1
2
3
4
Pressure [dbar]
0
10
20
30
40
50
60
26
27
28
29
30
31
Salinity
Potential density anomaly [kg/m3]
21
22
23
24
25
0.0000
0.0010
0.0020
N2 [s−2]
Potential Temperature [°C]
20
21
22
23
24
25
1
2
3
4
FKN_05
72
70
68
-135
-130
-125
-120

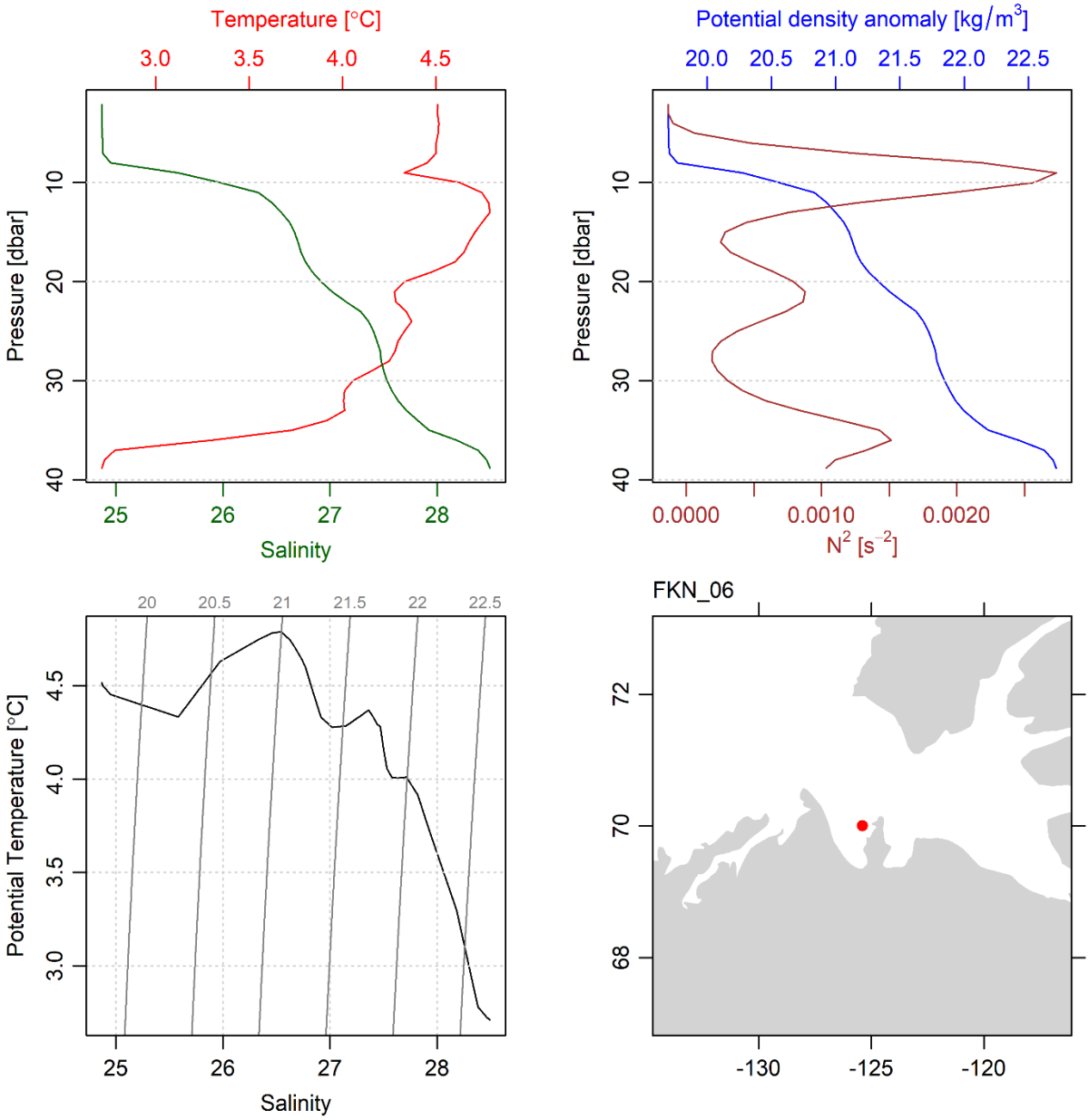
Temperature [°C]
3.0
3.5
4.0
4.5
Pressure [dbar]
10
20
30
40
25
26
27
28
Salinity
Potential density anomaly [kg/m3]
20.0
20.5
21.0
21.5
22.0
22.5
0.0000
0.0010
0.0020
N2 [s−2]
20
20.5
21
21.5
22
22.5
Potential Temperature [°C]
FKN_06
72
70
68
-130
-125
-120

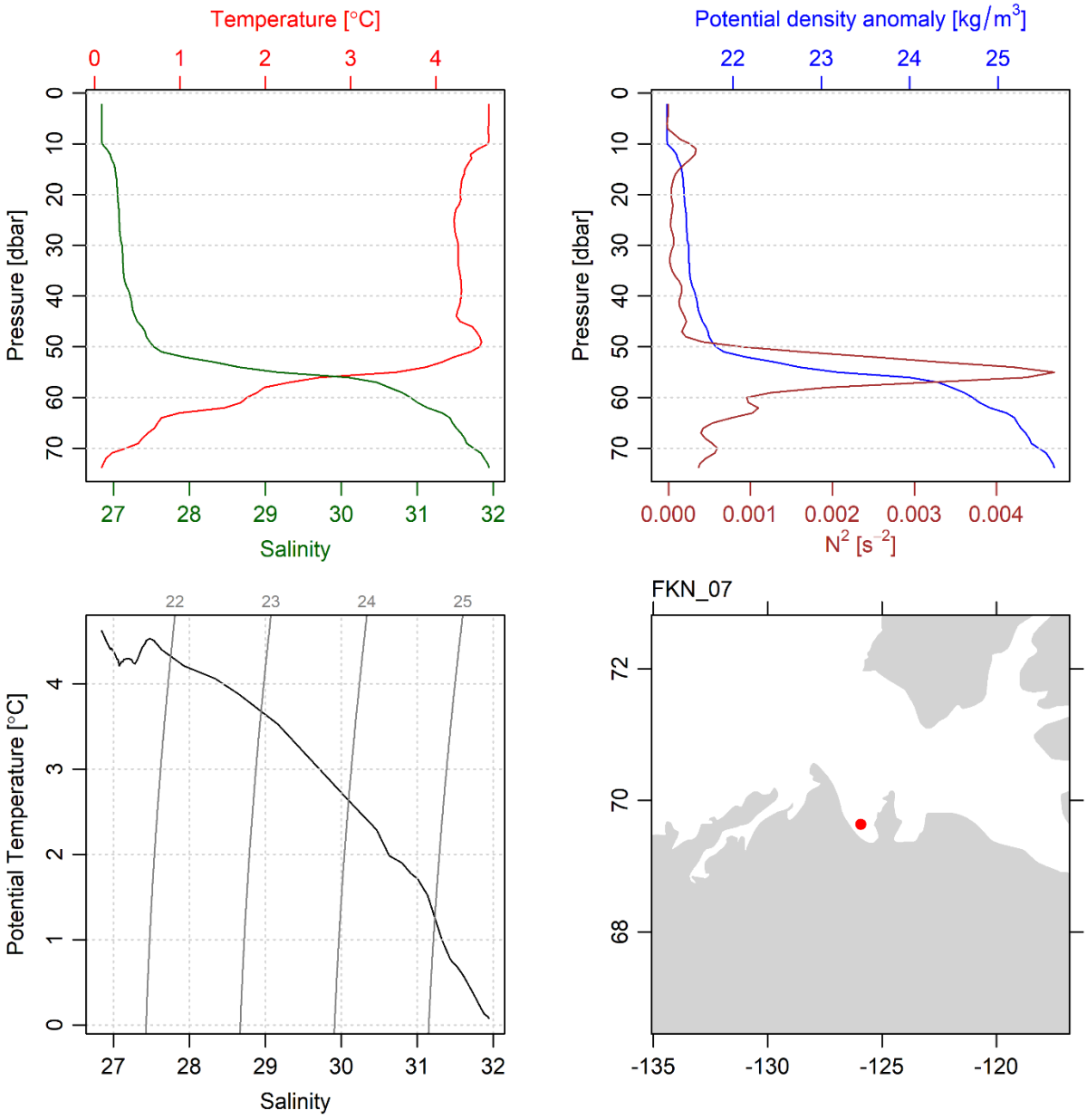
Temperature [°C]
0
1
2
3
4
Pressure [dbar]
0
10
20
30
40
50
60
70
27
28
29
30
31
32
Salinity
Potential density anomaly [kg/m3]
22
23
24
25
0.000
0.001
0.002
0.003
0.004
N2 [s−2]
Potential Temperature [°C]
FKN_07
72
70
68
-135
-130
-125
-120

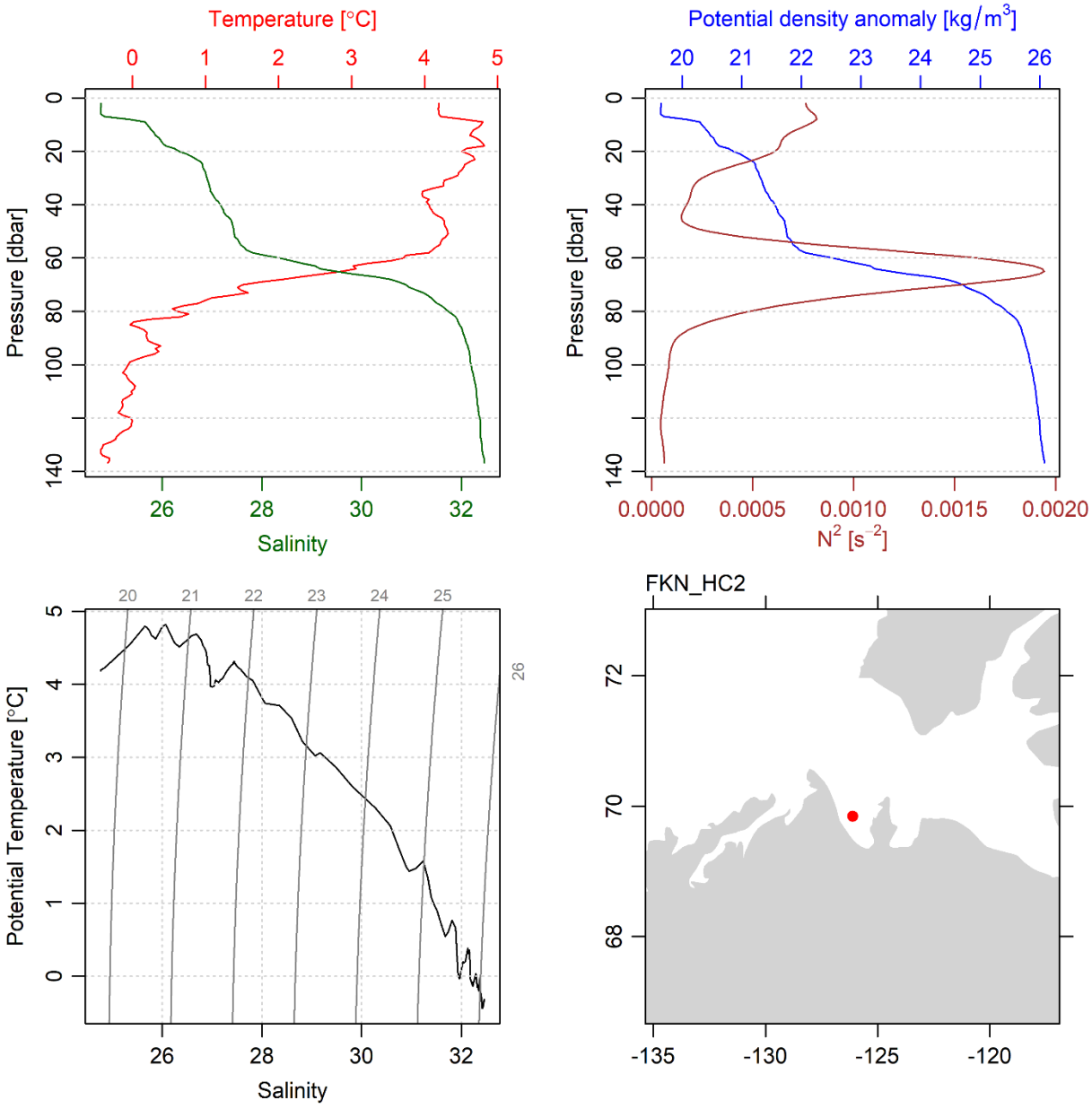
Temperature [°C]
0 1 2 3 4 5
Pressure [dbar]
0 20 40 60 80 100 140
26 28 30 32
Salinity
Potential density anomaly [kg/m3]
20 21 22 23 24 25 26
0.0000 0.0005 0.0010 0.0015 0.0020
N2 [s−2]
Potential Temperature [°C]
20 21 22 23 24 25
26
FKN_HC2
72 70 68
-135 -130 -125 -120

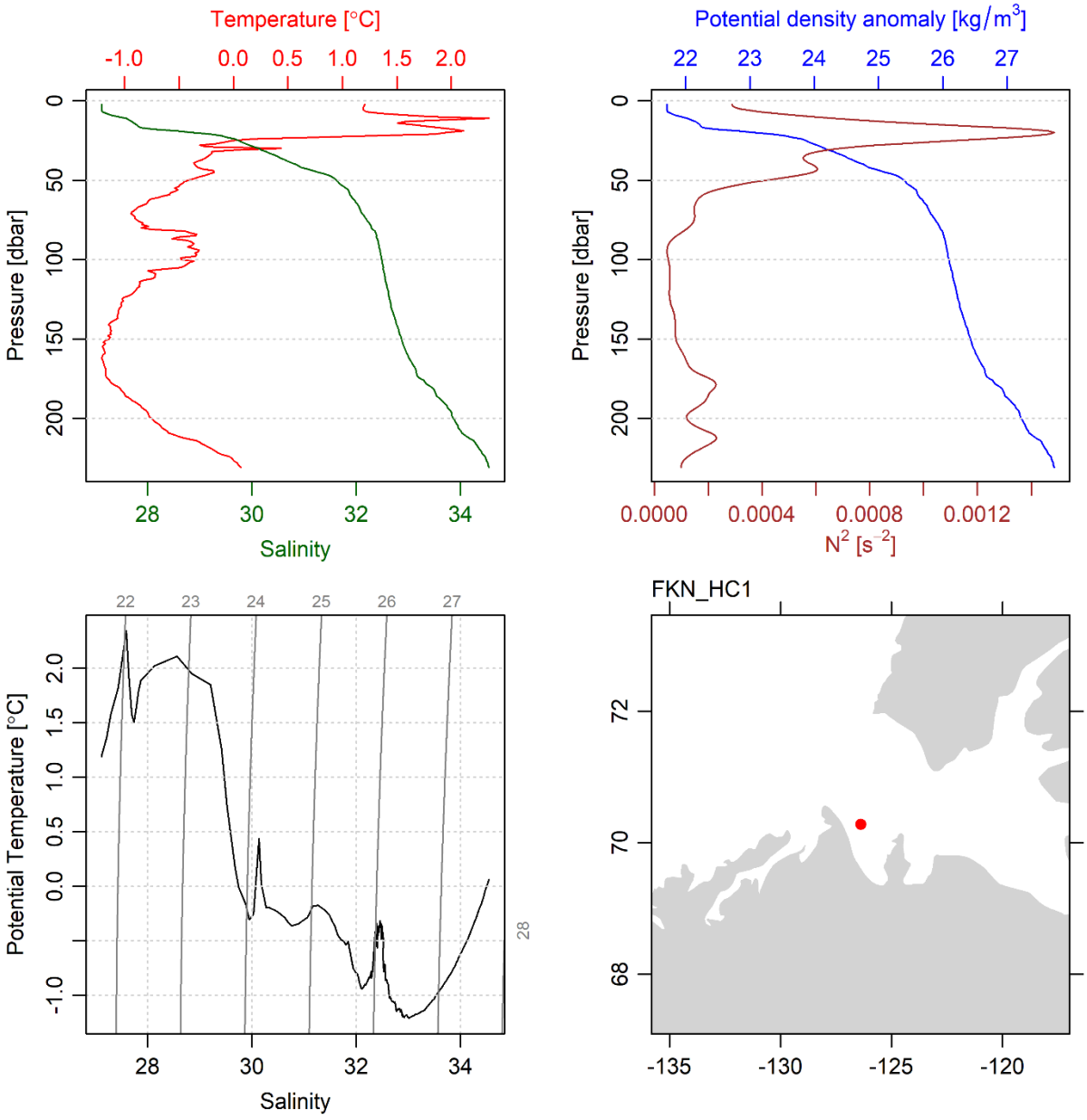
Temperature [°C]
-1.0
0.0
0.5
1.0
1.5
2.0
Pressure [dbar]
0
50
100
150
200
28
30
32
34
Salinity
Potential density anomaly [kg/m3]
22
23
24
25
26
27
0.0000
0.0004
0.0008
0.0012
N2 [s−2]
Potential Temperature [°C]
FKN_HC1
72
70
68
-135
-130
-125
-120

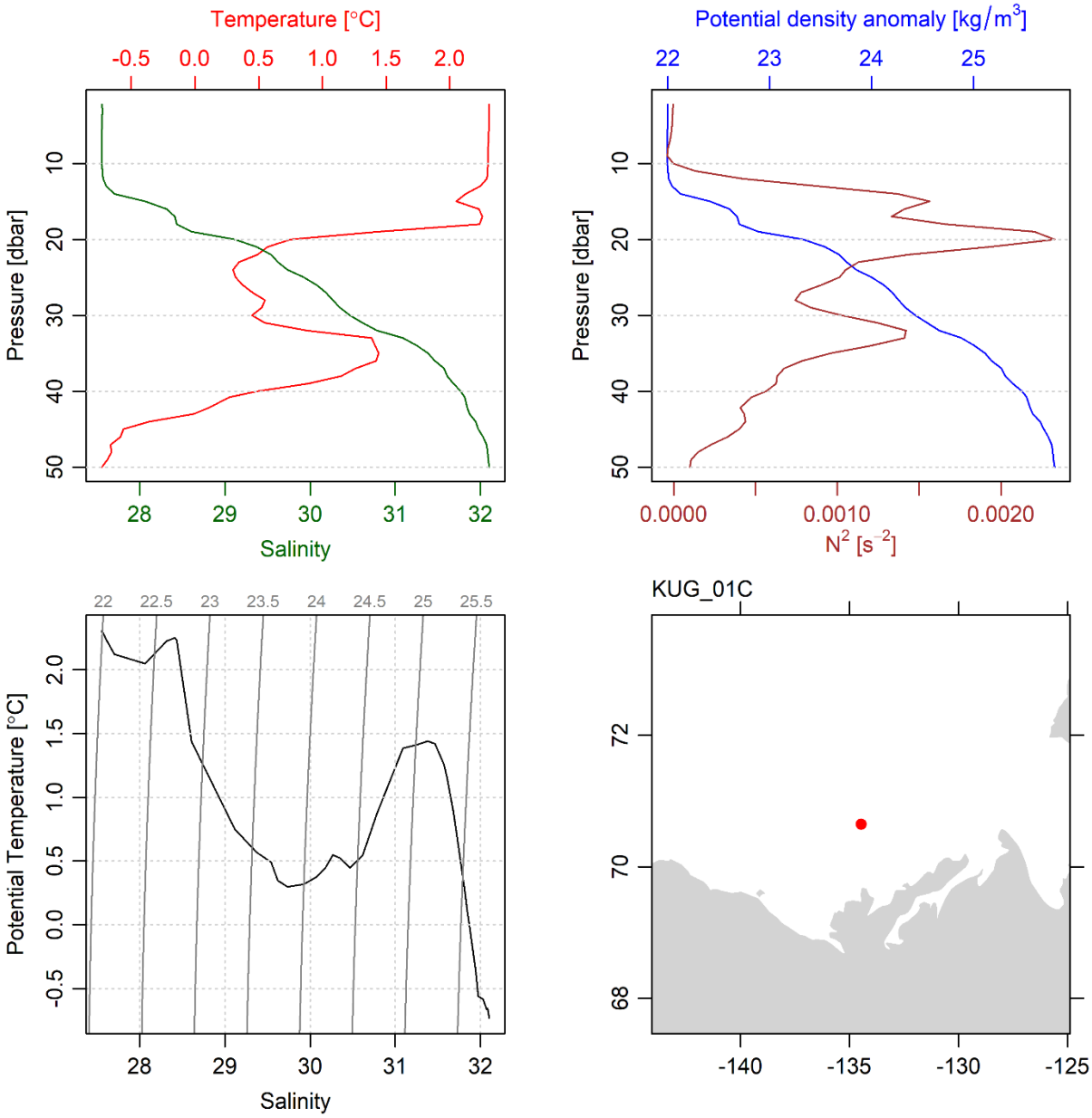
Temperature [°C]
-0.5 0.0 0.5 1.0 1.5 2.0
Pressure [dbar]
10 20 30 40 50
28 29 30 31 32
Salinity
Potential density anomaly [kg/m3]
22 23 24 25
0.0000 0.0010 0.0020
N2 [s−2]
22 22.5 23 23.5 24 24.5 25 25.5
Potential Temperature [°C]
-0.5 0.0 0.5 1.0 1.5 2.0
KUG_01C
68 70 72
-140 -135 -130 -125

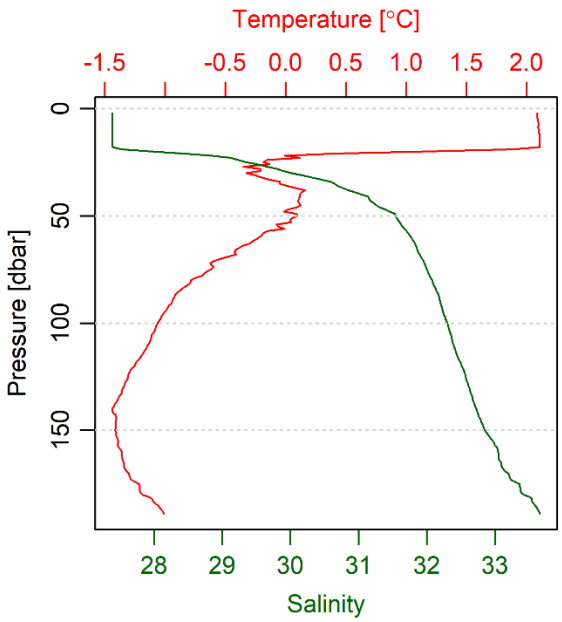
Temperature [°C]
-1.5
-0.5
0.0
0.5
1.0
1.5
2.0
Pressure [dbar]
0
50
100
150
28
29
30
31
32
33
Salinity

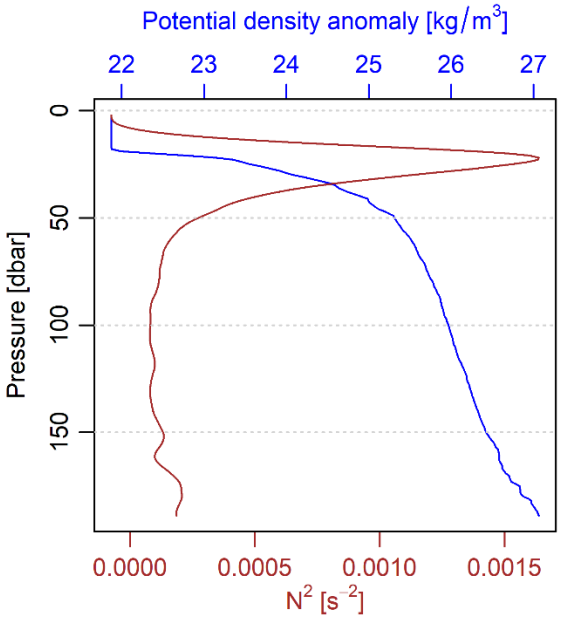
Potential density anomaly [kg/m3]
22
23
24
25
26
27
Pressure [dbar]
0
50
100
150
0.0000
0.0005
0.0010
0.0015
N2 [s−2]

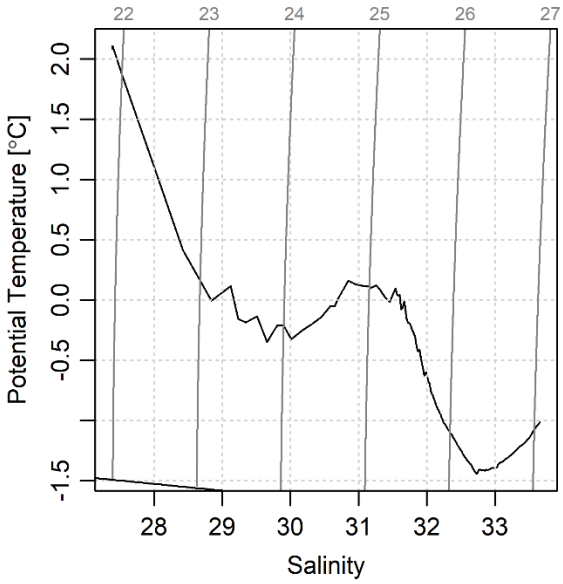
22
23
24
25
26
27
Potential Temperature [°C]
2.0
1.5
1.0
0.5
0.0
-0.5
-1.5
28
29
30
31
32
33
Salinity

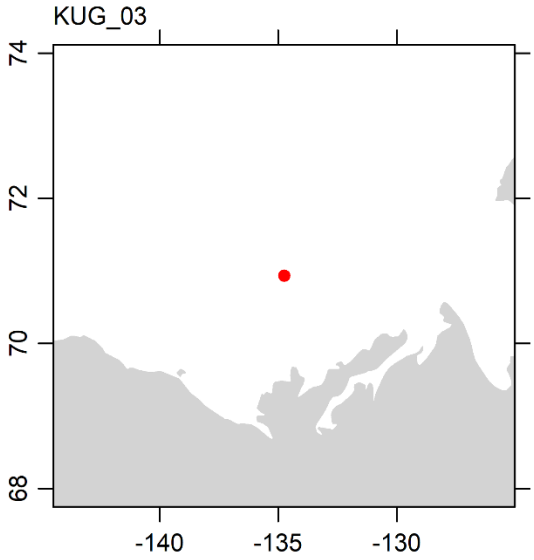
KUG_03
74
72
70
68
-140
-135
-130

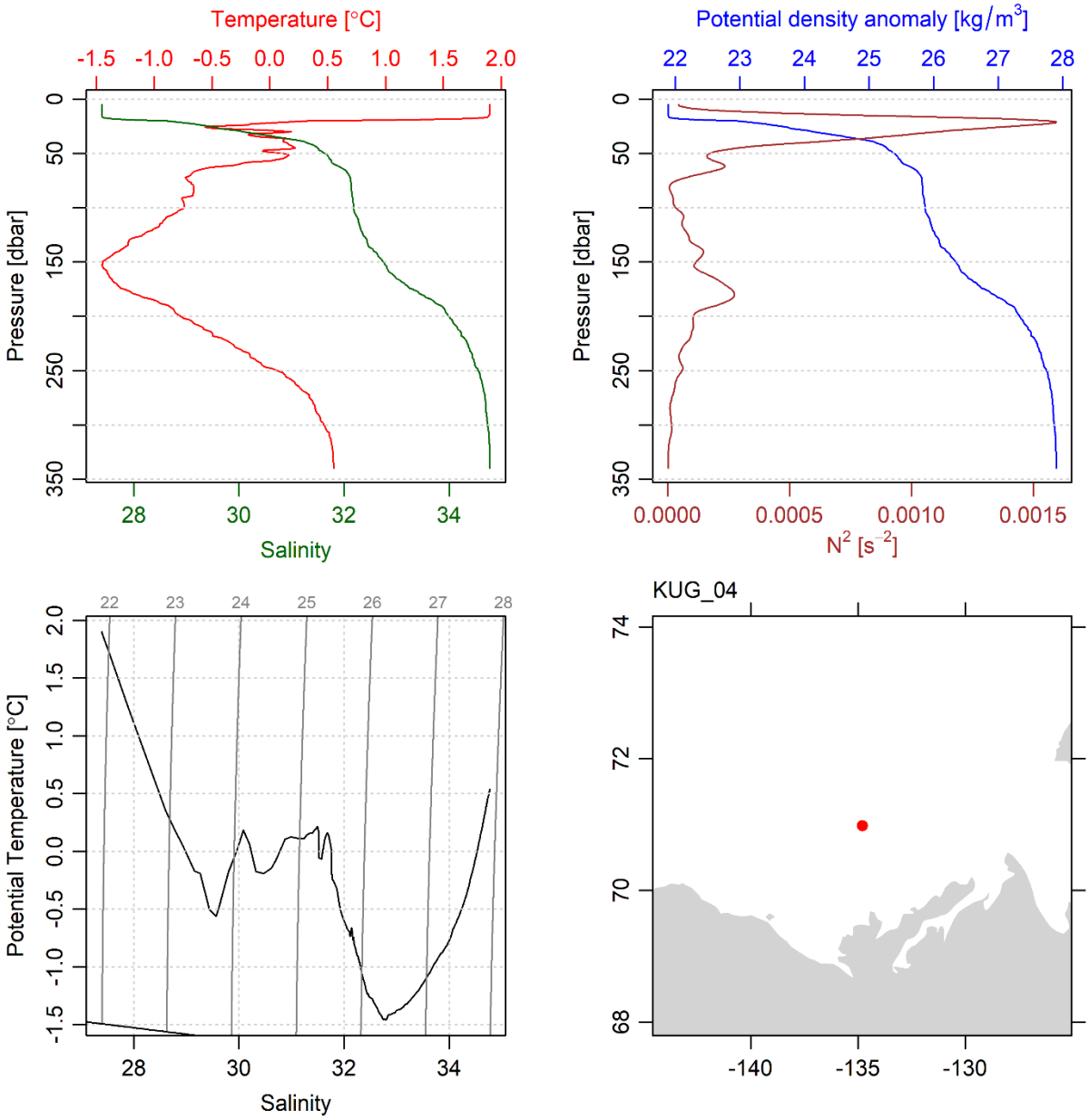
Temperature [°C]
-1.5 -1.0 -0.5 0.0 0.5 1.0 1.5 2.0
Pressure [dbar]
0 50 150 250 350
28 30 32 34
Salinity
Potential density anomaly [kg/m3]
22 23 24 25 26 27 28
0.0000 0.0005 0.0010 0.0015
N2 [s−2]
Potential Temperature [°C]
-1.5 -1.0 -0.5 0.0 0.5 1.0 1.5 2.0
KUG_04
74 72 70 68
-140 -135 -130

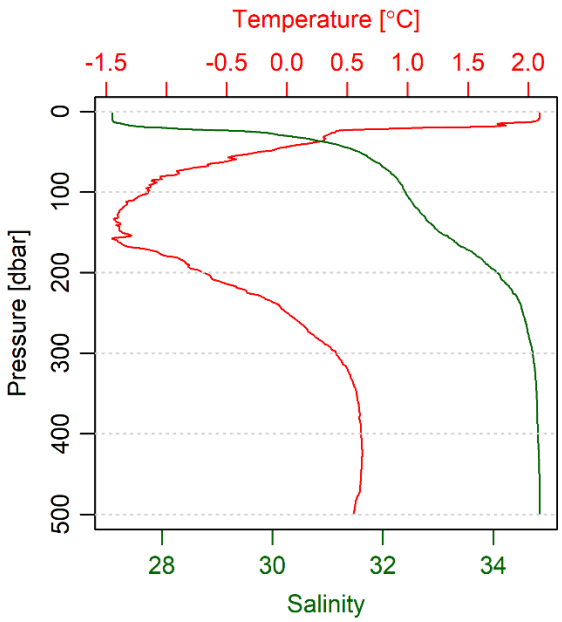
Temperature [°C]
-1.5
-0.5
0.0
0.5
1.0
1.5
2.0
Pressure [dbar]
0
100
200
300
400
500
28
30
32
34
Salinity

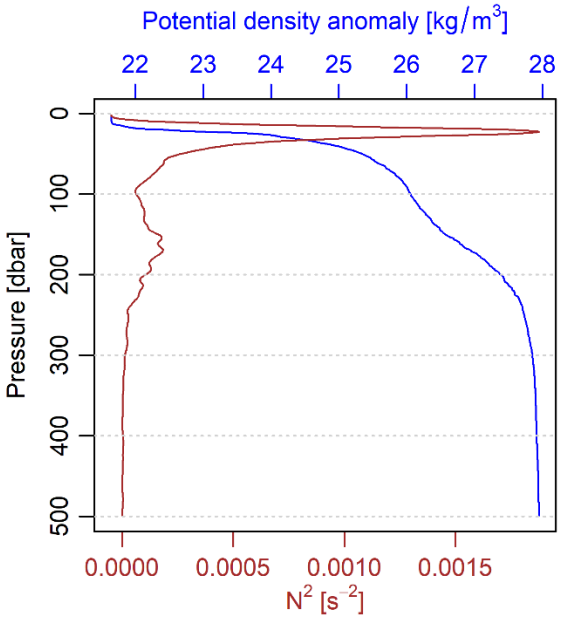
Potential density anomaly [kg/m3]
22
23
24
25
26
27
28
Pressure [dbar]
0
100
200
300
400
500
0.0000
0.0005
0.0010
0.0015
N2 [s−2]

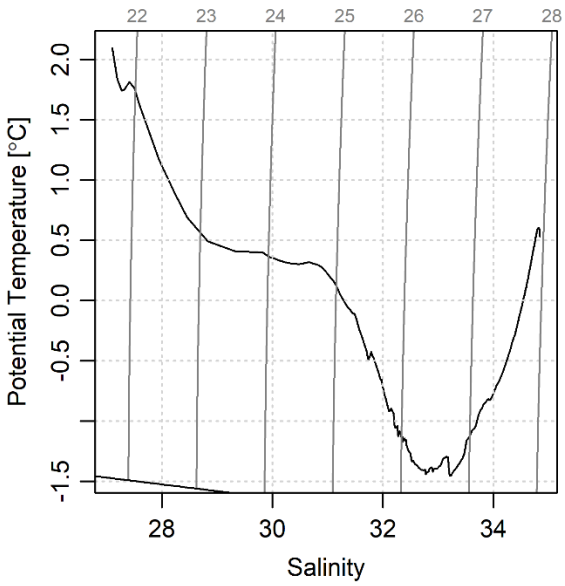
22
23
24
25
26
27
28
Potential Temperature [°C]
2.0
1.5
1.0
0.5
0.0
-0.5
-1.5
28
30
32
34
Salinity

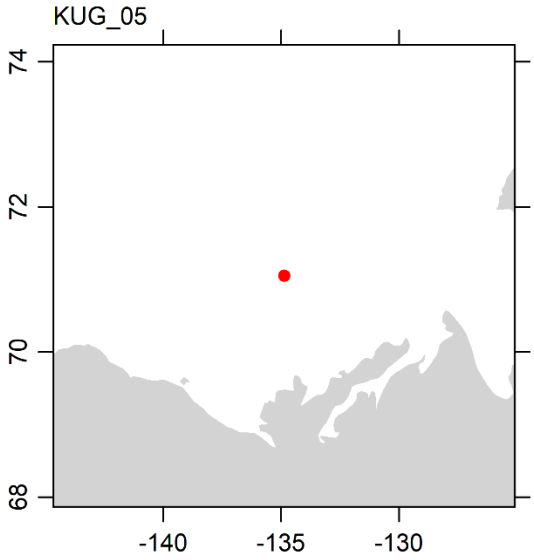
KUG_05
74
72
70
68
-140
-135
-130

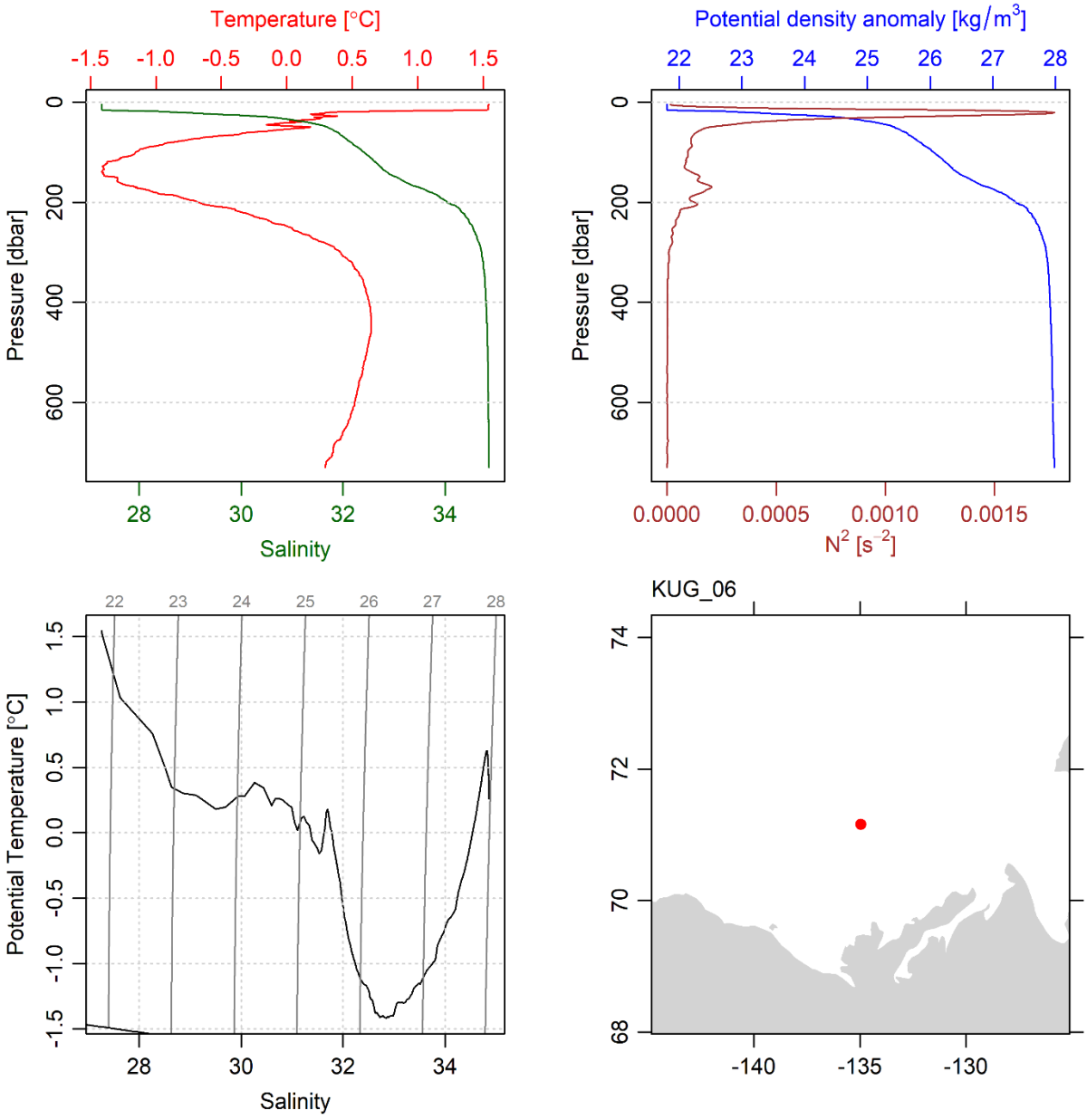
Temperature [°C]
-1.5 -1.0 -0.5 0.0 0.5 1.0 1.5
Pressure [dbar]
0 200 400 600
28 30 32 34
Salinity
Potential density anomaly [kg/m3]
22 23 24 25 26 27 28
0.0000 0.0005 0.0010 0.0015
N2 [s−2]
Potential Temperature [°C]
KUG_06
74 72 70 68
-140 -135 -130

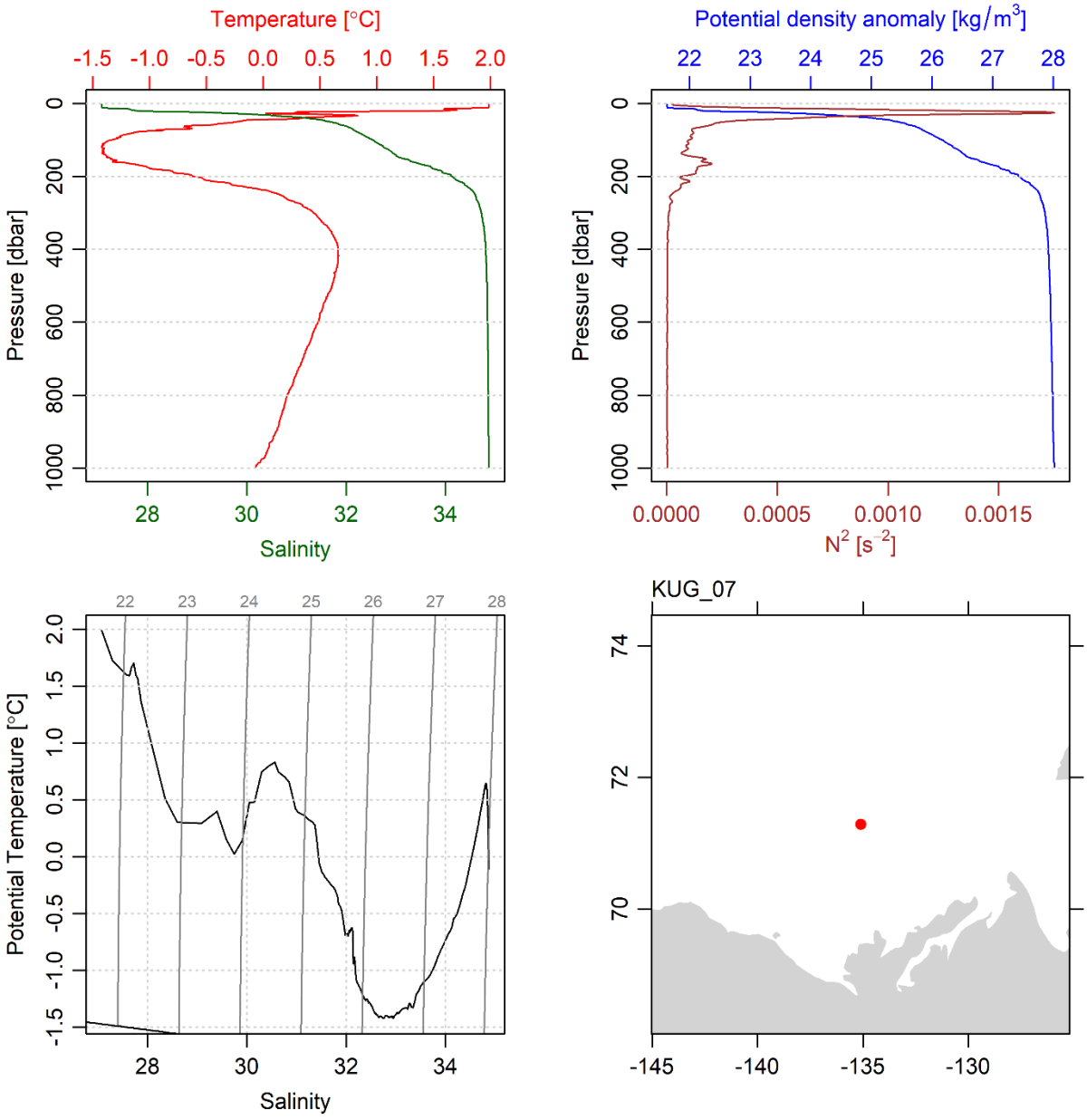
Temperature [°C]
-1.5 -1.0 -0.5 0.0 0.5 1.0 1.5 2.0
Pressure [dbar]
0 200 400 600 800 1000
28 30 32 34
Salinity
Potential density anomaly [kg/m3]
22 23 24 25 26 27 28
0.0000 0.0005 0.0010 0.0015
N2 [s−2]
Potential Temperature [°C]
-1.5 -1.0 -0.5 0.0 0.5 1.0 1.5 2.0
KUG_07
74 72 70
-145 -140 -135 -130

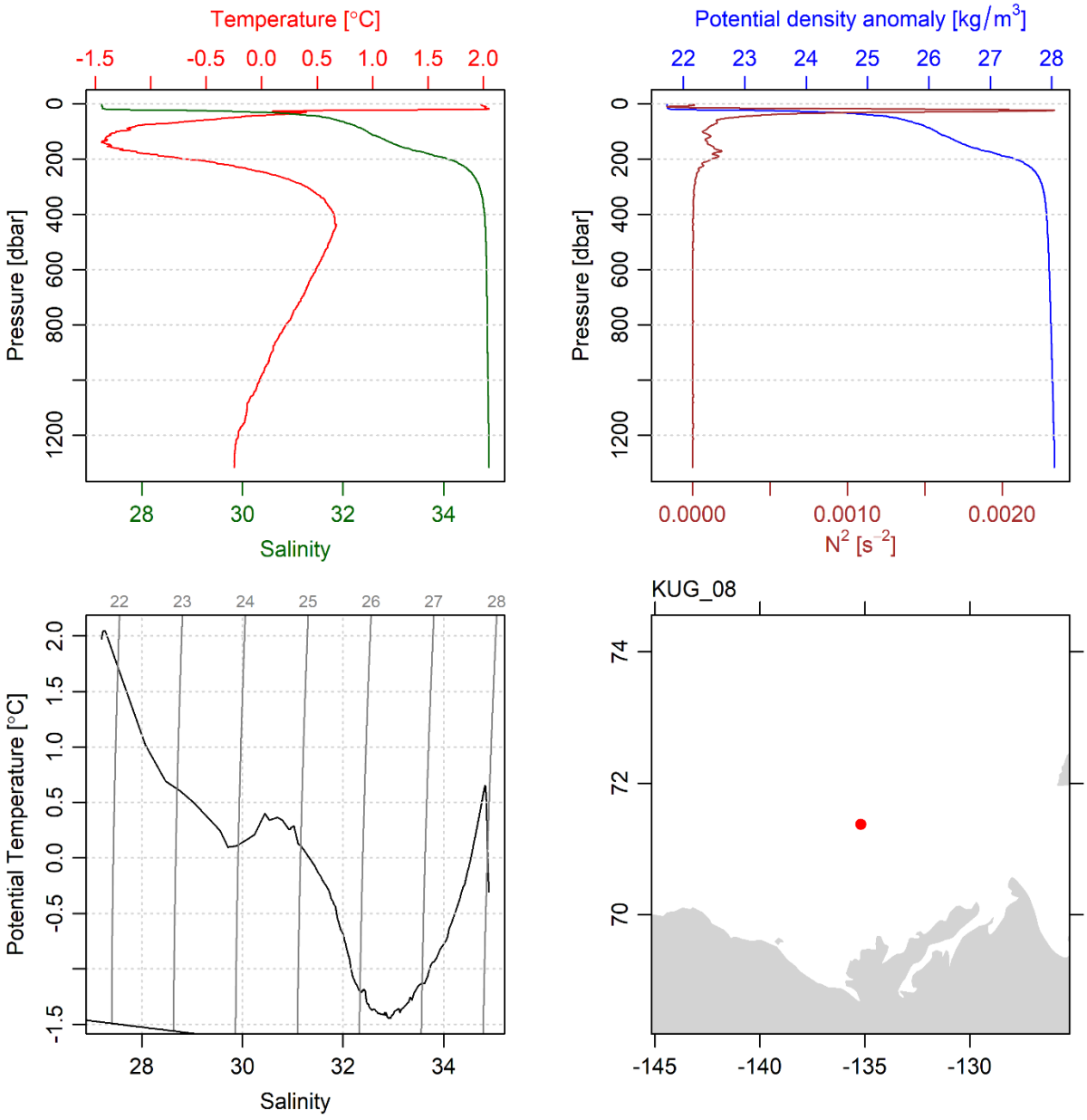
Temperature [°C]
-1.5
-0.5
0.0
0.5
1.0
1.5
2.0
Pressure [dbar]
0
200
400
600
800
1200
28
30
32
34
Salinity
Potential density anomaly [kg/m3]
22
23
24
25
26
27
28
0.0000
0.0010
0.0020
N2 [s−2]
Potential Temperature [°C]
KUG_08
74
72
70
-145
-140
-135
-130